UNIVERSITÀ DEGLI STUDI DI TORINO

Department of Clinical and Biological Sciences

PhD School "Health and Life Sciences"

PhD Programme "Complex Systems for Life Sciences"

PhD Thesis

"Investigating the role of iron in brain diseases: computational models for new diagnostic and therapeutic approaches"

Coordinator: Prof. Enzo Medico

Tutor: Prof. Caterina Guiot

PhD Candidate: Eleonora Ficiarà

Cycle XXXIV

Abstract

Iron is an essential element for brain metabolism and its imbalance is implicated in neurodegeneration, due to its potential neurotoxic effect. However, the role of iron in different pathologies, such as Alzheimer's disease, is not still clearly established.

This work aimed to investigate the potential impact of iron excess in biological fluids for early diagnosis (and the related therapeutic possibility), exploiting a combined computational and experimental approach.

In addition to standard clinical method to detect iron in serum, a precise quantification of total iron in cerebrospinal fluid was performed using graphite-furnace atomic absorption spectrometry in patients affected by Alzheimer's disease, mild cognitive impairment, frontotemporal dementia, and non-demented neurological controls. The application of machine learning techniques was able to detect a potential stratification of patients exploiting iron-related data.

The sensitive balance of iron in the brain is maintained by the brain barriers system, and the alteration of these mechanisms can be involved in neurodegeneration processes. Mathematical models for iron exchange were proposed, providing an indication for the most relevant biological functions that potentially affect the physiological transport of iron across brain barriers.

The results support the involvement of iron dysregulation and its potential interaction with the well-established biomarkers (Tau protein and Amyloid-beta) in the pathophysiology of dementia, fostering the need of further investigation to identify novel disease-modifying therapies counteracting the disease progression.

Furthermore, due to its magnetic properties iron can be managed by new nanomedical tools. Magnetic nanobubbles may act as theranostic carriers for delivering oxygen to improve chemotoxic effect in tumor, performing radio-chemotherapy treatment of brain tumors, and possibly to chelate iron in excess. Brain tumors in difficult locations could be reached by nanobubbles injected into the cerebrospinal fluid and properly guided, in order to release their contents in a sustained and continuous manner. In this work it was showed that magnetic nanobubble are safe, able to be internalized by endothelial cells forming brain barrier, and the stable coating with superparamagnetic iron oxides nanoparticles gives suitable magnetic properties to allow a monitored transport into the tissues by permanent magnets. A new setup aimed to simulate the brain environment and supported by in silico models of magnetic fields was proposed to help precise targeting of the tumors.

Finally, the safety of magnetic nanobubbles was evaluated, in order to finely tune the non-toxic amount of iron released in the tissues but at the same time allowing the nanovectors to be driven by ad hoc tailored magnetic fields.

Summary

Introduction

Iron dyshomeostasis and the consequent toxicity due to iron accumulation are implicated in the pathogenesis of neurodegenerative diseases, such as Alzheimer's disease, gaining an increasing interest in innovative potential diagnostic biomarkers and therapeutic targets.

In addition to the crucial role of iron in biological processes, its magnetic properties are exploited in nanomedicine for several theranostic applications in a broad range of brain diseases, such as brain tumors.

Joining experimental and computational approaches, this work sets goals to contribute to a thorough investigation on the role of iron in the pathophysiology of dementia and on the implementation of novel theranostic uses of nanovectors based on magnetic properties of this metal.

The evidence of excessive accumulation of brain iron in neurodegenerative diseases was assessed. However, the state-of-the-art presents contrasting results about the alteration of iron metabolism monitorable in biofluids, together with an uncomplete understanding of iron pathways involved in neurodegenerative conditions and its progression.

Furthermore, iron is fundamental for biomedical applications of nanotechnology but important issues due to its potential toxicity and methods of administration and monitoring, in particular for brain diseases, in which the management of iron is very sensitive have to be faced.

Starting from these debated points, quantitative measurements were supported by computational models, with the aims to describe the complex interactions and also to be extendable in different biological contexts, for diagnostic and therapeutic purposes.

The work presented in this thesis aims to answer to the following research questions:

1) Is iron overload in brain related to its altered levels in biofluids in dementia?

Quantitative measurements by means of an analytical and reliable method for iron detection in cerebrospinal fluid were performed, potentially helpful for early diagnosis and for a precise tuning of personalized therapy based on iron content. These data were supported by computational cutting-edge models to correlate iron indicators in biofluids with current biomarkers of Alzheimer's disease.

2) Is iron overload in brain related to impaired/excessive passage through the brain barriers?

Mathematical models describing the exchange of iron between blood and brain were proposed, highlighting potential factors involved in impaired mechanisms of passage across the brain barriers, which can guide innovative therapeutic approaches.

3) Can magnetic properties of iron be exploited in novel biomedical applications, such as brain tumors targeting and potential therapeutic strategies for neurodegenerative diseases based on iron chelating agents?

A new setup, supported by computational models, was proposed for magnetic driving and monitoring of multi-functional theranostic nanovectors, together with the assessment of their toxicity in a brain model.

The thesis is structured as follows:

- Chapter 1: the state-of-the-art of the role of iron in neurodegenerative diseases, especially Alzheimer's disease, as well as the techniques for the evaluation of the most popular iron indicators and the related interpretation is described; the second part focuses on the functions of the brain barriers system in the regulation of iron trafficking between the periphery and the brain, pointing out their emergent involvement in neurodegenerative diseases. In the third part, an up-to-date framework of the applications of magnetic nanoparticles (composed of iron) in the central nervous system is presented, underlining the critical issues related to their use.
- Chapter 2 presents the main objectives of the work.
- Chapter 3 concerns the accurate description of fine-tuned analytical protocol for the quantification of iron in cerebrospinal fluid, and the results obtained from the analysis of a population of patients affected by different form of dementia and neurological controls.
- In Chapter 4 mathematical models of brain barriers system are proposed to evaluate the potential alteration of mechanisms related to iron exchange between blood and brain, with a special focus on the relative parameters uncertainty.
- In Chapter 5 a model of physically drivable magnetic nanobubbles is presented as novel multipurpose theranostic carriers in the central nervous system, showing their potentiality to cross brain barriers and to be guided for a precise targeting.
- In Chapter 6 novel computational models for magnetic driving and monitoring of magnetic nanobubbles for applications in the central nervous system, such as brain tumors, are investigated especially concerning their magnetic properties and toxicity.

Lastly, after a final discussion of the overall findings of this work, conclusions and future perspectives are considered.

Chapter 1: Background

1.1 Role of Iron in CNS

This section is partly based on:
Ficiarà E. †, Munir Z. †, Boschi S., Caligiuri M.E., Guiot C., *Int. J. Mol. Sci.* 2021, 22(9), 4479.

Iron is a *d*-block transition metal, with reactive properties and with excellent redox potential. It can readily donate and accept electrons to participate in oxidation-reduction reactions that are essential for a number of fundamental biological processes (Pantopoulos et al., 2012). Iron exists in two ionic states, Fe^{3+} and Fe^{2+}. Free (unbound) iron can be toxic since it readily combines with oxygen and nitric oxide, catalyzing the formation of a highly reactive hydroxyl group (OH-) and peroxynitrite (ONOO-) resulting in oxidative and nitrosative damage to proteins, lipids, and nucleic acids (Koskenkorva-Frank et al., 2013).

Therefore, most of the circulating and stored iron is linked to proteins and other transporters, and cells are equipped with proteins for iron uptake to secure its vital functions and limit its potential toxicity. Not only iron binding to glycoprotein ligands prevents toxicity but the nature of the ligands finely modulates the redox potential of iron.

The crucial role of iron in health and diseases has been recognized for a long time, together with its very sensitive distribution in the human body, sophisticated pathways to import, chaperone, sequester, and export iron in order to maintain an appropriate balance (Hentze et al., 2010).

Healthy adult bodies contain 4–5 g of iron. Iron is mostly (65%) bound in red blood cell hemoglobin (Hb), and 30–35% is stored in the liver in the form of ferritin. Iron is also in the form of iron-sulfur clusters or heme in the enzymes and multiprotein complexes (Darshan et al., 2010; Muñoz et al., 2011). The body absorbs 1–2 mg of dietary iron a day, and this intake is balanced with losses in the form of sloughed intestinal mucosal cells, and other blood losses (Siah et al., 2006).

Iron is an essential micronutrient due to its relevance in the process of erythropoiesis, oxidative metabolism, and cellular immune responses (Manuel Muñoz et al., 2009). In humans, iron is incorporated into proteins as a component of heme (e.g. hemoglobin, myoglobin, cytochrome proteins, myeloperoxidase, nitric oxide synthetases), iron-sulfur clusters (e.g. respiratory complexes I-III, coenzyme Q_{10}, mitochondrial aconitase, DNA primase), or other functional groups (Evstatiev and Gasche, 2012). These iron-containing proteins are required for vital cellular and organism functions including oxygen transport, mitochondrial respiration, intermediary and xenobiotic metabolism, nucleic acid replication and repair, host defense, and cell signaling. The remaining iron-dependent proteins are specifically involved in iron absorption (divalent metal transporter-1, DMT1)), export (ferroportin, Fpn) storage (ferritin, Ft), and transport (transferrin, Tf).

The complex and multi-hierarchy iron metabolism may be divided into different steps:

a) Active transport of dietary iron in the gastrointestinal tract by enterocytes for iron entry into the bloodstream;

b) Transport of iron through the bloodstream;

c) Entry of iron into different tissues and cells;

d) Regulation of intracellular levels, trafficking, and metabolization of iron.

The major route of iron acquisition is intestinal absorption (Figure 1), where dietary Fe^{3+} is reduced to Fe^{2+} by the ferrireductase enzyme duodenal cytochrome B (DcytB), localized at the apical surface of enterocytes (Anderson and Frazer, 2017). The divalent Fe^{2+} ions enter the duodenal enterocytes via the divalent metal transporter 1 (DMT1), a duodenal brush-border membrane protein specific for ferrous iron, zinc(II), and copper(II) (Gunshin et al., 1997). This transport is a proton(H^+)-coupled and depends on the presence of luminal H^+ ions. When there is a low demand for iron in the body, iron is stored within the enterocytes in the form of ferritin, an intracellular iron storage protein (Gulec et al., 2014).

Ferritin is a ubiquitous, mainly cytosolic, globular protein of 450 kDa comprising 24 subunits of Ft-H and Ft-L chains (Arosio et al., 2009; Arosio and Levi, 2010). Ft-H possesses an active ferroxidase center that catalyzes the oxidation of Fe^{2+} to the Fe^{3+} form, while Ft-L promotes its nucleation within the protein shell for storage. Together, these chains form a nano-cage storing approximately 4500 Fe^{3+} ions in a bioavailable and non-toxic form (as mineral ferrihydrite) (Miller et al., 1991; Leggett et al., 1993; Theil, 2003). The precise mechanism of binding, storage, and release of iron from ferritin requires further clarification. Available information suggests that a cytosolic iron chaperone Poly (rC)-binding protein 1 binds cytosolic iron for delivery to ferritin (Shi et al., 2008). Ferritin-binding proteins, amino acids, and small molecules regulate the release of iron from ferritin, supporting the gated pore model, but requiring further characterization (Liu et al., 2003, 2007; Theil et al., 2008). Stored iron is released in response to low intracellular iron, thus maintaining equilibrium between ferritin iron and free iron, which constitutes the so-called Labile Iron Pool (LIP).

On the other hand, when iron demand is high, the absorbed ferrous iron is transported across the basolateral membrane into blood. This phase is controlled by ferroportin 1 (FPN1), a ferrous iron export protein modulating the quantity of enterocyte iron absorbed into the circulation and available to the body (McKie et al., 2000).

Iron transportation in the bloodstream is performed by the plasma protein transferrin (Tf) (Wessling-Resnick, 2006) which requires the transformation of ferrous iron back to ferric iron. This step is achieved by hephaestin (HEPH), a multi-copper ferroxidase enzyme anchored to the basolateral enterocyte membrane and coupled to FPN1, which catalyzes the oxidation of Fe^{2+} to Fe^{3+} ions (Chen et al., 2004). Then, Fe^{3+} binds to Tf, which has a high affinity for Fe^{3+} and enables iron transport around the body organs, i.e., in the brain. Apotransferrin (apo-Tf) is the unbound form of this transporter and contains two ferric binding sites, of which none, one, or both may be filled. Under physiological conditions, only about 30% of Tf is saturated (Pantopoulos et al., 2012). Tf is the primary iron-transport protein with a half-life of 8 to 10 days that reflects both protein and iron status. Iron with Tf maintains Fe^{3+} in a soluble form under physiological conditions, facilitates regulated iron transport and cellular uptake, and maintains Fe^{3+} in a redox-inert state, preventing the production of toxic free radicals (Gkouvatsos et al., 2012).

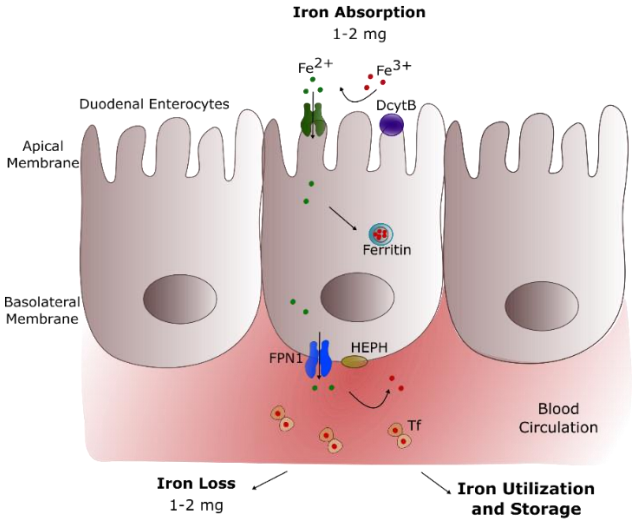

Figure 1.1 Mechanism of systemic iron metabolism. After being reduced by DcytB at the apical membrane of duodenal enterocytes, dietary iron is absorbed by DMT1 and driven to the basolateral membrane of these cells; iron is exported by FPN1 to the circulation, transformed from ferrous to ferric iron by HEPH, and finally transported by Tf in the blood. Abbreviations, DcytB—duodenal cytochrome B, DMT1—divalent metal transporter-1, FPN1— ferroportin-1, HEPH—hephaestin, Tf—transferrin. Adapted from (Ficiarà et al., 2021c).

1.1.1 Iron in Brain *(Ficiarà et al., 2021c)*

Brain iron levels are tightly regulated to ensure the normal function of the Central Nervous System (CNS) and to prevent high sensitivity of CNS to toxicity (Hentze et al., 2004; Moos et al., 2007).

The brain is among the most metabolically active organs in the body and accounts for at least 20% of the body's energy consumption, although representing only about 2% of its weight. Iron plays a fundamental role during ATP production, as a cofactor in the oxidative chain, for cytochromes and iron-sulfur complexes (Lill et al., 2012). About 75–80% of the energy supports neuronal activity, with the remainder utilized to sustain the functions of astrocytes, oligodendrocytes, and microglia (Magistretti and Allaman, 2015). Both axonal and synaptic signaling need neuronal energy, but the major part is used post-synaptically (Alle et al., 2009). The mitochondrial function must supply ATP, and iron is necessary to support oxidative phosphorylation.

Accordingly, an adequate supply of iron is necessary to sustain its high-energy needs (Beard and Connor, 2003; Falkowska et al., 2015; Magistretti and Allaman, 2015). Therefore, iron is the most abundant metal in the brain (Ashraf et al., 2018). It is a co-factor involved in oxygen transportation, DNA synthesis, mitochondrial respiration, myelin synthesis, neurotransmitter synthesis, and metabolism (Madsen and Gitlin, 2007; Salvador, 2010) but can become neurotoxic when there is excessive intracellular accumulation (Andersen et al., 2014; Dixon and Stockwell, 2014). The systemic organs and the brain share the same iron regulatory mechanisms and pathways based on iron-modulating proteins, providing a link to the maintenance of iron homeostasis within the brain (Singh et al., 2014).

The delicate balance of iron in the brain milieu is mainly maintained by the brain barrier systems, coordinating the direction of iron fluxes between the blood and brain/cerebrospinal fluid (CSF) (Zheng and Monnot, 2012).

Brain iron concentrations are not static: they increase with age and in many diseases and decrease when iron is deficient in the diet. *In vivo* Magnetic Resonance Imaging (MRI) shows that iron deposition increases in numerous age-dependent neurodegenerative diseases, such as Parkinson's and Alzheimer's disease (AD), and accumulates mainly in the basal ganglia (Bartzokis et al., 2004; Langkammer et al., 2014). Moreover, increased levels of iron have been associated with motor and cognitive impairment in the elderly (Pujol et al., 1992). Iron is believed to enter the brain via the blood-brain barrier (BBB) by Tf receptor-mediated endocytosis in the brain capillaries and released back to circulation via CSF (Moos et al., 2006). Iron is present in various cell types in the CNS but is abundant in the astrocytes (star-shaped glial cells), which has given rise to the idea that glial cells are involved in iron storage and regulation (Madsen and Gitlin, 2007).

Table 1.1 Table for the description of iron-related proteins involved in the uptake, regulation, transport, and storage of iron from blood to brain. Abbreviations: BBB —blood-brain barrier, BCSFB —blood-cerebrospinal fluid barrier, CSF—cerebrospinal fluid, Cp—ceruloplasmin, DcytB—duodenal cytochrome B, DMT1—divalent metal transporter-1, FPN1—ferroportin-1, Ft—ferritin, HEPH—hephaestin, LIP—labile iron pool, Tf—transferrin, TfR—transferrin receptor. Adapted from (Ficiarà et al., 2021c).

Body Compartment/Structure	Iron Uptake	Iron Transport/Regulation	Iron Storage
Intestinal Lumen-Enterocytes	DMT1	DcytB FPN1 HEPH Cp	Ft
Blood	Release from enterocytes (FPN1)	Tf Apo-Tf Hepcidin	Ft
	TfR DMT1	DcytB DMT1 FPN1 HEPH, Cp	Ft
Brain-CSF	Entry from brain barriers TfR DMT1	Tf, Apo-Tf FPN1, DMT1 Cp	Ft

Iron enters the brain cells through a variety of transporters, mainly via receptor-mediated endocytosis and it is released from Tf inside the cells following a fine molecular mechanism (Hare et al., 2013a). Iron uptake in neurons is regulated by the expression both Transferrin Receptors 1 (TfR1)

and Divalent Metal Transporters (DMT1) (Ke and Qian, 2007). TfR1 is a ubiquitously expressed membrane protein with high affinity to Fe2-Tf. At neutral pH, TfR1 has a low affinity for apo-Tf (iron-free), not acting unligated Tf as a competitive inhibitor of iron-bound uptake (Aisen, 2004). Fe2-Tf forms a complex with the TfR1 receptor at the cell surface. This complex colocalize to clathrin-coated pits, which invaginate to initiate the process of endocytosis and to form specialized endosomes. A proton pump mechanism lowers the pH within the endosome, with consequent conformational change to both the Fe2Tf and TfR1 units, in turn resulting in release of the iron from its chaperoning protein (Hentze et al., 2004). The newly freed Fe^{3+} is quickly reduced by the six-transmembrane epithelial antigen of prostate1-4 (STEP 1-4), exporting Fe^{2+} from the endosome into the cytosol by DMT1(De Domenico et al., 2008). In the acidic endosome, the interaction between apo-Tf and Tf receptor (strong affinity) prevents the degradation of free Tf when the endosome complexes with the lysosome before exocytosis. During exocytosis the pH returns to neutral, dissociating the apo-Tf from the TfR1, with an effective recycle of the Tf molecule for use in iron circulation and further round of iron delivery (Dautry-Varsat et al., 1983). The iron can be targeted to the mitochondria, and/or also stored in the form of ferritin and haemosiderin. The only known export pathway in mammalian cells is mediated via Fpn, allowing ferrous iron to be transported out of the cell (Ganz, 2005). This process requires a ferroxidase to oxidize the ferrous iron to ferric, so that Tf can bind the exported iron. In the brain, Fpn has been identified in both neurons and astrocytes. Astrocytes are ideally positioned to take up iron from the circulation and distribute it to other cells in the CNS, having the iron influx and efflux mechanisms needed for cell-to-cell transport of iron. DMT1 is expressed by astrocytes and probably mediates iron influx into these glial cells. Astrocytes are devoid of TfR1, and NTBI is most likely their major iron source (Moos and Morgan, 2004). Then, iron is required for myelin synthesis on oligodendrocytes but these latter import it through a TfR1-independent mechanism, based on the passage into the cytosol complexed with LMW ligands and the consequent incorporation into Tf produced within the oligodendrocyte itself (Moos et al., 2007). In 1999, a homolog Tf receptor, TfR2, was identified (Kawabata et al., 1999), which has a 30-fold lower affinity to iron-bound Tf, yet mutations to the TfR2 gene results in hereditary hemochromatosis (Camaschella et al., 2000). Neuronal iron supply is tightly controlled: it depends not only on transferrin-bound iron but also on non-transferrin-bound iron (NTBI), which represents a relevant quote of the iron physiologically present in the cerebrospinal fluid (CSF) (Codazzi et al., 2015).

1.1.2 Toxicity of Iron: Ferroptosis (Ficiarà et al., 2021c)

Excess iron can induce oxidative stress by generating Reactive Oxygen Species (ROS). Iron can promote radical formation by catalyzing autoxidation, initiating lipid peroxidation, and reacting with hydrogen peroxide with consequent production of more highly reactive and toxic species by means of specific reactions (Winterbourn, 1995), such as Fenton and Haber-Weiss reactions (Fenton 1894, Haber and Weiss 1934), inducing the release of iron from mitochondrial iron–sulphur cluster proteins of the respiratory chain and other iron storage proteins, which will lead to further ROS production via Fenton's reaction. Consequently, excess iron stores may increase pro-oxidant reactions and generation of free radicals, inducing cellular death in neurodegeneration. Furthermore, iron can be

involved in inflammation processes, which play a key role in mediating cellular death and destruction via poorly liganded iron (Kell, 2009). Different stress conditions (chronic or acute) lead to distinctive patterns of intracellular iron overload, an accumulation of redox inert iron in intracellular vesicles (ferritin and lysosomes) or an increase in the redox active free intracellular LIP (Eid et al., 2017).

In 2012, Dixon first proposed the concept of ferroptosis., i.e. iron-dependent cell death characterized by the accumulation of lipid ROS which is morphologically, biochemically, and genetically distinguished from other forms of cell death including apoptosis, necrosis, autophagy, and pyroptosis (Dixon et al., 2012; Xie et al., 2016; Yang and Stockwell, 2016).

Morphologically, cell ferroptosis has been featured by decreased mitochondrial volume, increased bilayer membrane density, and reduction or disappearance of mitochondrial cristae (Yang and Stockwell, 2008; Dixon et al., 2012; Xie et al., 2016), but the cell membrane is preserved and the nucleus remains normal in size. Biochemically, intracellular glutathione (GSH) depletion and decreased activity of glutathione peroxidase 4 (GPX4), lipid peroxides cannot be metabolized by the GPX4-catalyzed reduction reaction, and Fe^{2+} oxidizes lipids in a Fenton-like manner, resulting in a large amount of ROS, promoting ferroptosis (Yang and Stockwell, 2008; Friedmann Angeli et al., 2014; Stockwell et al., 2017). Genetically, ferroptosis is a biological process interesting iron homeostasis and lipid peroxidation metabolism, regulated by genes involved in iron metabolism via the Tf/TfR1 complex, iron-sulfur cluster assembly enzyme, and ferritin (Dixon et al., 2012).

Ferroptosis can be triggered by pharmacological impairment of anti-oxidant systems involving GSH and GPX4 (Stockwell et al., 2017). The glutamate/cystine antiporter (x_c^-) exports cellular glutamate in exchange for extracellular cystine. Once inside the cell, cystine is converted to cysteine, a precursor of the endogenous anti-oxidant, GSH (Dixon et al., 2012). Erastin and sorafenib, trigger ferroptosis via inhibition of x_c^-, depleting GSH and inactivating GPX4 (Yang et al., 2014; Stockwell et al., 2017). Ferroptosis may also be induced by administration of GPX4 inhibitors, RSL3 and ML162. GPX4 catalyzes potentially toxic lipid hydroperoxides to non-toxic lipid alcohols (Yang et al., 2016) and its inactivation, via GSH depletion or direct GPX4 inhibition, inducing lipid peroxidation/oxidative stress, and eventually cell death (Figure 2). Deferoxamine is able to prevent ferroptosis-induced cell death through quenching of excess iron (Murphy et al., 1989; Cao and Dixon, 2016).

Interestingly, the hallmarks of ferroptosis (iron dysregulation, lipid peroxidation, inflammation) are related to neurodegeneration and cognitive impairment (Hambright et al., 2017; Yan and Zhang, 2020).

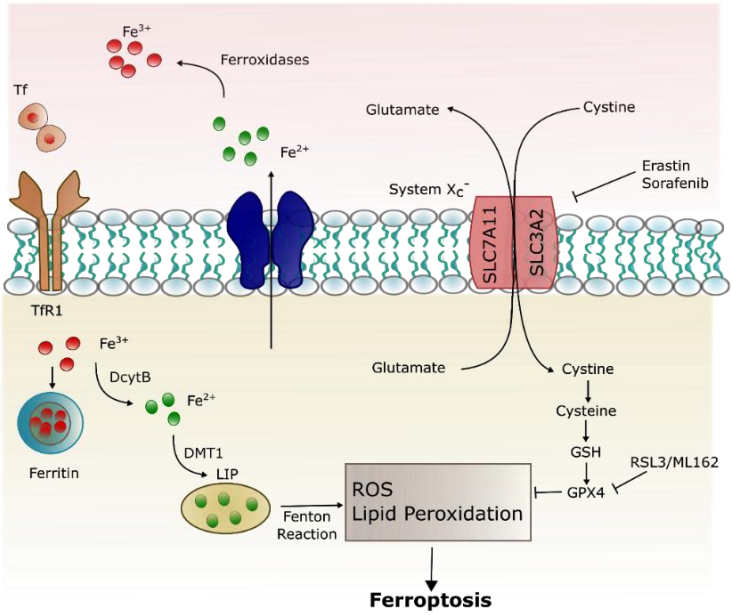

Figure 1.2. Ferroptosis pathway. Ferroptosis can be initiated through Tf endocytosis linked to TfR1. Ferric iron (also stored in ferritin) is released from the TfR1 complex and reduced to ferrous iron, that can be stored in ferritin or remain into the cytoplasm as a Labile Iron Pool (LIP). LIP is composed mainly by Fe^{2+}, which can generate ROS through Fenton reaction, and lipid peroxidation. Ferroptosis is inhibited by GPX4, which depend on GSH, synthesized via the entry of Cystine into the cell by the system x_c^-. Adapted from (Ficiarà et al., 2021c).

1.1.3 Involvement of Iron in Neurodegeneration and Alzheimer's Disease

Abnormal iron content or the presence of free iron may alter the brain metabolism by producing oxidative stresses, which could contribute to neurodegeneration due to the high susceptibility of brain to oxidative damage. Increases in iron can induce neurodegenerative processes through mechanisms different from Fenton's reaction (Ward et al., 2014). Moreover, functional mutation(s) in iron-modulating proteins disrupt iron homeostasis in systemic organs and the brain to a varying extent, and, in some cases, result in specific human disorders (Madsen and Gitlin, 2007; Bush and Curtain, 2008; Kell, 2010). Brain iron concentrations are not static: they increase with age and in many diseases and decrease when iron is deficient in the diet. The correlation between brain iron metabolism and neurotoxicity associated with neurodegenerative conditions such as Alzheimer's Disease (AD), remains to be fully elucidated (Altamura and Muckenthaler, 2009), however many evidences highlighted the involvement of iron in these diseases.

In this regard, a growing amount of evidence suggests the involvement of brain iron metabolism in the onset of several neurodegenerative diseases, in particular its accumulation in brain regions (Hare et al., 2013a; Ward et al., 2014) and its potential key role in the pathogenesis of AD (Silvestri and Camaschella, 2008; Kozlov et al., 2017).

Disruption of iron homoeostasis can interfere with mitochondrial functions and as a result accelerate the progression of neurodegenerative mechanisms (Horowitz and Greenamyre, 2010). Additionally, the neurodegenerative mechanisms leading to cell death caused by the 1-methyl-4-phenylpyridinium ion are thought to involve iron and changes in iron metabolism (Hare et al., 2013b).

Increased concentrations of total iron with aging might be caused by several factors that include increased blood–brain barrier permeability, inflammation, redistribution of iron within the brain, and changes in iron homoeostasis (Conde and Streit, 2006). Ageing processes might compromise the iron homoeostatic system, leading to an excess of iron that is not efficiently chelated by storage proteins or other molecules (Killilea et al., 2004). Total iron concentrations increase with age in the substantia nigra, putamen, globus pallidus, caudate nucleus, and cortices but why this increase is selective for some areas of the brain is unclear (Hallgren and Sourander, 1958). Regional distribution of total iron in a healthy adult brain is heterogeneous; the highest iron concentrations were detected in the basal ganglia (putamen, globus pallidus, and caudate nucleus), whereas low concentrations were detected in the cortical grey matter, white matter, midbrain, and cerebellum, and the lowest iron concentrations were in the pons, locus coeruleus, and medulla (House et al., 2012). Regional heterogeneity of brain iron and its change with age have both been confirmed *in vivo* by MRI (Bartzokis et al., 2007). Moreover, increased levels of iron have been associated to motor and cognitive impairment in the elderly (Pujol et al., 1992).

In vivo Magnetic Resonance Imaging (MRI) shows that iron deposition increases in numerous age-dependent neurodegenerative diseases, such as Parkinson's Disease (PD) and AD, and accumulates mainly in the basal ganglia (Bartzokis et al., 2004; Langkammer et al., 2014). (Ficiarà et al., 2021c)

AD is the most common cause of dementia (International, 2019), characterized by a complex etiology and unsatisfactory therapeutic approaches (Long and Holtzman, 2019). The duration of the preclinical and prodromal phase of AD varies from 10 to 20 years before clinical symptoms emerge (Vermunt et al., 2019). Mild Cognitive Impairment (MCI), which identifies a clinical condition that includes impairment in memory and/or non-memory cognitive domains, is assumed as a prodromal stage of AD, also referred to as MCI due to AD (Albert et al., 2011).

The presence of extracellular amyloid-beta (Aβ) deposition as neuritic plaques and of intracellular accumulation of hyperphosphorylated tau (p-Tau) as neurofibrillary tangles are the two hallmark lesions that histopathologically characterize the brains of AD patients (Ittner and Götz, 2011). However, there is evidence that significant accumulation of these pathological features can occur in non-demented individuals (Fagan et al., 2007; Aizenstein et al., 2008; Villemagne et al., 2008; Price et al., 2009) and also a high neuropathological heterogeneity is observed in patients with clinical diagnosis of AD (Rabinovici et al., 2016; Di Fede et al., 2018; Robinson et al., 2018). The abnormal concentration in the CSF of the proteins responsible for the plaque formation, i.e. Aβ42, p-Tau, and total-Tau (t-Tau), is assumed to be a measurable fingerprint of their brain deposition, reflecting neurochemical changes arising from AD pathology (Henry et al., 2013). (Ficiarà et al., 2021a)

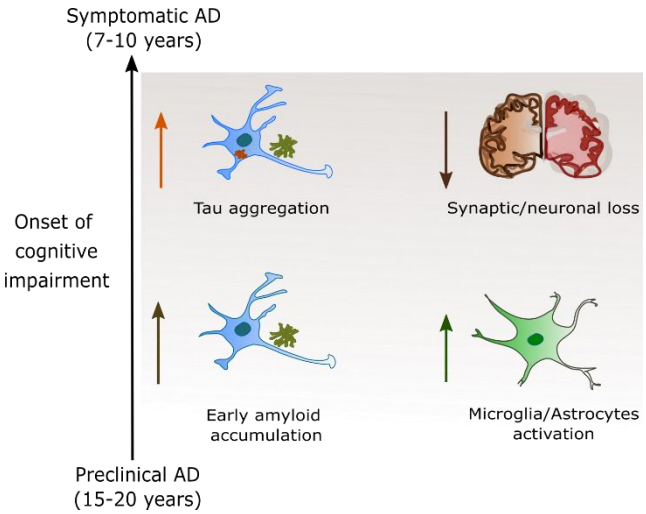

Figure 1.3. Timing of major pathophysiological events featuring AD in relation to clinical course, based on (Long and Holtzman, 2019): preclinical phase of disease is characterized by the early onset of amyloid deposition, detected by a reduction in CSF and plasma levels of Ab42 or increased global signal on amyloid PET imaging; concurrently, there are early neuroinflammatory changes (such as microglial activation); then, there is the spread of neurofibrillary tangle from the medial temporal lobes into neocortex; increased signal on tau PET imaging and increased CSF p-Tau levels mark this change; synaptic dysfunction, synapse loss, and neurodegeneration accumulate with pathologic spread of Tau aggregates; imaging analysis of hippocampal and cortical volumes allows for longitudinal tracking of neurodegenerative changes; onset and progression of cognitive impairment correlates with accumulation of Tau and hippocampal volume loss but not amyloid deposition.

The aggregation of proteins involved in neurodegenerative disorders have been shown *in vitro* to be triggered by elevated ferric iron concentrations (Yamamoto et al., 2002). Inclusion bodies containing damaged or aggregated proteins could cause endoplasmic reticulum stress, which is a common feature of several neurodegenerative diseases (Liu and Connor, 2012).

Defective homoeostasis of the redox-active metals iron and copper probably contributes to the neuropathology of AD. High concentrations of zinc, copper, and iron are present in the insoluble amyloid plaques and neurofibrillary tangles characteristic of AD. Focal accumulation of zinc, copper, and iron might deprive other brain tissues of these essential metals, leading to aberrant neuronal function (Roberts et al., 2012). Abnormal homoeostasis of zinc, copper, and iron metal ions has been implicated in the misfolding process associated with the production of Aβ, from amyloid precursor protein (APP), hyperphosphorylated tau (found in the plaques and tangles), and contributing to neuronal oxidative stress (Sayre et al., 2000). Increases of iron in animal brains produce pronounced cognitive defects (Schröder et al., 2013). Iron deposits in presenilin/APP transgenic mice models of AD (Holcomb et al., 1998), colocalizes with Aβ plaques (Smith et al., 1998), and increases in total brain iron coincide with early plaque formation (Leskovjan et al., 2011). (Ficiarà et al., 2021c)

Also the presence of an Iron-Responsive Element (IRE) in the 5'UTR of the Amyloid Precursor Protein transcript (APP 5'UTR) provided the first molecular biological support for the current model that APP of AD is a metalloprotein (Rogers and Lahiri, 2004).

Some studies suggest non-specific co-precipitation of iron and other metals with aggregated proteins, while others associate brain iron directly with disease pathogenesis (Rogers et al., 2008; Duce et al., 2010; Kozlov et al., 2017). In addition, dysfunction of ferritin or absence of Cp alter brain iron homeostasis and can induce neurotoxicity (Singh et al., 2014). (Ficiarà et al., 2021c)

In the most of neurodegenerative diseases, such as AD, iron accumulates in vesicles but without systematic iron overload (Andersen et al., 2014; Hadzhieva et al., 2014; Chen et al., 2016; Gozzelino and Arosio, 2016).

1.1.4 Quantification of Iron in Biological Fluids *(Ficiarà et al., 2021c)*

In the last years many evidences related to the abnormal iron concentration in biofluids, such as serum and CSF, of diseased patients, especially those affected by AD, accumulated.

The clinical parameters normally used to monitor iron concentration in can detect the quantity of circulating and stored iron. Besides standard indicators, also non-standard ones are emerging to evaluate alterations in iron metabolism and homeostasis. These indicators for iron transport, storage, and metabolism, can help to understand which biomarkers better reveal iron imbalances responsible for neurodegenerative diseases.

Iron in blood/serum

Specific self-standing indicators of iron status in the serum are difficult to be fully reliable because they span on different scales of measures and because of the presence of many confounding factors ranging from inflammation to analytic challenges. Moreover, iron status is a continuum from iron deficiency anemia (IDA) [i.e., reduced hemoglobin in red blood cells] to ID (i.e., depleted iron stores) to iron overload, and a combination of different indexes may be more useful than others depending on the situation. Available indicators include concentrations of hemoglobin, serum ferritin (s-F), Tf, soluble transferrin receptor (sTfR), serum iron, as well as total iron-binding capacity (TIBC) or transferrin saturation (TSAT) (Pfeiffer and Looker, 2017). Standards serum-based indicators are generally evaluated on fully automated clinical analyzers available in most hospitals. In addition, alternative methods and new protocols for iron evaluation mainly based on analytical techniques are in continuous development. However, the standardization of methodologies is complicated and the presence of physicochemical reference methods to establish true concentrations is challenging, even if international reference materials have been available (Pfeiffer and Looker, 2017). Details on typical range values of iron indicators and relative techniques to obtain these are given in Table S1 (Appendix).

Serum Ferritin

Although many indexes are available, determination of iron status by using s-F concentrations is the most commonly deployed strategy used in clinical and public health settings (Mei et al., 2005). Ferritin is an iron storage protein and, consequently, higher intracellular iron concentrations result in increased ferritin expression, whereas ID inhibits it (Muckenthaler et al., 2008). However, ferritin is also an acute-phase protein, and serum concentrations are increased in conditions of inflammation

(Elin et al., 1977), presenting a limitation for this indicator. During liver damage, ferritin leaks from hepatocytes, and plasma concentrations rise. The ferritin measurable in the serum appears to be chiefly derived from macrophages (Cohen et al., 2010) and reflects overall storage iron and ferritin concentrations in the liver and other tissues (Garcia-Casal et al., 2015).

The physiological task of ferritin is to protect cells from the redox-active ferrous iron (Fe^{2+}). So, under normal conditions, the response to a cytosol increase of Fe^{2+} is its rapid uptake into ferritin, where it is physiologically stored in a redox-inert form of iron oxyhydroxides containing only Fe^{3+} ions. The presence of ferrous iron inside pathological ferritin could reveal an alteration in the mineralization process, i.e., that the enzymatic oxidation process is faulty (Quintana et al., 2000, 2004). This process of Fe^{2+} oxidation inside ferritin takes place in specific ferroxidase sites in the Ft-H subunit (Chasteen and Harrison, 1999). Thus, dysfunction of ferritin could be a cause of the alterations in the mineralization of the ferritin cores, and this fact may be associated with aging processes and especially with neurological diseases, i.e., AD and Parkinson's Disease (Quintana and Gutiérrez, 2010).

The imbalance of iron metabolism in affected regions also causes mitochondrial abnormalities, accumulating oxidatively damaged DNA in the mitochondria of a mouse model of hereditary ferritinopathy (Deng et al., 2010). Interestingly, mutant Ft-L itself is targeted by ROS, resulting in its cleavage and disruption of the ferritin shell, confirming the role of free radicals in the process (Baraibar et al., 2012). Co-aggregation of wild-type Ft chains can be initiated by the free radicals generated by mutant Ft-L, creating an iron imbalance in the brain (Baraibar et al., 2008).

Several studies focused on the investigation of ferritin levels in neurodegenerative diseases. Blood ferritin levels were reported significantly higher in patients with AD in comparison to healthy controls (Giambattistelli et al., 2012) and the incidence of serum ferritin levels above the normal range was significantly greater in individuals with AD (Faux et al., 2014). Interestingly, different microscopy techniques were used to analyze the morphology of erythrocytes, showing relative substantial changes taken from high serum ferritin in AD individual and arguing that high ferritin levels may contribute to an accelerated pathology (Bester et al., 2013). Serum/plasma ferritin was investigated as a preclinical marker of AD, reporting that both plasma and serum ferritin correlated positively with the Neocortical Amyloid-β Load (NAL), underlining also a potential discriminating power between low and high NAL (Goozee et al., 2018).

Transferrin

Tf, involved in the transport of iron in the blood, is normally undersaturated (about 10-30% of the total Tf)(Gkouvatsos et al., 2012; Eid et al., 2017) . A huge iron-free reservoir with high affinity binding (apo-Tf) is used as buffer preventing excess iron from being free and inducing toxic effects. Therefore, the level of free iron in the circulatory system (Non-Transferrin Bound Iron, NTBI) is very low (Brissot et al., 2012). There is nevertheless a limit to the amount of Tf and free iron or NTBI will exist when Tf becomes ca. 60-70% saturated, with consequent detectable levels (Brissot et al., 2012; Eid et al., 2017).

Several cross-sectional studies have not found differences in blood transferrin levels between healthy controls and AD patients (Fischer et al., 1997; Squitti et al., 2010; Torsdottir et al., 2011). Interestingly, blood transferrin levels were positively associated with the Mini-Mental State Examination (MMSE) scores in AD patients by Fischer et al. (Fischer et al., 1997) but not by Squitti and colleagues (Squitti et al., 2010). Recently, it has been shown that no significant differences in the plasma Tf levels across control, Mild Cognitive Impairment (MCI), and AD groups but higher plasma Tf levels were associated with a steeper cognitive decline in MCI and AD patients (Guan et al., 2020).

Furthermore, it has been shown that disturbed brain iron metabolism is reflected in the periphery by a decrease in plasma iron and hemoglobin (Hb)(Faux et al., 2014) and has been assessed a decrease in plasma iron in AD patients related to Tf desaturation, providing potential role of Tf saturation as AD biomarker (Hare et al., 2015). The reasons for decreased plasma Tf saturation in AD remains unclear, though it appears indicative of a more widespread imbalance in metal homeostasis and also links with Cp activity, requiring further investigation.

Other non-standard serum biomarkers

The relevance of other iron status indicators (i.e., NTBI, hepcidin) proposed in the last years is under investigation (Pfeiffer and Looker, 2017), and laboratory methods require further improvements in terms of comparability. In particular, NTBI requires a more detailed definition of its clinically most relevant forms.

Free iron in the form of NTBI in the circulating blood becomes detectable only when Tf reaches 70% of saturation (Brissot et al., 2012; Coates, 2014; Berdoukas et al., 2015) and can cause significant damage to cells even at very low concentration (Brissot et al., 2012), due to its ability to catalyze the formation of ROS. NTBI is a heterogeneously speciated plasma iron and accounts for all forms of plasmatic iron bound to ligands other than Tf. Although the exact chemical nature of NTBI remains elusive, it is thought to circulate in the plasma in a form that is loosely bound to albumin or small organic acids, such as citrate (Hider, 2002; Brissot et al., 2012). This NTBI, iron bound to low-molecular-weight proteins or other compounds, usually comprises <1% of the plasma total iron pool and is usually not detected in most routine assays (Pfeiffer and Looker, 2017).

A clinically relevant level of sensitivity has yet to be achieved although the standardization of methods to accurately quantify NTBI can be useful in order to investigate its nature and possible health effects. To date, no gold standard methods for serum NTBI quantification have been established, facing technical difficulties related to the determination of heterogeneous forms of circulating NTBI and a relatively poor agreement between assays (Pfeiffer and Looker, 2017).

Routine clinical analysis is normally based on colorimetric tests, although other quantitative measures of total iron in serum with non-standard analytical techniques are possible, allowing advantages in precision and accuracy, simpler processing, and quicker analysis time. Their main drawbacks are that they are not commonly available in clinical laboratories and are relatively expensive, requiring regular and periodic technical maintenance, together with hard pre-treatments of the blood/serum samples, due to the presence of organic compounds.

Values for total iron in serum were found in the order of 1 mg/L. Quantification of iron in serum of healthy, MCI, and AD subjects was performed in several studies (González-Domínguez et al., 2014; Paglia et al., 2016). It has been reported that serum iron levels were significantly lower in AD patients than in healthy controls after excluded two studies (Li et al., 2017).

Iron Markers Related to Ferroptosis

Due to the emerging and relevant role of ferroptosis in neurodegeneration, it will be pivotal to propose novel therapeutic approaches in AD and other neurodegenerative diseases (Ashraf and So, 2020). Due to several factors associated with the ferroptotic process (Reichert et al., 2020), its explicit identification *in vivo* is hampered by the absence of specific biomarkers. However, iron is required for the accumulation of lipid peroxides and the execution of ferroptosis. Thus, iron import, export, storage, and turnover impact ferroptosis sensitivity (Stockwell et al., 2017).

Three essential hallmarks define ferroptosis: the loss of lipid peroxide repair capacity by the GPX4, the availability of redox-active iron, and oxidation of polyunsaturated fatty acid (PUFA)-containing phospholipids (Dixon and Stockwell, 2019).

Tf and TfR, which import iron from the extracellular environment, are required for ferroptosis (Gao et al., 2015) while silencing of the iron metabolism master regulator IREB2 decreases sensitivity to ferroptosis (Dixon et al., 2012). Furthermore, Anti-TfR1 antibodies can detect ferroptosis by immunofluorescence and flow cytometry in tumor cells (Feng et al., 2020).

Interestingly, in a different pathology (Amyotrophic Lateral Sclerosis) blood-based prognostic indicators using an array of pathological markers closely associated with ferroptosis in plasma samples were evaluated, and the identified markers of neuronal integrity, DNA and lipid oxidation, as well as iron status at baseline, enabled the accurate forecasting of functional decline (Devos et al., 2019). The development of ferroptosis-based markers is particularly timely, as iron chelation (Ashraf and So, 2020) and potential anti-ferroptotic therapy are currently under investigation for a range of neurodegenerative conditions, including AD.

Iron in CSF

CSF fills the intracerebral ventricles, subarachnoid spaces of the spine and brain (e.g. cisterns and sulci), and the central spinal cord canal, having accepted roles as a fluid cushion and a sink for nervous system waste. CSF protects the CNS by securing metabolic homeostasis and supply of nutrients, functioning as lymphatic system, and regulation of intracranial pressure (Lun et al., 2015).

CSF circulation is increasingly recognized as participating in volume transmission throughout the brain, and may also be an important actor of clearance of brain metabolites from parenchyma through its connection with the perivascular fluid circulation. The volume of CSF is estimated to be 150–270 mL (with a distribution of 125 ml within the subarachnoid spaces and 25 ml within the ventricles) and is renewed several times a day (from 400 to 600 ml per day) (The Choroid Plexus and Cerebrospinal Fluid System: Roles in Neurodegenerative Diseases, 2016; Telano and Baker, 2020).

CSF is daily produced by the choroid plexus, brain interstitium, and meninges, and it circulates in a craniocaudal direction from ventricles to spinal subarachnoid space from where it is

removed via craniocaudal lymphatic routes and the venous system. CSF is an ultrafiltrate of plasma; the different array of molecules in the CSF (e.g. protein, neuro-peptides, membrane bound vesicles) and the features of the fluid (e.g. direction and velocity of flow) provides an instructive CSF-based signaling that support the brain environment. Human CSF composition is reported (Spector et al., 2015).

The majority of CSF iron in CSF is bound to Tf, and iron levels in this compartment are lower than in serum. It has been suggested that Tf saturation in the CSF is much higher than in the periphery, and that a larger proportion of NTBI circulates the CNS (Leitner and Connor, 2012). Iron levels in CSF is very low and therefore very difficult to measure. In 1998 LeVine et al proposed a very demanding procedure and were able to get a value of (61.01 ± 18,3) μg/L in 8 normal samples (LeVine et al., 1998).

Although it is less common to evaluate the same iron indicators for plasma/serum in CSF, it has the advantage of being in direct contact with the brain thus potentially better reflects its iron content. One of the main limitations of CSF samples is their invasive collection technique (i.e., lumbar puncture) compared with blood sampling and also the low amount of iron requires very sensitive and reliable methods. (Ficiarà et al., 2021c)

CSF Ferritin

It has been hypothesized that CSF ferritin can reflect global brain iron (Ayton et al., 2015) and can be considered a surrogate marker of brain iron load, even if is not established as a relative biomarker (Ayton et al., 2018). CSF ferritin values not showed differences between cognitively normal, MCI, and AD population (Ayton et al., 2015).

However, it has been shown that ferritin levels in the CSF can predict AD outcomes, being strongly associated with apolipoprotein E (APOE) levels and elevated by the AD risk allele APOE-ε4, so revealing that elevated brain iron adversely impacts AD progression (Ayton et al., 2015). Moreover, ferritin levels are associated with longitudinal changes in CSF Aβ and tau protein accelerating AD pathology (Ayton et al., 2018).

CSF Transferrin

CSF contains glycan isoforms of Tf: one appears to be derived from the brain and the other from blood. The ratio of serum-type/brain-type Tf differentiates AD from idiopathic normal pressure hydrocephalus, elderly dementia caused by abnormal metabolism of CSF (Futakawa et al., 2012). Immunohistochemistry using an anti-Tf antibody suggested that brain-type Tf derived from choroid plexus, a CSF-producing tissue (Futakawa et al., 2012). It has been hypothesized that brain-type Tf secreted from the choroid plexus would be the alternative supply of iron to neurons, being potential biomarkers for various neurological diseases (Hoshi et al., 2017).

Furthermore, altered glycosylation of CSF Tf molecules could be present in AD, Tf glycosylation is thus a potential biological marker for AD diagnosis, and changes in this activity may play an important role in AD pathophysiology (Taniguchi et al., 2008).

Few studies reported values of Tf in CSF, requiring further investigation on the related biochemical status and mechanisms.

Non-Standard Measurements for Iron in CSF

Accurate evaluations of iron in CSF can be performed by FerroZine colorimetric analysis and related Ferrochem II analyzer methods for iron qualification in CSF, and ICP-MS (Hozumi et al., 2011), AAS (Lavados et al., 2008; Ficiarà et al., 2021a) for a more quantitative measure (Tao et al., 2014).

While NTBI is usually not detectable in the plasma of healthy individuals, it seems to be a normal constituent of brain interstitial fluid, acting as an important source of iron for several cell types in the CNS. Even under normal conditions, due to the full saturation of Tf in the CSF (Knutson, 2019), NTBI is considered to be a physiological form of iron. As a matter of fact, iron in CSF occurs in the two forms, of Tf-Fe and low molecular weight NTBI (less than 30 kDa), was evaluated in rats of different ages injected intravenously with [^{59}Fe^{125}I]Tf (Moos and Morgan, 1998).

1.1.5 Quantification of Iron in Brain: MRI *(Ficiarà et al., 2021c)*

Brain imaging technologies have been used to show that increased iron deposits in different brain regions might be markers of tissue damage in several neurological diseases (Dusek et al., 2013). MRI is the gold-standard methodology to assess and map brain iron *in vivo*.

Hydrogen nuclei (*i.e.*, protons) abundant in fat and water, are the main components of the human body and possesses a *spin*, generating a small magnetic moment interacting with properly designed external fields.

In particular, MRI acquisition employs a large magnet producing a strong magnetic field (B_0, much larger than the geomagnetic field. Within a body positioned inside the scanner, B_0 aligns the protons' spins along its direction. At equilibrium, the net magnetization corresponds to the longitudinal magnetization along the sagittal axis of the body and is parallel to B_0. Depending on the selected 'sequence', the net magnetization vector is suddenly changed by exposing the spins to radiofrequency pulses modifying their orientation (*e.g.*, overturning the vector onto the xy plane). Once the pulses are removed, the protons tend to return to their equilibrium position according to tissue-specific exponential relaxations. Two time constants are normally considered: the longitudinal, or spin-lattice, relaxation time (T_1) and the transverse, or spin-spin, relaxation time (T_2). In real settings the T_2 decay actually results from two sources: molecular (spin-spin) interactions (*pure* T_2) and variations in B_0 that may lead to inhomogeneities in T_2 effect. The time constant that characterizes these two processes together is called T_2*.

By applying different sequences of radiofrequency pulses, and collecting the resulting signal, images with different contrasts can be reconstructed. In particular gradient-echo T_2*-weighted images are usually generated by multiple, short echo times, small flip angles and variable repetition times.

Starting from these standard MRI techniques, combination of sequences and images reconstruction strategies may produce more specific mappings.

Quantification of iron levels can be carried out using several techniques, such as relaxation time mapping (Haacke et al., 2005; Langkammer et al., 2010), Quantitative Susceptibility Mapping (QSM) (Wang and Liu, 2015) magnetic field correlation (Jensen et al., 2006), and direct saturation imaging (Smith et al., 2009). So many different MRI acquisition schemes are due to the fact that the presence of iron in the brain has different effects: i) changes in relaxation characteristics of tissue water in presence of ferritin; ii) changes in tissue susceptibility changes induced by iron presence, and iii) microscopic field gradients in its surroundings. The nature and entity of these changes depend on the different magnetic properties of iron compounds and may affect image contrast in terms of quantitative relaxation parameters and of the phase of the complex MRI signal (Brooks et al., 1998).

Since the earliest MRI experiments, it has been observed that iron mainly accumulates in the grey matter of the brain, which appears hypointense on T2-weighted MRI. Subsequently, several studies reported associations between age and the transverse relaxation rates $R_2 = 1/T_2$ and $R_2^* = 1/T_2^*$, which are commonly used as surrogate markers for iron concentration in brain tissue. In particular, Langkammer and colleagues (Langkammer et al., 2010) investigated the relationship between these measurements and chemically determined iron concentrations in seven human brains *post mortem*. They found that the basal ganglia (pallidum, putamen, caudate nucleus) and the thalamus were the regions with the highest iron concentration and that the R_2^* rates showed the strongest linear correlation with chemical measurements throughout the brain ($r^2 = 0.90$, $p < 0.001$). These results support the fact that R_2^* is more sensitive than R_2 to variations in brain iron concentrations and might be considered the preferred parameter for the *in vivo* assessment of brain iron concentration. Figure 5 shows the typical processing workflow of T_2^*-weighted data.

In healthy subjects, a recent study (Cherubini et al., 2016) identified R_2^* measurements as the best age predictors in specific regions of the brain, such as the putamen and the globus pallidum, confirming the results of the abovementioned post-mortem study. Moreover, another recent systematic review (Pagnozzi et al., 2019) suggested that T_2^* and R_2^* sequences might also be useful to increase the accuracy of automated segmentation of subcortical brain structures, especially when the T_1-weighted contrast is reduced (e.g., due to age-related effects). About neurodegenerative diseases, Langkammer and colleagues investigated the currently available MR methods for quantitative iron mapping in the brain of patients with AD (Langkammer et al., 2014), suggesting R_2^* mapping as the best-validated technique for iron detection. In particular, these patients show increased iron levels not only in the hippocampus and temporal cortex, damage of which is a well-known hallmark of the disease, but also in the pulvinar thalamus (connected to the visual cortex) and in the putamen and red nucleus (both involved in motor control).

The role of iron accumulation as a potential imaging marker in patients with MCI or AD has also been suggested using Susceptibility-Weight Imaging, since motor cortex hypointensity on this sequence was more frequently found in patients with cognitive impairment than in age-matched controls, and also positively associated with age (Park et al., 2019).

Among novel methods for iron detection in the brain, QSM has been used for *in vivo* longitudinal monitoring of Aβ accumulation and iron deposition in a transgenic mouse model of AD (Gong et al., 2019). Increased iron concentrations correlate with Aβ aggregation in areas initially affected in AD

and offer an opportunity for MRI-based diagnosis. MRI scans of post-mortem human brains and a mouse model of AD show decreases in hippocampal T_2* MRI, which is sensitive to the magnetic properties of iron (Schenck, 2003) or its spatial variance, attributed in part to iron in Aβ plaques (Nabuurs et al., 2011). Although MRI resolution is not sufficient to detect individual plaques, T_2* abnormalities that result from plaque aggregates might be detected with MRI. When clearly distinguished from potential confounders originating from heme iron, changes in hippocampal T_2*-weighted MRI might be a valuable assessment of morphological changes and a potential biomarker for the early stages of AD (Holland et al., 2009).

Other findings of evidence for iron overload in several specific brain regions have been reviewed from Tao et al. (Tao et al., 2014).

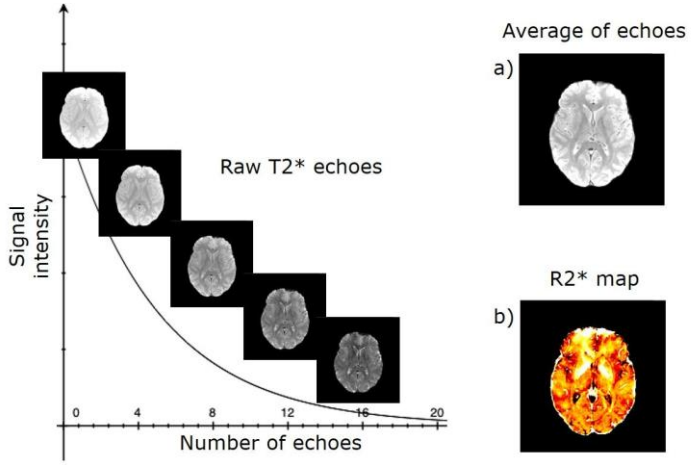

Figure 1.4. MRI processing workflow of T_2* to map brain iron. **a)** Each echo is aligned on the average image for motion correction. **b)** Realigned echoes are fitted through a voxel-by-voxel nonlinear least squares model to obtain a mono-exponential signal decay curve: $S = S_0 e^{-\frac{t}{T_{2*}}}$ and finally produce a transverse relaxation rate map (R_2*). Adapted from (Ficiarà et al., 2021c).

The role of iron accumulation as potential imaging marker in patients with MCI or AD has been suggested, since motor cortex hypointensity on Susceptibility-Weight Imaging was more frequently found in patients with cognitive impairment than in age-matched controls and positively associated with age (Park et al., 2019).

A longitudinally monitoring of beta amyloid accumulation and accompanied iron deposition has been evaluated *in vivo* by means of QSM MR imaging tangles or neuronal death. Interestingly, in the same study, the measured negative susceptibility map and positive susceptibility map could provide histology-like image contrast for identifying deposition of beta amyloid plaques and iron (Gong et al., 2019).

1.1.6 Investigation of iron toxicity in biological models

To investigate the lacking details of iron contribution to neuropathology, well-designed model systems (*in vitro* and *ex vivo*) are required to study iron movement and on-going damage at a cellular level (Healy et al., 2017). Several studies were conducted with cell lines of neurons, microglia and oligodendrocytes, highlighting that single cell types are not representative of the natural neuronal

response to iron perturbations in the brain, due to the lacking incorporation of the iron handling relationships of the other cells (Healy et al., 2017). In fact, once iron enters the brain, neurons, astrocytes, and oligodendrocytes are equipped with different sets of iron-related molecules responsible for uptake, storage, use and export of iron. Organotypic cultures are efficient and reliable *ex vivo* models, which preserve the complex brain milieu present in *in vivo* studies, combining the accessibility and convenience of *in vitro* models (Cho et al., 2007). However, few studies used these models to investigate iron loading are present.

The study of iron overload in cultured cells is not straightforward, due to the complex chemistry of iron (e.g. important variables are the solubility and stability of iron at particular pH). Various iron reagents at different concentrations have been used in *in vitro* models to promote oxidative stress, toxicity and iron accumulation, leading to a huge variations in experimental conditions between studies (Eid et al., 2017; Healy et al., 2017). Common iron reagents added to in vitro systems are based on ferric or ferrous iron reagents: Ferric Ammonium Citrate (FAC), Ferric Chloride, Ferric Citrate, Ferric-NTA, Ferrous Sulfate, Ferrous Ammonium Sulfate (FAS), Ferrocene etc. In literature, a wide range of iron concentrations has been used (0.1-1000 μM). Moreover, other important experimental conditions have to be considered, such as exposure time and the addition of serum or ascorbate into culture media, highlighting a need for further investigations in modelling iron management *in vitro*.

1.1.7 Chelation Therapies: an artificial way to block iron toxicity

Iron chelation has been proposed as a new therapeutic concept for the treatment of neurodegenerative diseases featuring iron overload.

Iron chelators, binding iron in a complex capable of being excreted (Coates et al., 2016), have been investigated since 1960. Three of them have been approved for clinical use and are relatively non-toxic (Templeton, 2015): desferrioxamine (DFO), Deferiprone (DFP) ; Deferasirox (DFS).
Iron chelators have been successful in the treatment of patients with overaccumulation of NTBI iron in the blood (Coates et al., 2016; Nurchi et al., 2016) while up to now, in spite of many clinical trials, there is an evident lack of success in a wide range of neurodegenerative diseases (Dusek et al., 2016). The main challenges remain the capability to cross BBB and the specific iron targeting in CNS.
A 2-year Phase II clinical trial reported that DFO attenuates cognitive decline in AD (Crapper McLachlan et al., 1991). However, DFO treatment was not further pursued owing to its lack of BBB penetrance.

Noninvasive intranasal DFO delivery targeting the CNS and bypassing the BBB has been applied in animal models to treat a variety of brain disorders and even to improve memory in normal mice (Kosyakovsky et al., 2021).

Furthermore, intranasal DFO has been shown to improve cognition in a mouse AD model (Fine et al., 2012, 2015). Iron chelation attenuated oxidative stress, lowered b-amyloid load, and tau hyperphosphorylation (Guo et al., 2013a, 2013b). DFP is an orally active, brain penetrant iron-chelator, approved for use in b-thalassemia, currently, undergoing a Phase II clinical trial in MCI and

AD (Deferiprone to Delay Dementia—clinicaltrials.gov identifier: NCT03235686; Nikseresht et al., 2019). This trial was preceded by Phase II clinical trials on Parkinson's disease which showed reduced brain iron assessed by MRI and CSF ferritin and concomitant ameliorated motor deficits (see Table 1 (Ashraf and So, 2020)).

Importantly, one trial on patients affected by Neurodegeneration with brain iron accumulation (NBIA) disorder showed no improvement with iron chelation therapy in spite of the fact that there was a significant reduction in brain iron deposits (Zorzi et al., 2011).

Moreover, secondary effects are not negligible, such as the chelation of other divalent cations, especially zinc and copper (Dusek and Schneider, 2012), the induction of cellular redistribution of intracellular iron pools leading to degradation of iron loaded ferritin or lysosomes (De Domenico et al., 2009) , increase in calcium, induction of cell differentiation and changes in the expression of multiple genes (Cabantchik, 2014). In the case of elevated amount of iron chelators, iron depletion can occur leading to iron deprivation mediated by activation of ER stress, autophagy and apoptotic pathway (Greene et al., 2002).

Although chelating the free iron in the brain is a tempting strategy, limitations must be taken into account. Iron is an essential cofactor in multi-fold cellular processes. Therefore, iron-chelation can have off-target effects and potentially cause untoward effects (Ashraf and So, 2020).

The exploration and tuning of both innovative formulation of chelating agents and alternative ways to administer besides the systemic delivery (i.e., intravertebral or intrathecal administration in the CSF) can be the basis for novel therapeutic strategies for neurological diseases.

1.1.8 Machine Learning in Alzheimer's Disease

Clinical heterogeneity and complex etiology at multiple levels (e.g. network, cellular and molecular) are increasingly recognized as common features of AD and related dementias, presenting big challenges to the development of early diagnostic tools and effective treatments, and also requiring advanced computational models.

Machine Learning (ML) is a subfield of artificial intelligence and it has been applied up to now to aid early diagnosis, interpretation of medical images, and the discovery of novel therapies (Myszczynska et al., 2020).

New technologies enabled the accumulation of high-dimensional datasets (i.e., MRI, "omics" profiles, electronic records) and ML can help overcoming the issues deriving from high-dimensionality and integration from different sources. Assembling multiomics measurements into highly predictive diagnostic tools can improve the goal of personalized medicine (Badhwar et al., 2020).

Different algorithms of ML (categorized in supervised, unsupervised and reinforcement learning) allow a robust investigation to identify undiscovered patterns and relationships in the data, and determining the best model for a given problem is a crucial factor to extract meaningful representation.

Supervised learning requires a set of data labelled to train the model ability to extract specific disease features. After training, the algorithm identifies the selected features in unlabelled datasets to aid diagnosis. Unsupervised learning is able to extract patterns and classes within the dataset without labels and can be very useful in identifying signatures categorizing heterogeneous groups into similar subtypes. In reinforcement learning algorithms, the process of decision making and the output is a result of knowledge gained from previous experiences, training the model on a trial- and-error basis. Supervised ML algorithms are currently the most commonly applied method to neurodegenerative disease-related data, i.e., classification task predicting the categorical output (diagnostic category) for each sample (patient). A detailed description of key machine learning methods and relative application in AD are reported (Myszczynska et al., 2020; Tanveer et al., 2020).

One of the most important unsupervised learning methods is clustering, a powerful tool for discovering patterns and structures in datasets. This method can reveal subgroups within heterogeneous data, with the goal to describe patient subtypes with shared similar profiles.
Several clustering methods have been applied to datasets of neurological diseases, especially AD, and different techniques are suitable for partitioning patients based on their similarity (Alashwal et al., 2019).

Furthermore, machine learning-supported analyses improve quantitative histological assessments of Amyloid-β deposits and activated microglia, allowing to include different objects or cell types in a single analysis, which is not possible with conventional methods (Bascuñana et al., 2021). Moreover, the implementation of machine learning methods (i.e. deep learning-assisted analyses) to analyse histopathological slides is likely to promote standardization of the assessment of neuropathological markers across research centers (Perosa et al., 2021).

1.2 Trafficking of iron from blood to brain: the brain barriers systems

The trafficking of iron in the brain milieu is mainly managed by the brain barrier systems, responsible for the direction of iron fluxes between the blood and brain/CSF (Zheng and Monnot, 2012).

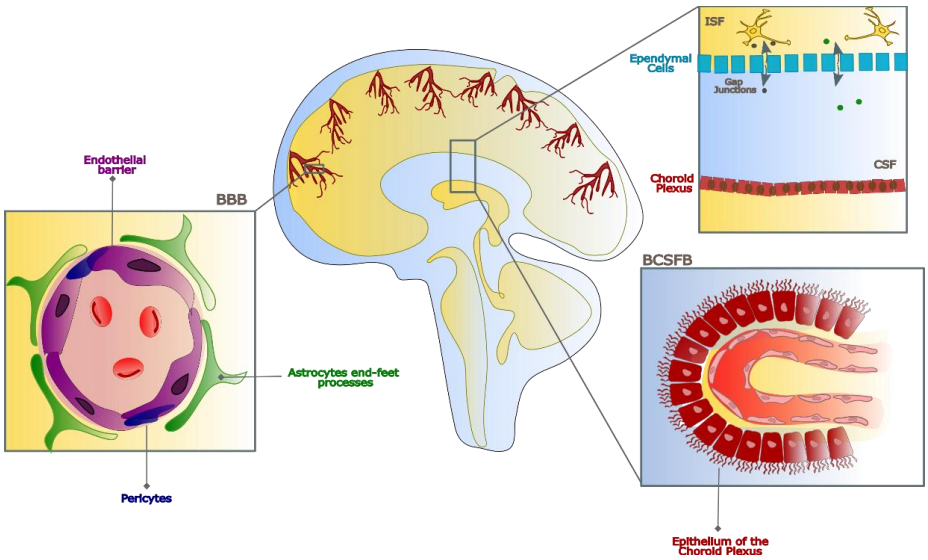

Figure 1.5. Structure of the blood-brain barrier (BBB) and the blood-cerebrospinal fluid barrier (BCSFB). The BBB separates blood and the brain parenchyma. BBB is a highly selective barrier, composed by endothelial cells with specialized tight junctions, and a very low rate of transcytosis. The "neurovascular unit" comprises also pericytes, a basement membrane and astrocyte end-feet processes from nearby astrocytes. Capillaries of the CP, not having tight junction, are relatively leaky and permeable to small molecules, also allowing the delivery of water through the bloodstream to the surrounding epithelium for CSF production in the CP and secretion into the ventricles. Areas of the ventricular lining of ependymal cells are connected by gap junctions, allowing free exchange of molecules between CSF and interstitial fluid (ISF) at these sites. CSF flows between the four connected ventricles to the subarachnoid space and into the perivascular space, and intermix with brain parenchymal interstitial fluid (also known as the "glymphatic system").

Iron moves from blood to brain by crossing a series of barriers directly connecting blood and brain (BBB) or by crossing the Blood-CSF-Barrier (BCSFB) and then entering brain through the Outer Brain Barriers (OBB). Consequently, iron overload or dysregulation may be related either to its abnormal concentration in blood and in the CSF or due to some alteration in the passage across the main barrier systems: the BBB, the BCSFB, and the OBB, being the last two far less studied than BBB (Nakada and Kwee, 2019). CSF and brain could be considered almost in direct contact, and their exchange occurs across the more permissive ependyma, composed by the single layer of ependymal cells joined with gap junctions, allowing a relatively freely communication of CSF and interstitial fluid (Johanson et al., 2011).

Note that also the Circumventricular Organs (CVOs) located around the third and fourth ventricles, and sealed off by special ependymal cells such as tanycytes, represent a special case of BCSFB. CVOs are often referred to as "windows to the brain" because of their physical closeness to

the brain, but are actually outside the brain barrier (Sisó et al., 2010; Langlet et al., 2013; Jiménez et al., 2014; Nakada and Kwee, 2019).

Since iron can accumulate in the brain and it is not fully consumed, also backward iron passage (from brain to blood) is expected to occur. The dysregulation of iron passage at blood-brain barriers system can lead to pathological conditions and impaired levels in biofluids and the brain/blood compartment. A compromised brain barriers system, either structurally or functionally, can cause an imbalance in iron needs and supplies in the CNS. Subsequently, a distorted iron brain homeostasis can gradually settle down, becoming a factor involved in the initiation and/or progression of neurodegenerative disorders.

1.2.1 Direct Mechanism: Blood-Brain Barrier *(Ficiarà et al., 2021c)*

Blood iron entrance into the brain is controlled by the BBB (McCarthy and Kosman, 2015) and to a lesser extent by the blood–cerebrospinal fluid barrier (BCSFB) (Moos and Morgan, 2000) . The role of the BBB is to protect the brain from neurotoxic plasma components and pathogens (Montagne et al., 2017), as well as to control the chemical composition of the neuronal milieu by regulating the transport of molecules required for normal neuronal functioning (Zhao et al., 2015). The BBB is formed by a monolayer of tightly sealed microvascular endothelial cells (BMVECs) extending along the vascular tree (Sweeney et al., 2019) and expressing low paracellular and transcellular permeability (Zlokovic, 2011). Those endothelial cells are surrounded by basal lamina and astrocytic perivascular end-feet, forming the neurovascular unit (Iadecola, 2017). The hydrophobic barricade formed by the BBB prevents diffusion of hydrophilic Fe2-Tf into the nervous system, as well as the migration of NTBI. The uptake of iron from the periphery starts with the transport of Fe2Tf across the BBB through BMVECs (Hare et al., 2013a). Iron enters the BMVECs as a low molecular weight complex, or via transferrin receptor-1 (TfR1) mediated endocytosis of Tf, or independently as Non-Transferrin-Bound Iron (NTBI), in a multi-step transcellular pathway. Binding of Tf to Tf receptors (TfR) at the lumen of the brain microvasculature facilitates iron uptake via receptor-mediated endocytosis (Abbott et al., 2006; Ke and Qian, 2007; Moos et al., 2007) (Figure 1.6).

The Tf/TfR1 pathway is considered to be the major route for iron transport across the luminal membrane of the capillary endothelium (Ke and Qian, 2007; Duck and Connor, 2016). The complex passes through the cell in the endocytosis vesicle, where the acid environment facilitates the release of ferric iron from Tf and its reduction to ferrous iron by endosomal reductase (Rouault and Cooperman, 2006), possibly DcytB. The next steps in this pathway are still not completely clear. One possibility is that ferrous iron is transported from the endosome to the cytosol by the DMT1 (Benarroch, 2009) and joins the intracellular labile iron pool (LIP) (Burkhart et al., 2016). It could be further utilized for metabolic purposes by the endothelial cells, stored in endothelial cell ferritin (Zecca et al., 2004a) or imported into mitochondria via mitoferrins and TfR2 (Horowitz and Greenamyre, 2010). It could be also released into the extracellular fluid by action of export protein ferroportin (Fpn) (Simpson et al., 2015) , and re-oxidized to Fe^{3+} by ferroxidases HEPH and ceruloplasmin (Cp) (McCarthy and Kosman, 2015), also expressed on the end-foot processes (Benarroch, 2009). Studies have confirmed that capillary endothelium of the BBB, neurons,

and astrocytes, has the ability to express Fpn and HEPH (Wu et al., 2004; Qian et al., 2007). The alternative mechanism that has been proposed is that the endosome containing Tf-TfR1 complex reaches the abluminal side and releases iron between the endothelial cells and astrocyte end-foot processes (Moos et al., 2007). Oxidized iron binds to apo-Tf circulating within the brain (Burkhart et al., 2016). The main source of Tf in the brain interstitium is its diffusion from the ventricles and oligodendrocytes synthesize a certain amount (Zerpa et al., 2000). Because of the low concentrations of Tf in the CSF, iron saturation of CSF Tf is almost 100%, while serum Tf is saturated by about 30% (Moos et al., 2007).

Different cell types in the brain acquire iron by distinct pathways. Neurons express high levels of TfR1. Therefore, Tf is the main source of iron for neurons (Benarroch, 2009), although neurons can also uptake NTBI from interstitial fluid. Oligodendrocytes and astrocytes less express TfR1 and NTBI can be a source of iron (Moos and Morgan, 2004; Rouault and Cooperman, 2006) (Figure 1).

Due to their peculiar position in the BBB, astrocytes take up iron from the circulation and distribute it to other cells in the CNS using different pathways: by DMT1 to glial cells, by binding ferrous iron in the brain interstitium to ATP or citrate released from astrocytes and transported to oligodendrocytes and astrocytes as NTBI (Moos et al., 2007) and finally iron can be stored as ferritin in astrocytes and exported by a mechanism involving Fpn and Cp (Dringen et al., 2007). Since most of the accumulated iron is within astrocytes, mainly iron-loaded astrocytes can cause brain toxicity (Jeong and David, 2006). Oligodendrocytes, which are responsible for myelin production, need high amounts of ATP (Todorich et al., 2009). Many of the enzymes involved in ATP production require a supply of iron, such as pathways for cholesterol and fatty acid synthesis for the myelination are iron-dependent. Some of these enzymes (i.e., NADH dehydrogenase and HMG-CoA reductase) are abundant in oligodendrocytes with respect to other CNS cell types (Todorich et al., 2009). A suitable supply of iron during myelination is needed, in fact dietary iron restriction decrease the amount and composition of myelin during gestation and early post-natal periods (Ortiz et al., 2004).

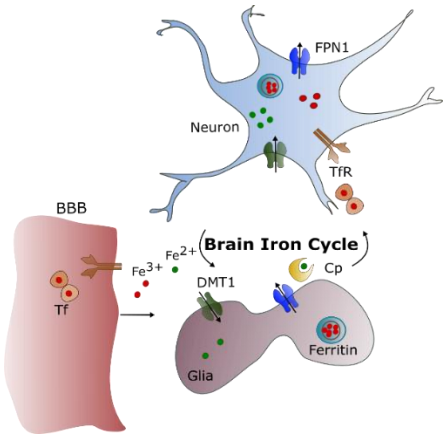

Figure 1.6. Summary of brain iron cycle. Iron crosses the BBB via the TfR pathway on the endothelium. The brain iron cycle involves glia and neurons. Astrocytes extend long processes that enclose the brain capillaries and help to form the BBB. The DMT1 transports iron. Near the ends of these processes a special form of the Fe oxidizing enzyme, Cp, is expressed. Iron binds to Tf circulating in CSF and enters the neurons mainly by TfR. The cells export iron mainly by FPN1. Modified from (Ficiarà et al., 2021c).

1.2.2 Indirect Mechanism: Blood-Cerebrospinal Fluid Barrier

As previously described, iron is believed to reach the brain through receptor-mediated endocytosis of iron-bound transferrin by the brain barriers, BBB and BCSFB, which respectively separate the systemic circulation from the CNS and from the CSF (Rouault et al., 2009; Mesquita et al., 2012). It is supposed that iron entry CNS mainly by BBB, however, it is not completely clear which barrier plays a prevalent role for iron transfer to the CNS across the BBB and BCSFB, requiring further elucidation. The CSF fills the cerebral ventricles and the spinal spaces. It is produced and finely controlled by the choroid plexus (CP), located in lateral (I/II), third (III), and fourth (IV) ventricles, and is strictly in contact with the CNS exchanging metabolically relevant compounds including metals. In particular, iron finally enters the CNS after being exchanged from blood to CSF at the BCSFB level. Previous studies investigated the mechanisms of iron passage by monitoring the uptake into the brain by radioactive iron (Bradbury, 1997) and using *in vitro* systems to assess its transepithelial transport across BCSFB, simulating *in vivo* condition (Wang et al., 2008). Being the BCSFB delimited overall by a monolayer of tight-junctioned epithelial cells, it is expected to be more permeable than BBB (D'Agata et al., 2017).

The CP is a highly vascularized structure inside the ventricles of the brain, containing a monolayer of choroid plexus epithelial (CPE) cells surrounding and enclosing a central stroma. CPE cells are interconnected with an apical localization of tight junctions, restricting the entry of molecules and pathogens from blood to brain and one of their main tasks is the CSF production, at a rate of 0.4 mL/minute (Plum, 1988; Spector and Johanson, 2013; Liddelow, 2015; Lun et al., 2015). CP is 10 μm thick, covering a total apical surface around 75 cm^2. In humans, the CP and enothelial cells of BBB are in a surface area ratio of 1:10, and its electrical resistance is in the range 10-100 Ohm, much lower than BBB (around 1000 Ohm) (Badaut 2016 (The Choroid Plexus and Cerebrospinal Fluid System: Roles in Neurodegenerative Diseases, 2016). The CP-CSF system has an active role in physiological process of brain homeostasis and it is considered the main locus of the permeability-regulating BCSFB (Balusu et al., 2016; Choroid Plexus Blood-CSF Barrier: Major Player in Brain Disease Modeling and Neuromedicine). Next to their barrier function, CPE cells strongly impact the CSF composition, express specific transport systems able to control the trafficking of various brain nutrients (i.e. ions, aminoacids, peptide hormones, and nucleosides) and also to modulate the clearance of toxic molecules and drugs from the brain (de Lange, 2004; Spector and Johanson, 2013; The Choroid Plexus and Cerebrospinal Fluid System: Roles in Neurodegenerative Diseases, 2016; Marques et al., 2017). Beyond restriction of the access of substances from the blood to the CSF, the BCB is known to remove substances from the CSF to the blood(Zheng et al., 2003).

CPE display the machinery to locally control iron delivery into the CSF (Marques et al., 2009), possibly playing a crucial role in the modulation of iron exchange between blood and CSF. When blood-borne iron reaches the capillaries of the CP network, the fenestrated CPE allow iron molecules, either TfR-bound or free, to enter the cells with similar mechanism of BBB (by receptor-mediated endocytosis).

1.2.3 From CSF to Brain and Efflux Mechanism

Since there is no structural barrier between the CSF and interstitial fluid (ISF), materials in these two fluids compartments can freely exchange, in a bidirectional way (Zheng and Monnot, 2012).

There are evidences that large molecules can reach the CNS through the CSF, and specifically that the flux of the interstitial fluid in the CNS parenchyma and the macro flux of CSF in the leptomeningeal space can interact since the layer of pia mater lining the CNS surface is not continuous, and there is some continuity of the leptomeningeal space with the perivascular spaces penetrating into the parenchyma (Nakada and Kwee, 2019).

This intimate exchange between CSF and ISF plays an essential role in maintaining the homeostasis of the CNS. The CSF occupies the brain's ventricles and subarachnoid space and, together with the ISF, forming a continuous fluidic network bathing CNS cells (Bjorefeldt et al., 2018). The interface between ventricular CSF and the ISF of the parenchyma presents a restricted molecular exchange across the choroid plexus epithelial lining, where cells are adjoined by tight junctions (BCSFB); on the contrary, areas of the ventricular lining of ependymal cells are connected by gap junctions, allowing free exchange of molecules between CSF and ISF at these sites (Bjorefeldt et al., 2018). CSF enters the brain parenchyma, mixes with ISF that is produced there, and is eliminated into reservoirs such as the subarachnoid space and ventricles from the brain parenchyma as CSF again (Matsumae et al., 2016).

Since CSF collects many waste substances from brain (in fact most of the popular AD biomarkers are dosed in CSF), it is important to consider the role of brain CSF-ISF exchange linked to the efflux of interstitial solutes through bulk flow. Recently, the role of so-called "glymphatic system" is of great relevance. The glymphatic system is a brain-wide network of perivascular pathways that supports exchange of CSF and ISF facilitating to the clearance of interstitial solutes, as well as Aβ, and contributing to clearing waste in the brain(Boespflug and Iliff, 2018).

Perivascular clearance comprises perivascular drainage and glymphatic pathways: CSF flows into the brain parenchyma via the periarterial space surrounding the artery, then enters the interstitium of the brain tissue via aquaporin 4 (AQP4)-controlled water channels (distributed in the end feet of astrocytes); CSF enters the ISF flows by convection, and it exchanges with ISF within the brain parenchyma; after washing the waste proteins from the tissue, it streams into the perivenous space, (perivascular space around the deep-draining vein) and is subsequently discharged outside the brain (Tarasoff-Conway et al., 2015).Brain solute efflux is likely driven by both bulk flow and diffusion, although their relative contributions remain undefined.

It is reported that metals such as iron and copper may enter the interstitial fluid of the brain via the BBB, be transported back into the blood via the efflux mechanism at the BCSFB (Zheng and Monnot, 2012). However, the knowledge on the mechanism involved in iron export is still limited, requiring elucidation on the transporters/pathways implicated.

1.2.4 Mathematical modeling in Brain Barriers

To understand complex biological systems is necessary a thorough understanding of the interaction between molecules and pathways. Mathematical models allow researchers to investigate how complex regulatory processes are connected and how alteration of these processes may concur to the development of a particular disease (Fischer, 2008). In addition, computational models help researchers to systematically analyze systems perturbations, guiding the design of new experimental tests and novel therapeutic targets. Numerous mathematical methods have been developed to address different categories of biological processes, such as metabolic processes or signaling and regulatory pathways (Fischer, 2008). Recently, many researchers applied mathematical approaches to evaluate iron kinetics at BBB level (Khan et al., 2018), iron metabolism (Lopes et al., 2010) and the aggregation of Amyloid-β in the presence of metal ions (Asili et al., 2019). At this regard, multi-compartmental modeling based on ordinary differential equations (ODEs) well describes some types of biological systems, as well as those separated by barriers (Bassingthwaighte et al., 2012). Furthermore, sensitivity analysis methods have been widely applied to study complex biological systems, investigating how the changes of the biological parameters values affect results and are consequently relevant in the model. Global sensitivity analysis evaluates which fraction of the variability of the output is attributed to each input parameter, based on a numerical simulation designed to explore the parameter space using a large variety of parameter combinations (Wu et al., 2008; Zi, 2011).

The access and regulation of iron into the brain involve various essential processes across blood-brain barriers but the complete mechanism is still unknown, leaving unsolved important implication both in physiological and pathological conditions.

1.3 Iron in Nanomedicine

This section is partly based on:
Ansari SAMK†, Ficiarà E.†, Ruffinatti F.A., Stura I., Argenziano M., Abollino O., Cavalli R., Guiot C., D'Agata F., *Materials* 2019,12(3), 465.

The several functional properties of iron can be exploited also in the field of theranostic, i.e. the use of nanomedicine for both diagnostic and therapeutic purposes. In fact, due to its magnetic properties, iron can be used to design magnetic nanoparticle with tunable functional properties. The magnetic properties are critical for the passage of nanoparticles across brain barriers, due to coordinated use of external magnetic forces for non-destructive BBB crossing and the site-specific delivery of therapeutics to treat CNS diseases, such as Alzheimer's and brain tumors.

1.3.1 Magnetic Nanoparticle in CNS: Characterization of SPIONs

The nanometric size of a material is in the same scale of several biological mechanisms allowing nanoparticles and nanomaterials to potentially cross the biological barriers to access the sites of delivery and to interact with DNA or small proteins at different levels, in blood or within organs, tissues or cells (Hauert and Bhatia, 2014). In recent years, much attention has been paid to the synthesis of a different kind of nanoparticles as nano-medical materials. Among them, engineered Magnetic Nanoparticles (MNPs) made of iron, cobalt, or nickel oxides exhibit special properties, including high surface-to-volume ratio and high magnetic moment, allowing potential manipulation by an external magnetic field (Cardoso et al., 2018). Especially, MNPs manufactured with ferromagnetic material, i.e., Iron Oxide Nanoparticles (IONPs), made of magnetite (Fe3O4) and maghemite (Fe2O3) combine ideal biocompatibility with superparamagnetic properties allowing widespread biomedical uses such as targeted drug delivery, bioimaging, hyperthermia, photoablation therapy, biosensors, and theranostic applications (Khanna et al., 2018).

The enhancement of effective drug delivery by magnetic driving of sensitive MNPs has been especially explored to treat diseases of the CNS. Current pharmacological treatments are mainly based on the systemic delivery of active substances into the CNS, whose effectiveness is seriously limited due to the presence of BBB. MNPs are therefore considered powerful tools to cross BBB by means of physical mechanisms and properly deliver the drug cargo in the brain. There are many in vitro and in vivo evidences of BBB trespassing by MNPs under magnetic fields to deliver therapeutic agents in the CNS (D'Agata et al., 2017).

As well as an improved biocompatibility and bioavailability, IONPs provide specific advantages for the treatment of neurological disorders based on their possibility to be imaged and externally driven through magnetic scanners for a targeted drug-delivery (theranostic approach). Importantly, external static magnetic fields could also be used to enhance BBB permeability against IONPs, whereas alternating magnetic fields are suitable for selectively killing tumor cells via localized hyperthermia (D'Agata et al., 2017).

The magnetic properties of IONPs can be assessed by measuring the magnetization of a samples when subjected to an externally applied magnetic field H varying from -10,000 Oe to 10,000 Oe, at a defined temperature. The Vibrating Sample Magnetometer (VSM) and Superconducting Quantum Interference Device (SQUID) are the most common techniques able to measure important magnetic parameters of MNPs, such as saturation magnetization, coercive field, and remnant magnetization (Ansari et al., 2019). To date, these measurements represent an essential characterization step, because of the interplay between MNPs and the external magnetic fields employed for magnetic-driven nanocarriers as useful strategies for numerous biomedical applications.

IONP physical characteristics impact on their magnetic properties. The various materials can be classified by different form of magnetic behaviors, based on their response to an external magnetic field that, at the microscopic level, interacts with atomic dipoles, causing a measurable macroscopic magnetic moment. Five basic types of magnetism are known: Diamagnetism, paramagnetism, ferromagnetism, antiferromagnetism, and ferrimagnetism. Ferrimagnetic and ferromagnetic materials are the most interesting ones, exhibiting remarkable magnetic properties. In particular, ferromagnetic materials show a high magnetization M during the interaction with the applied field H. The magnetization does not increase indefinitely, but reaches asymptotically the saturation magnetization Ms. After turning off the external field H a little amount of residual magnetization, Mr remains and the applied magnetic field required to reduce to zero the magnetization of the material is called coercive field or coercitivity Hc. This relationship between H and M is plotted in Figure 1.7, showing the magnetic hysteresis loop. (Ansari et al., 2019)

The dimension of IONPs, determines their surface-to-volume ratio, in turn linked with their reactivity, also responsible for attraction and agglomeration phenomena. In fact, IONPs magnetism is dominated by size effects, due to the magnetic domain structure of ferromagnetic material (i.e., Weiss domain, volume in which all atomic magnetic dipoles are aligned). In 1930, Frenkel and Dorfman suggested the principle of the superparamagnetism theory, stating that ferromagnetic materials transfer from multi-domains to a single-domain state by particle resizing to nanoscale (Figure 6b) (Ansari et al., 2019). The existence of a critical size at which the transition to single-domain (i.e., state of uniform magnetization) occurs is well established in the literature. It happens when the magnetic energy configuration of multi-domains is no more favorable compared to the single domain. The gain in energy through the division is less than the energy of the domain wall. It can be calculated analytically (Hubert and Schäfer, 1998) for a sphere or an infinite cylinder as:

$$D_c = P\,[(A\,K_u)^{1/2}/\mu_0\,M_s^2] \qquad (1)$$

where D_c is the critical diameter, P is a dimensionless constant depending on the shape (~17 for a cylinder, ~35 for a sphere), A is the exchange stiffness constant, K_u is the uniaxial anisotropy constant, μ_0 is the magnetic permeability in vacuum, and M_s is the saturation magnetization (Akbarzadeh et al., 2012; Ghazanfari et al., 2016). For real NPs (1) still approximately holds using a P that is generally in the range 10–40.

When the of IONPs size is small enough, they are generally called Superparamagnetic Iron Oxides Nanoparticles (SPIONs) or Ultra-Small Iron Oxides nanoparticles (USPIONs), with size >50 nm or <50 nm, respectively (Ansari et al., 2019).

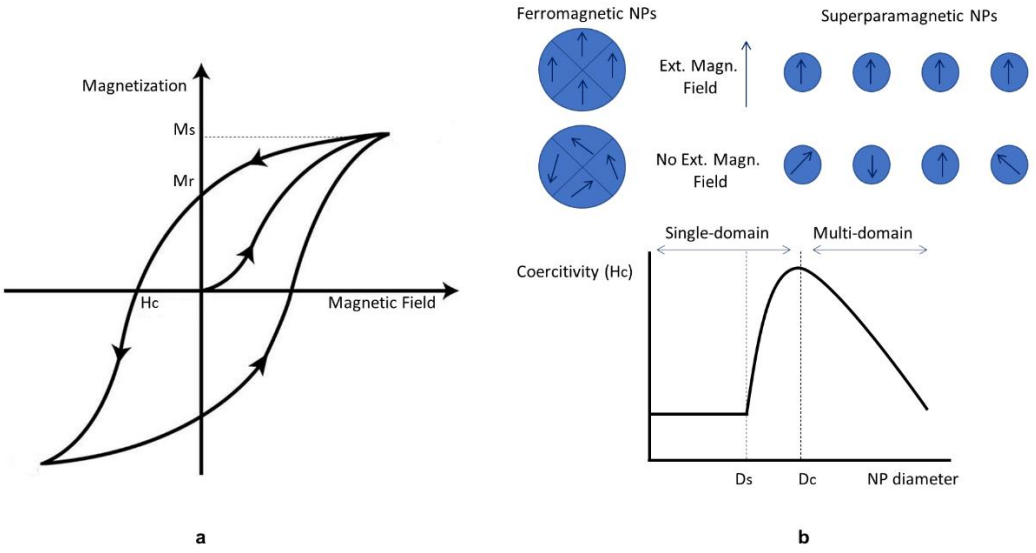

Figure 1.7. Principal features of magnetic material: (**a**) Hysteresis loop of ferromagnetic and ferrimagnetic materials. Critical magnetic parameters: Saturation magnetization (M_s), Coercive field (H_c), and Remnant Magnetization (M_r) are shown. (**b**) Magnetization behavior of ferromagnetic and superparamagnetic NPs under an external magnetic field. Domains of a ferromagnetic NP align with the applied fields. The magnetic moment of single domain superparamagnetic NPs aligns with the applied field. In the absence of an external field, ferromagnetic NPs will maintain a net magnetization, whereas superparamagnetic NPs will exhibit no net magnetization due to rapid reversal of the magnetic moment. The relationship between NP size, the magnetic domain structures, and coercive field is shown. Ds and Dc are the 'superparamagnetism' and 'critical' size threshold. Adapted from (Ansari et al., 2019).

Further decreasing their size, the IONPs reach the superparamagnetic diameter D_s, showing zero coercivity and no hysteresis, due to the thermal effects. In fact, when the external magnetic field is switched off, the magnetic domains point at random orientation, with zero resultant (Ansari et al., 2019). The degree of alignment of magnetic moments depends on temperature, it decreases when the temperature increases and vanishes beyond a critical temperature, where the magnetization becomes zero. Above this critical temperature (i.e., blocking temperature T_b), the characteristics of superparamagnets are identical to those of paramagnets with a very high reactivity, i.e., they lose magnetism after the removal of the applied field but maintain an extremely large moment during the interaction (Ansari et al., 2019). Working with SPIONs in the biomedical field is highly recommended, because of their high magnetization response under external field interaction and their no zero magnetization behavior without applied field, avoiding the risk of agglomeration, and reciprocal attraction (D'Agata et al., 2017).

Drawing the magnetization curve (*M-H* curve) for different preparation of IONPs (different size, shape, etc.) is useful to study the link between magnetic and physical properties. High M_s is an important parameter for characterizing IONPs, which is typically is measured in emu·g^{-1}, mainly depends on the chemical composition of NPs. Low values of coercive field H_c, measured in Oe,

together with the remnant magnetization M_r, are other important indicators of emerging superparamagnetic properties.

1.3.2 Toxicity of MNPs in CNS (Ansari et al., 2019)

Several IONPs applications for CNS pathologies have been proposed but safety concerns were raised due to contradictory results about neurotoxicity.

The high complexity of mechanisms that can induce cytotoxicity after NPs interaction and involve both cellular and molecular pathways it is well established in literature. They include physical damage of membrane, structural changes in cytoskeleton components, defects of transcription and oxidative damage of DNA, damage of mitochondria, disturbance of lysosome functioning, generation of reactive oxygen species (ROS), alteration of membrane protein functions, and synthesis of inflammatory factors and mediators (Sukhanova et al., 2018). Currently, several studies on their harmful effects are carried out in various in vitro and in vivo models, in order to investigate the relation between biocompatibility and NPs or MNPs features (Jeevanandam et al., 2018). The physicochemical features, such as size, shape, surface charge, and coatings, determine their cytotoxicity. For example, IONPs of few nanometers (approximatively <10 nm) are more toxic than larger ones, which cannot enter the nucleus. The dimension of IONPs is also a significant factor for the biodistribution at body level, affecting the blood circulation time and the filtration from spleen, liver, or kidneys.

In general, IONPs are assumed to be biocompatible, but upon intracellular degradation, IONPs do release iron ions, influencing iron homeostasis at general body level. Especially, due to the high vulnerability of CNS for iron imbalance, much work still has to be done to fully understand how different types of IONPs could affect the brain, BBB and what potential adverse effects on CNS can derive from their exposure. Yarjanli and colleagues reviewed a large number of studies concluding that IONPs, according to their physicochemical properties, can lead to iron accumulation, oxidative stress, protein aggregation in the neural cells, and may induce neurodegeneration (Yarjanli et al., 2017). Additionally, the review of Xie and coworkers evaluated the close links between biocompatibility and size, concentration, surface properties, morphologies and structures of IONPs, underlining the need of carefully engineering biocompatible NPs with in vitro study of degradation and cells availability to ensure in vivo safe metabolization (Xie et al., 2018).

In vitro experiments aimed at evaluating the effects of IONPs on the CNS, used different cell models (i.e human brain microvascular endothelial cells, astrocytes, or neurons cell cultures). The main indicators for toxicity considered by literature are (Costa et al., 2016) :

- dose and time-dependent cell viability and/or proliferation;
- production of Reactive Oxygen Species (ROS);
- cell membrane disruptions;
- alteration of mitochondrial activity;
- genotoxicity induction.

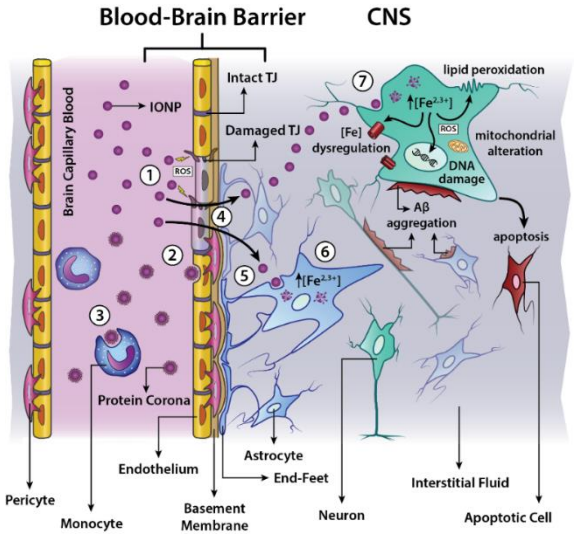

Figure 1.8. Interference of IONPs with CNS iron homeostasis and its involvement in neurodegeneration process. (1) IONPs in the bloodstream can alter the permeability of BBB. The integrity of BBB can be damaged by ROS production and/or inhibition of Occludin-proteins (belonging to tight junction proteins TJ); (2) based on their size, surface charge and coating IONPs are subject to the formation of protein corona around IONPs, leading to opsonization phenomena. This can alter physicochemical properties of IONPs and/or improve transport across BBB; (3) IONPs can be also eliminated from blood circulation by means of recognition and uptake by monocytes or other cells of Mononuclear Phagocytic System; (4) IONPs can cross BBB by means of paracellular or transcellular mechanism and enter in CNS [6]; (5) according to their size, IONPs can be internalized by pinocytosis (dimensions < 10 nm) or endocytosis (approximatively larger than 10 nm) into the CNS cells; (6) in the intracellular environment IONPs are degraded in the acid environment of endosomes (degradation time depending on IONP size) with consequent release of iron ions in the cytoplasm; astrocytes are more sensitive to uptake and accumulation of IONPs [111]; (7) in the neurons, after the IONPs internalization and degradation, iron ions participate to redox cycling taking part to many biological processes implicated in neurodegeneration and neural damage: (a) Fenton's reaction with production of ROS (consequent lipid peroxidation and/or DNA damage); (b) alteration of iron regulation proteins (responsible for iron transport, uptake and storage); (c) alteration of mitochondrial activity; (d) accumulation in iron pool; (e) apoptosis; and (f) protein aggregation (e.g., Aβ, α-synuclein). Adapted from (Ansari et al., 2019).

The majority of neurotoxicity studies on IONPs are performed in 2-dimensional in vitro cultures. There is, however, an increasing interest in co-cultured and 3-dimensional cells cultures, which are more realistic models with respect to 2D systems (Theumer et al., 2015; De Simone et al., 2018). For instance, brain cells can be cultured to form spheroids, which allow recreating the 3D-spatial environment of the CNS, in order to test advantageously and more precisely IONPs toxicity. In summary, the exploration of the impact of various IONPs on CNS functions and the development of new strategies to test it are a current research trend running in parallel with the study of iron homeostasis alterations involved in neurodegenerative disorders.

1.3.3 Computational Models for Magnetic Driving in the treatment of CNS tumors

Magnetic nanocarriers have been extensively investigated as hyperthermic agents in combination with radiotherapy to treat superficial and deep tumors (Sohail et al., 2017; Chang et al., 2018; Spirou et al., 2018). In particular, Magnetic Fluid Hyperthermia (MFH) consists of the in situ administration of a stable colloidal suspension of biocompatible SPIONs which can produce endogenous heat generation following activation by external magnetic fields (D'Agata et al., 2017).

Clinical applications of MFH have been approved by the Food and Drug Administration (FDA) and is already marketed (MagForce ® activated by MFH ® 300F or NanoActivator ®).

As tumor oxygenation is one of the main targets of the hyperthermic treatment, the use of oxygen carriers "decorated" by SPIONs as hyperthermic agent were investigated (Zullino et al., 2019), showing that in addition to heating (temperature increase of some °C could be reached already at low magnetic field) such Magnetic Oxygen-Loaded Nanobubbles (MOLNBs) are easily internalized by cells, do not produce toxic effects, deliver oxygen in a sustained way, and can be monitored either by using clinical Ultrasound (US) sonography and by Magnetic Resonance Imaging (MRI) (Zullino et al., 2019).

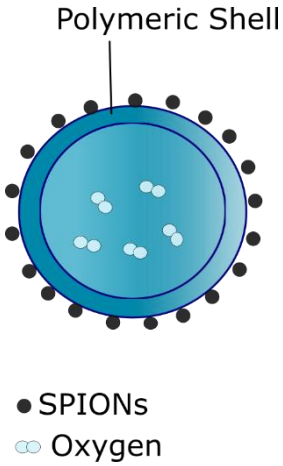

Figure 1.9. Schematic representation of MOLNBs structure: a spherical oxygen-filled structure characterized by a core-shell composition. The polymeric shell is covered by SPIONs, conferring it magnetic properties.

Beyond hyperthermia, MOLNBs can find applications in magnetic driving and delivery systems (Ficiarà et al., 2020a). In particular, the attention was focused on the quantitative methods for engineered nanoparticles to cross brain barriers and to effectively target the CNS (Guiot et al., 2016). As a matter of fact, MNPs have already been proposed to bypass the BBB to treat glioblastomas and neurodegenerative diseases (Chertok et al., 2011; Yao et al., 2015; Sintov et al., 2016; Tam et al., 2016; Mahmoudi et al., 2018) as well as in regenerative medicine (Huang et al., 2017; Falconieri et al., 2019) and drug delivery (Thomsen et al., 2015; Leterme et al., 2019). Very recently magnetic nanopartides have been proposed as transducers in advanced neuromodulation, via the hysteretic heat when exposed to alternated magnetic fields (Roet et al., 2019).

Tumors of the CNS are still poorly treated due to the difficulty to reach their site without seriously damaging the surrounding structures. Both surgery and less invasive approaches are critical because the presence of very selective membranes (such as the Blood-Brain Barrier) restricts the passage of drugs and substances. Since the main therapeutic approaches, such as radiotherapy and chemotherapy, are not enough effective individually, it may be favorable to identify alternative approaches inducing a synergistic effect of multiple therapies and taking into account the specific complexity of the CNS.

Therefore, alternative possibility could be to administer the NBs in the CSF and target the brain tumors in critical positions.
Tumors close to the walls of the cerebral ventricles could be reached by NBs injected into the CSF and properly guided, in order to release locally their contents in a sustained and continuous manner, allowing the optimization of the radio-chemotherapy treatment of these aggressive tumor forms (Ficiarà et al., 2020a).

The development of magnetically guided nanoplatforms can ensure a more effective treatment directed to high-grade gliomas, allowing in vivo tracking by MRI (Aguiar et al., 2017). Computational models can be helpful to validate such approach. In fact, they have the potential to accelerate the design of MNPs and also to simulate and to predict properties for medical imaging and targeted drug delivery (David, 2017). It is reported that MNPs can potentially be imaged using MRI technology and guided toward brain tumor locations using external magnets (Ramaswamy et al., 2015).

However, because of the complexity of the CNS, the magnetic driving and targeting of nanocarriers are still a challenge, and new studies in this field of nanomedicine are highly desirable (Aguiar et al., 2017). At this regard, *in silico* approach can optimize the use of magnetic nanocarriers, simulating in the same time the magnetic fields and the related interaction with nanocarriers.

Chapter 2: Aims of the Work

We supposed that iron dysregulation at brain barriers and its impaired levels on biological fluids and brain can play a role in the pathophysiological process in neurodegenerative diseases, such as AD, revealing potential strategic role for early diagnosis and personalized therapeutic strategies.
Furthermore, innovative applications in nanomedicine exploiting the magnetic properties of this metal are of great interest to overcome some of the critical issues of the current theranostic nanosystems in CNS applications.

On this basis, the work of this thesis has two main purposes:

1. A thorough investigation of the role of iron as potential biomarkers in the progression of dementia both for novel diagnostic (i.e., early detection of AD and MCI) and for therapeutic approaches (i.e., innovative chelating therapy in personalized medicine, treatments for blood brain barrier dysfunctions). This aim is achieved by joining mathematical modeling approaches to elucidate the potential altered mechanisms of iron exchange at blood-brain barriers level as well as machine learning techniques and exploiting reliable protocols for quantitative evaluation of iron in cerebrospinal fluid and standard iron-related clinical parameters.

2. A proposal for innovative methods exploiting magnetic properties of iron in functionalized nanoparticles to monitor and drive therapeutic agents (i.e., oxygen) under a precise targeting, crucial for CNS or critical tumors. After qualitative and quantitative assessments of the magnetic properties and the safety of the nanovectors under consideration, the integration of a new set up and computational models was studied to potentially guide magnetic nanoparticles toward tumor locations. This approach can be useful also for other cutting-edge nanosystems for neurodegenerative diseases.

Chapter 3: Machine Learning Profiling of Alzheimer's Disease Patients Based on Current Cerebrospinal Fluid Markers and Iron Content in Biofluids (Ficiarà et al., 2021a)

Ficiarà E., Boschi S., Ansari S., D'Agata F., Abollino O., Caroppo P., Di Fede G., Indaco A., Rainero I., Guiot C., 2021 *Front. Aging Neurosci.* 13:607858.

Abstract: Alzheimer's disease (AD) is the most common form of dementia, characterized by a complex etiology that makes therapeutic strategies still not effective. A true understanding of key pathological mechanisms and new biomarkers are needed, to identify alternative disease-modifying therapies counteracting the disease progression. Iron is an essential element for brain metabolism and its imbalance is implicated in neurodegeneration, due to its potential neurotoxic effect. However, the role of iron in different stages of dementia is not clearly established.
This study aimed to investigate the potential impact of abnormal concentration of iron both in cerebrospinal fluid (CSF) and in serum to improve early diagnosis and the related therapeutic possibilities.
In addition to standard clinical method to detect iron in serum, a precise quantification of total iron in CSF was performed using graphite-furnace atomic absorption spectrometry in patients affected by AD, mild cognitive impairment, frontotemporal dementia, and non-demented neurological controls. The application of machine learning techniques, such as clustering analysis and multiclassification algorithms, showed a new potential stratification of patients exploiting iron-related data.
The results support the involvement of iron dysregulation and its potential interaction with biomarkers (Tau protein and Amyloid-beta) in the pathophysiology and progression of dementia.

Although diagnostic criteria for AD and MCI are currently used (Dubois et al., 2007, 2010; Albert et al., 2011; McKhann et al., 2011; Sperling et al., 2011), defining the preclinical state of MCI/AD aiming at discovering therapies preventing the irreversible progression of AD (Fiandaca et al., 2014) remains a challenge.

New biomarkers and a deeper comprehension of the neuropathological processes involved in AD are urgently needed, with the aim to identify alternative disease-modifying therapies counteracting the disease progression. Actually, additional fluid biomarkers measured in CSF or in blood (Palmqvist et al., 2020) unraveled promising candidates, reflecting several inter-related mechanisms of AD pathophysiology (Molinuevo et al., 2018).

The imbalance in iron homeostasis in AD and its interaction with the more consolidated biomarkers Aβ and Tau have been described (Ndayisaba et al., 2019; Spotorno et al., 2020), supporting the conjecture of new therapeutic strategies based on iron chelators or other iron-toxicity counteracting drugs as a valuable approach for AD treatment (Liu et al., 2018; Ashraf and So, 2020). Several studies supported the notion that brain iron elevation (Lane et al., 2018; Ayton et al., 2019) or even the levels of iron-related proteins, e.g. plasma transferrin, are associated with AD and cognitive decline (Hare et al., 2015; Guan et al., 2020). Furthermore, the concentration of several elements

included iron in biological fluids (Duce and Bush, 2010; Schrag et al., 2011; Cicero et al., 2017) has been evaluated with different techniques but highlighting difficulties to compare results. However, a direct evaluation of iron concentration in the brain remains a difficult task and conclusive results about the combined role of iron and iron-protein levels on biological fluids (i.e., CSF and serum) with the preclinical stage of dementia are not still clearly established.

Recently, the application of machine learning techniques gave strong support to AD diagnosis, in particular for classification tasks (Tanveer et al., 2020) and clustering analysis (Alashwal et al., 2019), aiming at identifying which features are involved in the conversion from early-stage AD to dementia. In particular, clustering analysis is a potentially strategic tool able to establish subsets of individuals sharing similar patterns and has been applied to investigate disease-related profiles of different AD and dementia stages (Racine et al., 2016; Alashwal et al., 2019).

This study aimed to investigate potential patterns of iron imbalances both in CSF and in serum, to improve early diagnosis and the related therapeutic possibility. While the content of iron in serum was assessed using standard clinical methods to detect transferrin (s-Tf), an accurate quantification of total iron in CSF was obtained using atomic absorption spectrometry, not currently used in clinical practice, leading to a potential added value to the clinical information about the status of the patients.

Firstly, to discriminate iron profiles between different forms of dementia, iron concentration in CSF of AD patients was compared with patients affected by Frontotemporal Dementia (FTD), a heterogeneous disorder with distinct pathological features and clinical phenotypes, encompassing changes in behavior, language, executive control and often motor symptoms (Olney et al., 2017). Secondly, we compared patients affected by AD, MCI, and non-demented controls, to evaluate shared patterns and the ability to discriminate these conditions.

To check whether the new iron-related biomarkers could add significant improvements to AD early diagnosis, a step-by-step procedure was adopted, iteratively adding to the well-consolidated features (Aβ42, p-Tau and t-Tau) also the results from s-Tf and iron content in CSF.

Cluster analysis was performed, to unravel subgroups within heterogeneous data such that individual clusters classify similar profiles, having better homogeneity than the whole. In particular, the hierarchical agglomerative clustering (HAC) algorithm was applied, a suitable technique for partitioning patients based on their similarity.

Since clustering analysis can reveal similar (pathological) profiles and identify potential altered biological mechanisms, we investigated how such clusters are influenced by the addition of the iron-related parameters and whether MCI can be better discriminated from controls and AD. Multiclassification algorithms with different features sets are used to compare diagnostic power and to rank the relevance of features for the prediction of the model.

3.1 Materials and Methods

3.1.1 Participants

We retrospectively included 69 patients (35 males and 34 females, mean age: 70.5 years ± SD: 7.2), evaluated and followed at the Department of Neurosciences of University Hospital "Città della Salute e della Scienza", Torino and at Fondazione IRCCS Istituto Neurologico Carlo Besta, Milano, Italy. CSF samples from all 69 patients, including 14 non-demented neurological control (CT) patients, 17 patients affected by MCI, 16 AD and 22 FTD (behavioral variant) were collected.

Diagnosis of FTD was made according to Rascovsky Criteria (Rascovsky et al., 2011).

Diagnosis of AD has been made according to NIA-AA (National Institute of Aging - Alzheimer Association) criteria (McKhann et al., 2011).

For the classification of MCI, the Petersen criteria were used: cognitive complaint, decline or impairment; objective evidence of impairment in cognitive domains; essentially normal functional activities; not demented (Petersen, 2004; Petersen et al., 2009).

MCI group included a mix of amnestic, nonamnestic, and multidomain subjects, with disease onset before (N=3) and after (N=13) 65 years.

As control group, CSF of 14 patients with neurological conditions (see Supplementary Material) without dementia was analyzed.

Cognitive functions were assessed by Mini Mental State Examination (MMSE).

A complete description of data is available in Table 1. The experiments conformed to the principles of the Declaration of Helsinki and were approved by the local ethics committee. Informed consent for liquor collection and storage relative to the retrospective study was given by all subjects or by their caregivers.

Details of procedure for the collection of CSF and serum samples, also with determination of CSF levels of Aβ42, p-Tau and t-Tau and of serum transferrin, are reported in Supplementary Material.

3.1.2 Iron Determination in CSF by GF-AAS

Frozen aliquots of CSF samples were transported on dry ice until the shipment to the analytical chemistry laboratory, were kept frozen during storage and unfrozen one hour before the analysis.

The determination of iron in CSF samples was carried out by means of Graphite Furnace Atomic Absorption Spectrometer (GF-AAS). The determination of iron in CSF samples was carried out in a controlled atmosphere laboratory provided with filtered air and laminar flow hoods, adopting all precautions to avoid sample contaminations arising from vessels, reagents, and handling. Total iron was dosed in CSF using a Perkin Elmer Analyst 600 Graphite Furnace Atomic Absorption Spectrometer (GF-AAS), equipped with an autosampler, THGA (transverse heated graphite atomizer), and Zeeman-effect background correction. A hollow cathode lamp (Perkin-Elmer) was used for iron, setting the absorption wavelength at 248,3 nm. Pyrocoated graphite platform-integrated tubes were used throughout. The graphite furnace temperature program designed for the atomization of the analyte of interest, consisting of four-steps, is reported (Table 3.1).

High-purity water (HPW) with a specific resistivity of 18 MΩ cm^{-1}, obtained with a Milli-Q water system (Millipore, Bedford, MA), was used for the preparation of the standard and dilution of the samples. All chemicals employed in this work were of analytical grade purity. Iron standard solutions were prepared from a concentrated stock solution of 1000 mg/L iron (Sigma Aldrich). Blank solutions were prepared using HPW with 0.5% nitric acid.

Magnesium Nitrate $Mg(NO_3)_2$ (Sigma Aldrich) was used as matrix modifier (15 µg diluted in 10 mL of HPW) to improve the absorbance signal. The instrument was calibrated daily using freshly prepared iron standard solutions of concentration 5, 10, 15, 20 µg/L. The autosampler tubes were cleaned between measurements by aspirating aliquots of HPW with 0.1% Triton X-100.
After a minimum pre-treatment of CSF samples (1 mL diluted 1:3) iron was evaluated by means of the Standard Addition Method, using two additions for each sample. Concentration and absorbance were used to obtain the calibration for each sample and the final concentration of iron was estimated from the intercept of line calibration, corrected for the dilution factor. Measurements with $R^2 > 0.97$ were accepted.

Table 3.1. Four steps graphite furnace temperature program designed for the atomization of the analyte of interest (iron). Adapted from (Ficiarà et al., 2021a).

Step	Temperature		Ramp time	Hold Time
Drying	130°	Removal of acqueous component	15 s	30 s
Pyrolisis	1400°	Removal of organic matter and volatil component	10 s	20 s
Atomization	2100°	Atomization of analyte	0 s	3 s
Cleaning	2450°	Clean up of the furnace	1 s	3 s

3.1.3 Statistical and Machine Learning Analysis

The assumption of equality of variance and normal distribution were assessed through Levene's test and Shapiro-Wilk's test respectively. One-way analysis of variance (ANOVA) for normally distributed variables, Kruskal-Wallis test for variables not following a normal distribution, and chi-squared test (for categorical variables) were conducted to determine group differences. Post-hoc tests (t-test and Dunn's test adjusted for multiple comparisons errors according to Bonferroni) were performed respectively after significant results of ANOVA and Kruskal- Wallis test. The same procedures were applied to compare clusters in the cluster analysis, described below.

Bivariate correlations between clinical data, biomarkers, and the iron concentration levels were tested both using Spearman's test and Pearson's test for non-parametric and parametric relationships (r_s= Spearman's rank correlation coefficient, r= Pearson's correlation coefficient) respectively. We assumed as correlated only the variables simultaneously satisfying the two correlation criteria, with both $|r|$ and $|r_s| > 0.5$. Results from statistical analysis were evaluated against a threshold of $p < 0.05$.

Before the cluster analysis, Hopkins's test was applied to assess the clustering tendency of the datasets. For the hierarchical clustering, the clustering variables were selected based on the results of bivariate correlations, avoiding to include features with a high degree of collinearity (a threshold of $r > 0.7$ was set (Dormann et al., 2013)). For the variables presenting some association with age, additional analysis was performed including the age correction in the clustering analysis (Supplementary Material).

HAC was applied, a bottom-up approach in which each data point starts in a separate cluster, and pairs of clusters are merged at the bottom going up the hierarchy. After data standardization (Z-score unit), patients were grouped using HAC with Ward's method of minimum variance and Euclidean distance metric and visualized in dendrograms. Ward's method joins two clusters to make the smallest increases in the pooled within-cluster variation (Jr, 1963).

The number of resulting clusters was set finding clustering step where the acceleration of distance growth is the largest, stopping the process and selecting a distance cut-off in the dendrogram to determine the correct number of clusters (greater than 2 clusters). Different sets of features in two datasets were considered for clustering, and a heatmap was used to visualize the median value of the features in each cluster. The values of features within each cluster are reported for the different feature sets used (Supplementary Material).

The clusters obtained for each feature set were compared based on the following clustering scores: Adjusted Rand Index (ARI) and Adjusted Mutual Information (AMI), measuring the similarity and agreement of the two assignments; V-measure, evaluating the homogeneity and completeness of the clusters. In the subpopulation in which all features considered are available, the ratio (Fe CSF/s-Tf) was calculated for each cluster and the dataset was divided into quartiles to observe where the values of variables in each cluster fall with respect to the whole population.

The dataset was used to train two machine learning models based on Support Vector Machine (SVM) and Logistic Regression (LR) adapted for multiclass classification, using two different sets of features, comparing the performance of the classifiers and ranking the relevance of features. The SVM algorithm is very popular for discrimination tasks because it is able to reach good generalization ability and accurately combines features, finding the maximal margin hyperplane and minimizing the classification error to divide data belonging to different classes (Cortes and Vapnik, 1995).

Two feature sets used for the cluster analysis have been included in the model. After standardization of the datasets, an exhaustive search over parameter values for the estimators has been carried out by cross-validated grid search to optimally tune parameters of the classifiers.

For the present study, the OnevsRest (OVR) classifiers based on SVM with linear kernel and LR were used for the classification of the three groups (CT, AD, MCI) and to evaluate the importance assigned to the features. The classification performance of the constructed models, varying the input features presented to it, was computed using the macro-averaged Area Under the Receiving Operating Curve (AUROC). The performance of the classifiers was assessed via 100 times stratified shuffle split cross-validation method (proportion of train:test size = 60:40). This cross-validation method returns stratified randomized folds that preserve the percentage of samples for each class.

The values of the importance for each feature were obtained applying the model inspection technique based on repeated permutations of features on test datasets. The permutation feature importance is defined to be the change in a model score when a single feature value is randomly shuffled. This procedure indicates how much the model depends on the feature, breaking the relationship between the feature and the target, correcting possible bias of the model.

Statistical and machine learning analysis was carried out under the programming language Python, also using library Scikit-Learn (Pedregosa et al.).

3.2 Results

3.2.1 Demographic and clinical data

Demographic and clinical data of the patients classified by clinical diagnosis as described in section Materials and Methods2.1 are reported in Table 3.2 (see also Figure 3.1). Values of MMSE and s-Tf are available for different subgroups of the population composed of 69 patients.

In addition, the four groups were not significantly different for values of glucose and protein dosed in CSF (data not shown) and there were not significant differences in iron variables (s-Tf and iron in CSF) between men and women.

The variables p-Tau and t-Tau showed a strong positive correlation both for the whole population (r_s = 0.67, r=0.87, p< 0.001) and for the population including only AD, MCI and CT patients (r_s = 0.76, r= 0.92, p< 0.001). P-Tau and t-Tau indicated positive correlations also considering AD (r_s = 0.81, r=0.88, p< 0.001), MCI (r_s = 0.61, p = 0.01, r= 0.91, p< 0.001), and CT (r_s = 0.73, p = 0.003, r=0.66, p=0.002) groups. Considering the subpopulation (s-Tf available) the strong correlation between p-Tau and t-Tau was confirmed (r_s = 0.89, r=0.92, p< 0.001). In AD group s-Tf resulted negatively correlated with t-Tau (r_s = -0.70, p = 0.03, r= -0.67, p=0.02).

In addition, we reported significant associations satisfying the criteria of Spearman coefficient $|r_s|>0.5$, reflecting a non-parametric relationship between the variables. Considering the population of CT, MCI, and AD patients, we found a positive association between iron CSF and p-Tau (r_s= 0.53, p<0.001), and in the subpopulation in which s-Tf is available a negative association between iron CSF and Aβ42 (r_s= -0.54, p=0.003). A weak negative association has been found between s-Tf and age (r_s= -0.45, p= 0.014). In AD group, s-Tf showed a negative correlation with age (r_s= -0.63, p= 0.037). For the FTD patients, a negative association has been found between p-Tau and Aβ42 (rs= -0.56, p=0.007).

Table 3.2. Numbers indicate frequency for gender and mean ± standard deviation for age, CSF biomarkers, MMSE, s-Tf. Abbreviations: AD, Alzheimer's disease; Aβ42, forty-two amino acid-long amyloid-β peptide; CSF, cerebrospinal fluid; CT, neurological control; F, female; FTD, Frontotemporal dementia; M, male; MCI, mild cognitive impairment; MMSE, Mini-Mental State Examination; NS, Not significant; p-Tau, hyperphosphorylated tau; s-Tf, serum transferrin; t-Tau, total tau. † Kruskall-Wallis test and Dunn's post-hoc test (Bonferroni correction for p-value). Adapted from (Ficiarà et al., 2021a).

	CT n=14	**MCI n=17**	**AD n=16**	**FTD n=22**	**Statistical analysis**
Gender (M/F) (Count)	10/4	8/9	7/9	10/12	NS
Age at the time of CSF collection (yrs) (mean ± SD)	(72.13±6.96)	(72.36±4.11)	(68.47±7.38)	(69.45±8.69)	NS
	CT n=14	**MCI n=17**	**AD n=16**	**FTD n=22**	
Age onset (mean ± SD)	(68.64±7.16)	(66.82±6.57)	(65.87±7.20)	(65.91±8.11)	NS
Aβ42 CSF (pg/mL) (mean ± SD)	(917.93 ± 277.15)	(832.65±399.16)	(432.00 ± 200.68)	(819.45 ±322.91)	AD < CT: (p <0.001) †, AD < MCI: (p=0.002) † AD < FTD: (p<0.001) †
p-Tau CSF (pg/mL) (mean ± SD)	(19.9 ± 8.91)	(57.47± 58.14)	(84.65±45.18)	(41.12 ± 23.92)	AD > CT: (p<0.001) †, AD > FTD: (p=0.04) †
t-Tau CSF (pg/mL) (mean ± SD)	(102.76 ±72.24)	(326.18±363.71)	(465.81±329.45)	(154.53±102.28)	AD > CT (p=0.002) †, AD > FTD: (p=0.03) †
	CT n=10	**MCI n=12**	**AD n=16**	**FTD n=17**	
MMSE (mean ± SD)	(26.54±3.19)	(24.47±5.16)	(20.63±6.08)	(22.07±4.55)	AD < CT (p=0.03) †
	CT n=9	**MCI n=9**	**AD n=11**	**FTD n=11**	
s-Tf (mg/dL) (mean ± SD)	(231.44±38.01)	(230.78±34.22)	(235.55±17.99)	(255.72±57.11)	NS

Graphical representation of variables (Age, Biomarkers, s-Tf, MMSE)

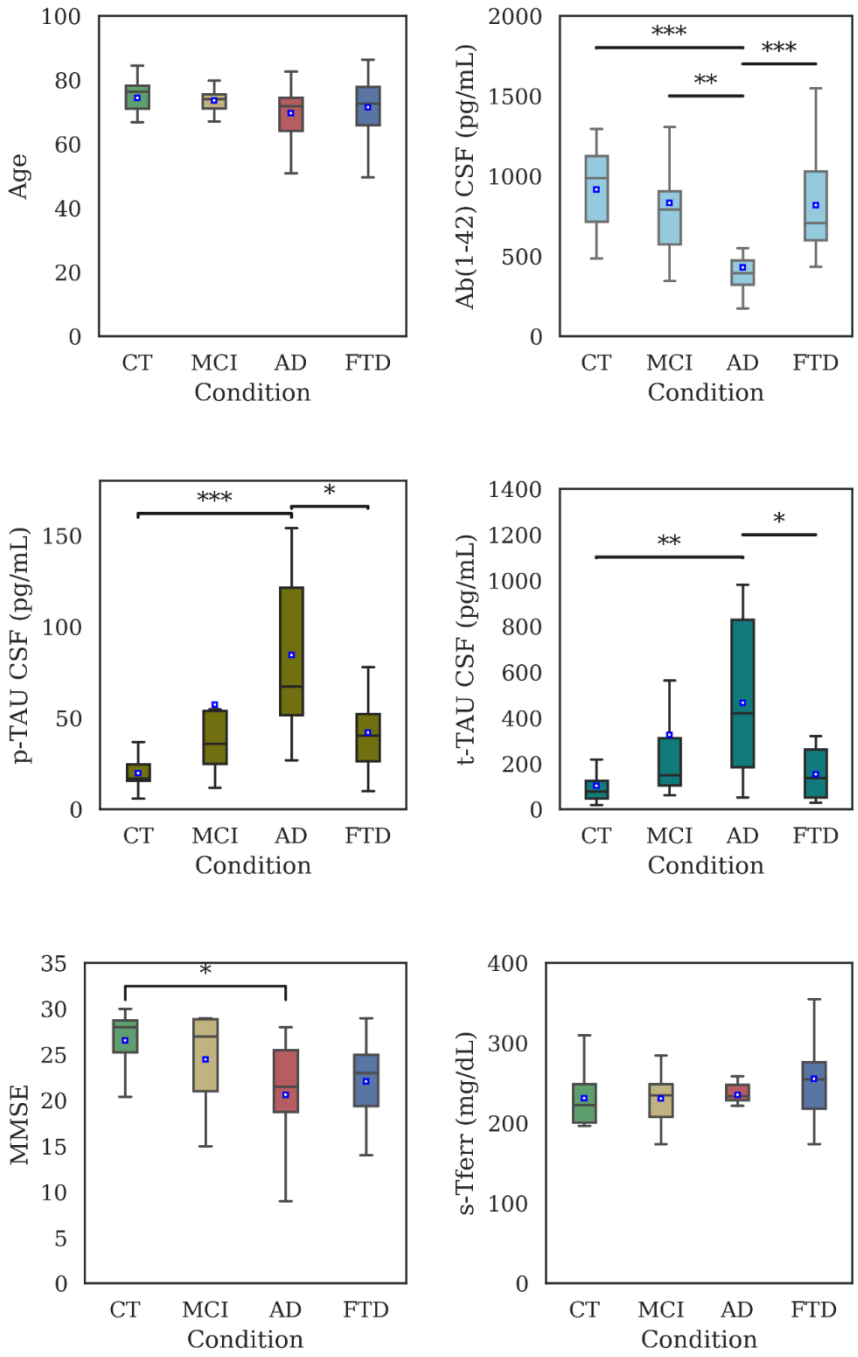

Figure 3.1. Boxplot for variables whose value is reported in Table 1. Significant differences have been indicated (* $p<0.05$; ** $p<0.01$; *** $p< 0.001$). Adapted from (Ficiarà et al., 2021a).

3.2.2 Iron concentration in CSF

Total iron concentration in CSF samples of patients is shown in Figure 1. Significant differences have been reported between AD and all the other groups, but not between CT and MCI. No difference was found between FTD and CT groups.

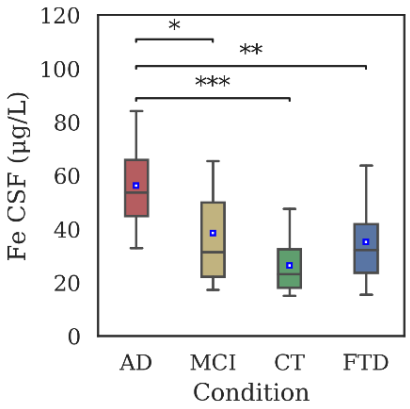

Figure 3.2. Distribution of iron concentration in CSF samples of AD (56.3 ± 15.6 µg/L), MCI (38.6 ± 21.2 µg/L), CT (26.5 ± 9.9 µg/L) and FTD (35.2 ± 16.8 µg/L) patients by means of GF-AAS. Iron levels were significantly different between AD and CT ($p < 0.001$), AD and FTD ($p = 0.003$), and AD and MCI ($p = 0.02$). Statistical differences have been evaluated by means of Kruskall-Wallis test and Dunn's post-hoc test using Bonferroni correction for p-value (* $p<0.05$; ** $p<0.01$; *** $p< 0.001$). Adapted from (Ficiarà et al., 2021a).

3.2.3 Clustering Analysis

Clustering analysis was performed including CT, MCI and AD groups on two different populations: total dataset comprising 47 patients, and the subset composed of 29 patients for which the measurement of s-Tf is available. The sets of features used to compare the results are the following:

a) Standard Biomarkers dosed in CSF (SBs) (p-Tau, Aβ42); b) SBs + Iron in CSF; c) SBs + s-Tf; d) SBs + s-Tf + Iron in CSF.

For the application of hierarchical clustering, we dropped t-Tau, due to its high correlation with p-Tau.

SBs

HAC based on standard biomarkers (p-Tau, Aβ42) (Figure 3.3) showed the emergence of three clusters (sizes: N=10, N=12, N=25). Differences in Aβ42 was very significant ($p<0.001$) between clusters 1 and 2 and cluster 2 and 3, while differences in p-Tau concentration ($p<0.001$) between clusters 1 and 2 and clusters 1 and 3. Values of MMSE have been calculated for each cluster (cluster 1=(20.9 ± 6.3); cluster 2=(25.1 ± 4.9); cluster 3= (24.1 ± 5.4)). External scores have been evaluated for the clustering: V-measure (0.22), ARI (0.09), AMI (0.18).

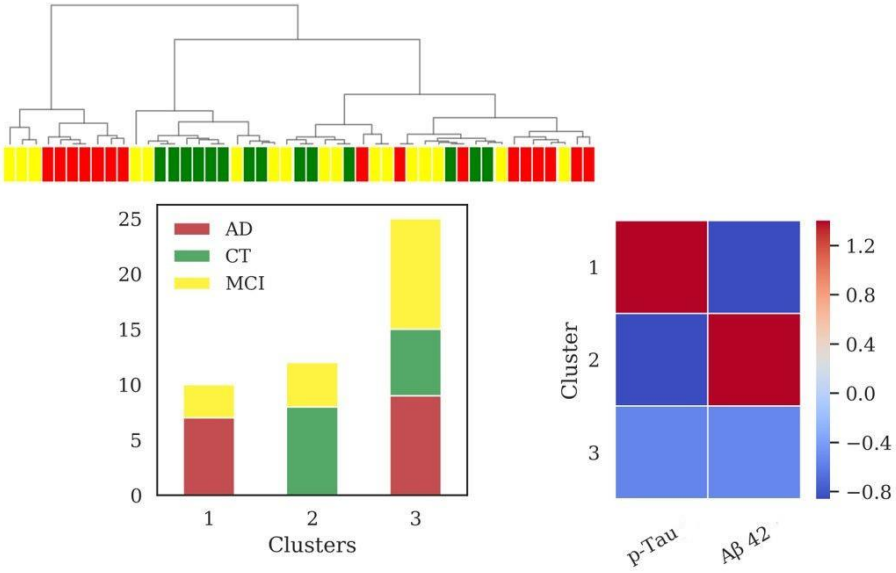

Figure 3.3. Results of hierarchical clustering using standard biomarkers Aβ42 and p-Tau, dosed in CSF. Left: Dendrogram (yellow =MCI; red =AD; green=CT) and distribution of patients within the three clusters. Right: Heatmap using the median value of the features (Z-score unit) in each cluster. Abbreviations: AD= Alzheimer's Disease; CT = neurological control; MCI = Mild Cognitive Impairment. Adapted from (Ficiarà et al., 2021a).

SBs + Iron in CSF

The addition of iron dosage in CSF unraveled four clusters (sizes: N=9, N=19, N=7, N=12) after the application of HAC, reported in Figure 3.4. The clusters composed of AD and MCI patients (cluster 3 and cluster 4) significantly differed among them for iron ($p=0.038$) and p-Tau ($p<0.001$) profiles and from cluster 2 (mainly composed of CT patients) for all variables with high significance ($p<0.001$), except for p-Tau between cluster 2 and 4 ($p=0.018$). Cluster 3 differed from cluster 1 for CSF iron content ($p=0.006$).

Values of MMSE have been calculated for each cluster (cluster 1= (24.7 ± 4.8); cluster 2= (25.2 ± 4.5); cluster 3= (22.1 ± 4.7); cluster 4= (21.6 ± 7.3)).

The addition of CSF iron improved V-measure (0.25), ARI (0.16) and AMI (0.20) with respect to the same scores obtained with the biomarkers set, described in the previous section.

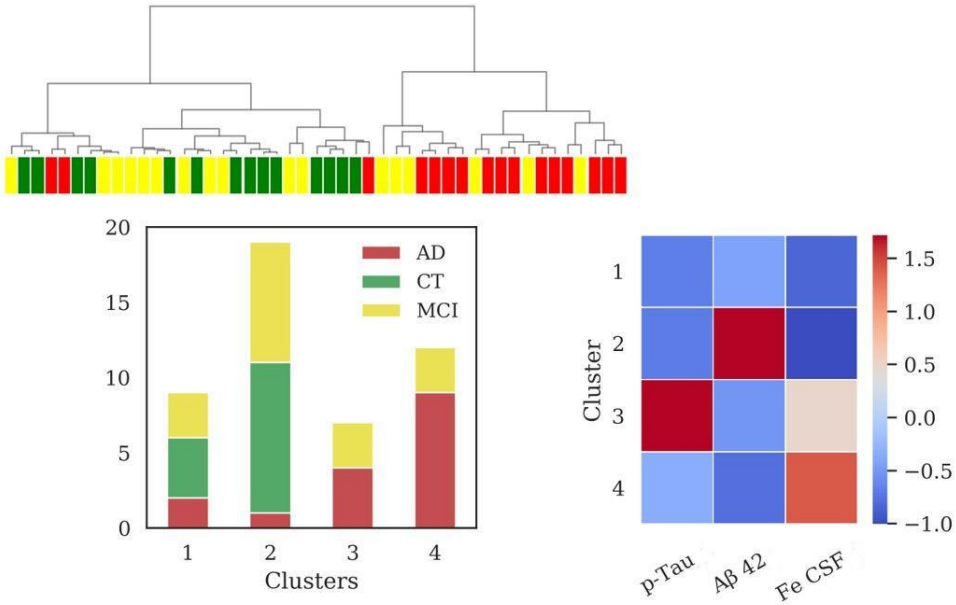

Figure 3.4. Results of hierarchical clustering using biomarkers and iron concentration in CSF. Left: Dendrogram (yellow =MCI; red =AD; green=CT) and distribution of patients within the four clusters. Right: Heatmap using the median value of the features (Z-score unit) in each cluster. Abbreviations: AD= Alzheimer's Disease; CT = neurological control; MCI = Mild Cognitive Impairment. Adapted from (Ficiarà et al., 2021a).

SBs + s-Tf

Considering the subpopulation including data of s-Tf (N=29 patients), the results for HAC using same feature sets as in previous sections are reported in Supplementary Material (S3). In this subpopulation, the application of HAC using the feature set comprising biomarkers and s-Tf revealed four clusters (sizes: N=7, N=6, N=9, N=7), reported in Figure 3.5. Significant differences among clusters were found for all the features values between cluster 1 and 2 (for Aβ42, p-Tau $p<0.001$; for s-Tf $p=0.02$), for the p-Tau values ($p<0.001$) when comparing clusters 1 and 3 and 1 and 4; s-Tf differed between clusters 2 and 4 ($p=0.001$) and 3 and 4 ($p<0.001$); Aβ42 was significantly different when comparing clusters 2 and 3 ($p<0.001$) while the difference in Aβ42 between clusters 3 and 4 is borderline ($p=0.05$).

Values of MMSE have been calculated for each cluster (cluster 1= (22.6 ± 4.8); cluster 2= (21.1 ± 3.6); cluster 3= (21.5 ± 6.9); cluster 4= (27.5 ± 2.8)).

In this case, clustering scores showed the following values: V-measure (0.32), ARI (0.18), AMI (0.25).

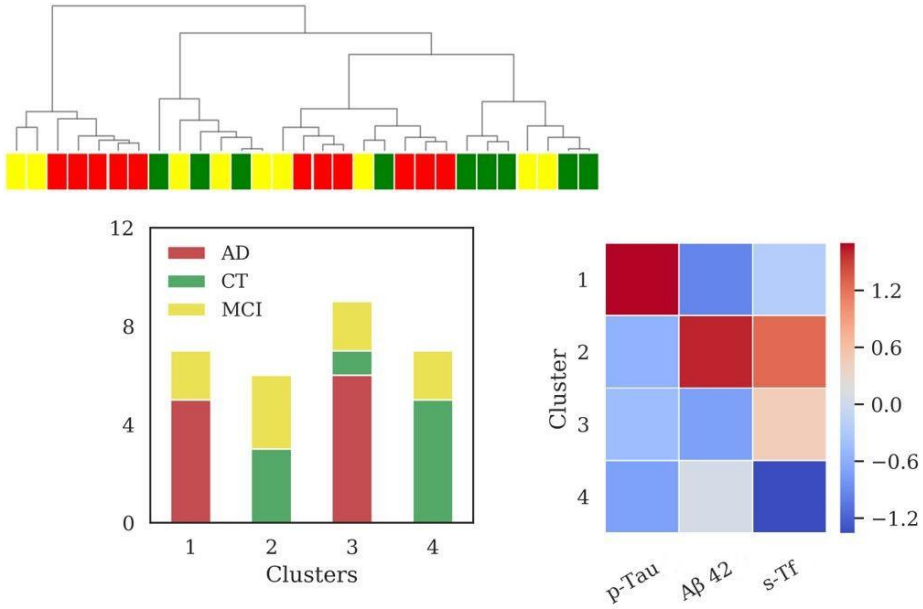

Figure 3.5. Results of hierarchical clustering using biomarkers and s-Tf. Left: Dendrogram (yellow =MCI; red =AD; green=CT) and distribution of patients within the four clusters. Right: Heatmap using the median value of the features (Z-score unit) in each cluster. Abbreviations: AD= Alzheimer's Disease; CT = neurological control; MCI = Mild Cognitive Impairment. Adapted from (Ficiarà et al., 2021a).

SBs + s-Tf + iron in CSF

Considering all the above features four clusters emerged (sizes: N=7, N=7, N=8, N=7). The application of HAC in the subpopulation for which s-Tf is available (Figure 3.6) reported an increase of clustering scores (V-measure =0.43; ARI = 0.28; AMI = 0.37). Cluster 1 and cluster 2 are composed only by AD and MCI patients. One of these clusters (cluster 1) presented significant difference in the levels of s-Tf (p=0.002), Iron CSF (p=0.004) and p-Tau (p=0.007) with respect to cluster 3 (mainly CT patients). Cluster 2 differed from cluster 4 (composed only by MCI and CT patients) in the biomarkers (for Aβ42 p=0.004; for p-Tau p<0.001) and s-Tf (p=0.008) profiles. Clusters 1 and 2, as well as clusters 2 and 3, significantly differed only for p-Tau (p<0.001). Finally, cluster 4 differed from cluster 3 only for the s-Tf values (p <0.001).

Values of MMSE for each cluster were: (cluster 1= (20.6 ± 6.9); cluster 2= (22.6 ± 4.8); cluster 3= (27.6 ± 2.5); cluster 4= (21.1 ± 3.6)).

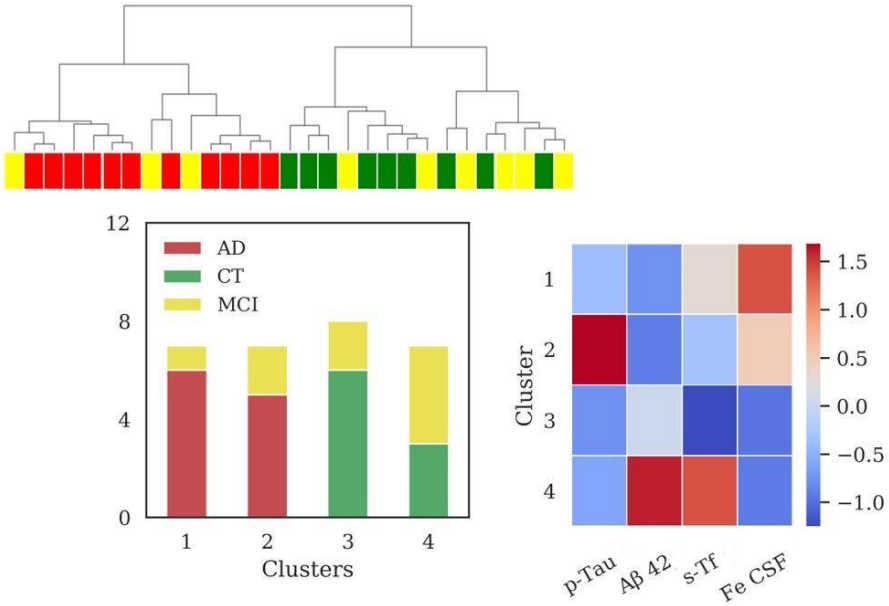

Figure 3.6. Results of hierarchical clustering using biomarkers, s-Tf and CSF iron. Left: Dendrogram (yellow =MCI; red =AD; green=CT) and distribution of patients within the four clusters. Right: Heatmap using the median value of the features (Z-score unit) in each cluster. Abbreviations: AD= Alzheimer's Disease; CT = neurological control; MCI= Mild Cognitive Impairment. Adapted from (Ficiarà et al., 2021a).

Cluster	Abeta	p-tau	Fe CSF	s-Tf
1	↓	↑	↑↑	↑
2	↓↓	↑↑	↑	↓
3	↑	↓↓	↓↓	↓↓
4	↑↑	↓	↓	↑↑

Table 3.3. Cluster profiles for the full set features (biomarkers, Fe CSF, s-Tf) according to the quartile (computed on the subpopulation) in which the median value of the variable of each cluster falls. ↓↓: under lower quartile; ↓: under median; ↑: up median; ↑↑: up upper quartile. Adapted from (Ficiarà et al., 2021a).

The (Fe CSF/ s-Tf) ratio in cluster 3 (0.15) and cluster 4 (0.11) is lower with respect to cluster 1 (0.23) and cluster 2 (0.24), in which the ratio is increased. Considering the relevant subpopulation, the (Fe CSF/ s-Tf) ratio showed highest values for AD (0.24 ± 0.07), followed by MCI (0.18 ± 0.09) and finally CT group (0.13± 0.06), reporting a significant difference between AD and CT ($p<0.01$).
We performed additional HAC analysis considering age correction for the variable s-Tf, showing a sharper separation on s-Tf profiles albeit without substantial differences in the cluster composition (Supplementary Figure 4,5 and 6).

3.2.4 Classification Models

We finally used a Linear SVM and LR model to evaluate the classification performance based on the same feature sets used for the clustering analysis in the population (N=47). For SVM, the classification performance (AUROC) using SBs (Aβ42, p-Tau) and SBs + Iron in CSF was (0.74 ± 0.14) and (0.73 ± 0.12) respectively. In the first case, the values of feature importance for the biomarkers set showed a higher weight for Aβ42 (0.21 ± 0.18) respect to p-Tau (0.15 ± 0.11). In the second case, CSF iron reported a higher value (0.07±0.09) respect to p-Tau (0.06±0.09) and Aβ42 (0.03 ± 0.12). For LR model, AUROC using SBs and SBs + Iron in CSF was (0.77 ± 0.12) and (0.75 ± 0.12) respectively. The values of feature importance for the biomarkers set showed a higher weight for Aβ42 (0.20 ± 0.14) respect to p-Tau (0.11 ± 0.13). Even in LR model, CSF iron reported a higher value (0.10 ± 0.02) respect to p-Tau (0.06 ± 0.13) and Aβ42 (0.09 ± 0.08). In our dataset, for both models the addition of age as feature did not improve the AUROC, and the value of feature importance for age was not relevant (around zero).

3.3 Discussion

The present results support the hypothesis that iron accumulation is involved in AD neurodegeneration. In clinical practice, the pathological changes occurring in AD can be detected by the use of biomarkers in different modalities, among which the evaluation on CSF (i.e. Tau and Aβ biomarkers) is less accessible but presents lower intrinsic protease activity than blood and reflects brain changes, helping to diagnose AD pathology in both the prodromal and the dementia stages (Lashley et al., 2018).

In our study, both the 'standard' biomarkers significantly differed between AD and CT groups (only CSF Aβ42 between AD and MCI), but this result requires confirmation in a larger cohort of patients also due to the large dispersion of biomarker values in our MCI population (Table 1). In fact, core-AD hallmarks are present also in elder healthy people with good cognitive function (Driscoll and Troncoso, 2011), probably showing different patterns only with respect to the AD brain. We added the information on iron content in CSF, intending to discover shared profiles and potentially improve early diagnosis. The analytical measurements of total iron in CSF by means of GF-AAS is expected to provide an accurate quantification, reflecting the iron status in brain patients more directly than brain imaging techniques. Indeed, biochemical changes in the brain, occurring in preclinical phases produce corresponding alterations in the CSF (Jack et al., 2010). Iron concentration in CSF is minimal and therefore very difficult to measure, requiring accurate and highly sensitive techniques such as atomic absorption spectrometry, providing reproducible and reliable results, without the need for hard pre-treatment of CSF samples. Moreover, this measurement is not currently used in clinical practice, leading an added value for the standard information on iron status in the brain.

Several studies evaluated iron levels in biological fluids, and meta-analysis conducted by Tao and colleagues showed lower iron in serum and an iron overload in several specific brain regions of

AD patients, however highlighting the need for further studies to evaluate iron in CSF (Tao et al., 2014).

In the present work, CSF iron concentration in 69 patients was analyzed, finding a statistically significant increase in the total iron concentration in AD with respect to CT patients, and between AD and MCI (Figure 1), showing a potential discriminating power of our analysis. Iron dysregulation could generate a progressively toxic environment during the different stages of dementia. In fact, a well-known consequence of increased iron concentration is the production of ROS, leading to DNA damage and cell death (Zecca et al., 2004b), that feature AD.

The concentration of iron in CSF is very low, and it has been suggested that Tf saturation in the CSF is much higher than in the periphery and that a larger proportion of free iron circulates the CNS (Leitner and Connor, 2012). An imbalance of free iron can be responsible for toxic damage taking part in Fenton reaction and consequently to the onset of neurodegeneration. Interestingly, it is reported that different stages of cognitive and functional impairment are associated with changes in CSF reactive iron, possibly in relation to the development of cognitive and functional decline (Lavados et al., 2008).

The importance of iron in AD and aging has been shown also from the evaluation of altered local levels of proteins regulating iron levels, such as transferrin (Loeffler et al., 1995; Lu et al., 2018). Then, it has been assessed that CSF ferritin, the iron storage protein of the body, plays a role in AD. It has been demonstrated that CSF ferritin, assumed to be an index of brain iron load, is strongly associated with CSF apolipoprotein E levels and was elevated by the Alzheimer's risk allele, APOE-ε4 (Ayton et al., 2015). Also, CSF ferritin levels have been associated with longitudinal changes in CSF Aβ and Tau, showing that iron might facilitate Aβ deposition in AD and accelerate the disease process (Ayton et al., 2018). These evidences provide proofs that a disturbance in iron metabolism can be involved in neurodegenerative processes.

To check whether our technique was accurate enough to detect small differences in the iron concentration in CSF and to evaluate the possibility to discriminate between AD and other dementias, in the first part of our study we compared AD and FTD patients. The results (Figure 1) showed a marked difference in iron concentrations in FTD patients with respect to AD, suggesting a possible different role for this metal in these two types of dementia. This result should be confirmed in larger cohorts, however, different levels of biological metals in CSF have been showed in different neurodegenerative diseases (Hozumi et al., 2011), in particular AD, Amyotrophic Lateral Sclerosis, and Parkinson disease, so it is plausible that a difference exists also in FTD (Ashraf and So, 2020).

AD is a complex disease (Devi and Scheltens, 2018), requiring advanced computational algorithms to discover deep relationships in the data and their relative patterns. In this work we applied clustering analysis, a powerful technique suitable to discover patterns and similar subgroups, which has been successfully applied in recent studies on AD (Racine et al., 2016; Alashwal et al., 2019; Toschi et al., 2019). We tested how considering different sets of features can better diagnose the progression of AD and point out new potential pathological mechanisms involved in neurodegeneration. Results from hierarchical clustering analysis revealed that using the standard AD biomarkers Aβ42 and p-Tau, two groups of patients presented alternative signatures (clusters 1 and

2, Fig 2). One of these (cluster 1, Fig 2) could be associated with the AD profile showing low levels of Aβ42 and high levels of p-Tau, reflecting the accumulation of amyloid plaques and neurofibrillary tangles. However, a third subgroup emerged (cluster 3, Fig 2) with a heterogeneous composition of AD, MCI, and CT, underlining that the two standard biomarkers alone are unable of a sharp discrimination of the patient status. Probably, the sparse presence of MCI patients in all the clusters is due to the wide spectrum of cognitive and functional impairment that is captured by the MCI designation, impacting the heterogeneity of outcomes (Roberts and Knopman, 2013).

Interestingly, the information on iron concentration in CSF added one more cluster, generating two separated groups composed of patients classified with diagnosis of AD and MCI (clusters 3 and 4, Fig 3), both presenting low values of MMSE. These clusters differed for p-Tau and CSF iron levels, albeit presenting similar Aβ42 profile. Cluster 3 could be considered as a typical AD profile, with low levels of Aβ42 and high values for p-Tau, and in addition higher values of iron with respect to the two clusters containing mainly CT patients (clusters 1 and 2, Fig 3). Cluster 4 presents low levels of Aβ42, lower levels of p-Tau with respect to cluster 3, and the highest levels of CSF iron. The improvement of clustering scores assessed a better discrimination of patients by adding the iron content in CSF to the standard biomarkers. One possible interpretation of these results is that cluster 4 could be associated to patients in stages of dementia in which p-Tau starts to aggregate but deposition of Aβ plaques is already present.

In fact, according to the current models describing the timing of pathophysiological brain events in relation to the clinical course, preclinical phases of AD are characterized by plaques deposition, followed by later spread of neurofibrillary tangles (Jack et al., 2010; Long and Holtzman, 2019). Furthermore, the higher iron concentration combined with lower levels of p-Tau could suggest a harmful interaction between iron and p-Tau accumulation at early stages, inducing or worsening neurodegenerative events. This hypothesis is consistent with several studies, supporting the evidence that iron can promote the aggregation and pathogenicity of Tau (Smith et al., 1997; Yamamoto et al., 2002; Lovell et al., 2004; Ahmadi et al., 2017; Spotorno et al., 2020). Tau proteins play a role in neurotransmission and iron metabolism by the trafficking of APP to the cell surface (Lei et al., 2012). Tau accumulation in tangles on the other hand leads to induction of heme-oxygenase 1, an antioxidant that promotes release of the redox-active Fe (II), which releases free radicals to generate oxidative stress (Ward et al., 2014).

Chelation therapies, based on intranasal deferoxamine treatment, may exert suppressive effects on the iron-induced tau phosphorylation, providing a valuable approach in preventing AD progression (Guo et al., 2013a). In addition, further studies on patients reported an investigation of novel treatment strategy based on a metal-protein-attenuating compound to reduce toxic properties of Aβ mediated by copper and zinc (Ritchie et al., 2003; Lannfelt et al., 2008).

According to our results, the clusters containing patients affected by AD showed an increased level of iron with low levels of Aβ42, hallmark for senile plaques deposition, which confirms the link between iron and Aβ plaques. There are evidences for a variety of interactions between iron and Aβ: iron accumulates and co-localizes with Aβ plaques (Connor et al., 1992; Meadowcroft et al., 2009; Ndayisaba et al., 2019), their binding can form redox reactive and toxic species (Nakamura et al., 2007;

Bousejra-ElGarah et al., 2011), with evidence for the formation of an iron-amyloid complex (Telling et al., 2017), and also iron levels can increase prior to plaques formation in an animal model of AD (Leskovjan et al., 2011). Increased iron levels are believed to enhance Aβ production via the downregulation of furin (Silvestri and Camaschella, 2008) and the iron regulatory pathways are also involved in proteostasis of Amyloid Precursor Protein (APP) (Rogers et al., 2008; Duce et al., 2010). It has been hypothesized that brain oxidative damage concurs to AD pathogenesis before Aβ accumulation (Praticò et al., 2001), therefore iron accumulation might precede and cause the formation of plaques. Recently it has been proposed that an increase in the intracellular labile iron levels, due to mitochondria dysfunction, enhances the rate of APP synthesis and the activity of APP cleavage by beta-secretase resulting in Aβ formation (Kozlov et al., 2017). In addition, a recent study confirmed the link between iron retention in cells and mislocalization of APP, due to alteration of ferroportin activity in the modulation of iron efflux: this effect causes a change in endocytic trafficking with consequent neuronal iron elevation and oxidative damage that feature AD pathology (Tsatsanis et al., 2020).

Induction of ROS has been shown from Aβ-iron complex via Fenton chemistry and the genetic manipulation of iron metabolism substantially influences Aβ toxicity in model organisms (Rival et al., 2009).Chelation of iron can prevent Aβ aggregation, and restore memory loss in animal models of AD (Huang et al., 2004; Guo et al., 2013b).

Further connections between iron and lipoprotein metabolism have been detected, highlighting causative interaction and synergies between genes of iron homeostasis and established genetic risk factors of AD, such as APOE4, suggesting the iron metabolism as a possible therapeutic target (Tisato et al., 2018).

Emerging evidence suggested that blood iron homeostasis is altered in AD and already in MCI (Faux et al., 2014; Ashraf et al., 2020b; Guan et al., 2020), including systemic variation of markers of iron metabolism, such as transferrin saturation and ceruloplasmin/transferrin ratio in serum (Squitti et al., 2010). Interestingly, in our case, we found a negative correlation between t-Tau and Tf in serum in AD that can support a role of Tf in neurodegeneration. Despite our observations require further confirmation in a larger cohort of patients, cluster analysis also found different concentrations of Tf in serum and iron levels in CSF for patients with MCI and dementia.

Using features set including standard biomarkers and s-Tf, four clusters emerged, with different profiles of s-Tf. Cluster 1 (Fig 4) containing mainly AD patients, associated typical AD profile with a lower level of s-Tf compared to two of three remaining clusters. This result might support that serum iron is lower in AD than in healthy controls (Tao et al., 2014), and that decreased plasmatic iron in AD could be due to transferrin desaturation (Hare et al., 2015), pointing out a role for systemic variations of iron metabolism in neurodegeneration. However, the other cluster comprising AD and MCI patients (cluster 3, Fig 4) reported a higher level of s-Tf with respect to the cluster 4 (Fig.4) composed of MCI and CT patients, requiring a further investigation on the s-Tf profiles in a larger population. Using a step-by-step approach, we finally used the full set of features, including also information on iron concentration in CSF, which largely improved the discrimination of patients according to their clinical diagnosis. Clustering analysis unraveled four clusters,

visualized in the dendrogram (Figure 5), in which AD and CT patients are well separated, supported by a good improvement of clustering scores. As previously discussed, the presence of MCI patients in all clusters reflected their wide spectrum in the current MCI diagnosis. Interestingly, a recent study reported that postmortem MRI and histology demonstrated differential iron accumulation in early- and late-onset AD (Bulk et al., 2018), showing the presence of various distribution patterns for iron accumulation in subtypes of AD patients.

Two subgroups containing AD and MCI patients (clusters 1 and 2, Figure 5) differed in p-Tau levels and showed CSF iron levels higher with respect to the clusters composed of CT and MCI (clusters 3 and 4, Fig 5). This result sustains our previous hypothesis that iron concentration and p-Tau levels in CSF could play a crucial role in differentiating the actual stage of dementia.

The overaccumulation of iron is not considered the root cause of AD but a factor that amplifies the diseases. A variety of reasons have been proposed such as a leaky BBB or the presence of excess hemoglobin from microbleeding (Peters et al., 2015) or finally it is a response to chronic stress similarly with aging, where ROS and iron accumulation are very well documented (Zecca et al., 2004b).

Elevated iron is also a feature of AD-effected post-mortem brains, in particular iron accumulation occurs in AD cortex and hippocampus but not cerebellum, reflecting the pathological scheme of neurodegeneration in AD (Zhu et al., 2009; Duce et al., 2010; Smith et al., 2010) .The importance of iron for the disease progression has been suggested, i.e. correlating the iron quantity In hippocampus of patients with AD with the mini-mental state examination(MMSE) and the disease duration (Ding et al., 2009; Zhu et al., 2009).

Finally, several genes of iron regulatory proteins are risk factors for sporadic AD, including Tf and human hemochromatosis protein (HFE) (Hare et al., 2013a).

In the review of Kozlov and colleagues a very innovative model has been proposed to explain the connections between all the symptoms of AD, with particular attention to metal metabolism disorders and aberrant cell cycle re-entry in neurons. Interestingly, the evaluated the age-related disruptions in mechanisms regulating the level of iron inside and outside neurons. An increase in iron concentration within the cells can lead to an amplification of ferritin and APP mRNA translation levels, and APP is cleaved with a formation of Abeta. The Abeta molecules tend to aggregate with a formation of soluble oligomers and then of insoluble plaques, leading to the local inflammatory response (Kozlov et al., 2017).

Firstly, mutations in mitochondrial DNA (accumulating with age) lead to structural damage of mitochondria and the consequent presence of oxidative stress and reduced production of ATP. Damaged mitochondria undergo to autophagy and lipofuscin globules are produced, containing a large amounts of iron ions (required in mitochondria for biosynthetic processes) and accumulating within autolysosomes. This environment increased ROS and reactively available ferrous irons in cytoplasm, stimulating the translation of ferritin, APP and ferroportin, responsible for the exit of iron from cell. Excessive iron ions accumulate outside the neurons enhancing oxidative stress and damage to other cells. Also the role of hepcidin is crucial to modulate ferroportin activity, and its modulation depends on extracellular iron, oxidative stress, hypoxic conditions and cytokines (Kozlov et al., 2017).

In fact, in physiological state, when too much iron is released, hepcidin binds to ferroportin and their complex is internalized and finally degraded in the cells (Myhre et al., 2013). When mitochondria are seriously damaged also this mechanism deteriorates.

The interpretation of clusters 3 and 4 (Figure 5) is less simple. The different profiles of s-Tf for these clusters, containing CT and MCI patients, could be due both to the small size of samples requiring further investigation in a larger cohort.

Significant differences in s-Tf profiles have been detected in the clusters containing mainly AD and CT respectively, showing also an increased ratio between the iron content in CSF and s-Tf in clusters only formed by patients affected by dementia and for the AD with respect to CT group. It is increasingly recognized that AD is a clinically heterogeneous disease with multiple causes, with an important role for brain vasculature (Montagne et al., 2017; Sweeney et al., 2018a). Our approach could be considered an indirect evaluation of the potential connection between iron homeostasis and blood-brain barrier (BBB) dysfunction. BBB dysfunction is a mechanism involved in the neurodegeneration and subsequently in cognitive impairment (Nation et al., 2019), and recently included in a hypothetical model of AD biomarkers (Sweeney et al., 2018b). Interestingly, the export mechanisms at the BBB level are altered in dementia, leading to potential targets for treatment (Pahnke et al., 2014). AD is characterized by altered BBB permeability and a link between iron-overload and BBB breakdown and brain mitochondrial dysfunction has been demonstrated (Sripetchwandee et al., 2016).

In fact, BBB prevents the diffusion of Tf from blood into CNS, as well as the migration of non-transferrin bound iron (NTBI), potentially toxic from the brain. Tf is transported across brain capillary endothelial cells following an endocytic mechanism mediated by Tf-receptors (Moos et al., 2007). The breakdown or alteration of this system could be part of the cause for pathological accumulation of iron into the brain and consequently in the CSF. In fact, CSF can be produced both via the choroid plexus or by the interstitial fluid of the brain (Nakada and Kwee, 2019).

Moreover, various studies proposed that iron trafficking across the blood-brain capillaries is involved in the aggregation of Aβ peptides leading to the potential onset of AD (McCarthy and Kosman, 2015), and also that iron accumulation may be associated with the age-induced changes in the expression of iron metabolism proteins in the brain (Lu et al., 2017).

To extract further information on the data, useful for future clinical studies, machine learning models have been trained to evaluate the impact of the inclusion of iron-related data in the diagnostic power of dementia. We selected LR model and linear SVM, one of the most used techniques for AD classification problem (Tanveer et al., 2020), giving good generalization performances also for small samples. In particular, the present results for both models were comparable, underlining a potential relevance of the iron-related feature (CSF iron) for the classification of AD, CT, MCI patients. Although AUROC did not detect a significant increase, in ranking the relevance of features the addition of CSF iron could suggest a potential role in the improvement of the diagnostic power of AD, MCI, and CT patients, provided further investigation on larger samples are performed. Moreover, the cross-sectional nature of our study is a limitation of the present investigation and longitudinal studies will be necessary to clarify the involvement of abnormal iron homeostasis in

different stages of the disease process, i.e., including iron-related data from blood or MRI. Additionally, further studies with larger samples will be useful to quantitatively parse out our results and to confirm the stratification of patients turned out in the cluster analysis.

3.4 Conclusion

Finally, the use of cluster analysis proved its potential utility for identifying patterns of variables that might characterize disease progression. The addition of iron-related data to the core-biomarkers can help to capture the multifaceted nature of AD, co-characterized by Aβ plaques deposition and neurofibrillary tangles aggregation as well as other related processes. Future works should focus on the evaluation of abnormal iron concentrations in different stages of dementia, which can generate deposition in CSF or changes in circulating iron (protein-bound or free) arising from possible imbalances of the blood-brain exchange of iron. The evaluation of iron in the CSF can improve the tuning of personalized therapeutic strategies based on systemic or intrathecal administration of chelating agents acting directly into the brain.

In conclusion, our results support the evidence of iron overload in AD, and consequently the hypothesis that different clinical conditions with specific backgrounds involve the actual iron brain levels. Cluster analysis revealed a new potential stratification of patients when new parameters, related to the iron concentration in serum and CSF, are accounted for, advancing our understanding of the role of iron dysregulation in AD pathophysiology. Tight regulation of iron metabolism is pivotal to warrant neuronal homeostasis and its investigation can prompt avenues for both research on new pathological mechanisms involved in neurodegeneration and development of new treatments. The potential addition of iron-related data in clinical evaluation of dementia could improve the early diagnostic power and support new personalized disease-modifying therapies based on iron chelation able to slow the progression and worsening of the neurodegenerative processes.

Chapter 4: Mathematical Models of Iron Trafficking across Brain Barriers System in Neurodegenerative Diseases

Under the hypothesis that disturbance in iron transport mechanisms at the BCSFB and/or BBB can be the underlying cause of the elevated CSF and brain tissue iron levels during the progression of dementia, two mathematical models of brain barriers system were proposed to evaluate the significance of the BCSFB and the BBB in controlling CSF and brain tissue iron levels and the potential biological implications of their functions/dysfunctions.

A special emphasis was given on the entry of iron from blood into the brain and the efflux from the brain, which are the main players for its exchange modulation within the different compartments of the brain.

Mathematical models are useful tools to simulate the biological dynamic of a system and the complex networks of their components. Results from mathematical models applied to biological systems are often perturbed by the presence of uncertainties in experimental data. Sensitivity analysis quantifies uncertainty, assessing how variations in model outputs can be apportioned, qualitatively or quantitatively, to different input sources.

4.1 Two-compartmental model for the evaluation of iron transport across the blood-cerebrospinal fluid barrier in neurodegenerative diseases

This section is partly based on: Ficiarà E., D'Agata F., Ansari S., Boschi S., Rainero I., Priano L., Cattaldo S., Abollino O., Cavalli R., Guiot C. 2020 *42nd Ann. Int. Conf. IEEE Eng. Med. Biol.* doi:10.1109/EMBC44109.2020.9175988

The work started with a first preliminary model to describe on a macroscopic scale the iron exchange at the BCSFB interface formed by the CP. Numerical simulations and global sensitivity analysis are performed to investigate the stability of the system. We provided a first estimation of the most relevant parameters for the asymptotic state based on experimental data obtained from patients affected by different forms of dementia and neurological controls, in order to foster differences in the iron regulation between blood and CSF in physiological and pathological conditions.

4.1.1 Materials and Methods © 2020 IEEE

Patients

The experimental data (iron concentration in CSF and blood samples) have been provided from patients affected by AD, Mild Cognitive Impairments (MCI), Frontotemporal Dementia (FTD) and neurological control (CT), collected at the Molinette Hospital Neurology ward of the Department of Neuroscience, Torino. Accurate detection of total iron concentration in CSF samples has been performed using Graphite-Furnace Atomic Absorption Spectrometry. Iron circulating in blood has been estimated from the routine analysis of the patients. Both for blood and for CSF we collected data

from a total of 44 subjects: 12 CT (age 72.1 ± 7.5), 15 MCI (age 72.1 ± 4.3), 14 FTD (age 71.0 ± 8.4), 3 AD (age 73.5 ± 3.8). The values of iron measurements have been reported as (mean ± stand ard deviation). Statistical differences were evaluated using ANOVA with Tukey's post-hoc correction.

Mathematical Model

A two-compartmental model (see Figure 4.1) based on a non-homogeneous system of first-order ODEs, described by (1) and (2), is proposed to study the passage of iron from blood to CSF. The parameters and variables entering the equations are listed in Table 4.1.

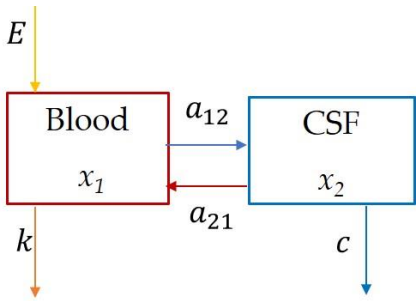

Figure 4.1. Schematic representation of BCSF barrier, considering blood and CSF as the two compartments in which the concentrations x_1 and x_2 are modulated by the constant E and the parameters k, a_{12}, a_{21}, c . From (Ficiarà et al., 2020b). © 2020 IEEE

$$\frac{dx_1}{dt} = -(\bar{a}_{12}+\bar{k})x_1+ \bar{a}_{21}\, x_2+\bar{E} \qquad (1)$$

$$\frac{dx_2}{dt} = \bar{a}_{12}\, x_1 - (\bar{a}_{21}+\bar{c})x_2 \qquad (2)$$

We defined $\tau = t/T$ (where T=1 day is the time scale for normalization) and replaced $t=T\cdot\tau$ in (1) and (2) in order to obtain rate constants as adimensional quantities. Equations (1) and (2) can be reduced to:

$$\frac{dx_1}{d\tau} = -(a_{12}+k)x_1+ a_{21}\, x_2+E \qquad (3)$$

$$\frac{dx_2}{d\tau} = a_{12}\, x_1-(a_{21}+c)x_2 \qquad (4)$$

The values of the parameters k, a_{12} , a_{21} , c and the constant E have been estimated based on reference values (see Appendix, section S4) and partly on our experimental data.

We modulated the values of parameters a_{12} and a_{21} , assuming they are the main regulators of the iron exchange, maintaining the different amount of iron in the two compartments and reflecting possible altered states. We supposed parameters k and c to have the same order of magnitude for each different condition (Table 4.3).

Table 4.1. Terms of equations

x_1	Iron concentration in blood (mg/L)
x_2	Iron concentration in CSF (mg/L)
E	Iron intake into the blood from food (mg/L); fixed quantity.
k	Iron consumption from blood and excretion mechanisms (tipically from metabolism and bleeding)
a_{12}	Kinetic constant rate for iron entering from blood to CSF
a_{21}	Kinetic constant rate for iron returning from CSF to blood
c	Consumption of iron in the CSF (fraction consumed into the brain)

Simulations and Sensitivity Analysis

Numerical simulations of the ODEs system are implemented by using Python codes, considering x_{10} and x_{20} as initial conditions and setting the value of parameters k, a_{12} , a_{21} , c and a constant intake of iron E according to Table 4.3 (see Results).

We used global sensitivity analysis to evaluate the overall effects of the perturbations of the model input, and thus to rank these parameters by influence on the model output. In particular, we applied the variance-based Sobol method exploiting SALib library of Python (Herman and Usher, 2017). The Sobol method returns the first- and second-order sensitivity indices and total effect sensitivity index, quantifying respectively the contribution of each parameter, the fractional contribution of parameter interactions and its overall effects on the output variance (Sobol', 2001; Saltelli et al., 2010).

We evaluated the Sobol indices for the concentration of iron in blood x_1 and in the CSF x_2 generating 5000 samples by means of Saltelli's sampling scheme to run in our model. We set the bounds of input parameters range accordingly to cover the different orders of magnitude of the values of a_{12} and a_{21} chosen for the simulations and allowing a 20% variation for the parameters k and c. The Sobol index threshold to consider an input parameter as sensitive was 0.01.

Parameter Estimation

The asymptotic condition of analytical solutions (eqs. (5) and (6)) was selected.

The analytical solutions for x_1 and x_2 of the system (3) and (4) were found analytically using fundamental matrix calculus.

$$x_1(\tau)=\frac{a_{12}}{(\lambda_1-\lambda_2)}\left[A\cdot\frac{a_{21}}{(\lambda_1+a_{12}+k)}\cdot e^{\lambda_1\tau}+B\cdot\frac{a_{21}}{(\lambda_2+a_{12}+k)}\cdot e^{\lambda_2\tau}\right]+$$
$$+\,D\cdot E\left[\left(e^{\lambda_1\tau}-1\right)\frac{a_{21}}{\lambda_1(\lambda_1+a_{12}+k)}+\left(1-e^{\lambda_2\tau}\right)\frac{a_{21}}{\lambda_2(\lambda_2+a_{12}+k)}\right] \qquad (5)$$

$$x_2(\tau)=\frac{a_{12}}{(\lambda_1-\lambda_2)}\left[A\cdot e^{\lambda_1\tau}+B\cdot e^{\lambda_2\tau}\right]+D\cdot E\left[\frac{(e^{\lambda_1\tau}-1)}{\lambda_1}+\frac{(1-e^{\lambda_2\tau})}{\lambda_2}\right] \qquad (6)$$

Where λ_1, λ_2 are the eigenvalues of coefficient matrix associated to the corresponding homogeneous system and A, B and D defined as below.

$$\lambda_{1,2}=\frac{-(c+a_{21}+a_{12}+k)\pm\sqrt{(c+a_{21}-a_{12}-k)^2+4a_{21}a_{12}}}{2} \quad (7)$$

$$A=X_{10}-X_{20}\frac{a_{21}}{(\lambda_2+a_{12}+K)}$$

$$B=-X_{10}+X_{20}\frac{a_{21}}{(\lambda_1+a_{12}+K)}$$

$$D=\frac{(\lambda_1+a_{12}+K)(\lambda_2+a_{12}+K)}{a_{21}(\lambda_2-\lambda_1)}$$

The iron concentrations were supposed to represent stable states of the system, after a long time from the initial condition. The asymptotic solutions are expressed by (8) and (9).

$$x_1(\tau\to\infty)=D\cdot E\left[-\frac{a_{21}}{\lambda_1(\lambda_1+a_{12}+k)}+\frac{a_{21}}{\lambda_2(\lambda_2+a_{12}+k)}\right] \quad (8)$$

$$x_2(\tau\to\infty)=D\cdot E\left[-\frac{1}{\lambda_1}+\frac{1}{\lambda_2}\right] \quad (9)$$

The non-linear system of asymptotic solutions was numerically solved for a_{12} and a_{21}, keeping fixed the parameters k and c and approaching as asymptotic values of x_1 and x_2 the experimental data of iron concentration (mean value) in blood and CSF.

4.1.2 Results © 2020 IEEE

Iron in CSF and Blood Samples

Iron concentrations measured in CSF and blood samples were reported in Table 4.2, showing a significant difference between AD and control patients in the CSF (P-value = 0.04). Furthermore, the quantity of iron circulating in blood highlighted dissimilar profiles of patients.

Table 4.2. Total iron measured in CSF and iron circulating measured in serum of CT, MCI, AD and FTD patients. *(P<0.05)

	CT	MCI	AD	FTD
Iron CSF	(26.6 ± 10.3)* μg/L	(38.8 ± 21.7) μg/L	(54.5 ± 18.9)* μg/L	(31.8 ± 11.6) μg/L
Iron Serum	(1.01 ± 0.36) mg/L	(0.89 ± 0.27) mg/L	(0.99 ± 0.33) mg/L	(0.74 ± 0.24) mg/L

Numerical Simulations

We performed numerical simulations of the two-compartmental model described by (3) and (4). By expressing the iron concentrations in blood and CSF in mg/L, we set the parameters values according to Table II and assumed as initial conditions x_{10} = 1 mg/L and x_{20} = 0.03 mg/L. The system turned out to be stable, showing different asymptotic states for different rates of exchange, adequately representing biological conditions (Figure 4.2).

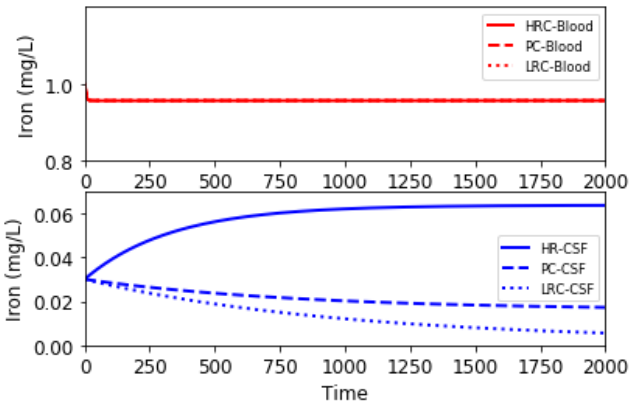

Figure 4.2. Simulations for physiological condition (PC), low-rate condition (LRC) and high-rate condition (HRC). Parameters as referred in Table 4.3. From (Ficiarà et al., 2020b). © 2020 IEEE

Table 4.3. Parameters values for the model

Parameter	Physiological Condition	Low Rate Condition	High Rate Condition
E (mg/L)	0.22	0.22	0.22
k	0.23	0.23	0.23
a_{12}	$2 \cdot 10^{-5}$	$2 \cdot 10^{-6}$	$2 \cdot 10^{-4}$
a_{21}	$2 \cdot 10^{-4}$	$2 \cdot 10^{-5}$	$2 \cdot 10^{-3}$
c	$1 \cdot 10^{-3}$	$1 \cdot 10^{-3}$	$1 \cdot 10^{-3}$

Sensitivity Analysis

We performed Sobol sensitivity analysis to determine how much of the variability in model output (x_1, x_2) is dependent upon each of the input parameters (k, a_{12} , a_{21}, c), either considering a single parameter or their interaction. The ranges of variations for a_{12} and a_{21} were assumed to be $[2{\cdot}10^{-6} : 2{\cdot}10^{-3}]$ and $[2{\cdot}10^{-5} : 2{\cdot}10^{-2}]$ respectively.

For the output x_1 we found that only a change of the parameter k strongly influences the iron concentration in blood, showing a first-order index $S_1 = 1.00 \pm 0.03$ and total order index $S_t = 1.00 \pm 0.03$. On the other hand, for the output x_2, i.e., the CSF iron concentration, the parameters related to the iron exchange, especially a_{21} , unraveled their crucial relevance. In the range of variations set for k and c, these parameters showed a slight influence on the variation of CSF iron concentration. We reported the values obtained for the first-order and total order Sobol index for x_2 (Figure 4.3).

Furthermore, the interactions of the two parameters regulating the barrier exchange, i.e. a_{12} and a_{21} , showed the strongest impact on the variability of iron concentration in CSF, reporting a significant value of the second-order index ($S_2 = 0.20 \pm 0.08$).

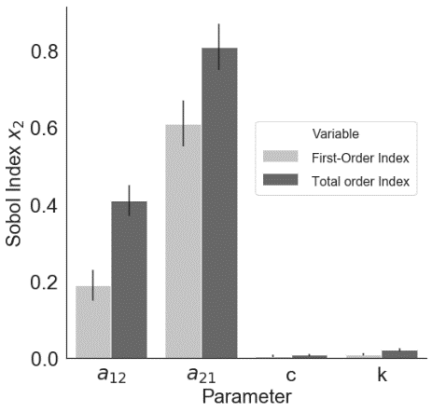

Figure 4.3. Bar plot shows the Sobol indices for the output x_2, highlighting a strong contribution of the parameter a_{21} and a minor one from the parameter a_{12}. From (Ficiarà et al., 2020b). © 2020 IEEE

Parameter Estimation

The values of parameters a_{12} and a_{21} have been estimated in the asymptotic state of the system, for different conditions. We found different rates for iron exchange in the various forms of dementia (AD, MCI and FTD) with respect to the control patients (Table 4.4). In particular, AD patients differed of one order of magnitude with respect to controls, suggesting the possibility of a severe alteration of the biological condition for the iron transport in the CSF.

Table 4.4. Model estimated parameter values (mean values) for condition of dementia and neurological control. The values obtained considering the minimum and maximum values of iron CSF and iron serum for each group were reported in brackets (min : max values).

Parameter	CT	AD	MCI	FTD
a_{12}	$5 \cdot 10^{-5}$ ($4 \cdot 10^{-5} : 1 \cdot 10^{-4}$)	$5 \cdot 10^{-4}$ ($2 \cdot 10^{-4} : 4 \cdot 10^{-4}$)	$2 \cdot 10^{-4}$ ($4 \cdot 10^{-5} : 4 \cdot 10^{-4}$)	$1 \cdot 10^{-4}$ ($7 \cdot 10^{-5} : 5 \cdot 10^{-4}$)
a_{21}	$1 \cdot 10^{-3}$ ($1 \cdot 10^{-4} : 3 \cdot 10^{-3}$)	$7 \cdot 10^{-3}$ ($3 \cdot 10^{-3} : 1 \cdot 10^{-2}$)	$4 \cdot 10^{-3}$ ($5 \cdot 10^{-4} : 1 \cdot 10^{-2}$)	$2 \cdot 10^{-3}$ ($7 \cdot 10^{-4} : 1 \cdot 10^{-2}$)

4.1.3 Additional Analysis

Starting from different initial condition for iron concentration in CSF (initial condition of patients and random distribution in the range [0:100 ppb], the following simulation were performed. It is worth to note the difference in the ratio a_{12}/a_{21} : for CT, MCI and FTD patients the value is 0.05, for AD patients is 0.07. Furthermore, the ratio a_{21}/a_{12} is reduced in AD (14.3) with respect to CT, MCI and FTD patients (20).

For completeness, in Figure 8 simulations were performed considering in the model the value of parameters numerically estimated from the asymptotic solution (Table 4.4).

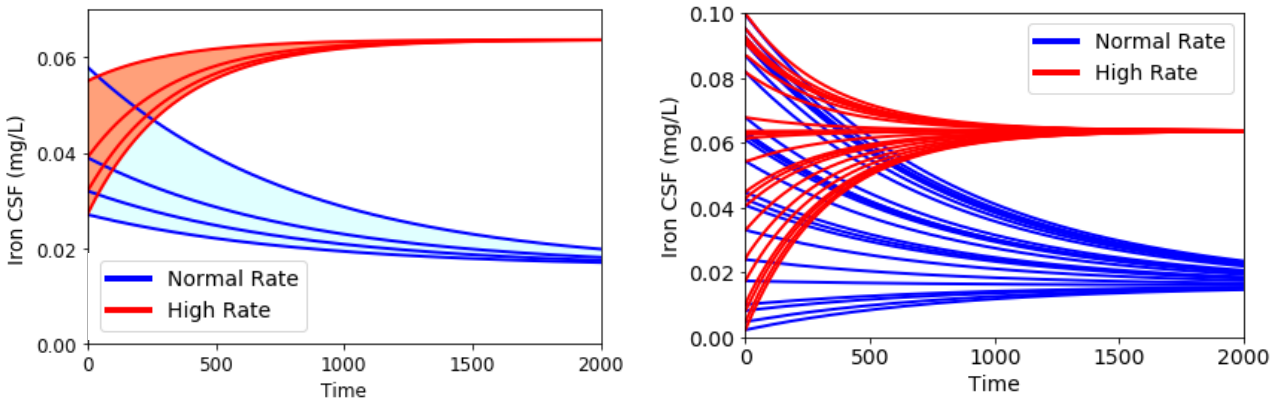

Figure 4.4. Simulations for iron concentration in CSF for normal rate and high-rate condition, starting from different initial conditions: initial conditions set based on mean values of iron concentrations of patients in the left; random distribution in the range [0:100 ppb] in the right. Parameters as referred in Table 4.3.

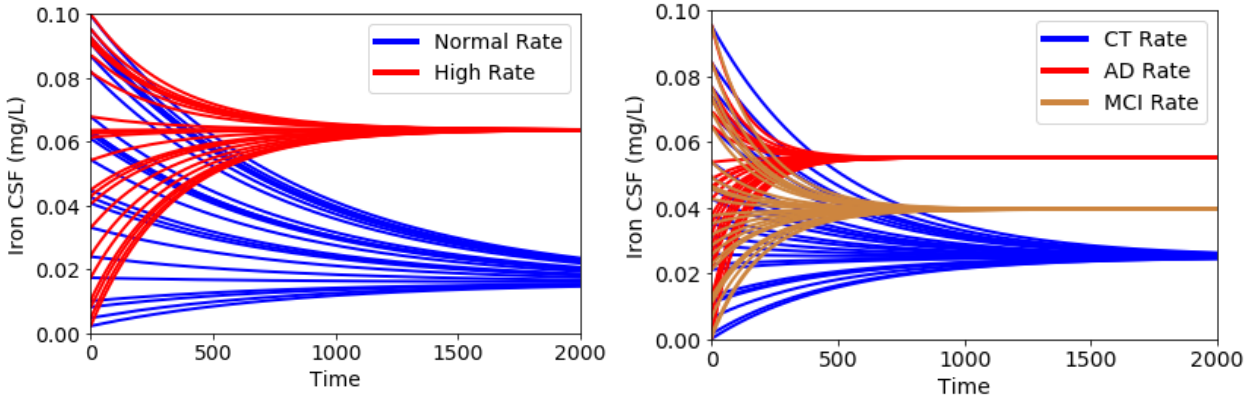

Figure 4.5. Simulations of the model considering values of parameters reported in Table III, starting from different initial conditions: initial conditions set based on mean values of iron concentrations of patients in the left; random distribution in the range [0:100 ppb] in the right.

Sensitivity Analysis Dependent on Time

Finally, in order to investigate the impact of total experiment time on our results, we repeated our numerical experiments using different simulation times (t=100, t=1000, t=2000, t=5000) for sensitivity analysis, considering physiological and pathological conditions, with related parameters estimated from the order of magnitude of the values found in Table 4.4 and reported in Table 4.5. The initial conditions for iron in blood and CSF were set to vary in the range [0.5 : 1.5] and [0.015 : 0.09] respectively.

Table 4.5. Range of variability of parameters chosen for physiological and pathological conditions.

	Physiological Condition	Pathological Condition
a_{12}	$[10^{-5}:10^{-4}]$	$[10^{-5}:10^{-3}]$
a_{21}	$[10^{-4}:10^{-3}]$	$[10^{-4}:10^{-2}]$

The significance of pathophysiological changes of the parameters in influencing the CSF iron concentration at different simulation times is shown in Figure 4.6.

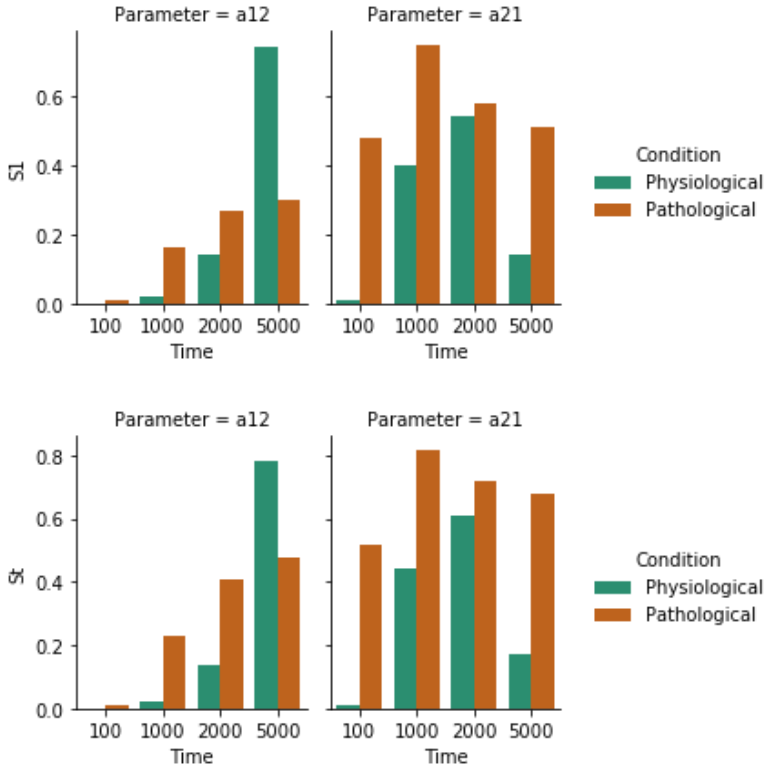

Figure 4.6. First-order (S1) and total-order Sobol index (St) evaluated for different times of simulations with range of parameters set based on supposed physiological and pathological conditions.

These results can be interpretated as CSF iron levels are highly sensitive to pathophysiological variations of a_{21} and these variations showed a decreasing course as simulation times increase, suggesting a potential impacting role of an alteration of efflux mechanism during the early stage of the disease progression. On the contrary, variations of a_{12} impact the CSF iron concentration at longer simulation times both in physiological and pathological condition, implying that the influx across BCSFB could become more relevant in controlling iron homeostasis as time passes.

4.1.3 Discussion

In this work we proposed a two-compartmental model based on ODEs to macroscopically describe the iron exchange across the BCSFB, providing a real data-based choice of the parameters sets for the numerical simulations and a global sensitivity analysis. The fine tuning of the parameters values was necessary to obtain stable system solutions, able to simulate the biological environment. Sobol analysis revealed that knowing the parameter values related to the exchange at the barrier level is crucial, especially for the iron concentration in the CSF, where its modulation is critical for the onset of neurodegeneration. In fact, they could reflect the permeability of cell barriers regulated by tight junctions, as well as the receptors-mediated activity (e.g., clearance of toxic substances from CSF) (Ficiarà et al., 2020b).

At this regard, the BBB has been extensively studied in AD (Sweeney et al., 2018b). On the other hand, the BCSFB and the relative dysfunctions in neurodegenerative disorders have been addressed but are largely understudied and not yet established. The dysfunctions of the CP and of CSF flow could precede the neurological symptoms in neurodegenerative diseases (The Choroid Plexus and Cerebrospinal Fluid System: Roles in Neurodegenerative Diseases, 2016) and recent studies suggested that BCSFB exhibited morphological changes and a functional decline with aging and in AD, accompanied to striking changes in CSF composition related to impaired CP functions (Spector and Johanson, 2013; Choroid plexus, aging of the brain, and Alzheimer's disease. - PubMed - NCBI).

Many evidences showed the impact of age-dependent alterations at the level of the BCSFB on the pathological events that take place in the AD brain, well described in recent review works (Mesquita et al., 2012; Marques et al., 2017). The senescence of CPE cells induces morphological changes, such as decrease in height and volume (Serot et al., 2000) or striking deterioration (Johanson et al., 2004), loss of barrier leakage (Chalbot et al., 2011), and extracellular deposition of Aβ near tight junctions enhancing the disruption of the BCSFB (Vargas et al., 2010). Furthermore, in aging and AD a decline of the CP capacity to promote the flow and the renewal of CSF has been observed (Preston, 2001). Interestingly, further findings highlighted an increased mitochondrial stress and apoptosis of CPE cells in AD (Vargas et al., 2010) as well as upregulation of oxidative stress markers (Anthony et al., 2003).

Notably, Aβ accumulation (hallmark of AD) may result from a decreased clearance of the Aβ peptides through the barriers of the brain. CP has a role in the clearance of toxic Aβ species via specific transporters (e.g. lipoprotein receptor-related protein 2, LRP-2) and secretion of Transthyretin (TTR), both preventing Aβ plaque formation (Mesquita et al., 2012). The ability of CP to secrete Aβ-carrier proteins and to express important receptors that scavenge amyloidogenic peptides was shown to decrease with age and to be compromised in AD, i.e. the decrease of CSF TTR in severe dementia and AD (Serot et al., 1997). Epithelial cells morphology and architecture of CP present a progressive decline during the aging process and these features worsen in AD, relating with increased oxidative stress and inflammation, and decreasing nutrient transport and secretion into the CSF (Mesquita et al., 2012).

Although very few studies have actually tested the value of biomarkers base on CP imaging (i.e., CP size, perfusion/permeability, glucose metabolism, inflammation) in patients with brain disorders, the study of Hubert and colleagues indicated CP changes as promising data for a better understanding of diseases such as schizophrenia, epilepsy and AD (Hubert et al., 2019).
All these factors strengthen the hypothesis that BCSFB undergoes harmful, but also functional and adaptive, changes in the pathophysiology related to aging, AD and dementia.
In addition to the endothelial cells, CP cells could play a crucial role in the modulation of iron exchange between the blood and the CSF, and consequently with the brain. Recently, the finding that the CPE cells display all the machinery to locally control iron delivery into the CSF, may suggest that the general and progressive senescence of the CP is correlated with the impairment of regional iron metabolism, iron-mediated toxicity, and the increase in inflammation and oxidative stress that occurs with aging and, particularly, in AD.
In fact, CPE cells express all the genes known to participate in the modulation of iron homeostasis (Marques et al., 2009) and important iron-related proteins such as HJV, HFE, TFR2, FTH, FTL, hephaestin, and ceruloplasmin (Rouault et al., 2009). It has been showed the ability of CPE cells to up-regulate genes that encode for iron-related proteins and transcription factors, in condition of peripheral inflammation (Marques et al., 2009). Similar to endothelial cells, CPE cells express TFR1 in the basolateral membrane, which binds to TF-bound iron arriving from the blood stream, inducing its internalization. Iron will then reach the cytosol of the epithelial cells following the TFR1 mechanism and involving the endosomal proteins DMT1 and DCYTB (Rouault and Cooperman, 2006; Rouault et al., 2009). Moreover, the presence of ferroportin FPN in the apical membrane of CP epithelial cells (Wu et al., 2004) leads to the release of iron into the CSF, where it circulates bound to TF.

Therefore, CP may participate in the regional regulation of brain iron metabolism, showing the presence of specific membrane and secreted proteins. The increasing levels of inflammation and oxidative stress, both in the periphery and in the brain, present in AD and aging process could elicit changes in the CPE functions and a dysregulation of BCSBF, contributing to iron levels impairments within the brain and taking part to the pathophysiology of AD (Mesquita et al., 2012).
Furthermore, it can be supposed that alteration of BCSFB can involve transporters for transport/clearance/modulation of iron (i.e., DMT1, FPN, TfR, HEPH), suggesting the need of experimental investigation at this level.
During the recent years it has been shown that insufficient Aβ export, physiologically facilitated by the ATP Binding Cassette (ABC) transporters at the brain's barriers, plays a crucial role in disease initiation and progression (Pahnke et al., 2014).
Cargo molecules of ABC are extremely different, involving also ions and ionic metals (Lewinson and Livnat-Levanon, 2017). Interestingly, ABC transporters have been shown to be related to iron uptake: components of three distinct families mediate the translocation of iron, siderophores, heme and vitamin B12 in bacteria (Köster, 2001).

In conclusion, although model validation requires a larger sample of data from patients for a more accurate estimation of the parameters, we showed a remarkable difference in the regulation of

iron exchange between blood and brain (via CSF) in the patients affected by different forms of dementia and neurological control, suggesting a possible increase of permeability to iron of the BCSFB, particularly in AD condition (Ficiarà et al., 2020b). These results support the biological hypothesis of iron dysregulation at BCSFB level previously described (Mesquita et al., 2012), also proposing the use of a mathematical approach to elucidate the altered mechanisms in neurodegenerative disorders, in addition to more detailed and conclusive biological investigation on possible impairments at transporters level or barrier leakage (Ficiarà et al., 2020b).

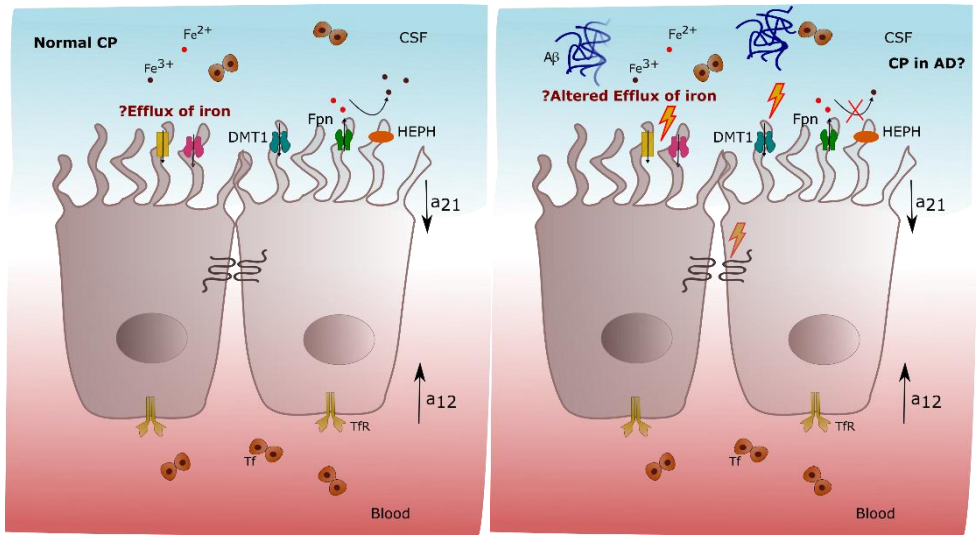

Figure 4.7. Hypothesis of iron dysregulation at BCSFB level in AD. Permeability of barrier may be altered by tight junctions' disruption as well as iron efflux from CSF to blood impaired, suggesting a reduced clearance of iron by means of specific iron transporters or alternative mechanisms involving in the removing of toxic substances from CSF.

4.2 Three-compartmental model for iron trafficking across the blood-brain barriers in neurodegenerative diseases

This section is partly based on: Ficiarà E., D'Agata F., Priano L., Cattaldo S., Mauro A., Guiot C. "A Compartmental Model for the Iron Trafficking Across the Blood- Brain Barriers in Neurodegenerative Diseases" 2021 ***IEEE Conference,*** © IEEE. Reprinted with permission.

In this part, an update and refinement of the two-compartmental model is proposed, adding a third compartment describing the iron content in the brain.

The iron balance in the brain depends on both iron influx and efflux rates, and over the course of life their changes reflect the change in the brain iron dynamics. Interestingly, the rate of iron accumulation depends on aging (Holmes-Hampton et al., 2012) and the relative imbalance of influx and efflux rate is involved in neurodegeneration. However, the understanding of the mechanisms of brain iron import/export is still limited, requiring further investigation.

It is reported that metals such as iron and copper may enter the interstitial fluid of the brain via the BBB, be transported back into the blood via the efflux mechanism at the BCSFB, known to remove substances from the CSF to the blood (Zheng and Monnot, 2012). Since there is no structural barrier between the CSF and interstitial fluid (ISF), materials in these two fluids compartments can freely exchange, in a bidirectional way (Matsumae et al., 2016).
Many techniques of sensitivity analysis have been developed to investigate multi-dimensional parameter spaces (Marino et al., 2008).

Based on our previous study (Ficiarà et al., 2020b), this work aims to implement a more complete mathematical model, able to describe macroscopically the iron exchange at the blood-brain interface, considering the functional role of the brain barriers. Numerical simulations and global sensitivity analysis are performed to investigate the behaviour of the system and how the most relevant parameters can affect brain iron regulation.

4.2.1 Methods © 2021 IEEE

Mathematical Model

A three-compartmental model (see Figure 4.8) based on a non-homogeneous system of first-order ordinary differential equations (ODEs), described by (10), (11) and (12), is proposed to study the passage of iron from blood to brain. The parameters and variables entering the equations are listed below.

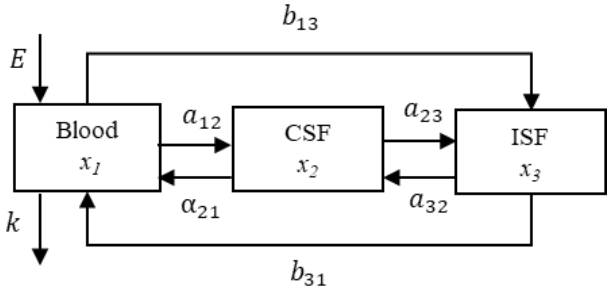

Figure 4.8. Schematic representation of the barriers forming blood-brain interface, considering blood, CSF and ISF as the three compartments in which the iron concentrations x_1, x_2, x_3 are modulated by the constant E and the parameters listed below. (Ficiarà et al., 2021b) © 2021 IEEE

$$\frac{dx_1}{d\tau} = -(a_{12} + k)x_1 + \alpha_{21}\, x_2 - b_{13}\, x_1 + b_{31}\, x_3 + E \quad (10)$$

$$\frac{dx_2}{d\tau} = a_{12}\, x_1 - (\alpha_{21} + a_{23})x_2 + a_{32}\, x_3 \quad (11)$$

$$\frac{dx_3}{d\tau} = b_{13}\, x_1 + a_{23} x_2 - (a_{32} + b_{31})x_3 \quad (12)$$

We defined $\tau = t/T$ (T=1 day, time scale for normalization) and replaced $t=T\cdot\tau$ in in order to obtain rate constants as adimensional quantities.

The values of the parameters k, a_{12} and the constant E have been estimated as described in the previous section. In this model, four parameters (a_{23}, a_{32}, b_{13}, b_{31}) were added to account for the exchange of iron to the third compartment (ISF), and one parameter was modified with respect to the two-compartmental model (α_{21} replaced to a_{21}). The proposed values for these new parameters were estimated taking into account data for iron concentrations, exchange and the description of the biological structure of brain barriers present in the literature (Bradbury, 1997; Lopes et al., 2010; Zheng and Monnot, 2012; Chen et al., 2014; Khan et al., 2018; Ficiarà et al., 2021a). The terms entering the equations (10), (11) and (12) are listed below:

- x_1 : Iron concentration in blood (mg/L);
- x_2 : Iron concentration in CSF (mg/L);
- x_3 : Iron concentration in ISF (mg/L);
- E : Iron intake into the blood from food (mg/L); fixed quantity;
- k: Iron consumption from blood and excretion mechanisms;
- a_{12} : Kinetic constant rate for iron entering from blood to CSF across BCSFB;
- α_{21} : Kinetic constant rate for iron returning from CSF and brain to blood;
- a_{23} : Kinetic constant rate for iron passing from CSF to ISF;
- a_{32} : Kinetic constant rate for iron passing from ISF to CSF;
- b_{13} : Kinetic constant rate for iron entering from blood to brain (consequently ISF), across BBB;
- b_{31} : Kinetic constant rate for iron returning from brain to blood.

Numerical Simulations and Stability Analysis

Numerical simulations of the ODEs system were performed, setting x_{10}, x_{20} and x_{30} as initial conditions and the value of parameters according to Table I (see Results).

Phase-plane analysis was pursued in order to investigate the system near an equilibrium point and how the most relevant parameters affect the dynamic of the system. The values of the steady state for each variable (x_{1s}, x_{2s}, x_{3s}) were obtained by obtained solving the system of ODEs described by (10), (11) and (12) setting the term $\frac{dx_i}{dt}$ =0 (i=1,2,3).

The expression of steady state for x_1, x_2 *and* x_3 were found as described in Methods.

$$x_{1s} = \frac{E}{k}$$

$$x_{2s} = \frac{E \cdot (a_{12} \cdot a_{32} + a_{12} \cdot b_{31} + a_{32} \cdot b_{13})}{C}$$

$$x_{3s} = \frac{E \cdot (a_{12} \cdot a_{23} + b_{13} \cdot a_{23} + \alpha_{21} \cdot b_{13})}{C}$$

Where C is defined as below.

$$C = a_{23} \cdot b_{31} \cdot k + a_{32} \cdot \alpha_{21} \cdot k + \alpha_{21} \cdot b_{31} \cdot k$$

Sensitivity Analysis

We used different methods to perform global SA to evaluate the overall effects of the perturbations of the model input, and thus to rank these parameters according to their influence on the model output. Firstly, we used the Morris method (Morris, 1991) to screen the variables and to obtain a qualitative sensitivity measure. The average of the elementary effects (μ*) quantifies the importance of the parameters for the model output, while the standard deviation of the elementary effects (σ) indicates the non-linear effect of the model parameters on the output. Then, we applied the variance-based Sobol method, returning the first- and second-order sensitivity indices and total effect sensitivity index (Sobol', 2001; Saltelli et al., 2010). We evaluated the results of Morris analysis and Sobol indices for the concentration of iron in blood x_1, in the CSF x_2 and in ISF x_3. 15000 samples of model inputs were generated based on Morris method for sampling. For the Sobol method 15000 samples were generated by means of Saltelli's sampling scheme. Bounds of input parameters range were set accordingly to cover the different values of the parameters, assuming physiological and pathophysiological conditions. The Sobol index threshold for sensitive input parameters was 0.01. SALib library of Python was used to perform SA (Herman and Usher, 2017).

4.2.2 Results © 2021 IEEE

Numerical Simulations

We performed numerical simulations of the three-compartmental model described by equations (1), (2) and (3). By expressing the iron concentrations in blood, CSF, and ISF in mg/L, we set the constant E=0.22, k=0.23 and the parameters values according to Table 4.6, assuming different set of initial conditions (i.e., reflecting possible biological state: concentration of ISF>CSF, CSF>ISF, and concentration of CFS and ISF comparable). We focused on the concentration of iron in the cerebral space, so we reported the results for iron in CSF and ISF, showing the time course of the system for different rates of exchange (Figure 4.9). As expected, the rate of iron income to brain is much lower from blood and ISF due to the presence of the BBB, while iron returns to blood mainly via CSF.

Table 4.6. Values of the parameters (a_{12}, α_{21} , a_{23}, a_{32}, b_{13}, b_{31}) of the model

Parameter	Physiological Condition	High Rate Condition
a_{12}	$2 \cdot 10^{-4}$	0.001
α_{21}	0.05	0.08
a_{23}	0.8	0.8
a_{32}	1	1
b_{13}	0.002	0.005
b_{31}	$1 \cdot 10^{-6}$	$5 \cdot 10^{-6}$

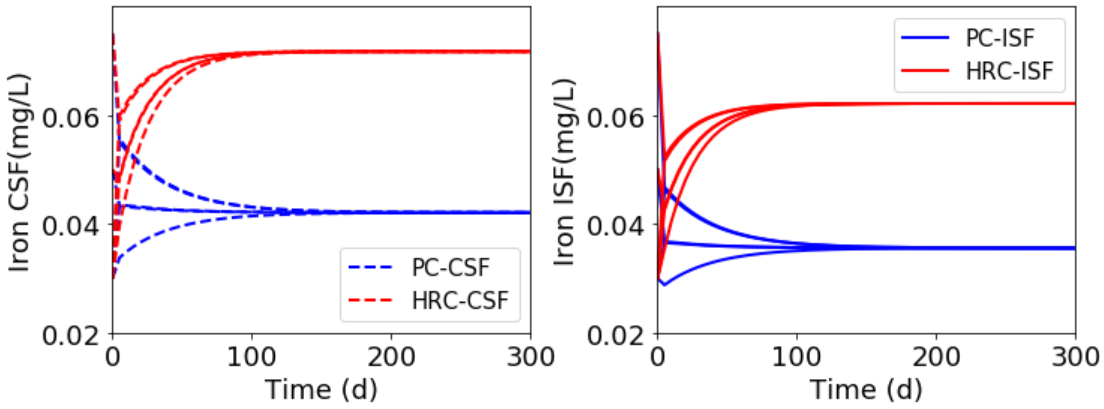

Figure 4.9. Simulations of iron concentration in CSF and ISF for physiological condition (PC), and high-rate condition (HRC). Different combinations of initial conditions: x_{10} = 1 mg/L; x_{20} = 0.03; 0.05; 0.075 mg/L; and x_{30} = 0.03; 0.05; 0.075 mg/L. Parameters as referred in Table I. d= days. (Ficiarà et al., 2021b), © 2021 IEEE

Finally, we proposed a simulation the condition of reduced clearance from CSF (α_{21}=0.05, a_{32} = 0.8) in presence of high rate, being a possible pathobiological situation in neurodegenerative diseases (Figure 4.10).

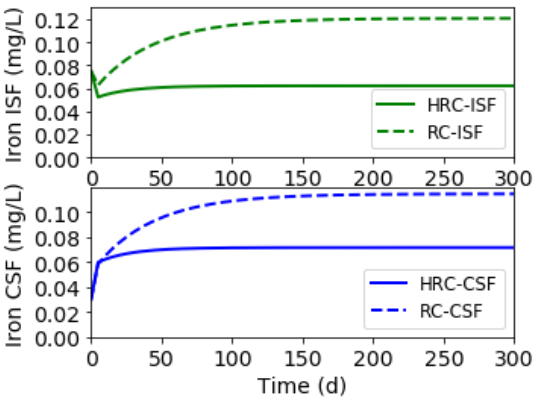

Figure 4.10. Simulations of iron concentration in CSF and ISF for high-rate condition (HR) and hypothesis of condition of reduced clearance (RC). Initial conditions: x_{10} = 1 mg/L; x_{20} = 0.03 mg/L; and x_{30} = 0.075 mg/L. Parameters as referred in Table I. d=days. (Ficiarà et al., 2021b), © 2021 IEEE

Starting from 30 random initial conditions for the blood, ISF and CSF we reported phase-plane for concentration of iron in CSF against ISF, and iron in blood against ISF (Figure 4.11).

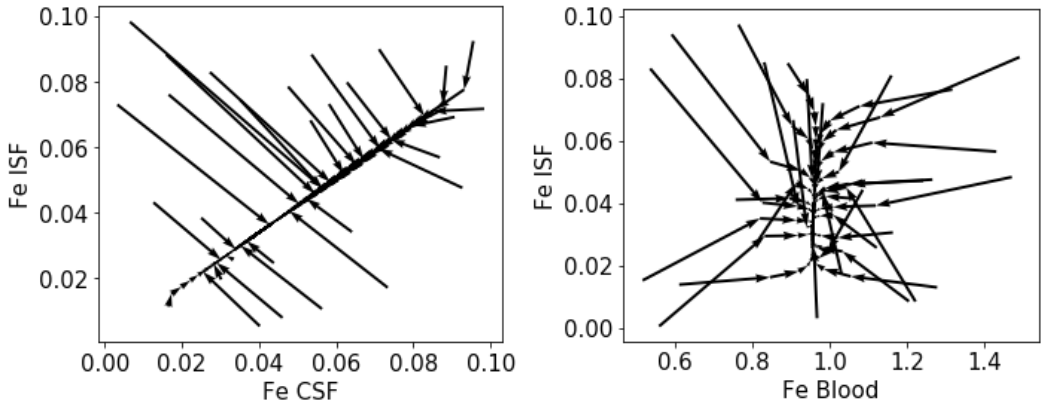

Figure 4.11. Phase-plane analysis for iron concentration in CSF against ISF in the left, and for iron in blood against ISF in the right. Iron concentration are expressed in mg/L. (Ficiarà et al., 2021b), © 2021 IEEE

Sensitivity Analysis

Sensitivity analysis determined how much of the variability in model output (x_1, x_2, x_3) is dependent upon each of the input parameters (k, E, a_{12}, α_{21}, a_{23}, a_{32}, b_{13}, b_{31}). Based on our previous results on iron concentration in CSF and blood (Ficiarà et al., 2021a), we proposed a variation from initial conditions of 30% for the physiologic condition, and of 50% for the pathological one. The ranges of variations of the parameters for pathological condition were assumed to be the following: for a_{12} [$2 \cdot 10^{-5} : 2 \cdot 10^{-3}$], for α_{21} [$0.005 : 0.4$], for b_{13} [$0.0002 : 0.01$], and for b_{31} [$8 \cdot 10^{-7} : 5 \cdot 10^{-6}$]. We considered a restriction to half of each interval for the physiological condition. In both cases the variation of the remaining parameters (k, E, a_{23}, a_{32}) is fixed to 20%.

Results from Morris analysis showed the four most relevant parameters affecting iron concentration in CSF and ISF, reported in Figure 5. Accordingly, the parameters α_{21} and b_{13} were the most important for CSF iron, especially in the pathological conditions. We found that the parameters E, a_{23}, a_{32}, b_{13} (especially b_{13}) mainly affect ISF iron, and α_{21} became relevant only in the pathological condition.

After screening the parameters by Morris method, Sobol analysis confirmed the previous results, showing that the parameters α_{21} and b_{13} were the most relevant for CSF iron (Figure 4.12).

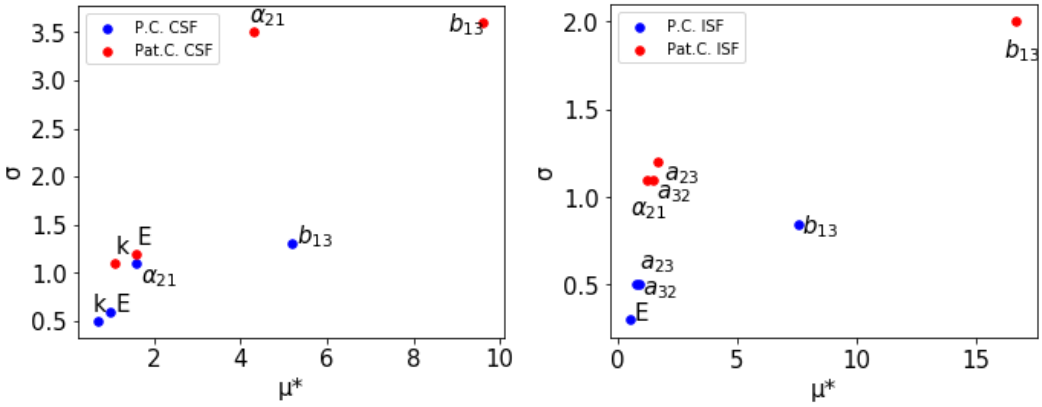

Figure 4.12. Plot of average elementary effects μ* against standard deviation σ of the most relevant parameters for iron concentration in CSF (left) and in ISF (right), considering physiological (P.C.) and pathological condition (Pat.C.). (Ficiarà et al., 2021b), © 2021 IEEE

In particular, α_{21} was more important for modulating iron in CSF in pathological with respect to physiological condition and became relevant ($S_1 > 0.01$) for ISF only in pathological condition. We reported the significant values obtained for the first-order Sobol index for CSF (x_2) and ISF iron concentration (x_3) (Figure 4.13).

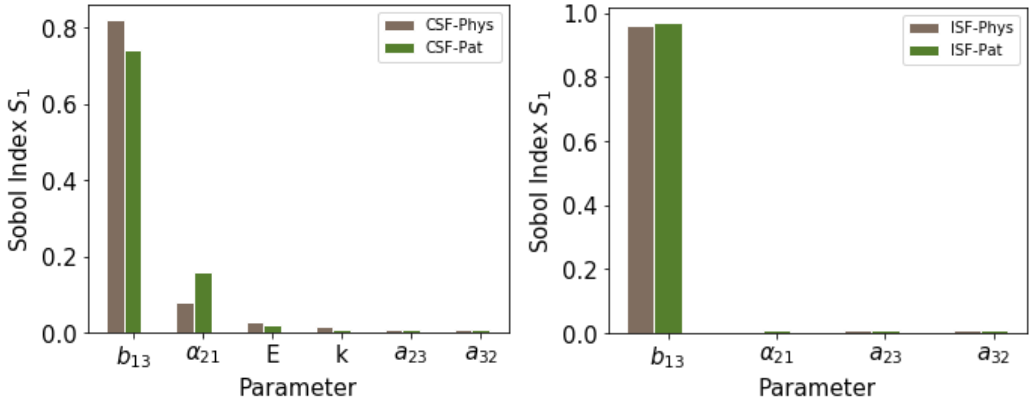

Figure 4.13. Bar plot of the first-order Sobol index S_1, for iron concentration in CSF (left) and ISF (right), showing the higher contribution of b_{13}. Both μ* and σ are adimensional. (Ficiarà et al., 2021b), © 2021 IEEE

Furthermore, the interactions of the two parameters regulating the barrier exchange, i.e., b_{13} and α_{21}, showed the strongest impact on the variability of iron concentration in CSF, reporting a significant value of the second-order index both in physiological ($S_2 = 0.02 \pm 0.01$) and pathological condition ($S_2 = 0.04 \pm 0.02$).

4.2.3 Discussion

In this work we improved our previous model, proposing a three-compartmental model based on ODEs to macroscopically describe the iron exchange across the blood-brain barriers. Numerical simulations were performed in two conditions (Table 4.6), being the high-rate condition supposed to be a consequence of the potential damage of the BBB causing higher exchange rates of iron. In both cases (Figure 4.9) the system reached a stable condition, showing that even starting from different initial conditions for ISF and CSF iron concentration, CSF stabilizes at larger concentration levels, potentially reflecting its biological function of "sink" for the removal of substances (i.e., redox-active metals) from ISF. Also, the condition of reduced clearance can reflect the pathobiological situation of altered removal mechanism from CSF (Figure 4.10) (Ficiarà et al., 2021b).

Phase-plane analysis suggested a possible correlation between the concentration of iron in CSF and ISF. Figure 4 underlines how iron content in CSF and ISF are linearly correlated (as expected in the absence of a selective barrier) while the relationship between iron in ISF and blood is highly non-linear due to the presence of the barriers. The CSF status (in which biomarkers for neurodegeneration are dosed) reflects that of the brain while iron content in blood is highly non-linearly related to that in ISF, indicating that dosing iron biomarkers in CSF is more suitable than blood ones. Also, the system converged to stable solutions starting from different initial conditions of ISF, CSF, and blood (Figure 4.11) (Ficiarà et al., 2021b).

In fact, CSF freely migrates to the brain parenchyma from the ventricular wall, then it enters the brain parenchyma, mixes with locally produced interstitial fluid, and is eliminated into reservoirs such as the subarachnoid space and ventricles from the brain parenchyma (Matsumae et al., 2016). Ependymal cells provide both an immunological barrier and a partial barrier that regulates the bidirectional transport of molecules between the ventricular CSF and interstitial fluid. Ependymal cells present gap junctions and appear to play an integral role in clearance of toxic metabolites, nutrient sensing, and metabolic regulation within the brain (Matsumae et al., 2016).

For the SA, we considered the range of parameters in the pathological condition as possibly reflecting the damage of BBB (i.e., breakdown or leakage in neurodegeneration, well reported in literature (Sweeney et al., 2019). Morris analysis revealed that parameters α_{21} and b_{13} are the most relevant for the modulation of iron in CSF, and b_{13} showed the higher contribution (highest μ^* and σ) for iron ISF in the pathological condition (Figure 4.12) (Ficiarà et al., 2021b).The high value of σ in pathological condition could reflect non-linear effects on the iron concentration due to variations of this parameter. These results were confirmed by Sobol analysis (Figure 4.13) and could be considered in agreement with the evidence that iron from blood circulation is primarily transported to the brain parenchyma by the BBB (Zheng and Monnot, 2012) (Ficiarà et al., 2021b). Also, CP express transferrin receptors (responsible for the entry of iron in brain barriers cells) at a lower density than the capillary endothelia (Moos, 1996). Furthermore, it has been demonstrated that brain iron turnover is at an extremely slow rate and dietary iron enters adult brain (in rat) at a significantly influx rate higher than efflux, leading to brain iron accumulation (Chen et al., 2014).

The parameter α_{21} became relevant to explain iron in ISF in pathological conditions (both in Morris and in Sobol method), suggesting the importance of efflux rate mechanism of iron, controlled

by bulk CSF flow and/or by the removal mechanism in the BCSFB back to the blood circulation (Bradbury, 1997; Zheng and Monnot, 2012). This interesting result (and also the parameter a_{32}) could reflect the role of the 'glymphatic' system (Ficiarà et al., 2021b).This is a network of perivascular pathways supporting exchanges between CSF and ISF and contributing to the efflux of interstitial solutes (i.e., the toxic amyloid β, hallmark of AD) (Iliff and Simon, 2019). Interestingly, the dysfunction in the CSF–ISF exchange has been hypothesized to participate in the development of AD (Iliff et al., 2012) and the hypothesis is supported with clinical observations showing that the CP–CSF system is altered in AD (Serot et al., 2012). Along the idea of the importance of the CSF–ISF flow for the clearance of Aβ, AQP4, which is present in all astrocyte end-feet in contact to all cerebral blood vessels (Badaut et al., 2014), has been proposed to have a role (Iliff et al., 2012).

Advantages and Limitations of the models

Different strengths of the models proposed in the previous sections can be considered. The initial conditions for the simulation were set taking into account our experimental data for iron concentration on patients. Then, the uncertainty of the parameters (mainly estimated based on the literature) due to the high intrinsic biological variability of iron measurements led us to the application of different techniques of SA (chosen based on the structure of our models), providing a good starting point to identify the parameters with a strong impact on the behaviour of the model output.

The models previously proposed present also some limitations. Firstly, the models need to be supported by ad-hoc experimental data (i.e., longitudinal data) for a more realistic and accurate estimation of the parameters and further implemented, i.e., taking into account additional factors, such as the time dependence of the parameters and also the quantification of iron in the brain tissues. Future experimental data necessary to validate the model can contribute to set the range of variability of the parameters more precisely, better distinguish the physiological from the pathological condition.

Furthermore, there is evidence for an accumulation of iron with aging, requiring more information about the time-dependent variations of brain barriers permeabilities and efflux mechanism to define more realistic time-dependent parameters. In fact, it was reported that a change in the brain iron accumulation rate suggests different brain iron dynamics including import/export of iron over the course of life (Chen et al., 2014).

Our macroscopic model does not distinguish between CSF in ventricular and subarachnoid space, including them in the same compartment. Thus, the current model can be improved to include the ventricular system and the subarachnoid space as separate compartments.

Finally, this macroscopical model can be improved considering the two different solute movements occurring in tissue: diffusion, thermally driven movement of solutes along their concentration gradients; and bulk flow (or convection), solute motion resulting from the pressure-driven movement of its solvent. Brain efflux is likely driven by both bulk flow and diffusion, although their relative contributions remain undefined (Iliff and Simon, 2019). The model could be expanded

to consider the convective CSF flow once information regarding the contribution of the glymphatic flow to the regulation of brain iron homeostasis becomes available.

4.2.4 Conclusions

In conclusion, simulating the regulation of iron homeostasis in the CNS and imbalance of influx/efflux rates in pathophysiological condition by means of computational models can support both diagnostic and therapeutic innovations. The influx and efflux across the BCSFB and the BBB of iron depend both on the permeability of the barriers and on the net effect of all transporters, channels and enzymes which contribute to its movement. Thus, variations of the exchange rates can be caused by damaged brain barriers and/or altered homeostasis of some iron transport mechanisms at the interfaces (Figure 4.14). Understanding iron pathophysiology is difficult, also because of the variability and complexity of iron metabolism among people and diseases. At this purpose, global sensitivity analysis helps to explore the entire parameters space taking into account this variability. We speculate that, provided the excess of iron transport to CNS through the BCSFB is experimentally confirmed, chelating therapies should target iron in the CSF, reducing the toxic side effects related to systemic delivery. Finally, in the last years, new treatments targeting the mechanisms at the brain barriers were of great interest driving to novel therapeutic strategies, and could be useful to counteract metal imbalance (i.e., chelation therapy) in neurological diseases. (Ficiarà et al., 2020b)

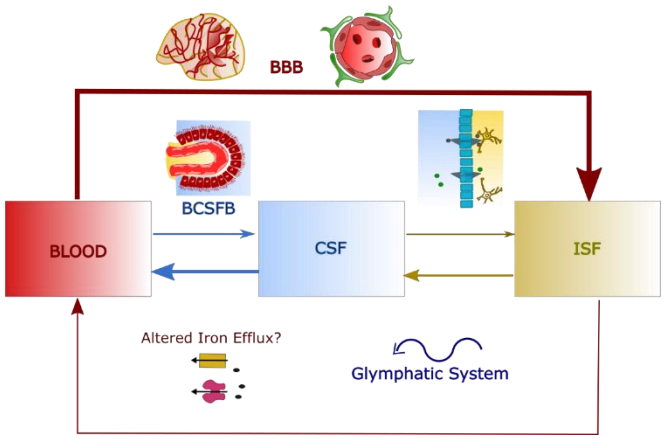

Figure 4.14. Summary of biological hypothesis for three-compartmental model. Iron may enter the brain mainly by BBB and secondly by BCSFB. Both barriers can be potentially damaged in AD with consequent major influx of iron in brain environment. Then iron can be removed from CSF and brain from efflux mechanisms (potentially altered in neurodegeneration) in BCSFB and glymphatic system.

Chapter 5: Beyond Oncological Hyperthermia: Physically Drivable Magnetic Nanobubbles as Novel Multipurpose Theranostic Carriers in the Central Nervous System

This chapter is based on: Ficiarà E., Ansari S. A., Argenziano M., Cangemi L., Monge, C. Cavalli, R., D'Agata F., *Molecules* 2020, 25(9), 2104

Magnetic Oxygen-Loaded Nanobubbles, manufactured by adding Superparamagnetic Iron Oxide Nanoparticles on the surface of polymeric nanobubbles are investigated as theranostic carriers useful for delivering oxygen and chemotherapy to brain tumors, especially focusing on their toxicity and interaction with the specific cells composing blood-brain barriers as well as their motion in a static magnetic field. The results showed the potentiality of these multipurpose nanocarriers to cross the brain barriers and to be magnetically drivable for a precise targeting of brain tumors.

In the present study we further investigated MOLNBs looking at possible applications besides hyperthermia, i.e., magnetic driving and delivery systems.
We propose MOLNBs as a new theranostic application for the treatment of cerebral tumors, based on their ability to carry oxygen (a well-known radiotherapy enhancer) and a proper load of chemotherapy drugs (doxorubicin and possibly temozolomide) (Khadjavi et al., 2018). Indeed, we speculate that they can be locally delivered to the Cerebro-spinal Fluid (CSF) by spinal injection, magnetically driven towards the part of the choroid plexus anatomically most proximal to the tumor mass where the drug and oxygen cargoes are delivered after crossing the barrier from the CSF to the brain interstitial fluids (Ficiarà et al., 2020a).

Previous imaging by Computed Tomography (CT) and/or MRI can guide the tailoring of the magnetic field required for optimal driving to the tumor, whereas post-treatment imaging by MRI and US (when the skull does not shield the target) allows the monitoring of the MOLNBs final concentration.

To assess the feasibility of this innovative delivery approach we investigated whether such nanocarriers are safe, biocompatible, not cytotoxic, and not hemolytic (in case of systemic administration or possible interactions with blood). In addition, we evaluated their internalization capability by human brain microvascular endothelial cells (hBMECs) and, finally, if we can drive the MOLNBs using proper magnetic fields, which is known to be a weakness of all the similar procedure (Ansari et al., 2019).

Accordingly, together with a specific assessment of the physicochemical and biocompatibility properties of the MOLNBs, their response to the external magnetic field produced by a permanent magnet has been investigated via ultrasonic imaging (Ficiarà et al., 2020a).

5.1 Materials and Methods (Ficiarà et al., 2020a)

Evaluation of MOLNBs Internalization by Human Brain Microvascular Endothelial Cells

Human brain microvascular endothelial cells (hBMECs), provided from Cell Systems (Kirkland, WA, USA), were cultured in EndoGRO Complete Medium (Merck Millipore), plated in 24-well plates on glass coverslip (5×10^4 cells per well) and incubated for 4h in a 500µL of medium with/without MOLNBs and OLNBs (dilution 1:100 and 1:200) internalized with 6-Coumarine (Sigma-Aldrich) in a humidified CO_2/air-incubator at 37 °C. Fixing was carried out by adding 500 µL of cold paraformaldehyde (PFA, 4%) and by incubating for 15 min at room temperature and rinsing the excess PFA with sterile PBS. After fixing, 4′,6-diamidino-2-phenylindole (DAPI) and Rhodamine-Phalloidin (R415, Invitrogen™, Thermo Fisher Scientific, MA, USA) staining reactions were performed to label cells nuclei and the actin filaments. Fixed cells were kept at 4 °C for 24 h and fluorescence images were acquired by a confocal laser scanning microscope (LSM 900, Carl Zeiss, Oberkochen, Germany) equipped with a 40X oil immersion objective, obtaining a field view of at least 5 cells. A wavelength of 505 nm was used to detect MOLNBs and OLNBs, of 565 nm and 460 nm to detect respectively the actin filaments and the nuclei. Images were processed using the software ImageJ (https://imagej.nih.gov/ij/).

In Vitro Cytotoxicity Study

The hBMECs cells were used to perform in vitro cytotoxicity test. Cells (800/well) were seeded in 96-well plates and incubated at 37 °C, 5% CO_2 for 24 h in EndoGRO Complete Medium. Then, the cells were treated with OLNBs, SPIONs, MOLNBs, in two different dilutions with medium (1:100 and 1:200). After 72 h incubation, viable cells were evaluated by 2,3-bis [2-methoxy-4-nitro-5sulphophenyl]-2Htetrazolium-5carboxanilide (MTT) inner salt reagent at 570 nm, as described by the manufacturer's protocol. The control cells were normalized to 100%, and the readings from treated cells were expressed as percent of cell viability. Eight replicates were used to determine each data point and four different experiments were performed.

Magnetic Field

The small tank (see Figure 2), where the MOLNBs were sonicated, was positioned with its horizontal axis aligned with the axial field along z-direction generated by a permanent cuboid magnet of neodymium covered with Ni-Cu-Ni with dimensions $50 \times 50 \times 20$ mm^3 (https://calamite.org) (Br= 1.26−1.29 T). The value of residual magnetization of the permanent magnet is in the range of $1.00-1.03 \times 10^6$ A/m. The field lines were investigated using iron filings showing an intense magnetic induction almost parallel to the axial direction. Simulations of magnetic field lines were obtained using the analytical expression of the three-dimensional flux density distribution (Permanent Magnet and Electromechanical Devices, 2001; Huang et al., 2017).

$$B_{ax} = \frac{M_r}{4\pi}\mu_0 \sum_{i=1}^{2}\sum_{j=1}^{2}(-1)^{i+j}\, ln\left\{\frac{(y-y_1)+\left[(x-x_i)^2+(y-y_1)^2+(z-z_j)^2\right]^{1/2}}{(y-y_2)+\left[(x-x_i)^2+(y-y_2)^2+(z-z_j)^2\right]^{1/2}}\right\} \qquad (16)$$

$$B_{ay} = \frac{M_r}{4\pi}\mu_0 \sum_{i=1}^{2}\sum_{j=1}^{2}(-1)^{i+j}\, ln\left\{\frac{(x-x_1)+\left[(x-x_1)^2+(y-y_i)^2+(z-z_j)^2\right]^{1/2}}{(x-x_2)+\left[(x-x_2)^2+(y-y_i)^2+(z-z_j)^2\right]^{1/2}}\right\} \quad (17)$$

$$B_{az} = \frac{M_r}{4\pi}\mu_0 \sum_{i=1}^{2}\sum_{j=1}^{2}\sum_{k=1}^{2}(-1)^{i+j+k}\, tan^{-1}\left\{\frac{(x-x_i)(y-y_j)}{(z-z_k)\left[(x-x_i)^2+(y-y_j)^2+(z-z_k)^2\right]^{1/2}}\right\} \quad (18)$$

$X_l = Y_l = 50\,mm$

$Z_l = 20\,mm$

$M_r = B_r/\mu_0 \qquad B_r = 1.27\,Tesla \qquad \mu_0 = 4\pi \times 10^{-7} H/m$

US Imaging Monitoring

B-mode US imaging was carried out to investigate the response of MOLNBs to the external magnetic field due to their excellent echogenicity (Zullino et al., 2019). MOLNBs at concentration 1×10^{10} NB/mL were injected in a plastic tank containing demineralized water by means of syringe positioned as indicated in Figure 5.1. The plastic tank was made by 3D printer to obtain the dimensions $7.5 \times 2 \times 3$ cm^3 to well fit with the probe dimension. A sketch of the setup is shown in Figure 5.1a. The experiment was performed at a temperature of 20 °C. MOLNBs were sonicated by an US clinical equipment (MyLab™25Gold Esaote, Genova, Italy), connected to a linear array transducer (LA523, 7.5 MHz central frequency, Esaote, Genova, Italy) operating in B-mode using the small parts imaging preset. B-mode cineloops (60 sec) were acquired and recorded for postproduction both in the absence and in the presence of the permanent magnet exerting a magnetic force in the direction of injection (see Figure 5.1b). Snapshots from cineloops were extracted at different time frames (5, 15, 25, 55 sec) after the initial injection and compared in the different conditions.

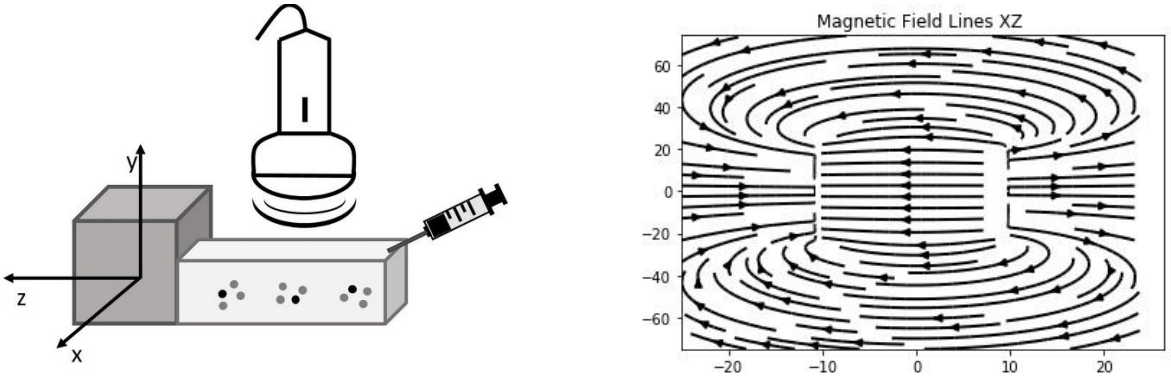

(**a**) (**b**)

Figure 5.1. (**a**) A sketch of the setup used for the imaging of MOLNBs in absence and presence of the magnetic field produced by the cuboid magnet. (**b**) Projection of magnetic field lines in the XZ plane assessed by the z-direction of the magnetic field. Adapted from (Ficiarà et al., 2020a).

5.2 Results *(Ficiarà et al., 2020a)*

Confocal microscopy was used to verify whether MOLNBs were internalized by hBMECs. Images showed that MOLNBs, as well as OLNBs, were significantly internalized by hBMECs (Figure 5.2). Cytotoxicity studies underlined very good viability of hBMECs after the treatment with SPIONs, MOLNBs and OLNBs (Figure 5.3).

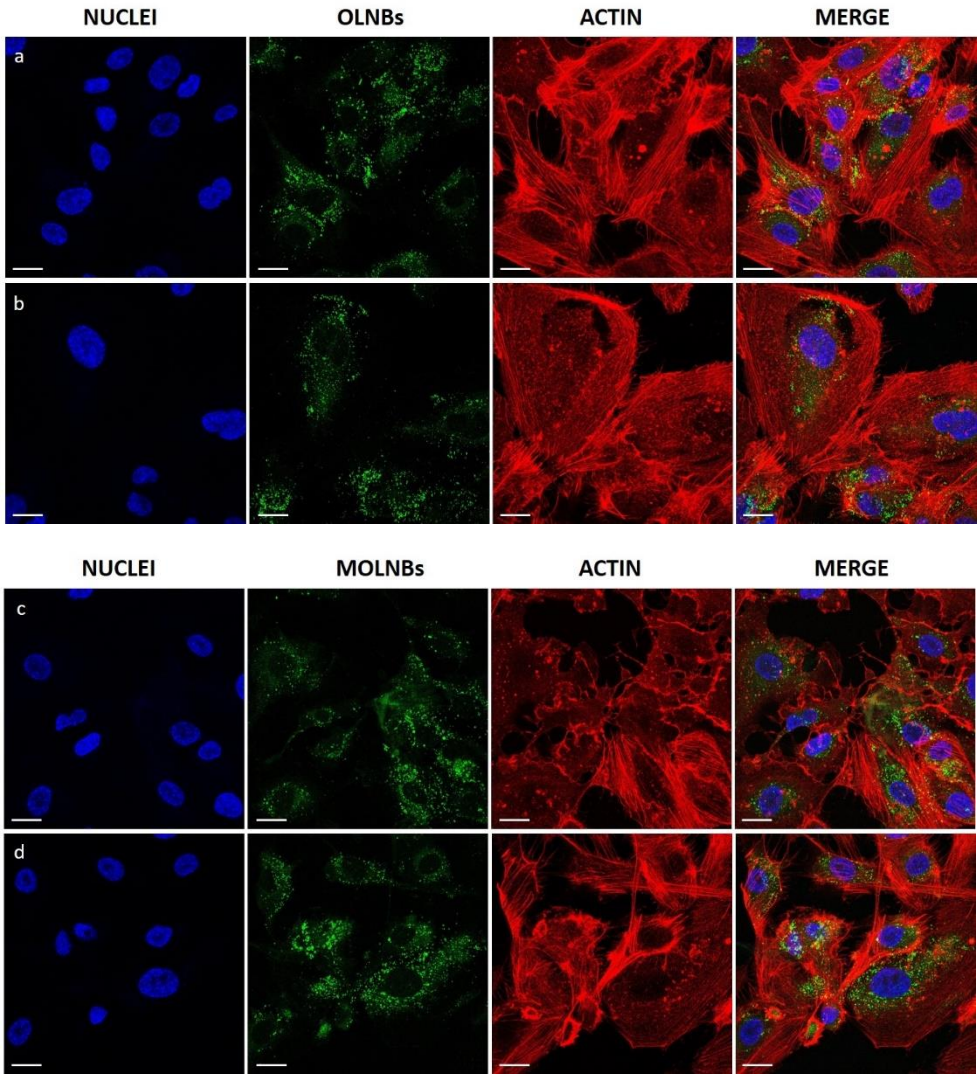

Figure 5.2. Confocal images of different formulation of nanocarriers internalized by hBMECs after 4 h of incubation. First and second rows: cells were treated with blank OLNBs (without SPIONs) in a dilution ratio 1:100 (**a**) and 1:200 (**b**) with the medium. Third and fourth rows: cells were treated with MOLNBs in a dilution ratio 1:100 (**c**) and 1:200 (**d**) with the medium. First Column: cell nuclei after DAPI staining, in blue. Second column: OLNBs and MOLNBs, conjugated with 6-Coumarine, in green. Third column: cell actin filaments after Rhodamine-Phalloidin staining, in red. Fourth column: merged images. Magnification: 40X. Calibration bar = 20 μm. Adapted from (Ficiarà et al., 2020a).

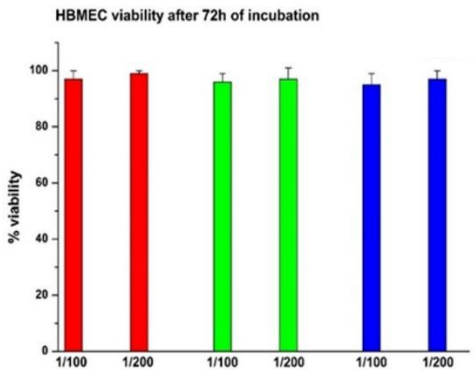

Figure 5.3. Percentage of viable cells after 72 h of incubation. The horizontal axis indicates the dilution (1:100 and 1:200) of NB. Red = MOLNBs; Green = SPIONs; Blue = OLNBs. Adapted from (Ficiarà et al., 2020a).

US Monitoring of MOLNBs in the Magnetic Field

The motion of the MOLNBs, located along the negative z-direction of the coordinate system, centered in the magnet, whose corresponding magnetization of the MOLNBs is dominated by the component along the *z*-axis, is significantly affected by the field. Snapshots at different time intervals from US imaging showed a different distribution of MOLNBs in the absence and in the presence of the magnetic field, which exerted a sensible effect driving a clearly detectable motion toward the magnet and along the axis (see Figure 5.4).

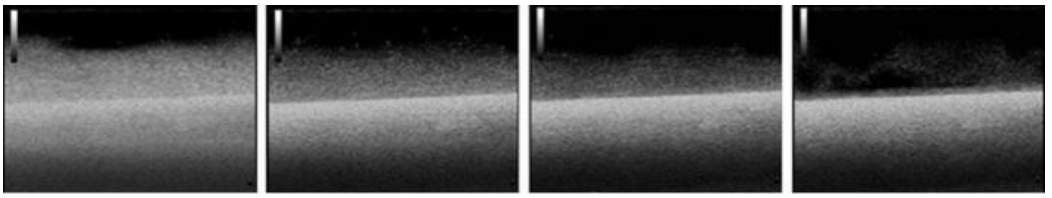

(**a**)

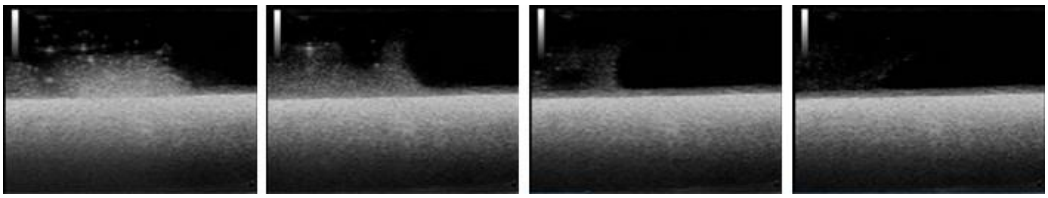

(**b**)

Figure 5.4. Snapshots from US imaging of MOLNBs in absence (**a**) and presence (**b**) of the magnetic field. Images were recorded at different time frames (5, 15, 25, 55 sec) from the injection. Adapted from (Ficiarà et al., 2020a).

5.3 Discussion (Ficiarà et al., 2020a)

MOLNBs are stable nanosystems showing a well-defined hollow structure, whose shell is densely decorated by SPIONs, as indicated by TEM analysis. The addition of SPIONs does not significantly increase neither their average diameter nor the polydispersity index, while the zeta potential is decreased but the value is still effective in preventing aggregation phenomena. This behavior suggested a good electrostatic interaction of SPIONs with the negatively charged NB shell. The combination of SPIONs with NB forming stable nanosystems was previously reported (Jiang et al., 2018).

Furthermore, the surface negative charge makes MOLNBs promising candidates to efficiently cross the BBB, being the zeta potential a crucial parameter for brain delivery (Decuzzi et al., 2010; Bramini et al., 2014; Saraiva et al., 2016).

MOLNBs were able to store in the perfluorocarbon core and slowly release oxygen by passive diffusion gradient, as previously evaluated (Zullino et al., 2019).

Interestingly, the versatile and peculiar architecture of MOLNBs can allow the incorporation of drugs with different chemical properties. In fact, the nanostructure consists of three domains: the core, the shell and the interface (Cavalli et al., 2016). Their different lipophilicity was exploited for the incorporation of drugs, enabling high payloads (Cavalli et al., 2012, 2015; Argenziano et al., 2017). Previously, chemotherapeutic drugs, such as doxorubicin and paclitaxel, were loaded in polymer-shelled NBs showing good stability and prolonged release kinetics (Marano et al., 2016b, 2016a, 2017). Moreover, they were intravenously injected in mice without any acute side effects.

The absence of hemolytic activity of MOLNBs is an important aspect, being a key parameter for assessing the safety of the nanocarrier and biocompatibility, and is strictly required for intravenous administration in early preclinical development (Dobrovolskaia et al., 2008b, 2008a).

In vitro cytotoxicity assay and confocal microscopy images indicate that MOLNBs interact in a non-toxic way with hBMECs and are localized in the cytoplasm compartment of the cells, as result of internalization, even if the uptake mechanisms are still not completely elucidated. These results highlight the potentiality of MOLNBs to enter in the CNS cells. Furthermore, these data pave the way for future investigation concerning the ability of MOLNBs to cross brain barriers in an *in vitro* model.

The magnetic properties of MOLNBs were already investigated in previous research showing their superparamagnetic behavior and the possibility of monitoring their concentration in tissue with MRI (Zullino et al., 2019). In the same study we were able to prove that also US may be effective in detecting MOLNBs, due to their vaporizable perfluoropentane core and the density contrast of the SPIONs on their surface. It is worthy of note that perfluoropentane can undergo to Acoustic Droplet Vaporization (ADV) phenomenon, when irradiated by US (Kripfgans et al., 2004). The ADV favor the liquid to gas phase shift of perfluoropentane, increasing the US backscattering. The US imaging contrast ability of SPIONs decorated polymer nanobubbles was previously demonstrated by Luo et al. (Luo et al., 2015).

Therefore, we manufactured a simple device able to visualize the motion of the MOLNBs in a static magnetic field with field lines in the direction of injection by sonication. This preliminary

magnetic investigation shows that MOLNBs can be magnetically guided using external permanent magnets.

The above results support our initial speculation, since MOLNBs might be safely administrated either systemically or locally via intravertebral injection in the CSF, monitoring their concentration by MRI or sonography. Several studies evaluated the distribution of intrathecally injected nanoparticles within the CNS, assessing the good ability of administration route via CSF rather than systemic delivery (Bottros and Christo, 2014; Householder et al., 2019). Interestingly, future investigation will involve the study of MOLNBs stability in real matrix fluids, such as serum or CSF.

Furthermore, MOLNBs may be magnetically driven towards target membranes, for instance the one separating CSF and the interstitial fluid of the brain located in the choroid plexus in the brain ventricles to deliver oxygen and chemotherapy drugs to brain tumors.

Tailoring the driving magnetic field based on the position and dimension of the brain tumor and the brain membranes to be crossed is a goal particularly challenging. Further investigations are required to validate such application by computational models based on MRI or CT tumor images (in silico models) and finally on in vivo animal models.

5.4 Conclusions (Ficiarà et al., 2020a)

Our study provides a complete characterization of the physicochemical properties of MOLNBs and demonstrates their biocompatibility and safety in the case of systemic administration. In addition, this nanoformulation might be considered a good starting point for developing a system able to cross the brain membranes, main obstacle to enter CNS. Furthermore, our preliminary results highlighted the capability of MOLNBs to be magnetically driven. Summarizing, this work opens new opportunities to consider MOLNBs in targeting brain tumors since they can deliver oxygen (potentiating radiotherapy) and chemotherapy drugs, being driven by ad hoc tailored magnetic fields under MRI and/or US monitoring.

Chapter 6: Computational Models for Magnetic Driving of Magnetic Nanobubbles in CNS Applications and Safety Assessment

This chapter presents the work selected as Best Communications Prizes at Società Italiana Fisica (SIF) 106° National Congress 2020 ("Potential therapeutic use of magnetic nanocarriers in brain tumors" *IL NUOVO CIMENTO 44 C (2021) 131, DOI: 10.1393/ncc/i2021-21131-5*) and the experiments performed in the ongoing collaboration with Institute of Materials for Electronics and Magnetism (IMEM)-National Research Council (CNR) (Parma) and Fondazione Italiana Fegato (FIF) (Basovizza, Trieste).

6.1 Computational Models for potential Magnetic Driving of MNBs

In the previous section, we described a novel multipurpose theranostic carrier designed as Magnetic Oxygen Loaded Nanobubbles (MOLNBs), able to be physically drivable and loadable with therapeutic drugs. MOLNBs are composed by a perfluoropentane core, a shell of biocompatible material (dextran or other polymers) and are covered with superparamagnetic iron oxide nanoparticles (SPIONs), conferring them proper magnetic properties.

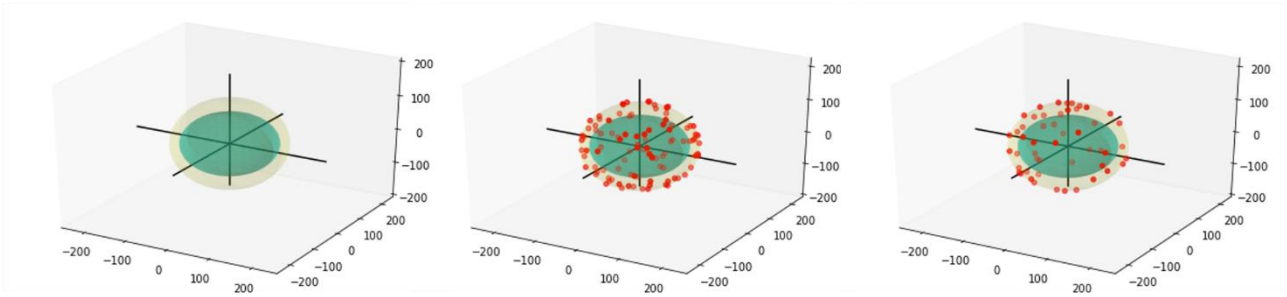

(a) (**b**) (**c**)

Figure 6.1. Simulation of nanobubbles as 3D sphere (average diameter 250 nm) (**a**) Nanobubbles with the perfluoropentane core and the polymer shell; (**b**) and (**c**): simulation of MOLNBs with random distribution of SPIONs at different concentration on the surface.

MOLNBs are potentially able to cross brain barriers when injected in the systemic circulation and to enter the CNS due to their non-toxic interplay with the BBB cells and also to be magnetically guided using external permanent magnets (Ficiarà et al., 2020a).
Due to the fact that the nanovectors can lose part of their cargo in the systemic circulation before overcoming the BBB, a possible alternative is the intravertebral injection in the CSF, in direct contact with the brain parenchyma. Several studies evaluated the administration route via CSF rather than systemic delivery, investigating the distribution of intrathecally injected nanoparticles within the CNS (Bottros and Christo, 2014; Householder et al., 2019).

Due to their properties, MOLNBs may be then magnetically driven towards target membranes, for instance the one separating the CSF and the interstitial fluid of the brain located in the choroid plexus in the brain ventricles, to deliver oxygen and chemotherapeutic drugs to brain tumors.
Locally administrated MOLNBs via intravertebral injection in the CSF can be monitored by MRI or sonography while exploiting their magnetic properties to precisely direct them to their target. Tailoring the driving magnetic field based on the position and dimension of the brain tumor and the brain membranes to be crossed is a very challenging goal. To validate such application, we present a setup aimed to simulate the brain environment and the motion of MOLNBs inside brain fluids in the presence of magnetic fields in different configurations (generated by magnets in particular positions), monitored by Ultrasound (US) imaging and supported by *in silico* models.

6.2 Magnetic Properties of MOLNBs

Firstly, the magnetic properties of OLNBs, SPIONs and MOLNBs were measured at room temperature by an Alternating Gradient Force Magnetometer (AGFM) by applying a maximum magnetic field $\mu_0 H$=1.8 T. These experiments were performed in collaboration with IMEM-CNR (Parma).

The sample of OLNBs showed a weak diamagnetic signal is obviously negligible with respect to that of SPIONSs and MOLNBs, whose magnetic cycle is respectively described in Figures 6.1a and 6.1b. In Figure 6.1a the magnetization cycle of SPIONs is reported. It showed a superparamagnetic behavior, with a magnetization value of 30 Am^2/kg at the maximum applied field $\mu_0 H$ =1.8 T. Also, the MOLNBs sample showed a superparamagnetic behavior with a specific magnetization value of 14 Am^2/kg at the maximum applied field $\mu_0 H$=1.8 T, which is compatible with the known mass concentration of SPIONs (i.e., around 40%) in MOLNBs by taking into account the experimental error of the magnetic measurements. In conclusion, these results confirm that MOLNBs show a superparamagnetic behavior with the magnetic moment expected for the specific quantity of SPIONs incorporated (Ansari et al., 2021).

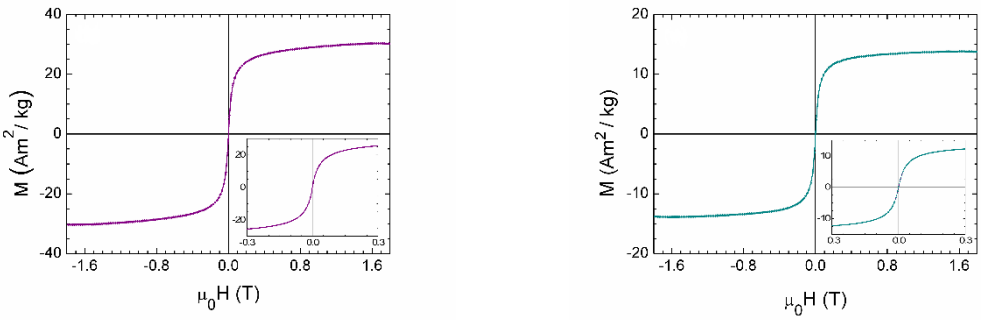

(**a**) (**b**)

Figure 6.2. (**a**) Magnetization cycle of SPIONs; (**b**) Magnetization cycle of MOLNBs. In the insets, a zoom of the measurements is reported, highlighting the superparamagnetic behavior of the samples (i.e., absence of magnetic hysteresis and remanence). Adapted from (Ansari et al., 2021).

6.3 Setup: Magnetic Field and US Imaging Monitoring *(Ficiarà E. et al., 2021, IL NUOVO CIMENTO 44 C (2021) 131)*

Suspension of MOLNBs were injected in a plastic cylinder and sonicated. Permanent cylindric magnets (diameter=6 mm, height=0.75 mm, Br= 1.17-1.21 T) of neodynium covered with Ni-Cu-Ni (https://calamite.org) were positioned on the cylinder wall in different configurations (see Figure 6.3) to generate the magnetic fields. The value of residual magnetization is in the range of 860-915 kA/m. Simulations of magnetic field lines were obtained using the Python package Magpylib (Ortner and Coliado Bandeira, 2020).

B-mode US imaging was carried out to study the response of MOLNBs to the external magnetic field due to their excellent echogenicity. MOLNBs were injected in the plastic cylinder containing demineralized water by means of syringe passing through a glass tube. The experiment was performed at a temperature of 25 °C. MOLNBs were sonicated by an US clinical equipment (MyLab™25Gold Esaote, Genova, Italy), connected to a linear array transducer (LA523, 7.5 MHz central frequency, Esaote, Genova, Italy) operating in B-mode with the use of the small parts imaging preset. B-mode cineloops (30 seconds) were acquired and recorded. Snapshots from cineloops were extracted at different time frames (5, 15, 30 sec) after the initial injection and compared in the different conditions.

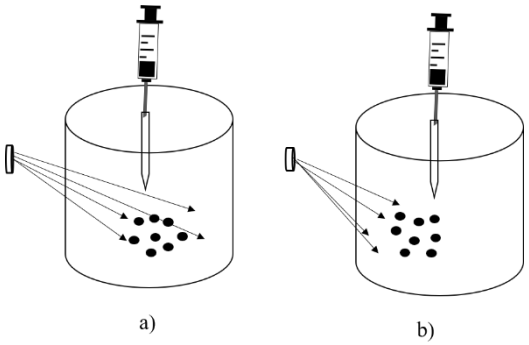

Figure 6.3. A sketch of setup used to investigate the response of MOLNBs to magnetic fields generated by two different configurations of magnets positioned on the cylinder wall: a) Four magnets at distance 4 cm each other in symmetric position with respect to the cylinder axis; b) Four magnets positioned in the left side of the cylinder at distance 2 cm each other. Adapted from (Ficiarà E. et al., "Potential therapeutic use of magnetic nanocarriers in brain tumors" 2021, IL NUOVO CIMENTO 44, DOI: 10.1393/ncc/i2021-21131-5)

First, we present simulations of magnetic fields generated by seven magnets, located on the wall of a sphere of 10 cm diameter as described in Figure 6.4, since the sphere might be considered as an ideal reproduction of the brain.

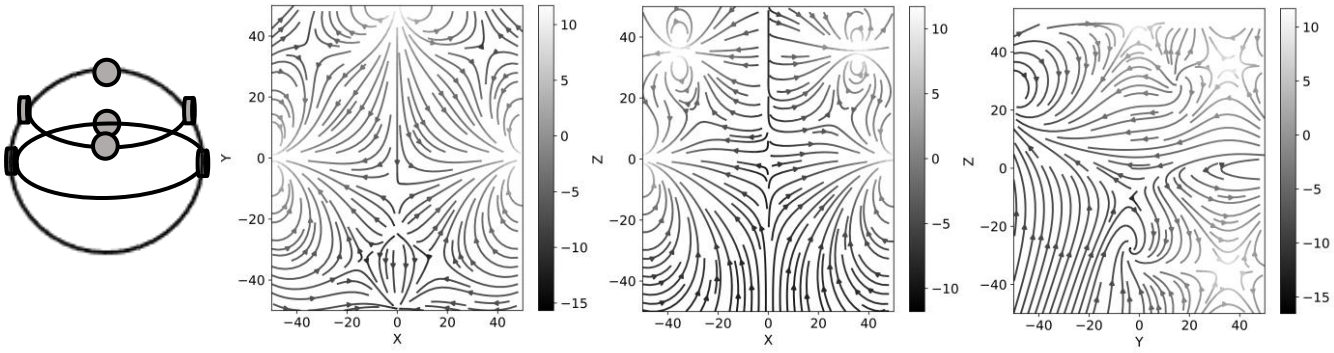

Figure 6.4. Seven magnets ideally located on the wall of a sphere (5 cm radius): three magnets located in the equatorial plane, and four magnets located in a fixed plane at the top of the sphere. Simulations of magnetic fields were performed revealing the direction of magnetic field. Adapted from (Ficiarà E. et al., "Potential therapeutic use of magnetic nanocarriers in brain tumors" 2021, IL NUOVO CIMENTO 44, DOI: 10.1393/ncc/i2021-21131-5)

Prior to applying a magnetic field, MOLNBs diffused in random directions. Next, using the setup previously described, snapshots at different time intervals from US imaging showed the flow of MOLNBs in the magnetic field generated by four magnets located in symmetric position, monitored by the US probe positioned on the cylinder wall in axial direction (Figure 6.5).

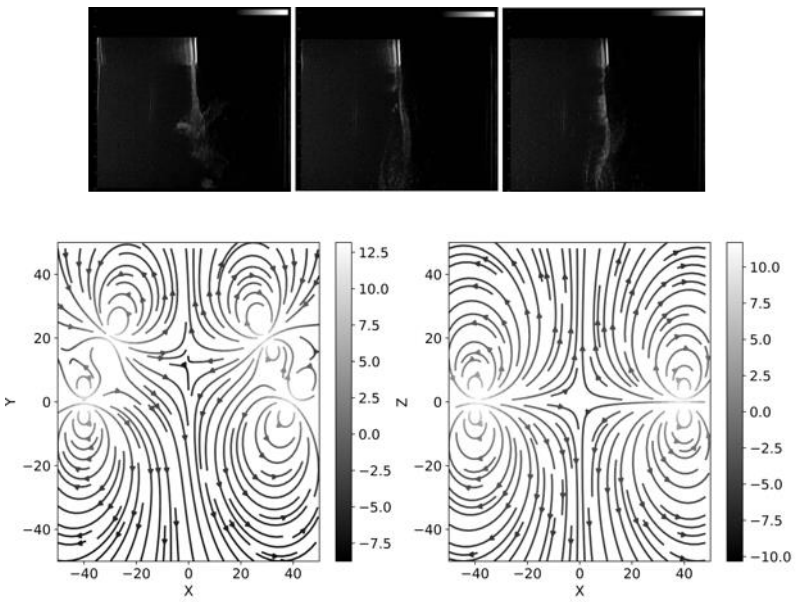

Figure 6.5. Snapshots from US imaging of MOLNBs in the magnetic field generated by four magnets in simmetric position with respect to vertical axis. Images were recorded at different time frames (5, 15, 30 sec) from the injection. Projection of magnetic fields lines in the XY and XZ plane were visualized. Adapted from

(Ficiarà E. et al., "Potential therapeutic use of magnetic nanocarriers in brain tumors" 2021, IL NUOVO CIMENTO 44, DOI: 10.1393/ncc/i2021-21131-5)

The configuration of four magnets in non-symmetric position revealed a significant deviation of MOLNBs motion towards the magnets, confirmed the effect of magnetic fields on MOLNBs. (Figure 6.5).

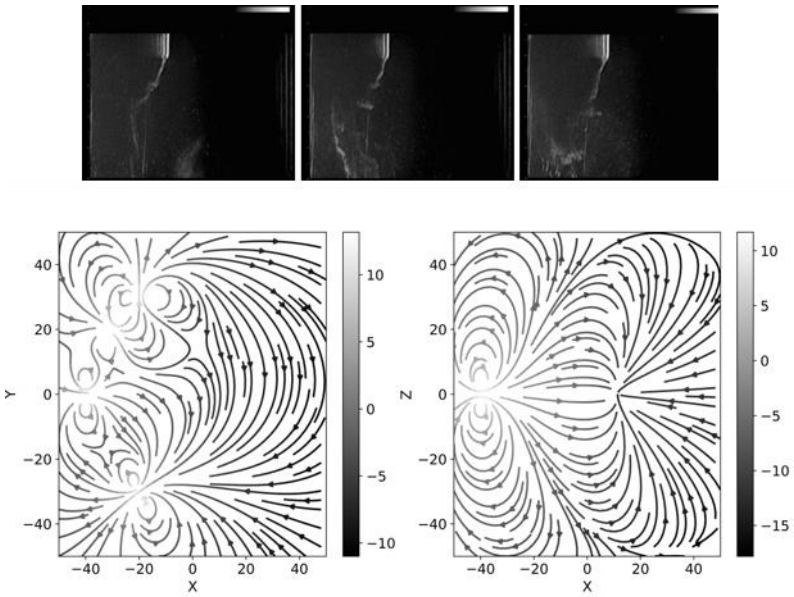

Figure 6.6. Snapshots from US imaging of MOLNBs in the magnetic field generated by four magnets in non-simmetric position with respect to vertical axis. Images were recorded at different time frames (5, 15, 30 sec) from the injection. Projection of magnetic fields lines in the XY and XZ plane were visualized. Adapted from (Ficiarà E. et al., "Potential therapeutic use of magnetic nanocarriers in brain tumors" 2021, IL NUOVO CIMENTO 44, DOI: 10.1393/ncc/i2021-21131-5)

In conclusion, we propose a new potential application of physically drivable magnetic nanobubbles to precisely target brain tumors, due to the interaction with magnetic fields allowing their manipulation. A new setup was developed, with the aim to simulate brain and motion of MOLNBs inside brain fluids. These preliminary results highlighted the possibility to precisely tune the motion of MOLNBs (monitored by sonography) using magnetic fields tailored by *in silico* modelling.

6.4 Safety of iron and Magnetic Nanobubbles in ex vivo models of brain

Optimal driving of magnetic nanovectors under external magnetic fields requires that the concentration of iron conferring their magnetic properties is large enough for its driving but small enough to remain safe for the organism, especially for the brain, very sensitive to iron balance.
In order to investigate the values of iron concentration delivered by SPIONs, in this second section the potential toxicity of both free iron and different formulation of NB and magnetic NBs (MNBs) was tested in a model of organotypic brain cultures (OBCs), obtained by slicing specific regions of the brain. The major advantage of the OBCs is that they maintain all the cells composing the brain in the 3D architecture typical of that region of the CNS, as in the *in vivo* situation, but they can be growth and challenged *in vitro*.

6.4. Materials and Methods

The experiments were performed in collaboration with the laboratory of Fondazione Italiana Fegato (FIF) (located in Basovizza, Trieste, Italia).

The viability of OBCs after challenging with different types of NBs (magnetic and not) has been assessed by LDH assay (reflecting cell's membrane leakage/ opening, with the release of the lactate dehydrogenase in the culture medium) and MTT assay (evaluation of activity of mitochondria) tests, after 24 hours of treatment. Different concentration of free-iron (Iron (III) reagent) ranging from 25 to 1000 μM (corresponding to a range of 0.27, 6.76, 27.03, 135.15, 270.3 μg/mL), NBs (without SPIONs) and MNBs (SPIONs concentration 1 mg/mL) at different dilution (1:8,1:64,1:192) were considered, based on our previous results of cell viability under MNBs (see Chapter 5, Figure 5.3).
OBCs of substantia nigra (brain slices from 5 days old Wistar rat) were used, reproducing the *in vivo* situation and containing all the cells typical of the region, including the dopaminergic neurons (DOPAn), extremely sensitive and with a crucial role in brain diseases, especially in Parkinson's disease. For details of protocol refers to (Dal Ben et al., 2017, 2019).

Immunofluorescence based on Tyrosine hydroxylase was performed for counting the dopaminergic neurons number (DOPAn) in the slices after treatments of NBs and MNBs. The data presented was obtained from 6 biological repetitions. Linear regression analysis was applied to data related to free-iron treatments. Statistical differences were evaluated using t-Student's test against a threshold of $P<0.05$.

6.4.2 Results

Based on MTT test, the treatment with iron presents a dose-dependent trend in the range of concentrations used, giving a statistically significant toxicity for 1mM ($P < 0.05$) when directly compared to the control condition (Figure 6.7, left). NBs formulations are safe for healthy slices at all dilutions considered and NBs containing SPIONs are safe at concentration 1:64 and 1:192 (dilution factor 1:8 was not considered due to the possible agglomeration of SPIONs at this high concentration) (Figure 6.7, right).

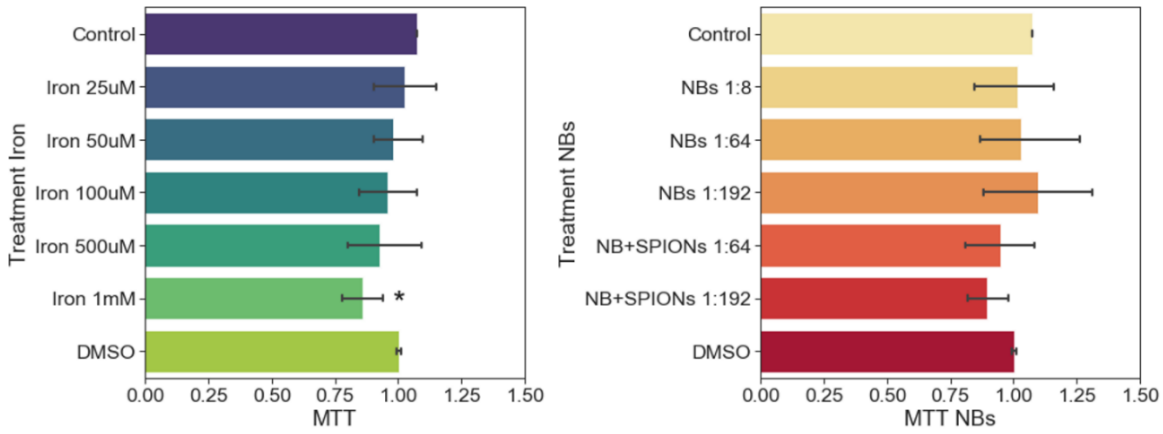

Figure 6.7. Bar plot presenting the activity of mitochondria (from MTT assay) compared with the control and DMSO condition, respectively for the iron treatment with doses in the range of 25 μM-1 mM (Left) and for treatment with NBs (without SPIONs) at different formulations and dilution (1:8,1:64,1:192) and MNBs (NBs + addition of SPIONs on the shell) (Right). Data are presented as mean and standard deviation of 6 biological repetition. * P<0.05, t-Student's test.

Linear regression showed a statistically significant relationship between free-iron concentration and toxicity data related to MTT. The negative coefficient suggests that as the free-iron concentration increases, the mitochondrial activity tends to decrease (Figure 6.8), presenting a dose-dependent trend for the toxicity.

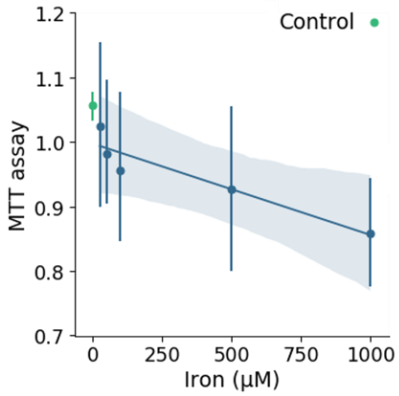

R^2=0.22		
Prob(F-statistics) = 0.006)	Coefficient	P-value
Std error= $5.78\text{-}10^{-5}$		
const	1.0193	P<0.0001
Iron	-0.0002	P=0.006

Figure 6.8. Linear regression applied to data related to iron treatment indicates a significant association between the changes in the iron concentration and the shifts in the toxicity data related to MTT assay.

Results from LDH assay reported that only NBs at 1:8 dilution induced a significant damage (P<0.01), disappearing when the NBs dilution increases.

While both MTT and LDH give an information about the health status of the whole tissue, the effects of the challenging on DOPAn only can be evaluated by immunofluorescence staining. Because the DOPAn are extremely sensitive to stressors, they might be damaged, while the rest of the tissue is not. Based on the dopaminergic neurons number, iron is already toxic at 100 μM (P<0.001) and 500

μM ($P<0.05$). NBs without SPIONs showed to be toxic for neurons only at 1:8 dilution ($P<0.01$). Formulation containing SPIONs diluted 1:64 induced a non-statistically significant reduction in DOPAn, while NBs with SPIONs at 1:192 are well tolerated.

6.4.3 Discussion

In Figure 6.7 the results from experiments concerning the exposure of substantia nigra OBCs to treatments with iron and MNBs were presented, showing that MNBs are surely safe for the tissue at 1:192 dilution. Furthermore, iron revealed a dose-dependent response for the mitochondria activity and becoming toxic at lower threshold (100 μM) for DOPAn.

Other types of iron reagents are available to perform experiments in iron loading condition. Ferrous iron reagents can simulate a more pathologically relevant sources of iron (due to the participation to Fenton reaction) rather than ferric reagents, but ferrous iron rapidly oxidizes at neutral pH and it has to be maintained in its reduced state by adding other compounds, such as ascorbate (Healy et al., 2017).

In these experiments an Iron (III) (Ferric) reagent was used, in order to better compare the iron concentration in SPIONs (mainly composed of ferric iron) and the iron amount potentially tolerated by the brain cells, for a fine-tuning of functional but not toxic iron concentration in NBs.

Although the internalization mechanisms for iron and NBs in the cells could be different and can occur at different rates, this comparison can be useful for a quantitative evaluation of iron concentration in OBCs, currently considered the best *in vitro* model for the toxicity assessment (see Chapter 1, section 1.1.6).

In the literature a different sensitivity to iron toxicity between neurons, astrocytes and oligodendrocytes has been assessed, with different thresholds for impaired viability after iron treatment. Astrocytes seem unsusceptible to iron toxicity and capable of withstanding high iron loading, without compromising viability (Healy et al., 2017). On the contrary, neurons appear more vulnerable, and several studies show that values ranging from 10-100μM already give a significant decrease in viability (review of (Healy et al., 2017)). For instance, a comparison between three cell types grown as single primary rat cultures, co-cultures of astrocytes-neurons and microglia-neurons showed that 50 μM of ferric citrate was enough to impair viability in neurons and microglia, whereas astrocytes were not perturbed at this concentration and 200 μM of ferric citrate did not affect the viability of co-cultures, suggesting that astrocytes and microglia protect neurons against toxicity (Oshiro et al., 2008).

Our data are in line with this biological interpretation, showing high resistance of OBCs under iron treatment (significant difference with respect to control at high dose 1mM) and lower threshold for DOPAn (100 μM, corresponding to ~ 27 μg/mL). In fact, OBCs can better replicate the complex iron homeostasis machinery and interplay between cells with respect to single-cell cultures.

Also, the interplay between iron homeostasis and the molecular signals associated with oxidative stress and mitochondrial injury is assessed (Belaidi and Bush, 2016), confirming our dose-dependent response in viability assay (MTT) and the reduced number of dopaminergic neurons after iron treatment.

Moreover, the management of iron presents some difficulty, due to the conversion to its insoluble form, chelation by proteins or salts, or precipitation with other salts becoming significantly less toxic. Several culture models used for studying iron overload can include additional stress, such as the use of serum-free media, making the cells more quiescent and reducing the number of extracellular components able to sequester iron (Eid et al., 2017).

In our case, iron was directly added to the culture medium and this can present a limitation for the comparison of our experiments with those present in literature: the proportion of iron entering the cells, possibly a minor part, is not exactly known (Healy et al., 2017). In fact, Fetal Bovine Serum (FBS) (added to media culture of OBCs) contains transferrin, an iron chelator. After chelation by transferrin, only the cells possessing the transferrin receptor are able to internalize iron. Most of the experiments for iron loading present in literature removed the FBS during the iron challenging. This increases the quantity of "free iron" in the medium (not chelated by transferrin), but it is considered an additional stress and it can be an un-physiological situation for the slices, inducing sufferance and increasing their sensitivity to iron. In our experiments, the toxic concentration for iron potential damage to healthy tissues was investigated, so serum was not removed from the media culture.
Considering toxicity of NBs (with and without SPIONs), we compared our results with several *in vitro* assessments of IONPs toxicity in CNS, by investigating the toxicity of NPs for glial and neuronal cells activity. We reported a potential toxic effect for DOPA neurons considering NBs with SPIONs at 16 μg/mL (1:64 dilution) but not at 5 μg/mL, and for NBs at 1:8 dilution, corresponding to very high concentration of NBs (~10^9 NBs/mL). The results are in agreement with several studies (reviewed by (Xie et al., 2018)), showing that IONPs in the concentration range of 0.1-10 μg/mL are not toxic for different types of human glial, breast cancer and normal cell lines, assessing the biocompatibility of IONPs, while cytotoxicity could be noticed at 100 μg/mL. However, in our case the lower threshold found for neurons can be due to the higher sensitivity for iron of these brain cells or due to interplay with the other cell types present in the slice, that can protect or amplify the toxicity. Conversely, Dextran-coated SPIONs showed to be safer, did not impair the hippocampal cell viability at doses until 250 μg/mL after 24 h of incubation (Khalid et al., 2018), which can confirm the positive effect of the polymeric coating.

Moreover, after short and long-term exposure of human brain cells to IONPs, cytotoxicity and proliferation impairment are proved, also revealing that astrocytes are more vulnerable than neurons (Petters et al., 2014; Coccini et al., 2017). This suggests the need for further studies for the elucidation of mechanisms involved in the interaction of brain tissue in its complexity and MNPs.
Finally, the threshold of iron concentration able to induce toxicity is lower in the case of MNBs with respect to free-iron added to the medium, especially for the DOPAn (16 μg/mL for MNBs vs 27 μg/mL for iron in the medium). This can be due to several possible reasons: free-iron directly added to the media can be chelated from transferrin/other molecules or precipitate, not entering the cells; on the other hand, based on our previous results (see section 5, Figure 5.2), the MNBs are able to be internalized in the cells, increasing the probability that iron interacts with cells with consequent potential toxic effects.

A strength of these experiments is that OBCs can better replicate the intricate cellular relationships of brain than monocultures in the handling of iron homeostasis and MNPs, giving useful information for a careful tuning of iron concentration of MNPs into the CNS for both safety and magnetic driving.

Chapter 7: Discussion

Most of this work focused on the evaluation of iron imbalance in neurodegenerative diseases at different levels: starting from the setting of an analytical and reliable protocol for the iron quantification in CSF (together with the collection of other clinical iron-related parameters), computational models were developed to foster potential alterations of iron concentration and mechanisms involved in iron trafficking from blood to brain.

A literature revision showed the need for additional investigations of methods, relative analytic standardization, and interpretation of indicators for a better assessment of iron profile (Ficiarà et al., 2021c). Recent works highlighted the conflicting results in the evaluation of metal concentrations, such as iron, in different biological samples (i.e., blood/serum/plasma and CSF) (Duce and Bush, 2010; Schrag et al., 2011; Cicero et al., 2017).

This could be due to differences in the treatment of samples and in the methods used to quantify iron in biological fluids, requiring very accurate measurements to detect it.

The contrasting results about iron quantification and the importance of measuring out biomarkers in CSF (due to their close contact to the brain) moved to the first step of this work, i.e. the development of an accurate and reliable protocol for the quantification of iron in CSF, performed by the GF-AAS.

In fact, the core AD CSF biomarkers (amyloid-β and tau) are dosed in CSF and recently many other molecules have been proposed or investigated as candidate biomarkers for differentiating AD from healthy controls or other causes of dementia, for monitoring disease progression, target engagement of novel candidate drugs, or for predicting the rate of cognitive decline (Fagan and Perrin, 2012; Pawlowski et al., 2017). One of the main limitations of CSF samples is the invasiveness of the collection technique (i.e., lumbar puncture) compared with blood sampling. Also, the low amount of iron present in CSF requires very sensitive and reliable methods.

The work presented in the second chapter strengthened the hypothesis that iron dyshomeostasis is crucial for AD pathophysiology. Our measurements showed an increase total iron content in CSF in AD patients, consistent with several studies reporting altered levels of iron and iron-related proteins in AD patients, and suggesting that iron dyshomeostasis worsens as cognitive impairment increases (Smith et al., 2010; Sternberg Zohara and Sternberg Zohara, 2017).

Furthermore, iron in CSF has been reported to show very low and variable concentrations, and our results on total iron in CSF are in accordance with the order of magnitude indicated in several studies (Bradbury, 1997; Núñez et al., 2012).

However, a discrepancy of our quantitative values in CSF compared with those present in literature is emerged. This can be due to differences in the instrument and procedure used to perform these measurements (i.e., environment controlled by contamination, sensibility of the instrument, quantitative or qualitative technique used).

In particular, although the results need a wider validation to assess their effectiveness and reliability, the workflow of the machine learning analysis can be reproducible and stimulates the need for future works taking into account further iron-related indicators in different biofluids, fitting the complexity of iron metabolism. In fact, this approach could provide an added value to the current

research, given the recent exploration of other indicators related to iron burden and metabolism in AD (Ashraf et al., 2019, 2020b, 2020a; Diouf et al., 2020; González-Sánchez et al., 2020), helping to point out the complex pattern of iron indicators in neurodegenerative conditions.
Heterogeneity in clinical manifestations, disease progression and biological measurements often occurs within groups of individuals diagnosed with the same neurodegenerative disease (Young et al., 2018). This heterogeneity makes it difficult to understand the disease mechanisms from studying the diagnosed group as a whole, as different mechanisms could be responsible for the disease in different individuals, and makes more challenging to identify effective therapies. Therefore, stratifying participants to the study according to their features may be very useful, and with the use of machine learning techniques for this purpose becomes increasingly popular.
Our results revealed a potential pattern involving both iron in CSF and transferrin in serum for AD patients, leading to a parallel and thorough investigation on the pathways of iron between blood and brain.

After a careful revision of the literature regarding the mechanisms of brain barriers and the relative iron transport across them (described in section 1.2), starting from our measurements available for the CSF and for the iron circulating in the blood, two mathematical models were developed in an iterative way, aimed to a macroscopic description of iron trafficking between blood and brain.

Sensitivity analysis for the study of this models was made due to the high intrinsic biological variability of the iron values and, to the best of our knowledge, the lacking of consistent values of parameters describing the iron exchange from blood to brain. By means of this computational technique, we hypothesized which potential mechanisms for the iron exchange at brain barriers levels could be altered, also showing the relevance in the guide of new experiments of specific transporters involved in iron influx/efflux to/from the brain. In fact, iron accumulates inevitably when the balance of influx/efflux rate is impaired, potentially worsening neurodegenerative conditions.

The results presented in the third chapter can be considered a strong support to reveal potential pathologic alterations for iron at the brain barrier function level. To sum up, the importance of a higher influx rate at BBB/BCSFB level can reflect the damage of the related barrier and the consequent iron accumulation in the brain. After a further validation with suitable (longitudinal) data, these models can provide computational methods to quantify these alterations. Then, the relevance of the efflux mechanism was assessed, paying attention to the need for further experimental investigations of the pathways responsible for removing iron from the brain. In fact, without an appropriate route out of the brain, iron can accumulate and affect neurodegenerative conditions, posing a threat to the brain (oxygen-rich environment) by inducing ROS formation (Zecca et al., 2004b).

Moreover, this work showed the need for a deeper investigation on the relation between serum/blood iron indicators and CSF/brain iron indicators, advantageous to define a complete iron profile (Ficiarà et al., 2021c).

Interestingly, Connor and colleagues studied the potential communication between peripheral iron and CSF, showing that iron transport correlates positively with plasma Hb concentrations but not with s-F levels (Connor et al., 2020). The study suggested that erythropoietic demands for iron

are predominant over brain requirements, and therefore total body iron store indicators (i.e., s-F) may not be the best peripheral indicator to evaluate brain iron uptake (Connor et al., 2020).

Additional iron indicators can be very useful to quantify other non-standard forms of iron, especially those responsible for the toxicity, such as NTBI (Ficiarà et al., 2021c). It is not clear whether NTBI is generated locally or it is transported from the blood across the BBB and BCSFB, and direct evidence of the transport of NTBI to the brain has been reported, also revealing a complex interplay between inflammation and brain iron homeostasis (Tripathi et al., 2017). However, a few numbers of studies are available, and further investigation on the quantification of NTBI and redox-active iron in CSF is essential since NTBI could be a crucial indicator, being responsible for a toxic environment contributing to neurodegeneration and neuronal death (Ficiarà et al., 2021c).

The second part of the work focused on the potentiality of iron to confer magnetic properties to nanovectors and the issues related to safety and toxicity, especially in the brain environment.

Due to their unique physicochemical properties, nanovectors composed by iron oxides nanoparticles (IONPs) are a promising tool for biomedical applications based on their magnetic driving via external field. In particular, IONPs could be ideal for the physical targeting of CNS, optimizing the crossing of BBB and the drug delivery into the brain (Ansari et al., 2019). For this reason, the development of engineered IONPs by means of controllable synthesis methods and a careful tuning of their properties are in constant progression.

The need for an accurate selection of physicochemical properties, such as size, shape, and structure, and the functionalization of IONPs with different polymers or chemical compound is essential for the improvement of various biomedical applications in CNS (Ansari et al., 2019). A deeper investigation on the magnetic characterization of IONPs is necessary, in order to better understand the interaction of IONPs with the external magnetic field. The emergent property of superparamagnetism makes IONPs appealing nanomaterials, as proved by the large number of current studies focused on the detailed analysis of magnetic properties, such as saturation magnetization, coercive field, and remnant magnetization (Ansari et al., 2019). These parameters are crucial for the interplay with the applied magnetic field, allowing the fine modulation of magnetic-driven nanocarriers in the biological environment.

In particular, in the Chapters 5 and 6 we assessed the superparamagnetic properties of magnetic nanobubbles in different formulations, proposing also a new method for their potential driving in a controlled manner, to improve the targeting in case of difficult locations of the tumor (e.g., brain tumors).

Firstly, the superparamagnetic behavior of MOLNBs is fundamental to achieve strong magnetization and at the same time to avoid attractive force between particles, responsible for phenomena of movement and agglomeration.

Then, the idea consists in the use of a tunable grid of external magnets creating a magnetic field able to interact with the MOLNBs for a precise targeting in the brain. Obviously, this proposal needs to be matched with further considerations about the fine-tuning of iron amount in nanovectors, responsible of both the acquisition of magnetic properties and the related safety issues.

In fact, special attention must be paid to the assessment of biocompatibility and potential risk associated with the IONPs exposure. The low toxicity of IONPs is generally assumed, but since results are often contradictory, further investigation is required, also developing innovative cell models to test it (Ansari et al., 2019). This is a critical point due to the high vulnerability of CNS for iron imbalance, especially in the alteration of iron homeostasis.

We demonstrated that MOLNBs are safe at specific dilution and can be internalized from human brain endothelial cells (composing the BBB). However, a limitation of our study is the lacking of the validation of BBB crossing of nanobubbles in *in vitro* BBB (i.e., transwell assay) or *in vivo* models.
Several studies showed that magnetic nanoparticles can cross the BBB and reach targets in brain tissue without disrupting the barrier in rat models (Kong et al., 2012; Sensenig et al., 2012).
A challenging aspect is the need of new smart magnetic nanocarriers able to cross BBB and to reach the brain from bloodstream effectively and safely. For this purpose, the use of an integrated approach taking into account composition, functionalization, magnetic properties and minimization of toxicity can promote the optimal choice for magnetic-field-directed NPs. In fact, the resulting ability for magnetic fields to effectively move magnetic nanobubbles through tissue depend on their properties. However, overcoming the BBB is the main obstacle for the entry of therapeutic compound into the CNS. Therefore, novel delivery and monitoring systems are needed to optimize the targeting in CNS. In this context, proposals for an alternative approach avoiding the systemic delivery and the related drawbacks are currently of great interest. Our results might encourage the possibility of non-systemic administration approaches, e.g., the feasibility of magnetic driving of the MOLNBs from the brain ventricles (filled by CSF, in which MOLNBs could be injected from the intravertebral spaces) to the nearby tumors. The contact of CSF to the CNS makes it an attractive medium for drug delivery circumventing systemic barriers. Several studies demonstrated the validity of the intrathecal administration of nanoparticles (Householder et al., 2019) and of active agents directly into the ventricles (Sandberg et al., 2015).
BCSFB is more permeable than BBB, allowing also a direct access to the brain environment, e.g., by means of intravertebral or intrathecal injection in the CSF.
Several studies showed that leptomeningeal transport depends in a very complex way on the local processes: macromolecules and nanoparticles delivery maybe favoured by pulsation-assisted convectional transport of the solutes with CSF or even by active "pumping" of CSF into the periarterial spaces, allowing solute transport from the latter to and within the parenchyma, and finally neuronal uptake and axonal transport (Papisov et al., 2013).
We proposed the applications of magnetic nanobubbles coupled with tunable external magnetic field to potentially cross BCSFB and reach the site of interest in the brain.
The use of *in silico* models can help optimizing the investigation of the force acting on a magnetic carrier, tuning the magnetic field to generate a sufficiently strong uniform field (maximizing the induced magnetization) and gradients at the target region. Several conditions including carrier size and surface charge, brain tumor flow dynamics, administration route and topography of a magnetic field should be carefully considered to enable effective brain targeting (Sensenig et al., 2012).

A further quantitative evaluation of the interaction between magnetic nanobubbles and magnetic field is strictly needed, due to the "sink" role of CSF by "washing" the brain, cleaning it from exogenous and toxic substances. Therefore, a magnetic field is necessary not only for a precise driving of nanovectors but possibly to force the entry in the brain across BCSFB.
Then, results for both the safety of MNBs and the fine tuning of SPIONs in the NBs were presented. *Ex vivo* models of a brain region (substantia nigra) were used to evaluate the toxicity of NBs and MNBs, as well as of bulk iron.
Considering the similarity of organotypic brain cultures with the *in vivo* situation (due to the crosstalk of different brain cells), the indication that MNBs are safe at dilutions corresponding to a quantity of SPIONs lower than 16 μg/mL is reliable, and suggests their potential use in CNS.
Future investigations are necessary, in order to evaluate the magnetic properties of MNBs at these particular concentrations and the consequent potential interaction with external magnetic fields. Then, the set up and computational models presented in the last chapter could perhaps be translated to more realistic situation and the related potential application in nanotherapy.
Finally, a "personalized" model, based on CT or MRI imaging and a grid of permanent magnets producing the required magnetic field can illustrate this driving approach, exploiting the theranostic properties of MOLNBs for a real-time tracing of their path.

Chapter 8: Conclusions and Future Perspectives

Based on the assumption that iron dysregulation at brain barriers and its impaired concentration levels in biological fluids and brain can be part of the pathophysiological process in dementia such as Alzheimer's disease, our investigation applied machine learning techniques approaches as well as mathematical modeling on data obtained by quantitative evaluation of iron in cerebrospinal fluid.

In this work, we showed that some iron-related indicators might explain the stratification of AD, MCI and neurological control patients and interact with core-biomarkers, highlighting the potentiality of a deeper investigation of further parameters related to iron homeostasis and metabolism for the discrimination of patients affected by dementia at different stages.

Moreover, the computational models presented in this study can not only shed light on the (probably altered) dynamics of iron exchange between CSF, brain tissue and blood, but can also provide insight for future experimental studies of these mechanisms (especially the efflux/removal of iron from brain) and potentially offer a new strategy based on restoring brain-barriers functions to normalize the elevated levels of brain iron in condition of dementia.

Future perspectives can exploit the collection of further iron-related parameters to increase the space of features for the application of machine learning techniques, i.e., considering the evaluation of brain iron from MRI, to validate the correlation with CSF measurements. Also, it can be useful to investigate experimental protocols for novel non-standard iron indicators, helping to evaluate the toxicity of iron in brain diseases more accurately.

Due to the involvement of iron in neurodegenerative diseases, chelation of iron could be a therapeutic strategy, positively interfering with the mechanisms involved in the pathogenesis, such as overproduction of Amyloid beta and neurofibrillary tangles. However, this requires the capacity of therapeutic agents (with chelating power) to effectively target specific brain regions.

Furthermore, in the second part of the work, we investigated iron-loaded nanoparticles for two main reasons:

a) How iron defines the magnetic behavior of the nanotools and its consequent magnetic driving
b) How iron impacts on iron homeostasis of the body and in the CNS, highly sensitive to iron imbalance, especially in neurodegenerative diseases

Following qualitative and quantitative assessments of magnetic properties and safety of the nanovectors under consideration (magnetic nanobubbles), a new set up and computational models able to potentially guide magnetic nanoparticles toward out-of-reach locations (such as brain tumors) using external permanents magnets were originally proposed.

However, future experiments are needed to evaluate the effective crossing of brain barriers of magnetic nanobubbles to target the brain. In parallel, a deeper quantitative investigation of their interaction with magnetic fields at the dilution considered safe for CNS applications is needed, in order to elucidate and potentially control their motion and manipulation in the complex brain environment.

Appendix

S1. Table for the standard and non-standard iron indicators (Ficiarà et al., 2021c)

Supplementary Table 1. CSF: cerebro-spinal fluid; s-F: serum ferritin; HS: Healthy Subjects; M=men; W=women; Tf: transferrin; s-Tf: serum transferrin; TIBC: total iron binding capacity; UIBC: unsaturated iron binding capacity; NTBI: non-transferrin bound iron); Ft: ferritin; S: standard; NS: non-standard; HPLC: High Performance Liquid Chromatography; MS: Mass Spectrometry; AAS: Atomic Absorption Spectrometry.

Marker	Tissue	Normal Concentration	Standard/Non standard	Techniques
s-F	Serum	Mean s-F concentration of adults by sex and age: 56 μg/L (W) 121 μg/L (M)(Worwood), 120.25±3.46 μmol/L (Ref. 15-200 μg/L (M) 30-370 μg/L (W))(Faux et al., 2014)	S	Enzyme immunoassays (IA) (Organization, 2011); Agglutination assay: turbidimetric, nephelometric, Latex photometric IA (Faux et al., 2014; Garcia-Casal et al., 2018). Sandwich IA using direct chemiluminometric technology (Goozee et al., 2018).
Tf	Serum	204-360 mg/dL(Ogun and Adeyinka, 2021), 32.96±0.18 μmol/L (Ref. 23-46 μmol/L)(Faux et al., 2014)	S	IA; MS analysis (Ashton et al., 2019; Ashraf et al., 2020b). Iron-binding proteins evaluated by chromatography-inductively coupled plasma-mass spectrometry (ICP-MS) (Hare et al., 2015).
Indirect s-Tf concentration: TIBC, UIBC	Serum	TIBC: 250–400 μg/dL; 42.0- 64.3 μmol/L (Jovičić et al., 2005)	S	Colorimetric Tests (Jovičić et al., 2005). Fully automated TIBC Assay (Yamanishi et al., 2002).
Serum Iron: ferric iron (Fe^{3+}) bound mainly to s-Tf		12.5-26 μmol/L (M); 10.5-23 μmol/L (W)(Penkova and Ivanova, 2019)	S	Chemistry analyzers, i.e., colorimetric reaction with ferrine or ferrozine as a chromogen to form a color complex with iron.
NTBI	Serum	0.21±0.10μM (Sasaki et al., 2011)	NS	Ultrafiltration ICP-MS (Matta et al., 2018); HPLC (Sasaki et al., 2011); Isotope Dilution MS (Yang et al., 2019); Novel NTBI measuring system using Nitrilotriacetate and PSAP as chromogen (Ito et al., 2012); Chelatable fluorescent beads based on flow cytometry (Ma et al., 2014); Fluorescent bead assay CP851 Chelator based (Garbowski et al., 2016).
Total Iron	Serum	~ 1 mg/L	NS	AAS, ICP-MS (González-Domínguez et al., 2014; Tao et al., 2014; Paglia et al., 2016).

Ft	CSF	HS: 6.4±2.1 ng/mL(Ayton et al., 2015) 10.7-16.4 ng/mL(Khalil et al., 2014)	S	IA
Tf	CSF	0.10–0.28 μmol/L (Bradbury, 1997); ~ 2 mg/dL(LeVine et al., 1999; Khalil et al., 2014)	S	Nephelometry (Khalil et al., 2014). Lectin microarray, HPLC, matrix assisted laser desorption/ionization-time of flight MS, and tandem MS (Futakawa et al., 2012; Hoshi et al., 2017).
Total Iron	CSF	0.29–1.12 μmol/L (Bradbury, 1997); 0.12- 2.00 μM (Lavados et al., 2008) (26.5 ± 9.9 μg/L) in neurological control (Ficiarà et al., 2021a)	NS	Colorimetric analysis; ICP-MS (Hozumi et al., 2011), AAS (Lavados et al., 2008; Ficiarà et al., 2021a).
Lactoferrin	Saliva	Control subjects (10.24 ± 1.96 μg/mL) (Carro et al., 2017) (7.7 ± 2.4 μg/mL)(González-Sánchez et al., 2020)	NS	MS; IA
Total Iron (indirect)	Brain	Putamen: (56 ± 11 sec^{-1}) Globus Pallidus: (72 ± 10 sec^{-1}) Caudeate Nucleus: (40 ± 6 sec^{-1}) Thalamus: (30 ± 6 sec^{-1}) (*postmortem* study) (Langkammer et al., 2010)	S	MRI (R2* sec^{-1})

Serum/Plasma Tf, Serum Iron and Tf Saturation

It is customary to measure Tf concentration indirectly from TIBC of plasma. A TIBC test measures the blood's ability to attach itself to iron and transport it around the body, indicating the maximum amount of iron needed to saturate plasma or serum Tf. TIBC correlates well with Tf concentration, and the theoretical ratio of TIBC (in mol/L) to Tf (in g/L) is 25.1: TIBC (mol/L) = 25.1 x Tf (g/L) (Yamanishi et al., 2003). Theoretically, 1 mol of Tf (average molecular mass, 79 570 Da) can bind 2 mol of iron (55.8 Da) at two high-affinity binding sites for ferric iron.

Serum iron concentration measures the amount of ferric iron (Fe^{3+}) mainly bound to serum Tf but does not include the divalent iron contained in serum, e.g., hemoglobin residues. It has been reported

that serum iron levels were significantly lower in AD patients than in healthy controls after excluded two studies (Li et al., 2017).

Transferrin saturation (TSAT) provides additional information for the evaluation of iron transport and about the adequacy of iron supply. In blood, iron bounds with Tf provided 30% of the total transferrin is in the form of apo-transferrin (Gkouvatsos et al., 2012). TSAT indicates the percentage of binding sites of all the Tf molecules occupied by iron and is calculated as the ratio (serum iron)/Tf or (serum iron)/TIBC. If the unsaturated iron-binding capacity (UIBC) is measured, then TIBC is calculated as the sum of serum iron and UIBC (Pfeiffer and Looker, 2017).

It is reported that the average value of TSAT is 25% (Pfeiffer et al., 2009). Reference ranges depend on multiple factors like age, sex, race, and test devices. Normal values for TSAT are in the range of 25-45% (typically 30%) (Kelly et al., 2017), and lower values of TSAT are reported for female (i.e., 25-27%) with respect to male (28-31%) (Hematological and nutritional biochemistry reference data for persons 6 months-74 years of age: United States, 1976-80, 1982). In humans, values of TSAT < 15% indicate iron deficiency, whereas TSAT > 45% are consistent with iron overload (Hentze et al., 2010). A relatively low TSAT in conjunction with its high affinity for iron makes Tf able to efficiently buffer any alterations in plasma iron levels and to capture unshielded iron, minimizing the risk of toxicity. Above 50% the risk of the presence of toxic NTBI rises exponentially, potentially causing organ damage (Brissot et al., 2012; Patel and Ramavataram, 2012).

Non-standard approaches allowed a more specific evaluation of iron-Tf binding than the indirect clinical assay, as other biological iron ligands (such as ferritin) are isolated from the iron-Tf complex, providing interesting consideration in potential AD biomarkers. Soluble transferrin receptors (sTfR) are proteins found in the blood that are cleaved from the membrane-bound Tf receptors found on nearly all cells, and the level of serum sTfR is closely related to cellular iron demands and the erythroid proliferation rate (Speeckaert et al., 2010). Concentrations of sTfR are inversely related to iron status; sTfR elevates in response to iron deficiency and decreases in response to iron repletion. Because TfR expression is upregulated when a cell needs more iron and because sTfR is proportional to total TfR, concentrations of sTfR are increased in plasma or serum of an iron-deficient subject (Allen et al., 1998). Together, sTfR and s-F concentrations can cover the full range of iron status (Pfeiffer and Looker, 2017).To sum up, in the condition of iron overload serum iron and TSAT are increased and sTfR and Tf reduced, and vice versa in IDA.

S2. Details of Participants for CSF Iron Measurements (Ficiarà et al., 2021a)

Control group (N=14) included patients with suspected polyneuropathy (N=5), muscular dystrophy (N=1), vascular encephalopathy (N=3), multiple sclerosis (N=5). All patients underwent lumbar puncture with determination of CSF levels of Aβ42, p-Tau and t-Tau. All CSF samples were obtained early in the morning after overnight fasting by lumbar puncture using an atraumatic needle (Doherty and Forbes, 2014). CSF samples were collected in polypropylene tubes using standard sterile techniques. CSF samples were centrifuged to eliminate cells and cellular debris, and immediately

frozen at -80°C to measure orexin, t-Tau, p-Tau and Aβ42 levels. CSF Aβ42, t-Tau and p-Tau levels were determined using commercially available sandwich enzyme-linked immunosorbent assays (ELISA; Innotest b-Amyloid 1-42, Innotest h-T-tau, Innotest Phospho-T-tau 181; Fujirebio Ghent, Belgium). All the samples were analysed in duplicate. Blood samples were collected in polypropylene tubes using standard sterile techniques. Serum samples were obtained from the removal of the clot by centrifuging whole blood samples. Transferrin in serum (s-Tf) was evaluated using immunoturbidimetry optimized with polyethylene glycol (ADVIA Chemistry TRF Transferrin Reagent). Range of normality for s-Tf = [200 – 330] mg/dL.

S3. Additonal Clustering Analysis (Ficiarà et al., 2021a)

After the application of hierarchical clustering for different set of features, values of features within each cluster are reported.

a) Clustering Standard Biomarkers (SBs) (p-Tau, Aβ42);

Supplementary Table 2. Biomarkers values in each cluster using the features set SBs.

Cluster	p-Tau Mean ± sd	p-Tau Median	Aβ42 Mean ± sd	Aβ42 Median
1	(144.2±29.2)	147.8	(469.7±185.6)	432.5
2	(20.1±9.8)	18.5	(1229.0±228.5)	1165.0
3	(37.1±16.1)	36.0	(578.9±216.67)	534.0

b) Clustering SBs+ CSF iron

Supplementary Table 3. Biomarkers values in each cluster using the features set SBs and iron concentration in CSF.

Cluster	p-Tau Mean ± sd	p-Tau Median	Aβ42 Mean ± sd	Aβ42 Median	Fe CSF Mean ± sd	Fe CSF Median
1	(33.0±19.1)	25.0	(512.7±98.5)	497.0	(27.7±9.2)	28.5
2	(27.2±15.5)	24.0	(1091.2±264.5)	1081.0	(27.7±9.2)	24.9
3	(156.5±23.3)	154.2	(489.1±214.2)	473.0	(48.6±11.0)	50.0
4	(58.4 ±37.4)	43.2	(428.9±146.4)	403.0	(67.7±13.8)	65.2

c) Clustering SBs in the subpopulation

Hierarchical clustering in the subpopulation N=29, in which s-Tf is available, using set of features comprising p-Tau and Aβ. Three clusters (sizes: N=7, N=12, N=10) are emerged (Figure S1). Differences in Aβ was very significant ($p<0.001$) between clusters 1, while differences in p-Tau concentration was highly significant ($p<0.001$) between clusters 1 and 3 and clusters 1 and 3 ($p=0.005$). External scores have been evaluated for the clustering: V-measure (0.26), ARI (0.12), AMI (0.20).

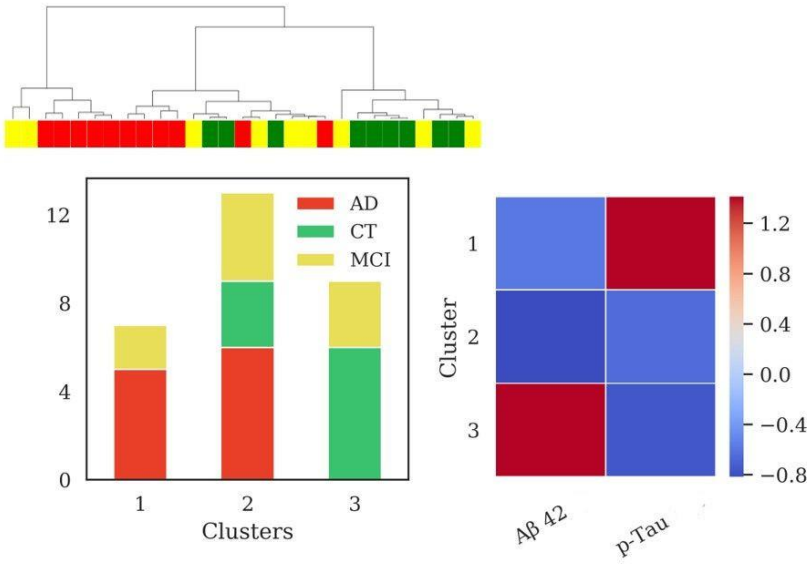

Supplementary Figure 1. Results of hierarchical clustering using standard biomarkers Aβ and p-Tau. Left: Dendrogram (yellow =MCI; red =AD; green=CT) and distribution of patients within the three clusters. Right: Heatmap using the median value of the features (Z-score unit) in each cluster. (AD= Alzheimer's Disease; CT = neurological control; MCI = Mild Cognitive Impairment).

Supplementary Table 4. Biomarkers values in each cluster using the features set SBs in the subpopulation in which s-Tf is available.

Cluster	p-Tau Mean ± sd	p-Tau Median	Aβ42 Mean ± sd	Aβ42 Median
1	(144.7±29.4)	154.0	(477.6±217.4)	392.0
2	(33.6±18.03)	27.0	(490.8±170.4)	486.0
3	(22.0±9.87)	21.0	(1272.3±246.0)	1283.0

d) Clustering SBs+ CSF iron in the subpopulation

Hierarchical clustering in the subpopulation N=29, in which s-Tf is available, using set of features comprising p-Tau, Aβ and iron concentration in CSF. The addition of iron dosage in CSF unraveled four clusters (sizes: N=5, N=9, N=6, N=9) after the application of hierarchical clustering algorithm, reported in Figure S2. The clusters composed of AD and MCI patients (cluster 3 and cluster 4) significantly differed among them for p-Tau ($p<0.001$) profile. Cluster 3 differed from cluster 2 (mainly composed of CT patients) for p-tau with high significance ($p<0.001$), while they differ from cluster 1 for iron content ($p=0.04$) and p-Tau ($p<0.001$).

The addition of CSF iron levels improved V-measure (0.40), ARI (0.25) and AMI (0.33) with respect to the same scores obtained with the biomarkers set, described in the previous section.

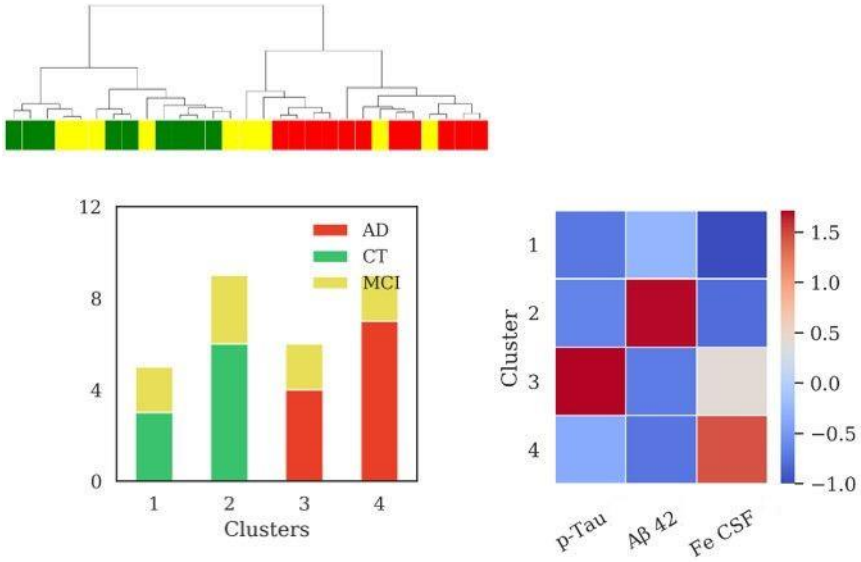

Supplementary Figure 2. Results of hierarchical clustering using biomarkers and iron concentration in CSF. Left: Dendrogram (yellow =MCI; red =AD; green=CT) and distribution of patients within the four clusters. Right: Heatmap using the median value of the features (Z-score unit) in each cluster. (AD= Alzheimer's Disease; CT = neurological control; MCI = Mild Cognitive Impairment).

Supplementary Table 5. Biomarkers values in each cluster using the features set SBs and iron concentration in CSF for the subpopulation in which s-Tf is available.

Cluster	p-Tau Mean ± sd	p-Tau Median	Aβ42 Mean ± sd	Aβ42 Median	Fe CSF Mean ± sd	Fe CSF Median
1	(19.6±5.0)	17.0	(603.4±121.1)	576.0	(25.4±8.5)	26.6
2	(22.0±9.9)	21.0.	(1272.3±246.0)	1283.0	(31.4±10.8)	30.3
3	(152.6±22.8)	154.1	(491.8±234.5)	420.0	(47.7±11.7)	47.8
4	(48.5 ±24.8)	37.3	(417.2±153.1)	406.0	(59.6±12.4)	62.6

e) Clustering SBs+ s-Tf

Supplementary Table 6. Biomarkers values in each cluster using the features set SBs and s-Tf.

Cluster	p-Tau Mean ± sd	p-Tau Median	Aβ42 Mean ± sd	Aβ42 Median	s-Tf Mean ± sd	s-Tf Median
1	(144.7±29.4)	154.0	(446.6±161.6)	392.0	(220.0±16.5)	226.0
2	(23.5±11.7)	26.0	(1334.7±275.8)	1295.5	(263.0± 25.3)	256.5
3	(39.5±18.8)	32.0	(477.6±217.4)	471.0	(247.1±18.6)	240.0
4	(19.7±4.5)	17.0	(829.14±328.84)	753.0	(201.3±14.7)	201.0

f) Clustering SBs+ s-Tf+ CSF iron

Supplementary Table 7. Biomarkers values in each cluster using full features set: SBs, CSF iron and s-Tf.

Cluster	p-Tau Mean ± sd	p-Tau Median	Aβ42 Mean ± sd	Aβ42 Median
1	(45.1±17.3)	37.3	(422.4±176.3)	449.0
2	(144.7±29.4)	154.0	(477.6±217.4)	392.0
3	(19.1±4.4)	16.5	(786.3±327.7)	729.0
4	(23.7±10.7)	25.0	(1226.3±381.6)	1283.0
Cluster	**Fe CSF Mean ± sd**	**Fe CSF Median**	**s-Tf Mean ± sd**	**s-Tf Median**
1	(57.49±9.19)	62.58	(244.14±12.73)	240.0
2	(52.9±17.46)	49.97	(220.0±16.49)	226.0
3	(31.24±12.84)	29.38	(204.88±16.97)	203.0
4	(29.94±9.88)	30.02	(266.14±24.53)	264.0

Clustering analysis (s-Tf corrected for age by means of linear regression)

In our population only s-Tf showed some significant association with age (r_s= -0.45, p=0.014, not significant Pearson's correlation) in the subpopulation including data of s-Tf (N=29 patients), and within group in CT (r=-0.68, p=0.046, not significant Spearman's test) and AD (r_s= -0.63, p=0.04, not significant Pearson's correlation). To be more accurate, we applied the correction for age for this variable using a linear regression model (p=0.03, R^2=0.15). The application of HAC using the features set comprising biomarkers and s-Tf (corrected for age) revealed four clusters (sizes: N=6, N=5, N=9, N=9), reported in Supplementary Figure 3. Significant differences among clusters were found for the p-Tau values when comparing clusters 1and 3 (p=0.004) and 1 and 4 (p<0.001); s-Tf differed between clusters 2 and 3 (p=0.003); Aβ42 was significantly different when comparing clusters 1 and 4, 2 and 4,3 and 4 (p<0.001). Clustering scores showed the following values: V-measure (0.36), ARI (0.18), AMI (0.28).

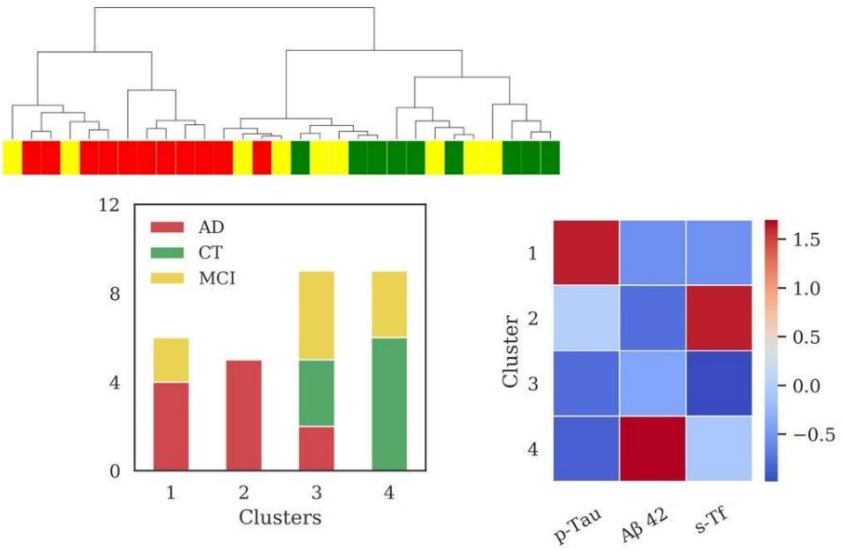

Supplementary Figure 3. Results of hierarchical clustering using biomarkers and s-Tf (corrected for age). Left: Dendrogram (yellow =MCI; red =AD; green=CT) and distribution of patients within the four clusters. Right: Heatmap using the median value of the features (Z-score unit) in each cluster. Abbreviations: AD= Alzheimer's Disease; CT = neurological control; MCI = Mild Cognitive Impairment.

Considering all the features (biomarkers, s-Tf, and iron CSF) we reported two different situations:

1. Number of resulting clusters=5 (set finding clustering step where the acceleration of distance growth is the largest). The five clusters (size: N=6, N=8, N=5, N=5, N=5), reported in Supplementary Figure 4. Significant differences among clusters were found for the p-Tau values when comparing clusters 1and 3 (p=0.01),2 and 3 (p<0.001) and 2 and 5 (p=0.04); s-Tf differed between clusters 1 and 2, and 3 and 5 (p=0.01), 2 and 5 (p<0.001) and 4 and 5 (p=0.003); Aβ42 was significantly different when comparing clusters 1 and 3(p=0.04), 1 and 4 (p=0.02),1 and 5 (p=0.002); iron CSF differed between cluster 1 and 4 (p=0.013), 2 and 4 (p=0.002), 2 and 5 (p=0.017). Clustering scores showed the following values: V-measure (0.42), ARI (0.22), AMI (0.34). The (Fe CSF/ s-Tf) ratio in cluster 1 (0.14) and cluster 2 (0.12) is lower with respect to cluster 3 (0.22), cluster 4 (0.27) and cluster 5 (0.20), in which the ratio is increased.
2. Number of clusters =4, set manually in order to better compare with our previous analysis. The four clusters (size: N=6, N=8, N=5, N=10), reported in Supplementary Figure 5. Cluster 3 and cluster 4 are composed only of AD and MCI patients. One of these clusters (cluster 4) presented a significant difference in the levels of s-Tf (p=0.004), Iron CSF (p<0.001), p-Tau (p=0.03), and Aβ42 (p=0.013) with respect to cluster 2 (mainly CT patients). Cluster 3 differed from cluster 1 (composed only by MCI and CT patients) in the biomarkers (for Aβ42 p=0.004; for p-Tau p=0.007) ad from cluster 2 for p-Tau (p<0.001). Clusters 1 and 2 significantly differed for Aβ42 (p=0.04) and for s-Tf (p=0.008). Finally, cluster 1 differed from cluster 4 for the Aβ42 and iron CSF values (p <0.001). Clustering scores showed the following values: V-measure (0.42), ARI (0.30), AMI (0.35). The (Fe CSF/ s-Tf) ratio in cluster 1 (0.14) and cluster 2 (0.12) is lower with respect to cluster 3 (0.22) and cluster 4 (0.25) in which the ratio is increased.

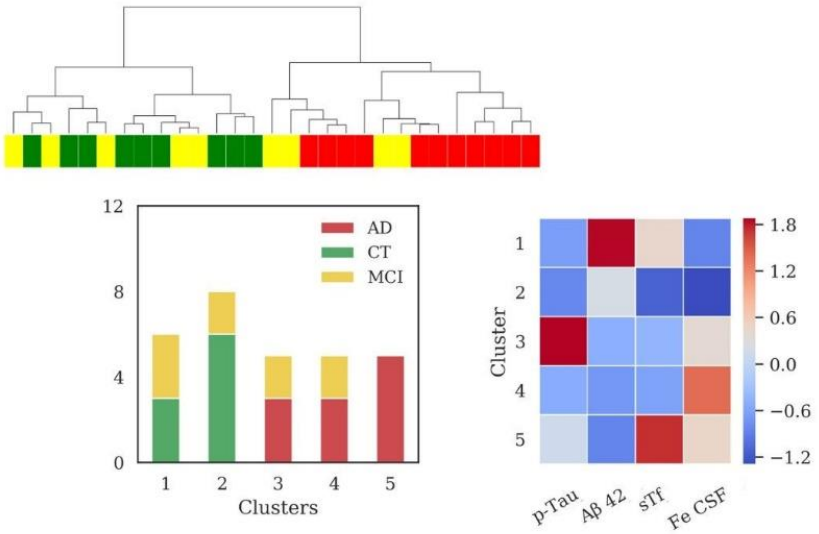

Supplementary Figure 4. Results of hierarchical clustering using biomarkers, iron CSF and s-Tf (corrected for age). Left: Dendrogram (yellow =MCI; red =AD; green=CT) and distribution of patients within the four clusters. Right: Heatmap using the median value of the features (Z-score unit) in each cluster. Abbreviations: AD= Alzheimer's Disease; CT = neurological control; MCI = Mild Cognitive Impairment

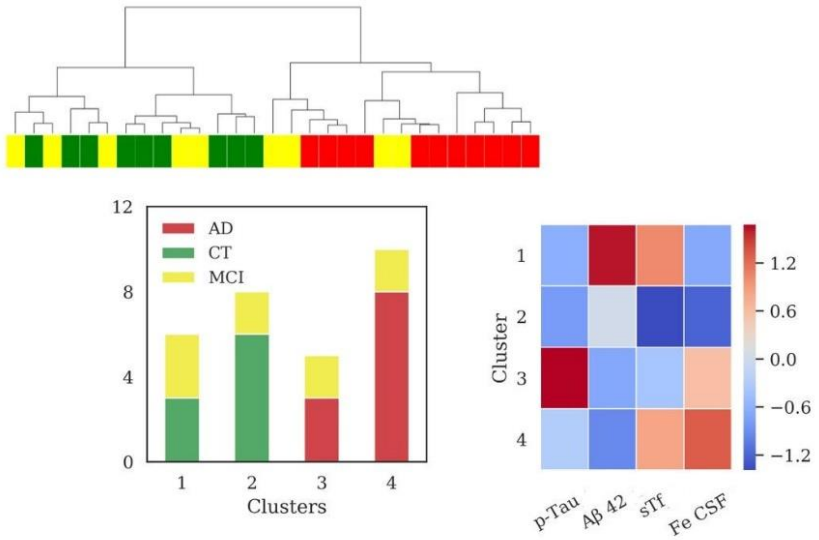

Supplementary Figure 5. Results of hierarchical clustering using biomarkers, iron CSF and s-Tf (corrected for age), setting number of clusters=4. Left: Dendrogram (yellow =MCI; red =AD; green=CT) and distribution of patients within the four clusters. Right: Heatmap using the median value of the features (Z-score unit) in each cluster. Abbreviations: AD= Alzheimer's Disease; CT = neurological control; MCI = Mild Cognitive Impairment

Description of the population of patients

Supplementary Table 8. Description of the population of patients (N=47)

	Mean	Median	Lower Quartile	Upper quartile
Aβ42CSF (pg/mL)	721.7	582.0	455.0	989.0
p-Tau CSF (pg/mL)	55.5	36.0	22.0	60.5
t-Tau CSF (pg/mL)	307.2	151.0	78.5	421.0
Fe CSF (µg/L)	41.0	37.2	23.6	53.1

Supplementary Table 9. Description of the subpopulation (in which s-Tf is available) of patients (N=29).

	Mean	Median	Lower Quartile	Upper quartile
Aβ42 CSF (pg/mL)	730.1	576.0	406.0	1059.0
p-Tau CSF (pg/mL)	56.8	31.0	21.0	69.8
t-Tau CSF (pg/mL)	322.8	151.0	77.0	426.0
Fe CSF (µg/L)	42.5	41.0	29.8	52.1
s-Tf (mg/dL)	232.8	231.0	208.0	249.0

S4. References for the Estimation of the Parameters of Mathematical Model

Supplementary Table 10. Values from literature used for the estimation of parameters used in mathematical models described in Chapter 4.

Parameter	Value	Model	Ref
Iron transported as bound to Tf to brain side	2.9 pg/cm^2 (2h)	In vitro model of microvessel endothelial cells	(Khan et al., 2018)
Iron transported as free iron to brain side	0.32 pg/cm^2 (2h)	In vitro model of microvessel endothelial cells	(Khan et al., 2018)
Iron influx into brain	83 nmol/kg·h (149 pmol/h per brain of 1.8 g)	Adult Rat	(Bradbury, 1997)
Iron efflux	131 pmol h per brain of 1.8 g	Adult Rat	(Bradbury, 1997)
Half-life of dietary iron taken up by the brain	9.4 ± 3.2 months	Male rats (Wistar)	(Chen et al., 2014)
Absolute Flux rates (microgram/body)/day	0.03-0.048	Male young adult mice	(Lopes et al., 2010)
$K_{plasma/brain}$			
Residence times in brain	16 days and longer	Male young adult mice	(Lopes et al., 2010)

Other constants values: 1-2 mg intake of dietary iron absorbed by body per day (Abbaspour et al., 2014); Lose 1-2 mg iron/day (Abbaspour et al., 2014); Volume of blood (4.5 – 5 L); Surface Area of BBB:15-25 m^2 (Wong et al., 2013).

Acknowledgements

I sincerely thank my Tutor, Prof. Caterina Guiot (Department of Neurosciences, UNITO), for guiding me in the world of research and for allowing me with her experience and availability to shed light on the projects.

I also thank Prof. Roberta Cavalli (Department of Drug Science and Technology, UNITO) and Prof. Ornella Abollino (Department of Drug Science and Technology, UNITO), for having allowed the realization of important experimental parts of my project with their availability and competence.

Thanks also to Dr. Federico D'Agata (Department of Neurosciences, UNITO), for his help in the work of data analysis, and to Dr. Silvia Boschi (Department of Neurosciences, UNITO), for the great availability in collecting patient data in the Neurology Section of the Molinette Hospital.

Thanks to Shoeb Ansari (Department of Neurosciences, UNITO), colleague who took part in this PhD program with me, for his great contribution in the experiments conducted for this thesis project.

I would also like to express my gratitude to Dr. Claudio Franchino (Department of Drug Science and Technology, UNITO), Dr. Sandro Buoso (Department of Chemistry, UNITO), for their great help in the chemical and biological experimental part; to Dr. Silvia Gazzin (FIF, Trieste), for having made possible the collaboration and the realization of the experiments in the laboratory of Italian Liver Foundation (Trieste).

References

Abbaspour, N., Hurrell, R., and Kelishadi, R. (2014). Review on iron and its importance for human health. *J Res Med Sci* 19, 164–174.

Abbott, N. J., Rönnbäck, L., and Hansson, E. (2006). Astrocyte–endothelial interactions at the blood–brain barrier. *Nature Reviews Neuroscience* 7, 41–53. doi:10.1038/nrn1824.

Aguiar, M. F. de P., Mamani, J. B., Felix, T. K., Reis, R. F. dos, Silva, H. R. da, Nucci, L. P., et al. (2017). Magnetic targeting with superparamagnetic iron oxide nanoparticles for in vivo glioma. *Nanotechnology Reviews* 6, 449–472. doi:10.1515/ntrev-2016-0101.

Ahmadi, S., Ebralidze, I. I., She, Z., and Kraatz, H.-B. (2017). Electrochemical studies of tau protein-iron interactions—Potential implications for Alzheimer's Disease. *Electrochimica Acta* 236, 384–393. doi:10.1016/j.electacta.2017.03.175.

Aisen, P. (2004). Transferrin receptor 1. *Int. J. Biochem. Cell Biol.* 36, 2137–2143. doi:10.1016/j.biocel.2004.02.007.

Aizenstein, H. J., Nebes, R. D., Saxton, J. A., Price, J. C., Mathis, C. A., Tsopelas, N. D., et al. (2008). Frequent Amyloid Deposition Without Significant Cognitive Impairment Among the Elderly. *Arch Neurol* 65, 1509–1517. doi:10.1001/archneur.65.11.1509.

Akbarzadeh, A., Samiei, M., and Davaran, S. (2012). Magnetic nanoparticles: preparation, physical properties, and applications in biomedicine. *Nanoscale Research Letters* 7, 144. doi:10.1186/1556-276X-7-144.

Alashwal, H., El Halaby, M., Crouse, J. J., Abdalla, A., and Moustafa, A. A. (2019). The Application of Unsupervised Clustering Methods to Alzheimer's Disease. *Front Comput Neurosci* 13. doi:10.3389/fncom.2019.00031.

Albert, M. S., DeKosky, S. T., Dickson, D., Dubois, B., Feldman, H. H., Fox, N. C., et al. (2011). The diagnosis of mild cognitive impairment due to Alzheimer's disease: recommendations from the National Institute on Aging-Alzheimer's Association workgroups on diagnostic guidelines for Alzheimer's disease. *Alzheimers Dement* 7, 270–279. doi:10.1016/j.jalz.2011.03.008.

Alle, H., Roth, A., and Geiger, J. R. P. (2009). Energy-Efficient Action Potentials in Hippocampal Mossy Fibers. *Science* 325, 1405–1408. doi:10.1126/science.1174331.

Allen, J., Backstrom, K. R., Cooper, J. A., Cooper, M. C., Detwiler, T. C., Essex, D. W., et al. (1998). Measurement of soluble transferrin receptor in serum of healthy adults. *Clin Chem* 44, 35–39.

Altamura, S., and Muckenthaler, M. U. (2009). Iron Toxicity in Diseases of Aging: Alzheimer's Disease, Parkinson's Disease and Atherosclerosis. *Journal of Alzheimer's Disease* 16, 879–895. doi:10.3233/JAD-2009-1010.

Andersen, H. H., Johnsen, K. B., and Moos, T. (2014). Iron deposits in the chronically inflamed central nervous system and contributes to neurodegeneration. *Cell. Mol. Life Sci.* 71, 1607–1622. doi:10.1007/s00018-013-1509-8.

Anderson, G. J., and Frazer, D. M. (2017). Current understanding of iron homeostasis. *The American Journal of Clinical Nutrition* 106, 1559S-1566S. doi:10.3945/ajcn.117.155804.

Ansari, S. A., Ficiarà, E., D'Agata, F., Cavalli, R., Nasi, L., Casoli, F., et al. (2021). Step-by-Step Design of New Theranostic Nanoformulations: Multifunctional Nanovectors for Radio-Chemo-Hyperthermic Therapy under Physical Targeting. *Molecules* 26, 4591. doi:10.3390/molecules26154591.

Ansari, S. A. M. K., Ficiarà, E., Ruffinatti, F. A., Stura, I., Argenziano, M., Abollino, O., et al. (2019). Magnetic Iron Oxide Nanoparticles: Synthesis, Characterization and Functionalization for Biomedical Applications in the Central Nervous System. *Materials (Basel)* 12. doi:10.3390/ma12030465.

Anthony, S. G., Schipper, H. M., Tavares, R., Hovanesian, V., Cortez, S. C., Stopa, E. G., et al. (2003). Stress protein expression in the Alzheimer-diseased choroid plexus. *Journal of Alzheimer's Disease* 5, 171–177. doi:10.3233/JAD-2003-5301.

Argenziano, M., Banche, G., Luganini, A., Finesso, N., Allizond, V., Gulino, G. R., et al. (2017). Vancomycin-loaded nanobubbles: A new platform for controlled antibiotic delivery against methicillin-resistant Staphylococcus aureus infections. *Int J Pharm* 523, 176–188. doi:10.1016/j.ijpharm.2017.03.033.

Arosio, P., Ingrassia, R., and Cavadini, P. (2009). Ferritins: a family of molecules for iron storage, antioxidation and more. *Biochim Biophys Acta* 1790, 589–599. doi:10.1016/j.bbagen.2008.09.004.

Arosio, P., and Levi, S. (2010). Cytosolic and mitochondrial ferritins in the regulation of cellular iron homeostasis and oxidative damage. *Biochimica et Biophysica Acta (BBA) - General Subjects* 1800, 783–792. doi:10.1016/j.bbagen.2010.02.005.

Ashraf, A. A., Dani, M., and So, P.-W. (2020a). Low Cerebrospinal Fluid Levels of Hemopexin Are Associated With Increased Alzheimer's Pathology, Hippocampal Hypometabolism, and Cognitive Decline. *Front Mol Biosci* 7, 590979. doi:10.3389/fmolb.2020.590979.

Ashraf, A., Alepuz Guillen, J. A., Aljuhani, M., Hubens, C., and So, P.-W. (2019). Low Cerebrospinal Fluid Levels of Melanotransferrin Are Associated With Conversion of Mild Cognitively Impaired Subjects to Alzheimer's Disease. *Front. Neurosci.* 13. doi:10.3389/fnins.2019.00181.

Ashraf, A., Ashton, N. J., Chatterjee, P., Goozee, K., Shen, K., Fripp, J., et al. (2020b). Plasma transferrin and hemopexin are associated with altered Aβ uptake and cognitive decline in Alzheimer's disease pathology. *Alzheimer's Research & Therapy* 12, 72. doi:10.1186/s13195-020-00634-1.

Ashraf, A., Clark, M., and So, P.-W. (2018). The Aging of Iron Man. *Front. Aging Neurosci.* 10. doi:10.3389/fnagi.2018.00065.

Ashraf, A., and So, P.-W. (2020). Spotlight on Ferroptosis: Iron-Dependent Cell Death in Alzheimer's Disease. *Front. Aging Neurosci.* 12. doi:10.3389/fnagi.2020.00196.

Ashton, N. J., Nevado-Holgado, A. J., Barber, I. S., Lynham, S., Gupta, V., Chatterjee, P., et al. (2019). A plasma protein classifier for predicting amyloid burden for preclinical Alzheimer's disease. *Science Advances* 5, eaau7220. doi:10.1126/sciadv.aau7220.

Asili, E., Yarahmadian, S., Khani, H., and Sharify, M. (2019). A Mathematical Model for Amyloid-$\boldsymbol{\beta}$ Aggregation in the Presence of Metal Ions: A Timescale Analysis for the Progress of Alzheimer Disease. *Bull Math Biol* 81, 1943–1964. doi:10.1007/s11538-019-00583-3.

Ayton, S., Diouf, I., Bush, A. I., and Alzheimer's disease Neuroimaging Initiative (2018). Evidence that iron accelerates Alzheimer's pathology: a CSF biomarker study. *J. Neurol. Neurosurg. Psychiatry* 89, 456–460. doi:10.1136/jnnp-2017-316551.

Ayton, S., Faux, N. G., and Bush, A. I. (2015). Ferritin levels in the cerebrospinal fluid predict Alzheimer's disease outcomes and are regulated by APOE. *Nature Communications* 6, 1–9. doi:10.1038/ncomms7760.

Ayton, S., Wang, Y., Diouf, I., Schneider, J. A., Brockman, J., Morris, M. C., et al. (2019). Brain iron is associated with accelerated cognitive decline in people with Alzheimer pathology. *Molecular Psychiatry*, 1–10. doi:10.1038/s41380-019-0375-7.

Badaut, J., Fukuda, A. M., Jullienne, A., and Petry, K. G. (2014). Aquaporin and brain diseases. *Biochim. Biophys. Acta* 1840, 1554–1565. doi:10.1016/j.bbagen.2013.10.032.

Badhwar, A., McFall, G. P., Sapkota, S., Black, S. E., Chertkow, H., Duchesne, S., et al. (2020). A multiomics approach to heterogeneity in Alzheimer's disease: focused review and roadmap. *Brain* 143, 1315–1331. doi:10.1093/brain/awz384.

Balusu, S., Brkic, M., Libert, C., and Vandenbroucke, R. E. (2016). The choroid plexus-cerebrospinal fluid interface in Alzheimer's disease: more than just a barrier. *Neural Regen Res* 11, 534–537. doi:10.4103/1673-5374.180372.

Baraibar, M. A., Barbeito, A. G., Muhoberac, B. B., and Vidal, R. (2008). Iron-mediated Aggregation and a Localized Structural Change Characterize Ferritin from a Mutant Light Chain Polypeptide That Causes Neurodegeneration *. *Journal of Biological Chemistry* 283, 31679–31689. doi:10.1074/jbc.M805532200.

Baraibar, M. A., Barbeito, A. G., Muhoberac, B. B., and Vidal, R. (2012). A mutant light-chain ferritin that causes neurodegeneration has enhanced propensity toward oxidative damage. *Free Radical Biology and Medicine* 52, 1692–1697. doi:10.1016/j.freeradbiomed.2012.02.015.

Bartzokis, G., Tishler, T. A., Lu, P. H., Villablanca, P., Altshuler, L. L., Carter, M., et al. (2007). Brain ferritin iron may influence age- and gender-related risks of neurodegeneration. *Neurobiol Aging* 28, 414–423. doi:10.1016/j.neurobiolaging.2006.02.005.

Bartzokis, G., Tishler, T. A., Shin, I.-S., Lu, P. H., and Cummings, J. L. (2004). Brain Ferritin Iron as a Risk Factor for Age at Onset in Neurodegenerative Diseases. *Annals of the New York Academy of Sciences* 1012, 224–236. doi:https://doi.org/10.1196/annals.1306.019.

Bascuñana, P., Brackhan, M., and Pahnke, J. (2021). Machine Learning-Supported Analyses Improve Quantitative Histological Assessments of Amyloid-β Deposits and Activated Microglia. *Journal of Alzheimer's Disease* 79, 597–605. doi:10.3233/JAD-201120.

Bassingthwaighte, J. B., Butterworth, E., Jardine, B., and Raymond, G. M. (2012). Compartmental modeling in the analysis of biological systems. *Methods Mol Biol* 929, 391–438. doi:10.1007/978-1-62703-050-2_17.

Beard, J. L., and Connor, J. R. (2003). Iron status and neural functioning. *Annu. Rev. Nutr.* 23, 41–58. doi:10.1146/annurev.nutr.23.020102.075739.

Belaidi, A. A., and Bush, A. I. (2016). Iron neurochemistry in Alzheimer's disease and Parkinson's disease: targets for therapeutics. *Journal of Neurochemistry* 139, 179–197. doi:10.1111/jnc.13425.

Benarroch, E. E. (2009). Brain iron homeostasis and neurodegenerative disease. *Neurology* 72, 1436–1440. doi:10.1212/WNL.0b013e3181a26b30.

Berdoukas, V., Coates, T. D., and Cabantchik, Z. I. (2015). Iron and oxidative stress in cardiomyopathy in thalassemia. *Free Radical Biology and Medicine* 88, 3–9. doi:10.1016/j.freeradbiomed.2015.07.019.

Bester, J., Buys, A., Lipinski, B., Kell, D. B., and Pretorius, E. (2013). High ferritin levels have major effects on the morphology of erythrocytes in Alzheimer's disease. *Front. Aging Neurosci.* 5. doi:10.3389/fnagi.2013.00088.

Bjorefeldt, A., Illes, S., Zetterberg, H., and Hanse, E. (2018). Neuromodulation via the Cerebrospinal Fluid: Insights from Recent in Vitro Studies. *Front. Neural Circuits* 12. doi:10.3389/fncir.2018.00005.

Boespflug, E. L., and Iliff, J. J. (2018). The Emerging Relationship Between Interstitial Fluid-Cerebrospinal Fluid Exchange, Amyloid-β, and Sleep. *Biol Psychiatry* 83, 328–336. doi:10.1016/j.biopsych.2017.11.031.

Bottros, M. M., and Christo, P. J. (2014). Current perspectives on intrathecal drug delivery. *J Pain Res* 7, 615–626. doi:10.2147/JPR.S37591.

Bousejra-ElGarah, F., Bijani, C., Coppel, Y., Faller, P., and Hureau, C. (2011). Iron(II) binding to amyloid-β, the Alzheimer's peptide. *Inorg Chem* 50, 9024–9030. doi:10.1021/ic201233b.

Bradbury, M. W. B. (1997). Transport of Iron in the Blood-Brain-Cerebrospinal Fluid System. *Journal of Neurochemistry* 69, 443–454. doi:10.1046/j.1471-4159.1997.69020443.x.

Bramini, M., Ye, D., Hallerbach, A., Nic Raghnaill, M., Salvati, A., Aberg, C., et al. (2014). Imaging approach to mechanistic study of nanoparticle interactions with the blood-brain barrier. *ACS Nano* 8, 4304–4312. doi:10.1021/nn5018523.

Brissot, P., Ropert, M., Le Lan, C., and Loréal, O. (2012). Non-transferrin bound iron: A key role in iron overload and iron toxicity. *Biochimica et Biophysica Acta (BBA) - General Subjects* 1820, 403–410. doi:10.1016/j.bbagen.2011.07.014.

Brooks, R. A., Vymazal, J., Goldfarb, R. B., Bulte, J. W. M., and Aisen, P. (1998). Relaxometry and magnetometry of ferritin. *Magnetic Resonance in Medicine* 40, 227–235. doi:https://doi.org/10.1002/mrm.1910400208.

Bulk, M., Abdelmoula, W. M., Nabuurs, R. J. A., van der Graaf, L. M., Mulders, C. W. H., Mulder, A. A., et al. (2018). Postmortem MRI and histology demonstrate differential iron accumulation and cortical myelin organization in early- and late-onset Alzheimer's disease. *Neurobiology of Aging* 62, 231–242. doi:10.1016/j.neurobiolaging.2017.10.017.

Burkhart, A., Skjørringe, T., Johnsen, K. B., Siupka, P., Thomsen, L. B., Nielsen, M. S., et al. (2016). Expression of Iron-Related Proteins at the Neurovascular Unit Supports Reduction and Reoxidation of Iron for Transport Through the Blood-Brain Barrier. *Mol Neurobiol* 53, 7237–7253. doi:10.1007/s12035-015-9582-7.

Bush, A. I., and Curtain, C. C. (2008). Twenty years of metallo-neurobiology: where to now? *Eur Biophys J* 37, 241–245. doi:10.1007/s00249-007-0228-1.

Cabantchik, Z. I. (2014). Labile iron in cells and body fluids: physiology, pathology, and pharmacology. *Front Pharmacol* 5, 45. doi:10.3389/fphar.2014.00045.

Camaschella, C., Roetto, A., Calì, A., De Gobbi, M., Garozzo, G., Carella, M., et al. (2000). The gene TFR2 is mutated in a new type of haemochromatosis mapping to 7q22. *Nat. Genet.* 25, 14–15. doi:10.1038/75534.

Cao, J. Y., and Dixon, S. J. (2016). Mechanisms of ferroptosis. *Cell. Mol. Life Sci.* 73, 2195–2209. doi:10.1007/s00018-016-2194-1.

Cardoso, V. F., Francesko, A., Ribeiro, C., Bañobre-López, M., Martins, P., and Lanceros-Mendez, S. (2018). Advances in Magnetic Nanoparticles for Biomedical Applications. *Advanced Healthcare Materials* 7, 1700845. doi:https://doi.org/10.1002/adhm.201700845.

Carro, E., Bartolomé, F., Bermejo-Pareja, F., Villarejo-Galende, A., Molina, J. A., Ortiz, P., et al. (2017). Early diagnosis of mild cognitive impairment and Alzheimer's disease based on salivary lactoferrin. *Alzheimers Dement (Amst)* 8, 131–138. doi:10.1016/j.dadm.2017.04.002.

Cavalli, R., Argenziano, M., Vigna, E., Giustetto, P., Torres, E., Aime, S., et al. (2015). Preparation and in vitro characterization of chitosan nanobubbles as theranostic agents. *Colloids Surf B Biointerfaces* 129, 39–46. doi:10.1016/j.colsurfb.2015.03.023.

Cavalli, R., Bisazza, A., Trotta, M., Argenziano, M., Civra, A., Donalisio, M., et al. (2012). New chitosan nanobubbles for ultrasound-mediated gene delivery: preparation and in vitro characterization. *Int J Nanomedicine* 7, 3309–3318. doi:10.2147/IJN.S30912.

Cavalli, R., Soster, M., and Argenziano, M. (2016). Nanobubbles: a promising efficient tool for therapeutic delivery. *Ther Deliv* 7, 117–138. doi:10.4155/tde.15.92.

Chalbot, S., Zetterberg, H., Blennow, K., Fladby, T., Andreasen, N., Grundke-Iqbal, I., et al. (2011). Blood-cerebrospinal fluid barrier permeability in Alzheimer's disease. *J. Alzheimers Dis.* 25, 505–515. doi:10.3233/JAD-2011-101959.

Chang, D., Lim, M., Goos, J. A. C. M., Qiao, R., Ng, Y. Y., Mansfeld, F. M., et al. (2018). Biologically Targeted Magnetic Hyperthermia: Potential and Limitations. *Front Pharmacol* 9. doi:10.3389/fphar.2018.00831.

Chasteen, N. D., and Harrison, P. M. (1999). Mineralization in Ferritin: An Efficient Means of Iron Storage. *Journal of Structural Biology* 126, 182–194. doi:10.1006/jsbi.1999.4118.

Chen, H., Attieh, Z. K., Su, T., Syed, B. A., Gao, H., Alaeddine, R. M., et al. (2004). Hephaestin is a ferroxidase that maintains partial activity in sex-linked anemia mice. *Blood* 103, 3933–3939. doi:10.1182/blood-2003-09-3139.

Chen, J.-H., Singh, N., Tay, H., and Walczyk, T. (2014). Imbalance of iron influx and efflux causes brain iron accumulation over time in the healthy adult rat. *Metallomics* 6, 1417–1426. doi:10.1039/c4mt00054d.

Chen, P., Miah, M. R., and Aschner, M. (2016). Metals and Neurodegeneration. *F1000Res* 5. doi:10.12688/f1000research.7431.1.

Chertok, B., David, A. E., and Yang, V. C. (2011). Brain tumor targeting of magnetic nanoparticles for potential drug delivery: effect of administration route and magnetic field topography. *J Control Release* 155, 393–399. doi:10.1016/j.jconrel.2011.06.033.

Cherubini, A., Caligiuri, M. E., Péran, P., Sabatini, U., Cosentino, C., and Amato, F. (2016). Importance of Multimodal MRI in Characterizing Brain Tissue and Its Potential Application for Individual Age Prediction. *IEEE Journal of Biomedical and Health Informatics* 20, 1232–1239. doi:10.1109/JBHI.2016.2559938.

Cho, S., Wood, A., and Bowlby, M. R. (2007). Brain Slices as Models for Neurodegenerative Disease and Screening Platforms to Identify Novel Therapeutics. *Current Neuropharmacology* 5, 19–33. doi:10.2174/157015907780077105.

Choroid plexus, aging of the brain, and Alzheimer's disease. - PubMed - NCBI Available at: https://www.ncbi.nlm.nih.gov/pubmed/12700093 [Accessed April 22, 2020].

Choroid Plexus Blood-CSF Barrier: Major Player in Brain Disease Modeling and Neuromedicine Available at: https://www.jneurology.com/articles/choroid-plexus-bloodcsf-barrier-major-player-in-brain-disease-modeling-and-neuromedicine.html [Accessed April 22, 2020].

Cicero, C. E., Mostile, G., Vasta, R., Rapisarda, V., Signorelli, S. S., Ferrante, M., et al. (2017). Metals and neurodegenerative diseases. A systematic review. *Environ. Res.* 159, 82–94. doi:10.1016/j.envres.2017.07.048.

Coates, T. D. (2014). Physiology and pathophysiology of iron in hemoglobin-associated diseases. *Free Radical Biology and Medicine* 72, 23–40. doi:10.1016/j.freeradbiomed.2014.03.039.

Coates, T. D., Carson, S., Wood, J. C., and Berdoukas, V. (2016). Management of iron overload in hemoglobinopathies: what is the appropriate target iron level? *Ann. N. Y. Acad. Sci.* 1368, 95–106. doi:10.1111/nyas.13060.

Coccini, T., Caloni, F., Ramírez Cando, L. J., and De Simone, U. (2017). Cytotoxicity and proliferative capacity impairment induced on human brain cell cultures after short- and long-term exposure to magnetite nanoparticles. *J Appl Toxicol* 37, 361–373. doi:10.1002/jat.3367.

Codazzi, F., Pelizzoni, I., Zacchetti, D., and Grohovaz, F. (2015). Iron entry in neurons and astrocytes: a link with synaptic activity. *Front. Mol. Neurosci.* 8. doi:10.3389/fnmol.2015.00018.

Cohen, L. A., Gutierrez, L., Weiss, A., Leichtmann-Bardoogo, Y., Zhang, D., Crooks, D. R., et al. (2010). Serum ferritin is derived primarily from macrophages through a nonclassical secretory pathway. *Blood* 116, 1574–1584. doi:10.1182/blood-2009-11-253815.

Conde, J. R., and Streit, W. J. (2006). Microglia in the Aging Brain. *Journal of Neuropathology & Experimental Neurology* 65, 199–203. doi:10.1097/01.jnen.0000202887.22082.63.

Connor, J. R., Duck, K., Patton, S., Simpson, I. A., Trotti, L. M., Allen, R., et al. (2020). Evidence for communication of peripheral iron status to cerebrospinal fluid: clinical implications for therapeutic strategy. *Fluids and Barriers of the CNS* 17, 28. doi:10.1186/s12987-020-00190-8.

Connor, J. R., Snyder, B. S., Beard, J. L., Fine, R. E., and Mufson, E. J. (1992). Regional distribution of iron and iron-regulatory proteins in the brain in aging and Alzheimer's disease. *J. Neurosci. Res.* 31, 327–335. doi:10.1002/jnr.490310214.

Cortes, C., and Vapnik, V. (1995). Support-vector networks. *Mach Learn* 20, 273–297. doi:10.1007/BF00994018.

Costa, C., Brandão, F., Bessa, M. J., Costa, S., Valdiglesias, V., Kiliç, G., et al. (2016). In vitro cytotoxicity of superparamagnetic iron oxide nanoparticles on neuronal and glial cells. Evaluation of nanoparticle interference with viability tests. *Journal of Applied Toxicology* 36, 361–372. doi:https://doi.org/10.1002/jat.3213.

D'Agata, F., Ruffinatti, F. A., Boschi, S., Stura, I., Rainero, I., Abollino, O., et al. (2017). Magnetic Nanoparticles in the Central Nervous System: Targeting Principles, Applications and Safety Issues. *Molecules* 23. doi:10.3390/molecules23010009.

Dal Ben, M., Bongiovanni, R., Tuniz, S., Fioriti, E., Tiribelli, C., Moretti, R., et al. (2019). Earliest Mechanisms of Dopaminergic Neurons Sufferance in a Novel Slow Progressing Ex Vivo Model of Parkinson Disease in Rat Organotypic Cultures of Substantia Nigra. *International Journal of Molecular Sciences* 20, 2224. doi:10.3390/ijms20092224.

Dal Ben, M., Bottin, C., Zanconati, F., Tiribelli, C., and Gazzin, S. (2017). Evaluation of region selective bilirubin-induced brain damage as a basis for a pharmacological treatment. *Sci Rep* 7, 41032. doi:10.1038/srep41032.

Darshan, D., Frazer, D. M., and Anderson, G. J. (2010). Molecular basis of iron-loading disorders. *Expert Reviews in Molecular Medicine* 12. doi:10.1017/S1462399410001687.

Dautry-Varsat, A., Ciechanover, A., and Lodish, H. F. (1983). pH and the recycling of transferrin during receptor-mediated endocytosis. *Proc Natl Acad Sci U S A* 80, 2258–2262.

David, A. W. (2017). Computational Modelling of Magnetic Nanoparticle Properties and In Vivo Responses. *Current Medicinal Chemistry* 24, 483–496.

De Domenico, I., McVey Ward, D., and Kaplan, J. (2008). Regulation of iron acquisition and storage: consequences for iron-linked disorders. *Nature Reviews Molecular Cell Biology* 9, 72–81. doi:10.1038/nrm2295.

De Domenico, I., Ward, D. M., and Kaplan, J. (2009). Specific iron chelators determine the route of ferritin degradation. *Blood* 114, 4546–4551. doi:10.1182/blood-2009-05-224188.

de Lange, E. C. M. (2004). Potential role of ABC transporters as a detoxification system at the blood–CSF barrier. *Advanced Drug Delivery Reviews* 56, 1793–1809. doi:10.1016/j.addr.2004.07.009.

De Simone, U., Roccio, M., Gribaldo, L., Spinillo, A., Caloni, F., and Coccini, T. (2018). Human 3D Cultures as Models for Evaluating Magnetic Nanoparticle CNS Cytotoxicity after Short- and Repeated Long-Term Exposure. *International Journal of Molecular Sciences* 19, 1993. doi:10.3390/ijms19071993.

Decuzzi, P., Godin, B., Tanaka, T., Lee, S.-Y., Chiappini, C., Liu, X., et al. (2010). Size and shape effects in the biodistribution of intravascularly injected particles. *J Control Release* 141, 320–327. doi:10.1016/j.jconrel.2009.10.014.

Deng, X., Vidal, R., and Englander, E. W. (2010). Accumulation of oxidative DNA damage in brain mitochondria in mouse model of hereditary ferritinopathy. *Neuroscience Letters* 479, 44–48. doi:10.1016/j.neulet.2010.05.025.

Devi, G., and Scheltens, P. (2018). Heterogeneity of Alzheimer's disease: consequence for drug trials? *Alzheimer's Research & Therapy* 10, 122. doi:10.1186/s13195-018-0455-y.

Devos, D., Moreau, C., Kyheng, M., Garçon, G., Rolland, A. S., Blasco, H., et al. (2019). A ferroptosis–based panel of prognostic biomarkers for Amyotrophic Lateral Sclerosis. *Scientific Reports* 9, 2918. doi:10.1038/s41598-019-39739-5.

Di Fede, G., Catania, M., Maderna, E., Ghidoni, R., Benussi, L., Tonoli, E., et al. (2018). Molecular subtypes of Alzheimer's disease. *Sci Rep* 8, 3269. doi:10.1038/s41598-018-21641-1.

Ding, B., Chen, K.-M., Ling, H.-W., Sun, F., Li, X., Wan, T., et al. (2009). Correlation of iron in the hippocampus with MMSE in patients with Alzheimer's disease. *J Magn Reson Imaging* 29, 793–798. doi:10.1002/jmri.21730.

Diouf, I., Bush, A. I., and Ayton, S. (2020). Cerebrospinal fluid ceruloplasmin levels predict cognitive decline and brain atrophy in people with underlying β-amyloid pathology. *Neurobiology of Disease* 139, 104810. doi:10.1016/j.nbd.2020.104810.

Dixon, S. J., Lemberg, K. M., Lamprecht, M. R., Skouta, R., Zaitsev, E. M., Gleason, C. E., et al. (2012). Ferroptosis: An Iron-Dependent Form of Nonapoptotic Cell Death. *Cell* 149, 1060–1072. doi:10.1016/j.cell.2012.03.042.

Dixon, S. J., and Stockwell, B. R. (2014). The role of iron and reactive oxygen species in cell death. *Nature Chemical Biology* 10, 9–17. doi:10.1038/nchembio.1416.

Dixon, S. J., and Stockwell, B. R. (2019). The Hallmarks of Ferroptosis. *Annu. Rev. Cancer Biol.* 3, 35–54. doi:10.1146/annurev-cancerbio-030518-055844.

Dobrovolskaia, M. A., Aggarwal, P., Hall, J. B., and McNeil, S. E. (2008a). Preclinical Studies To Understand Nanoparticle Interaction with the Immune System and Its Potential Effects on Nanoparticle Biodistribution. *Mol Pharm* 5, 487–495. doi:10.1021/mp800032f.

Dobrovolskaia, M. A., Clogston, J. D., Neun, B. W., Hall, J. B., Patri, A. K., and McNeil, S. E. (2008b). Method for Analysis of Nanoparticle Hemolytic Properties In Vitro. *Nano Lett* 8, 2180–2187. doi:10.1021/nl0805615.

Doherty, C. M., and Forbes, R. B. (2014). Diagnostic Lumbar Puncture. *Ulster Med J* 83, 93–102.

Dormann, C. F., Elith, J., Bacher, S., Buchmann, C., Carl, G., Carré, G., et al. (2013). Collinearity: a review of methods to deal with it and a simulation study evaluating their performance. *Ecography* 36, 27–46. doi:10.1111/j.1600-0587.2012.07348.x.

Dringen, R., Bishop, G. M., Koeppe, M., Dang, T. N., and Robinson, S. R. (2007). The Pivotal Role of Astrocytes in the Metabolism of Iron in the Brain. *Neurochem Res* 32, 1884–1890. doi:10.1007/s11064-007-9375-0.

Driscoll, I., and Troncoso, J. (2011). Asymptomatic Alzheimer's Disease: A Prodrome or a State of Resilience? *Curr Alzheimer Res* 8, 330–335.

Dubois, B., Feldman, H. H., Jacova, C., Cummings, J. L., Dekosky, S. T., Barberger-Gateau, P., et al. (2010). Revising the definition of Alzheimer's disease: a new lexicon. *Lancet Neurol* 9, 1118–1127. doi:10.1016/S1474-4422(10)70223-4.

Dubois, B., Feldman, H. H., Jacova, C., Dekosky, S. T., Barberger-Gateau, P., Cummings, J., et al. (2007). Research criteria for the diagnosis of Alzheimer's disease: revising the NINCDS-ADRDA criteria. *Lancet Neurol* 6, 734–746. doi:10.1016/S1474-4422(07)70178-3.

Duce, J. A., and Bush, A. I. (2010). Biological metals and Alzheimer's disease: implications for therapeutics and diagnostics. *Prog. Neurobiol.* 92, 1–18. doi:10.1016/j.pneurobio.2010.04.003.

Duce, J. A., Tsatsanis, A., Cater, M. A., James, S. A., Robb, E., Wikhe, K., et al. (2010). Iron-export ferroxidase activity of β-amyloid precursor protein is inhibited by zinc in Alzheimer's disease. *Cell* 142, 857–867. doi:10.1016/j.cell.2010.08.014.

Duck, K. A., and Connor, J. R. (2016). Iron uptake and transport across physiological barriers. *Biometals* 29, 573–591. doi:10.1007/s10534-016-9952-2.

Dusek, P., Dezortova, M., and Wuerfel, J. (2013). Imaging of iron. *Int. Rev. Neurobiol.* 110, 195–239. doi:10.1016/B978-0-12-410502-7.00010-7.

Dusek, P., and Schneider, S. A. (2012). Neurodegeneration with brain iron accumulation. *Current Opinion in Neurology* 25, 499–506. doi:10.1097/WCO.0b013e3283550cac.

Dusek, P., Schneider, S. A., and Aaseth, J. (2016). Iron chelation in the treatment of neurodegenerative diseases. *J Trace Elem Med Biol* 38, 81–92. doi:10.1016/j.jtemb.2016.03.010.

Eid, R., Arab, N. T. T., and Greenwood, M. T. (2017). Iron mediated toxicity and programmed cell death: A review and a re-examination of existing paradigms. *Biochimica et Biophysica Acta (BBA) - Molecular Cell Research* 1864, 399–430. doi:10.1016/j.bbamcr.2016.12.002.

Elin, R. J., Wolff, S. M., and Finch, C. A. (1977). Effect of induced fever on serum iron and ferritin concentrations in man. *Blood* 49, 147–153.

Evstatiev, R., and Gasche, C. (2012). Iron sensing and signalling. *Gut* 61, 933–952. doi:10.1136/gut.2010.214312.

Fagan, A. M., and Perrin, R. J. (2012). Upcoming candidate cerebrospinal fluid biomarkers of Alzheimer's disease. *Biomark Med* 6, 455–476. doi:10.2217/bmm.12.42.

Fagan, A. M., Roe, C. M., Xiong, C., Mintun, M. A., Morris, J. C., and Holtzman, D. M. (2007). Cerebrospinal fluid tau/beta-amyloid(42) ratio as a prediction of cognitive decline in nondemented older adults. *Arch. Neurol.* 64, 343–349. doi:10.1001/archneur.64.3.noc60123.

Falconieri, A., De Vincentiis, S., and Raffa, V. (2019). Recent advances in the use of magnetic nanoparticles to promote neuroregeneration. *Nanomedicine (Lond)* 14, 1073–1076. doi:10.2217/nnm-2019-0103.

Falkowska, A., Gutowska, I., Goschorska, M., Nowacki, P., Chlubek, D., and Baranowska-Bosiacka, I. (2015). Energy Metabolism of the Brain, Including the Cooperation between Astrocytes and Neurons, Especially in the Context of Glycogen Metabolism. *International Journal of Molecular Sciences* 16, 25959–25981. doi:10.3390/ijms161125939.

Faux, N. G., Rembach, A., Wiley, J., Ellis, K. A., Ames, D., Fowler, C. J., et al. (2014). An anemia of Alzheimer's disease. *Molecular Psychiatry* 19, 1227–1234. doi:10.1038/mp.2013.178.

Feng, H., Schorpp, K., Jin, J., Yozwiak, C. E., Hoffstrom, B. G., Decker, A. M., et al. (2020). Transferrin Receptor Is a Specific Ferroptosis Marker. *Cell Reports* 30, 3411-3423.e7. doi:10.1016/j.celrep.2020.02.049.

Fiandaca, M. S., Mapstone, M. E., Cheema, A. K., and Federoff, H. J. (2014). The critical need for defining preclinical biomarkers in Alzheimer's disease. *Alzheimers Dement* 10, S196-212. doi:10.1016/j.jalz.2014.04.015.

Ficiarà, E., Ansari, S. A., Argenziano, M., Cangemi, L., Monge, C., Cavalli, R., et al. (2020a). Beyond Oncological Hyperthermia: Physically Drivable Magnetic Nanobubbles as Novel

Multipurpose Theranostic Carriers in the Central Nervous System. *Molecules* 25, 2104. doi:10.3390/molecules25092104.

Ficiarà, E., Boschi, S., Ansari, S., D'Agata, F., Abollino, O., Caroppo, P., et al. (2021a). Machine Learning Profiling of Alzheimer's Disease Patients Based on Current Cerebrospinal Fluid Markers and Iron Content in Biofluids. *Front. Aging Neurosci.* 13. doi:10.3389/fnagi.2021.607858.

Ficiarà, E., D'Agata, F., Ansari, S., Boschi, S., Rainero, I., Priano, L., et al. (2020b). A mathematical model for the evaluation of iron transport across the blood-cerebrospinal fluid barrier in neurodegenerative diseases. in *2020 42nd Annual International Conference of the IEEE Engineering in Medicine Biology Society (EMBC)*, 2270–2273. doi:10.1109/EMBC44109.2020.9175988.

Ficiarà, E., D'Agata, F., Cattaldo, S., Priano, L., Mauro, A., and Guiot, C. (2021b). A Compartmental Model for the Iron Trafficking Across the Blood-Brain Barriers in Neurodegenerative Diseases. in *2021 43rd Annual International Conference of the IEEE Engineering in Medicine Biology Society (EMBC)*, 4200–4203. doi:10.1109/EMBC46164.2021.9629893.

Ficiarà, E., Munir, Z., Boschi, S., Caligiuri, M. E., and Guiot, C. (2021c). Alteration of Iron Concentration in Alzheimer's Disease as a Possible Diagnostic Biomarker Unveiling Ferroptosis. *International Journal of Molecular Sciences* 22, 4479. doi:10.3390/ijms22094479.

Fischer, H. P. (2008). Mathematical Modeling of Complex Biological Systems. *Alcohol Res Health* 31, 49–59.

Fischer, P., Götz, M. E., Danielczyk, W., Gsell, W., and Riederer, P. (1997). Blood transferrin and ferritin in Alzheimer's disease. *Life Sci.* 60, 2273–2278. doi:10.1016/s0024-3205(97)00282-8.

Friedmann Angeli, J. P., Schneider, M., Proneth, B., Tyurina, Y. Y., Tyurin, V. A., Hammond, V. J., et al. (2014). Inactivation of the ferroptosis regulator Gpx4 triggers acute renal failure in mice. *Nature Cell Biology* 16, 1180–1191. doi:10.1038/ncb3064.

Futakawa, S., Nara, K., Miyajima, M., Kuno, A., Ito, H., Kaji, H., et al. (2012). A unique N-glycan on human transferrin in CSF: a possible biomarker for iNPH. *Neurobiology of Aging* 33, 1807–1815. doi:10.1016/j.neurobiolaging.2011.02.023.

Ganz, T. (2005). Cellular iron: ferroportin is the only way out. *Cell Metab.* 1, 155–157. doi:10.1016/j.cmet.2005.02.005.

Gao, M., Monian, P., Quadri, N., Ramasamy, R., and Jiang, X. (2015). Glutaminolysis and Transferrin Regulate Ferroptosis. *Molecular Cell* 59, 298–308. doi:10.1016/j.molcel.2015.06.011.

Garbowski, M. W., Ma, Y., Fucharoen, S., Srichairatanakool, S., Hider, R., and Porter, J. B. (2016). Clinical and methodological factors affecting non-transferrin-bound iron values using a novel fluorescent bead assay. *Translational Research* 177, 19-30.e5. doi:10.1016/j.trsl.2016.05.005.

Garcia-Casal, M. N., Pasricha, S.-R., Martinez, R. X., Lopez-Perez, L., and Peña-Rosas, J. P. (2015). Serum or plasma ferritin concentration as an index of iron deficiency and overload. *Cochrane Database of Systematic Reviews*. doi:10.1002/14651858.CD011817.

Garcia-Casal, M. N., Peña-Rosas, J. P., Urrechaga, E., Escanero, J. F., Huo, J., Martinez, R. X., et al. (2018). Performance and comparability of laboratory methods for measuring ferritin concentrations in human serum or plasma: A systematic review and meta-analysis. *PLoS One* 13. doi:10.1371/journal.pone.0196576.

Ghazanfari, M. R., Kashefi, M., Shams, S. F., and Jaafari, M. R. (2016). Perspective of Fe3O4 Nanoparticles Role in Biomedical Applications. *Biochemistry Research International* 2016, e7840161. doi:10.1155/2016/7840161.

Giambattistelli, F., Bucossi, S., Salustri, C., Panetta, V., Mariani, S., Siotto, M., et al. (2012). Effects of hemochromatosis and transferrin gene mutations on iron dyshomeostasis, liver dysfunction and on the risk of Alzheimer's disease. *Neurobiol. Aging* 33, 1633–1641. doi:10.1016/j.neurobiolaging.2011.03.005.

Gkouvatsos, K., Papanikolaou, G., and Pantopoulos, K. (2012). Regulation of iron transport and the role of transferrin. *Biochimica et Biophysica Acta (BBA) - General Subjects* 1820, 188–202. doi:10.1016/j.bbagen.2011.10.013.

Gong, N.-J., Dibb, R., Bulk, M., van der Weerd, L., and Liu, C. (2019). Imaging beta amyloid aggregation and iron accumulation in Alzheimer's disease using quantitative susceptibility mapping MRI. *Neuroimage* 191, 176–185. doi:10.1016/j.neuroimage.2019.02.019.

González-Domínguez, R., García-Barrera, T., and Gómez-Ariza, J. L. (2014). Characterization of metal profiles in serum during the progression of Alzheimer's disease. *Metallomics* 6, 292–300. doi:10.1039/c3mt00301a.

González-Sánchez, M., Bartolome, F., Antequera, D., Puertas-Martín, V., González, P., Gómez-Grande, A., et al. (2020). Decreased salivary lactoferrin levels are specific to Alzheimer's disease. *EBioMedicine* 57. doi:10.1016/j.ebiom.2020.102834.

Goozee, K., Chatterjee, P., James, I., Shen, K., Sohrabi, H. R., Asih, P. R., et al. (2018). Elevated plasma ferritin in elderly individuals with high neocortical amyloid-β load. *Molecular Psychiatry* 23, 1807–1812. doi:10.1038/mp.2017.146.

Gozzelino, R., and Arosio, P. (2016). Iron Homeostasis in Health and Disease. *International Journal of Molecular Sciences* 17, 130. doi:10.3390/ijms17010130.

Greene, B. T., Thorburn, J., Willingham, M. C., Thorburn, A., Planalp, R. P., Brechbiel, M. W., et al. (2002). Activation of caspase pathways during iron chelator-mediated apoptosis. *J. Biol. Chem.* 277, 25568–25575. doi:10.1074/jbc.M110345200.

Guan, J., Wang, P., Lu, L., and Zhao, G. (2020). Association of Plasma Transferrin With Cognitive Decline in Patients With Mild Cognitive Impairment and Alzheimer's Disease. *Front. Aging Neurosci.* 12. doi:10.3389/fnagi.2020.00038.

Guiot, C., Zullino, S., Priano, L., and Cavalli, R. (2016). The physics of drug-delivery across the blood-brain barrier. *Ther Deliv* 7, 153–156. doi:10.4155/tde-2016-0001.

Gulec, S., Anderson, G. J., and Collins, J. F. (2014). Mechanistic and regulatory aspects of intestinal iron absorption. *American Journal of Physiology-Gastrointestinal and Liver Physiology* 307, G397–G409. doi:10.1152/ajpgi.00348.2013.

Gunshin, H., Mackenzie, B., Berger, U. V., Gunshin, Y., Romero, M. F., Boron, W. F., et al. (1997). Cloning and characterization of a mammalian proton-coupled metal-ion transporter. *Nature* 388, 482–488. doi:10.1038/41343.

Guo, C., Wang, P., Zhong, M.-L., Wang, T., Huang, X.-S., Li, J.-Y., et al. (2013a). Deferoxamine inhibits iron induced hippocampal tau phosphorylation in the Alzheimer transgenic mouse brain. *Neurochem. Int.* 62, 165–172. doi:10.1016/j.neuint.2012.12.005.

Guo, C., Wang, T., Zheng, W., Shan, Z.-Y., Teng, W.-P., and Wang, Z.-Y. (2013b). Intranasal deferoxamine reverses iron-induced memory deficits and inhibits amyloidogenic APP processing in a transgenic mouse model of Alzheimer's disease. *Neurobiol. Aging* 34, 562–575. doi:10.1016/j.neurobiolaging.2012.05.009.

Haacke, E. M., Cheng, N. Y. C., House, M. J., Liu, Q., Neelavalli, J., Ogg, R. J., et al. (2005). Imaging iron stores in the brain using magnetic resonance imaging. *Magnetic Resonance Imaging* 23, 1–25. doi:10.1016/j.mri.2004.10.001.

Hadzhieva, M., Kirches, E., and Mawrin, C. (2014). Review: iron metabolism and the role of iron in neurodegenerative disorders. *Neuropathol. Appl. Neurobiol.* 40, 240–257. doi:10.1111/nan.12096.

Hallgren, B., and Sourander, P. (1958). The Effect of Age on the Non-Haemin Iron in the Human Brain. *Journal of Neurochemistry* 3, 41–51. doi:https://doi.org/10.1111/j.1471-4159.1958.tb12607.x.

Hambright, W. S., Fonseca, R. S., Chen, L., Na, R., and Ran, Q. (2017). Ablation of ferroptosis regulator glutathione peroxidase 4 in forebrain neurons promotes cognitive impairment and neurodegeneration. *Redox Biology* 12, 8–17. doi:10.1016/j.redox.2017.01.021.

Hare, D., Ayton, S., Bush, A., and Lei, P. (2013a). A delicate balance: Iron metabolism and diseases of the brain. *Front Aging Neurosci* 5, 34. doi:10.3389/fnagi.2013.00034.

Hare, D. J., Adlard, P. A., Doble, P. A., and Finkelstein, D. I. (2013b). Metallobiology of 1-methyl-4-phenyl-1,2,3,6-tetrahydropyridine neurotoxicity. *Metallomics* 5, 91–109. doi:10.1039/c2mt20164j.

Hare, D. J., Doecke, J. D., Faux, N. G., Rembach, A., Volitakis, I., Fowler, C. J., et al. (2015). Decreased Plasma Iron in Alzheimer's Disease Is Due to Transferrin Desaturation. *ACS Chem. Neurosci.* 6, 398–402. doi:10.1021/cn5003557.

Hauert, S., and Bhatia, S. N. (2014). Mechanisms of cooperation in cancer nanomedicine: towards systems nanotechnology. *Trends Biotechnol* 32, 448–455. doi:10.1016/j.tibtech.2014.06.010.

Healy, S., McMahon, J. M., and FitzGerald, U. (2017). Modelling iron mismanagement in neurodegenerative disease in vitro: paradigms, pitfalls, possibilities & practical considerations. *Progress in Neurobiology* 158, 1–14. doi:10.1016/j.pneurobio.2017.08.004.

Hematological and nutritional biochemistry reference data for persons 6 months-74 years of age: United States, 1976-80 (1982). *Vital Health Stat 11*, i–vi, 1–173.

Henry, M. S., Passmore, A. P., Todd, S., McGuinness, B., Craig, D., and Johnston, J. A. (2013). The development of effective biomarkers for Alzheimer's disease: a review. *International Journal of Geriatric Psychiatry* 28, 331–340. doi:10.1002/gps.3829.

Hentze, M. W., Muckenthaler, M. U., and Andrews, N. C. (2004). Balancing acts: molecular control of mammalian iron metabolism. *Cell* 117, 285–297. doi:10.1016/s0092-8674(04)00343-5.

Hentze, M. W., Muckenthaler, M. U., Galy, B., and Camaschella, C. (2010). Two to Tango: Regulation of Mammalian Iron Metabolism. *Cell* 142, 24–38. doi:10.1016/j.cell.2010.06.028.

Herman, J., and Usher, W. (2017). SALib: An open-source Python library for Sensitivity Analysis. *Journal of Open Source Software* 2, 97. doi:10.21105/joss.00097.

Hider, R. C. (2002). Nature of nontransferrin-bound iron. *European Journal of Clinical Investigation* 32, 50–54. doi:https://doi.org/10.1046/j.1365-2362.2002.0320s1050.x.

Holcomb, L., Gordon, M. N., McGowan, E., Yu, X., Benkovic, S., Jantzen, P., et al. (1998). Accelerated Alzheimer-type phenotype in transgenic mice carrying both mutant amyloid precursor protein and presenilin 1 transgenes. *Nature Medicine* 4, 97–100. doi:10.1038/nm0198-097.

Holland, D., Brewer, J. B., Hagler, D. J., Fennema-Notestine, C., Dale, A. M., and Initiative, the A. D. N. (2009). Subregional neuroanatomical change as a biomarker for Alzheimer's disease. *PNAS* 106, 20954–20959. doi:10.1073/pnas.0906053106.

Holmes-Hampton, G. P., Chakrabarti, M., Cockrell, A. L., McCormick, S. P., Abbott, L. C., Lindahl, L. S., et al. (2012). Changing iron content of the mouse brain during development. *Metallomics.* 4, 761–770. doi:10.1039/c2mt20086d.

Horowitz, M. P., and Greenamyre, J. T. (2010). Mitochondrial iron metabolism and its role in neurodegeneration. *J. Alzheimers Dis.* 20 Suppl 2, S551-568. doi:10.3233/JAD-2010-100354.

Hoshi, K., Matsumoto, Y., Ito, H., Saito, K., Honda, T., Yamaguchi, Y., et al. (2017). A unique glycan-isoform of transferrin in cerebrospinal fluid: A potential diagnostic marker for neurological diseases. *Biochimica et Biophysica Acta (BBA) - General Subjects* 1861, 2473–2478. doi:10.1016/j.bbagen.2017.07.005.

House, E., Esiri, M., Forster, G., Ince, P. G., and Exley, C. (2012). Aluminium, iron and copper in human brain tissues donated to the medical research council's cognitive function and ageing study. *Metallomics* 4, 56–65. doi:10.1039/c1mt00139f.

Householder, K. T., Dharmaraj, S., Sandberg, D. I., Wechsler-Reya, R. J., and Sirianni, R. W. (2019). Fate of nanoparticles in the central nervous system after intrathecal injection in healthy mice. *Scientific Reports* 9, 1–11. doi:10.1038/s41598-019-49028-w.

Hozumi, I., Hasegawa, T., Honda, A., Ozawa, K., Hayashi, Y., Hashimoto, K., et al. (2011). Patterns of levels of biological metals in CSF differ among neurodegenerative diseases. *J. Neurol. Sci.* 303, 95–99. doi:10.1016/j.jns.2011.01.003.

Huang, L., Xia, B., Liu, Z., Cao, Q., Huang, J., and Luo, Z. (2017). Superparamagnetic Iron Oxide Nanoparticle-Mediated Forces Enhance the Migration of Schwann Cells Across the Astrocyte-Schwann Cell Boundary In vitro. *Front Cell Neurosci* 11, 83. doi:10.3389/fncel.2017.00083.

Huang, X., Atwood, C. S., Moir, R. D., Hartshorn, M. A., Tanzi, R. E., and Bush, A. I. (2004). Trace metal contamination initiates the apparent auto-aggregation, amyloidosis, and oligomerization of Alzheimer's Abeta peptides. *J. Biol. Inorg. Chem.* 9, 954–960. doi:10.1007/s00775-004-0602-8.

Hubert, A., and Schäfer, R. (1998). *Magnetic Domains: The Analysis of Magnetic Microstructures*. Berlin Heidelberg: Springer-Verlag doi:10.1007/978-3-540-85054-0.

Hubert, V., Chauveau, F., Dumot, C., Ong, E., Berner, L.-P., Canet-Soulas, E., et al. (2019). Clinical Imaging of Choroid Plexus in Health and in Brain Disorders: A Mini-Review. *Front. Mol. Neurosci.* 12. doi:10.3389/fnmol.2019.00034.

Iadecola, C. (2017). The Neurovascular Unit Coming of Age: A Journey through Neurovascular Coupling in Health and Disease. *Neuron* 96, 17–42. doi:10.1016/j.neuron.2017.07.030.

Iliff, J. J., Wang, M., Liao, Y., Plogg, B. A., Peng, W., Gundersen, G. A., et al. (2012). A Paravascular Pathway Facilitates CSF Flow Through the Brain Parenchyma and the Clearance of Interstitial Solutes, Including Amyloid β. *Science Translational Medicine* 4, 147ra111-147ra111. doi:10.1126/scitranslmed.3003748.

Iliff, J., and Simon, M. (2019). CrossTalk proposal: The glymphatic system supports convective exchange of cerebrospinal fluid and brain interstitial fluid that is mediated by perivascular aquaporin-4. *The Journal of Physiology* 597, 4417–4419. doi:https://doi.org/10.1113/JP277635.

International, A. D. (2019). World Alzheimer Report 2019: Attitudes to dementia | Alzheimer's Disease International. Available at: https://www.alz.co.uk/research/world-report-2019 [Accessed August 27, 2020].

Ito, S., Ikuta, K., Sasaki, K., Shindo, M., Torimoto, Y., and Kohgo, Y. (2012). Nobel Non-Transferrin-Bound Iron (NTBI) Measuring System Utilizing Automatic Analyzer. *Blood* 120, 3207–3207. doi:10.1182/blood.V120.21.3207.3207.

Ittner, L. M., and Götz, J. (2011). Amyloid-β and tau — a toxic pas de deux in Alzheimer's disease. *Nature Reviews Neuroscience* 12, 67–72. doi:10.1038/nrn2967.

Jack, C. R., Knopman, D. S., Jagust, W. J., Shaw, L. M., Aisen, P. S., Weiner, M. W., et al. (2010). Hypothetical model of dynamic biomarkers of the Alzheimer's pathological cascade. *Lancet Neurol* 9, 119–128. doi:10.1016/S1474-4422(09)70299-6.

Jeevanandam, J., Barhoum, A., Chan, Y. S., Dufresne, A., and Danquah, M. K. (2018). Review on nanoparticles and nanostructured materials: history, sources, toxicity and regulations. *Beilstein J. Nanotechnol.* 9, 1050–1074. doi:10.3762/bjnano.9.98.

Jensen, J. H., Chandra, R., Ramani, A., Lu, H., Johnson, G., Lee, S.-P., et al. (2006). Magnetic field correlation imaging. *Magnetic Resonance in Medicine* 55, 1350–1361. doi:https://doi.org/10.1002/mrm.20907.

Jeong, S. Y., and David, S. (2006). Age-Related Changes in Iron Homeostasis and Cell Death in the Cerebellum of Ceruloplasmin-Deficient Mice. *J. Neurosci.* 26, 9810–9819. doi:10.1523/JNEUROSCI.2922-06.2006.

Jiang, Z., Tian, Y., Shan, D., Wang, Y., Gerhard, E., Xia, J., et al. (2018). pH protective Y1 receptor ligand functionalized antiphagocytosis BPLP-WPU micelles for enhanced tumor imaging and therapy with prolonged survival time. *Biomaterials* 170, 70–81. doi:10.1016/j.biomaterials.2018.04.002.

Jiménez, A. J., Domínguez-Pinos, M.-D., Guerra, M. M., Fernández-Llebrez, P., and Pérez-Fígares, J.-M. (2014). Structure and function of the ependymal barrier and diseases associated with ependyma disruption. *Tissue Barriers* 2. doi:10.4161/tisb.28426.

Johanson, C., McMillan, P., Tavares, R., Spangenberger, A., Duncan, J., Silverberg, G., et al. (2004). Homeostatic capabilities of the choroid plexus epithelium in Alzheimer's disease. *Cerebrospinal Fluid Research* 1, 3. doi:10.1186/1743-8454-1-3.

Johanson, C., Stopa, E., McMillan, P., Roth, D., Funk, J., and Krinke, G. (2011). The Distributional Nexus of Choroid Plexus to Cerebrospinal Fluid, Ependyma and Brain: Toxicologic/Pathologic Phenomena, Periventricular Destabilization, and Lesion Spread. *Toxicol Pathol* 39, 186–212. doi:10.1177/0192623310394214.

Jovičić, S., Ignjatović, S., Dajak, M., Kangrga, R., and Majkić-Singh, N. (2005). Reference interval for calculated total iron-binding capacity using Olympus AU2700 analyzer. *Jugoslovenska medicinska biohemija* 24, 45–49.

Jr, J. H. W. (1963). Hierarchical Grouping to Optimize an Objective Function. *Journal of the American Statistical Association* 58, 236–244. doi:10.1080/01621459.1963.10500845.

Kawabata, H., Yang, R., Hirama, T., Vuong, P. T., Kawano, S., Gombart, A. F., et al. (1999). Molecular cloning of transferrin receptor 2. A new member of the transferrin receptor-like family. *J. Biol. Chem.* 274, 20826–20832. doi:10.1074/jbc.274.30.20826.

Ke, Y., and Qian, Z. M. (2007). Brain iron metabolism: Neurobiology and neurochemistry. *Progress in Neurobiology* 83, 149–173. doi:10.1016/j.pneurobio.2007.07.009.

Kell, D. B. (2009). Iron behaving badly: inappropriate iron chelation as a major contributor to the aetiology of vascular and other progressive inflammatory and degenerative diseases. *BMC Medical Genomics* 2, 2. doi:10.1186/1755-8794-2-2.

Kell, D. B. (2010). Towards a unifying, systems biology understanding of large-scale cellular death and destruction caused by poorly liganded iron: Parkinson's, Huntington's, Alzheimer's, prions, bactericides, chemical toxicology and others as examples. *Arch Toxicol* 84, 825–889. doi:10.1007/s00204-010-0577-x.

Kelly, A. U., McSorley, S. T., Patel, P., and Talwar, D. (2017). Interpreting iron studies. *BMJ* 357, j2513. doi:10.1136/bmj.j2513.

Khadjavi, A., Stura, I., Prato, M., Minero, V. G., Panariti, A., Rivolta, I., et al. (2018). "In Vitro", "In Vivo" and "In Silico" Investigation of the Anticancer Effectiveness of Oxygen-Loaded Chitosan-Shelled Nanodroplets as Potential Drug Vector. *Pharm. Res.* 35, 75. doi:10.1007/s11095-018-2371-z.

Khalid, M. K., Asad, M., Henrich-Noack, P., Sokolov, M., Hintz, W., Grigartzik, L., et al. (2018). Evaluation of Toxicity and Neural Uptake In Vitro and In Vivo of Superparamagnetic Iron Oxide Nanoparticles. *Int J Mol Sci* 19. doi:10.3390/ijms19092613.

Khalil, M., Riedlbauer, B., Langkammer, C., Enzinger, C., Ropele, S., Stojakovic, T., et al. (2014). Cerebrospinal fluid transferrin levels are reduced in patients with early multiple sclerosis. *Mult Scler* 20, 1569–1577. doi:10.1177/1352458514530020.

Khan, A. I., Liu, J., and Dutta, P. (2018). Iron Transport Kinetics through Blood-Brain Barrier Endothelial Cells. *Biochim Biophys Acta* 1862, 1168–1179. doi:10.1016/j.bbagen.2018.02.010.

Khanna, L., Verma, N. K., and Tripathi, S. K. (2018). Burgeoning tool of biomedical applications - Superparamagnetic nanoparticles. *Journal of Alloys and Compounds* 752, 332–353. doi:10.1016/j.jallcom.2018.04.093.

Killilea, D. W., Wong, S. L., Cahaya, H. S., Atamna, H., and Ames, B. N. (2004). Iron Accumulation during Cellular Senescence. *Annals of the New York Academy of Sciences* 1019, 365–367. doi:https://doi.org/10.1196/annals.1297.063.

Knutson, M. D. (2019). Non-transferrin-bound iron transporters. *Free Radical Biology and Medicine* 133, 101–111. doi:10.1016/j.freeradbiomed.2018.10.413.

Kong, S. D., Lee, J., Ramachandran, S., Eliceiri, B. P., Shubayev, V. I., Lal, R., et al. (2012). Magnetic targeting of nanoparticles across the intact blood–brain barrier. *Journal of Controlled Release* 164, 49–57. doi:10.1016/j.jconrel.2012.09.021.

Koskenkorva-Frank, T. S., Weiss, G., Koppenol, W. H., and Burckhardt, S. (2013). The complex interplay of iron metabolism, reactive oxygen species, and reactive nitrogen species: Insights into the potential of various iron therapies to induce oxidative and nitrosative stress. *Free Radical Biology and Medicine* 65, 1174–1194. doi:10.1016/j.freeradbiomed.2013.09.001.

Köster, W. (2001). ABC transporter-mediated uptake of iron, siderophores, heme and vitamin B12. *Research in Microbiology* 152, 291–301. doi:10.1016/S0923-2508(01)01200-1.

Kosyakovsky, J., Fine, J. M., Frey, W. H., and Hanson, L. R. (2021). Mechanisms of Intranasal Deferoxamine in Neurodegenerative and Neurovascular Disease. *Pharmaceuticals* 14, 95. doi:10.3390/ph14020095.

Kozlov, S., Afonin, A., Evsyukov, I., and Bondarenko, A. (2017). Alzheimer's disease: as it was in the beginning. *Rev Neurosci* 28, 825–843. doi:10.1515/revneuro-2017-0006.

Kripfgans, O. D., Fabiilli, M. L., Carson, P. L., and Fowlkes, J. B. (2004). On the acoustic vaporization of micrometer-sized droplets. *J. Acoust. Soc. Am.* 116, 272–281. doi:10.1121/1.1755236.

Lane, D. J. R., Ayton, S., and Bush, A. I. (2018). Iron and Alzheimer's Disease: An Update on Emerging Mechanisms. *J. Alzheimers Dis.* 64, S379–S395. doi:10.3233/JAD-179944.

Langkammer, C., Krebs, N., Goessler, W., Scheurer, E., Ebner, F., Yen, K., et al. (2010). Quantitative MR Imaging of Brain Iron: A Postmortem Validation Study. *Radiology* 257, 455–462. doi:10.1148/radiol.10100495.

Langkammer, C., Ropele, S., Pirpamer, L., Fazekas, F., and Schmidt, R. (2014). MRI for iron mapping in Alzheimer's disease. *Neurodegener Dis* 13, 189–191. doi:10.1159/000353756.

Langlet, F., Mullier, A., Bouret, S. G., Prevot, V., and Dehouck, B. (2013). Tanycyte-Like Cells Form a Blood–Cerebrospinal Fluid Barrier in the Circumventricular Organs of the Mouse Brain. *J Comp Neurol* 521, 3389–3405. doi:10.1002/cne.23355.

Lannfelt, L., Blennow, K., Zetterberg, H., Batsman, S., Ames, D., Harrison, J., et al. (2008). Safety, efficacy, and biomarker findings of PBT2 in targeting Abeta as a modifying therapy for Alzheimer's disease: a phase IIa, double-blind, randomised, placebo-controlled trial. *Lancet Neurol* 7, 779–786. doi:10.1016/S1474-4422(08)70167-4.

Lashley, T., Schott, J. M., Weston, P., Murray, C. E., Wellington, H., Keshavan, A., et al. (2018). Molecular biomarkers of Alzheimer's disease: progress and prospects. *Dis Model Mech* 11. doi:10.1242/dmm.031781.

Lavados, M., Guillón, M., Mujica, M. C., Rojo, L. E., Fuentes, P., and Maccioni, R. B. (2008). Mild cognitive impairment and Alzheimer patients display different levels of redox-active CSF iron. *J. Alzheimers Dis.* 13, 225–232. doi:10.3233/jad-2008-13211.

Leggett, B. A., Fletcher, L. M., Ramm, G. A., Powell, L. W., and Halliday, J. W. (1993). Differential regulation of ferritin H and L subunit mRNA during inflammation and long-term iron overload. *Journal of Gastroenterology and Hepatology* 8, 21–27. doi:https://doi.org/10.1111/j.1440-1746.1993.tb01170.x.

Lei, P., Ayton, S., Finkelstein, D. I., Spoerri, L., Ciccotosto, G. D., Wright, D. K., et al. (2012). Tau deficiency induces parkinsonism with dementia by impairing APP-mediated iron export. *Nat. Med.* 18, 291–295. doi:10.1038/nm.2613.

Leitner, D. F., and Connor, J. R. (2012). Functional roles of transferrin in the brain. *Biochim. Biophys. Acta* 1820, 393–402. doi:10.1016/j.bbagen.2011.10.016.

Leskovjan, A. C., Kretlow, A., Lanzirotti, A., Barrea, R., Vogt, S., and Miller, L. M. (2011). Increased brain iron coincides with early plaque formation in a mouse model of Alzheimer's disease. *Neuroimage* 55, 32–38. doi:10.1016/j.neuroimage.2010.11.073.

Leterme, G., Guigou, C., Oudot, A., Collin, B., Boudon, J., Millot, N., et al. (2019). Superparamagnetic Nanoparticle Delivery to the Cochlea Through Round Window by External Magnetic Field: Feasibility and Toxicity. *Surg Innov* 26, 646–655. doi:10.1177/1553350619867217.

LeVine, S. M., Lynch, S. G., Ou, C.-N., Wulser, M. J., Tam, E., and Boo, N. (1999). Ferritin, transferrin and iron concentrations in the cerebrospinal fluid of multiple sclerosis patients. *Brain Research* 821, 511–515. doi:10.1016/S0006-8993(98)01360-2.

LeVine, S. M., Wulser, M. J., and Lynch, S. G. (1998). Iron Quantification in Cerebrospinal Fluid. *Analytical Biochemistry* 265, 74–78. doi:10.1006/abio.1998.2903.

Lewinson, O., and Livnat-Levanon, N. (2017). Mechanism of Action of ABC Importers: Conservation, Divergence, and Physiological Adaptations. *Journal of Molecular Biology* 429, 606–619. doi:10.1016/j.jmb.2017.01.010.

Li, D.-D., Zhang, W., Wang, Z.-Y., and Zhao, P. (2017). Serum Copper, Zinc, and Iron Levels in Patients with Alzheimer's Disease: A Meta-Analysis of Case-Control Studies. *Front. Aging Neurosci.* 9. doi:10.3389/fnagi.2017.00300.

Liddelow, S. A. (2015). Development of the choroid plexus and blood-CSF barrier. *Front Neurosci* 9. doi:10.3389/fnins.2015.00032.

Lill, R., Hoffmann, B., Molik, S., Pierik, A. J., Rietzschel, N., Stehling, O., et al. (2012). The role of mitochondria in cellular iron–sulfur protein biogenesis and iron metabolism. *Biochimica et Biophysica Acta (BBA) - Molecular Cell Research* 1823, 1491–1508. doi:10.1016/j.bbamcr.2012.05.009.

Liu, J.-L., Fan, Y.-G., Yang, Z.-S., Wang, Z.-Y., and Guo, C. (2018). Iron and Alzheimer's Disease: From Pathogenesis to Therapeutic Implications. *Front. Neurosci.* 12. doi:10.3389/fnins.2018.00632.

Liu, X., Jin, W., and Theil, E. C. (2003). Opening protein pores with chaotropes enhances Fe reduction and chelation of Fe from the ferritin biomineral. *PNAS* 100, 3653–3658. doi:10.1073/pnas.0636928100.

Liu, X. S., Patterson, L. D., Miller, M. J., and Theil, E. C. (2007). Peptides Selected for the Protein Nanocage Pores Change the Rate of Iron Recovery from the Ferritin Mineral*,. *Journal of Biological Chemistry* 282, 31821–31825. doi:10.1074/jbc.C700153200.

Liu, Y., and Connor, J. R. (2012). Iron and ER stress in neurodegenerative disease. *Biometals* 25, 837–845. doi:10.1007/s10534-012-9544-8.

Loeffler, D. A., Connor, J. R., Juneau, P. L., Snyder, B. S., Kanaley, L., DeMaggio, A. J., et al. (1995). Transferrin and iron in normal, Alzheimer's disease, and Parkinson's disease brain regions. *J. Neurochem.* 65, 710–724. doi:10.1046/j.1471-4159.1995.65020710.x.

Long, J. M., and Holtzman, D. M. (2019). Alzheimer Disease: An Update on Pathobiology and Treatment Strategies. *Cell* 179, 312–339. doi:10.1016/j.cell.2019.09.001.

Lopes, T. J., Luganskaja, T., Vujić Spasić, M., Hentze, M. W., Muckenthaler, M. U., Schümann, K., et al. (2010). Systems analysis of iron metabolism: the network of iron pools and fluxes. *BMC Syst Biol* 4, 112. doi:10.1186/1752-0509-4-112.

Lovell, M. A., Xiong, S., Xie, C., Davies, P., and Markesbery, W. R. (2004). Induction of hyperphosphorylated tau in primary rat cortical neuron cultures mediated by oxidative stress and glycogen synthase kinase-3. *J. Alzheimers Dis.* 6, 659–671; discussion 673-681. doi:10.3233/jad-2004-6610.

Lu, C.-D., Ma, J.-K., Luo, Z.-Y., Tai, Q.-X., Wang, P., and Guan, P.-P. (2018). Transferrin is responsible for mediating the effects of iron ions on the regulation of anterior pharynx-defective-1α/β and Presenilin 1 expression via PGE2 and PGD2 at the early stage of Alzheimer's Disease. *Aging (Albany NY)* 10, 3117–3135. doi:10.18632/aging.101615.

Lu, L.-N., Qian, Z.-M., Wu, K.-C., Yung, W.-H., and Ke, Y. (2017). Expression of Iron Transporters and Pathological Hallmarks of Parkinson's and Alzheimer's Diseases in the Brain of Young, Adult, and Aged Rats. *Mol. Neurobiol.* 54, 5213–5224. doi:10.1007/s12035-016-0067-0.

Lun, M. P., Monuki, E. S., and Lehtinen, M. K. (2015). Development and functions of the choroid plexus–cerebrospinal fluid system. *Nature Reviews Neuroscience* 16, 445–457. doi:10.1038/nrn3921.

Luo, B., Zhang, H., Liu, X., Rao, R., Wu, Y., and Liu, W. (2015). Novel DiR and SPIO nanoparticles embedded PEG-PLGA nanobubbles as a multimodalimaging contrast agent. *Biomed Mater Eng* 26 Suppl 1, S911-916. doi:10.3233/BME-151384.

Ma, Y., Podinovskaia, M., Evans, P. J., Emma, G., Schaible, U. E., Porter, J., et al. (2014). A novel method for non-transferrin-bound iron quantification by chelatable fluorescent beads based on flow cytometry. *Biochemical Journal* 463, 351–362. doi:10.1042/BJ20140795.

Madsen, E., and Gitlin, J. D. (2007). Copper and Iron Disorders of the Brain. *Annu. Rev. Neurosci.* 30, 317–337. doi:10.1146/annurev.neuro.30.051606.094232.

Magistretti, P. J., and Allaman, I. (2015). A Cellular Perspective on Brain Energy Metabolism and Functional Imaging. *Neuron* 86, 883–901. doi:10.1016/j.neuron.2015.03.035.

Mahmoudi, K., Bouras, A., Bozec, D., Ivkov, R., and Hadjipanayis, C. (2018). Magnetic hyperthermia therapy for the treatment of glioblastoma: a review of the therapy's history, efficacy and application in humans. *Int J Hyperthermia* 34, 1316–1328. doi:10.1080/02656736.2018.1430867.

Manuel Muñoz, I. V., Garc&iacute, A., and a-Erce (2009). An update on iron physiology. *World Journal of Gastroenterology* 15, 4617–4626. doi:10.3748/wjg.15.4617.

Marano, F., Argenziano, M., Frairia, R., Adamini, A., Bosco, O., Rinella, L., et al. (2016a). Doxorubicin-Loaded Nanobubbles Combined with Extracorporeal Shock Waves: Basis for a New Drug Delivery Tool in Anaplastic Thyroid Cancer. *Thyroid* 26, 705–716. doi:10.1089/thy.2015.0342.

Marano, F., Frairia, R., Rinella, L., Argenziano, M., Bussolati, B., Grange, C., et al. (2017). Combining doxorubicin-nanobubbles and shockwaves for anaplastic thyroid cancer treatment: preclinical study in a xenograft mouse model. *Endocr. Relat. Cancer* 24, 275–286. doi:10.1530/ERC-17-0045.

Marano, F., Rinella, L., Argenziano, M., Cavalli, R., Sassi, F., D'Amelio, P., et al. (2016b). Targeting Taxanes to Castration-Resistant Prostate Cancer Cells by Nanobubbles and Extracorporeal Shock Waves. *PLoS ONE* 11, e0168553. doi:10.1371/journal.pone.0168553.

Marino, S., Hogue, I. B., Ray, C. J., and Kirschner, D. E. (2008). A methodology for performing global uncertainty and sensitivity analysis in systems biology. *Journal of Theoretical Biology* 254, 178–196. doi:10.1016/j.jtbi.2008.04.011.

Marques, F., Falcao, A. M., Sousa, J. C., Coppola, G., Geschwind, D., Sousa, N., et al. (2009). Altered iron metabolism is part of the choroid plexus response to peripheral inflammation. *Endocrinology* 150, 2822–2828. doi:10.1210/en.2008-1610.

Marques, F., Sousa, J. C., Brito, M. A., Pahnke, J., Santos, C., Correia-Neves, M., et al. (2017). The choroid plexus in health and in disease: dialogues into and out of the brain. *Neurobiology of Disease* 107, 32–40. doi:10.1016/j.nbd.2016.08.011.

Matsumae, M., Sato, O., Hirayama, A., Hayashi, N., Takizawa, K., Atsumi, H., et al. (2016). Research into the Physiology of Cerebrospinal Fluid Reaches a New Horizon: Intimate Exchange between Cerebrospinal Fluid and Interstitial Fluid May Contribute to Maintenance of Homeostasis in the Central Nervous System. *Neurol Med Chir (Tokyo)* 56, 416–441. doi:10.2176/nmc.ra.2016-0020.

Matta, M. K., Beekman, C. R., Gandhi, A., Narayanasamy, S., Thomas, C. D., Mohammad, A., et al. (2018). Determination of Non-Transferrin Bound Iron, Transferrin Bound Iron, Drug Bound Iron and Total Iron in Serum in a Rats after IV Administration of Sodium Ferric Gluconate Complex by Simple Ultrafiltration Inductively Coupled Plasma Mass Spectrometric Detection. *Nanomaterials (Basel)* 8. doi:10.3390/nano8020101.

McCarthy, R. C., and Kosman, D. J. (2015). Iron transport across the blood-brain barrier: development, neurovascular regulation and cerebral amyloid angiopathy. *Cell. Mol. Life Sci.* 72, 709–727. doi:10.1007/s00018-014-1771-4.

McKhann, G. M., Knopman, D. S., Chertkow, H., Hyman, B. T., Jack, C. R., Kawas, C. H., et al. (2011). The diagnosis of dementia due to Alzheimer's disease: Recommendations from the

National Institute on Aging-Alzheimer's Association workgroups on diagnostic guidelines for Alzheimer's disease. *Alzheimers Dement* 7, 263–269. doi:10.1016/j.jalz.2011.03.005.

McKie, A. T., Marciani, P., Rolfs, A., Brennan, K., Wehr, K., Barrow, D., et al. (2000). A Novel Duodenal Iron-Regulated Transporter, IREG1, Implicated in the Basolateral Transfer of Iron to the Circulation. *Molecular Cell* 5, 299–309. doi:10.1016/S1097-2765(00)80425-6.

Meadowcroft, M. D., Connor, J. R., Smith, M. B., and Yang, Q. X. (2009). MRI and histological analysis of beta-amyloid plaques in both human Alzheimer's disease and APP/PS1 transgenic mice. *J Magn Reson Imaging* 29, 997–1007. doi:10.1002/jmri.21731.

Mei, Z., Cogswell, M. E., Parvanta, I., Lynch, S., Beard, J. L., Stoltzfus, R. J., et al. (2005). Hemoglobin and Ferritin Are Currently the Most Efficient Indicators of Population Response to Iron Interventions: an Analysis of Nine Randomized Controlled Trials. *The Journal of Nutrition* 135, 1974–1980. doi:10.1093/jn/135.8.1974.

Mesquita, S. D., Ferreira, A. C., Sousa, J. C., Santos, N. C., Correia-Neves, M., Sousa, N., et al. (2012). Modulation of iron metabolism in aging and in Alzheimer's disease: relevance of the choroid plexus. *Front Cell Neurosci* 6. doi:10.3389/fncel.2012.00025.

Miller, L. L., Miller, S. C., Torti, S. V., Tsuji, Y., and Torti, F. M. (1991). Iron-independent induction of ferritin H chain by tumor necrosis factor. *PNAS* 88, 4946–4950. doi:10.1073/pnas.88.11.4946.

Molinuevo, J. L., Ayton, S., Batrla, R., Bednar, M. M., Bittner, T., Cummings, J., et al. (2018). Current state of Alzheimer's fluid biomarkers. *Acta Neuropathol.* 136, 821–853. doi:10.1007/s00401-018-1932-x.

Montagne, A., Zhao, Z., and Zlokovic, B. V. (2017). Alzheimer's disease: A matter of blood–brain barrier dysfunction? *J Exp Med* 214, 3151–3169. doi:10.1084/jem.20171406.

Moos, T. (1996). Immunohistochemical localization of intraneuronal transferrin receptor immunoreactivity in the adult mouse central nervous system. *J Comp Neurol* 375, 675–692. doi:10.1002/(SICI)1096-9861(19961125)375:4<675::AID-CNE8>3.0.CO;2-Z.

Moos, T., and Morgan, E. H. (1998). Evidence for low molecular weight, non-transferrin-bound iron in rat brain and cerebrospinal fluid. *Journal of Neuroscience Research* 54, 486–494. doi:https://doi.org/10.1002/(SICI)1097-4547(19981115)54:4<486::AID-JNR6>3.0.CO;2-I.

Moos, T., and Morgan, E. H. (2000). Transferrin and Transferrin Receptor Function in Brain Barrier Systems. *Cell Mol Neurobiol* 20, 77–95. doi:10.1023/A:1006948027674.

Moos, T., and Morgan, E. H. (2004). The significance of the mutated divalent metal transporter (DMT1) on iron transport into the Belgrade rat brain. *J. Neurochem.* 88, 233–245. doi:10.1046/j.1471-4159.2003.02142.x.

Moos, T., Rosengren Nielsen, T., Skjørringe, T., and Morgan, E. H. (2007). Iron trafficking inside the brain. *J. Neurochem.* 103, 1730–1740. doi:10.1111/j.1471-4159.2007.04976.x.

Moos, T., Skjoerringe, T., Gosk, S., and Morgan, E. H. (2006). Brain capillary endothelial cells mediate iron transport into the brain by segregating iron from transferrin without the involvement of divalent metal transporter 1. *J. Neurochem.* 98, 1946–1958. doi:10.1111/j.1471-4159.2006.04023.x.

Morris, M. D. (1991). Factorial Sampling Plans for Preliminary Computational Experiments. *Technometrics* 33, 161–174. doi:10.2307/1269043.

Muckenthaler, M. U., Galy, B., and Hentze, M. W. (2008). Systemic Iron Homeostasis and the Iron-Responsive Element/Iron-Regulatory Protein (IRE/IRP) Regulatory Network. *Annu. Rev. Nutr.* 28, 197–213. doi:10.1146/annurev.nutr.28.061807.155521.

Muñoz, M., García-Erce, J. A., and Remacha, Á. F. (2011). Disorders of iron metabolism. Part 1: molecular basis of iron homoeostasis. *Journal of Clinical Pathology* 64, 281–286. doi:10.1136/jcp.2010.079046.

Murphy, T. H., Miyamoto, M., Sastre, A., Schnaar, R. L., and Coyle, J. T. (1989). Glutamate toxicity in a neuronal cell line involves inhibition of cystine transport leading to oxidative stress. *Neuron* 2, 1547–1558. doi:10.1016/0896-6273(89)90043-3.

Myhre, O., Utkilen, H., Duale, N., Brunborg, G., and Hofer, T. (2013). Metal dyshomeostasis and inflammation in Alzheimer's and Parkinson's diseases: possible impact of environmental exposures. *Oxid Med Cell Longev* 2013, 726954. doi:10.1155/2013/726954.

Myszczynska, M. A., Ojamies, P. N., Lacoste, A. M. B., Neil, D., Saffari, A., Mead, R., et al. (2020). Applications of machine learning to diagnosis and treatment of neurodegenerative diseases. *Nature Reviews Neurology* 16, 440–456. doi:10.1038/s41582-020-0377-8.

Nabuurs, R. J. A., Hegeman, I., Natté, R., Duinen, S. G. van, Buchem, M. A. van, Weerd, L. van der, et al. (2011). High-field MRI of single histological slices using an inductively coupled, self-resonant microcoil: application to ex vivo samples of patients with Alzheimer's disease. *NMR in Biomedicine* 24, 351–357. doi:https://doi.org/10.1002/nbm.1598.

Nakada, T., and Kwee, I. L. (2019). Fluid Dynamics Inside the Brain Barrier: Current Concept of Interstitial Flow, Glymphatic Flow, and Cerebrospinal Fluid Circulation in the Brain. *Neuroscientist* 25, 155–166. doi:10.1177/1073858418775027.

Nakamura, M., Shishido, N., Nunomura, A., Smith, M. A., Perry, G., Hayashi, Y., et al. (2007). Three histidine residues of amyloid-beta peptide control the redox activity of copper and iron. *Biochemistry* 46, 12737–12743. doi:10.1021/bi701079z.

Nation, D. A., Sweeney, M. D., Montagne, A., Sagare, A. P., D'Orazio, L. M., Pachicano, M., et al. (2019). Blood–brain barrier breakdown is an early biomarker of human cognitive dysfunction. *Nature Medicine* 25, 270–276. doi:10.1038/s41591-018-0297-y.

Ndayisaba, A., Kaindlstorfer, C., and Wenning, G. K. (2019). Iron in Neurodegeneration - Cause or Consequence? *Front Neurosci* 13, 180. doi:10.3389/fnins.2019.00180.

Núñez, M. T., Urrutia, P., Mena, N., Aguirre, P., Tapia, V., and Salazar, J. (2012). Iron toxicity in neurodegeneration. *Biometals* 25, 761–776. doi:10.1007/s10534-012-9523-0.

Nurchi, V. M., Crisponi, G., Lachowicz, J. I., Medici, S., Peana, M., and Zoroddu, M. A. (2016). Chemical features of in use and in progress chelators for iron overload. *J Trace Elem Med Biol* 38, 10–18. doi:10.1016/j.jtemb.2016.05.010.

Ogun, A. S., and Adeyinka, A. (2021). "Biochemistry, Transferrin," in *StatPearls* (Treasure Island (FL): StatPearls Publishing). Available at: http://www.ncbi.nlm.nih.gov/books/NBK532928/ [Accessed March 9, 2021].

Olney, N. T., Spina, S., and Miller, B. L. (2017). Frontotemporal Dementia. *Neurol Clin* 35, 339–374. doi:10.1016/j.ncl.2017.01.008.

Organization, W. H. (2011). Serum ferritin concentrations for the assessment of iron status and iron deficiency in populations. *Concentrations sériques de ferritine permettant d'évaluer le statut et les carences en fer dans les populations*. Available at: https://apps.who.int/iris/handle/10665/85843 [Accessed February 8, 2021].

Ortiz, E., Pasquini, J. M., Thompson, K., Felt, B., Butkus, G., Beard, J., et al. (2004). Effect of manipulation of iron storage, transport, or availability on myelin composition and brain iron content in three different animal models. *Journal of Neuroscience Research* 77, 681–689. doi:https://doi.org/10.1002/jnr.20207.

Ortner, M., and Coliado Bandeira, L. G. (2020). Magpylib: A free Python package for magnetic field computation. *SoftwareX* 11, 100466. doi:10.1016/j.softx.2020.100466.

Oshiro, S., Kawamura, K., Zhang, C., Sone, T., Morioka, M. S., Kobayashi, S., et al. (2008). Microglia and astroglia prevent oxidative stress-induced neuronal cell death: Implications for aceruloplasminemia. *Biochimica et Biophysica Acta (BBA) - Molecular Basis of Disease* 1782, 109–117. doi:10.1016/j.bbadis.2007.12.002.

Paglia, G., Miedico, O., Cristofano, A., Vitale, M., Angiolillo, A., Chiaravalle, A. E., et al. (2016). Distinctive Pattern of Serum Elements During the Progression of Alzheimer's Disease. *Scientific Reports* 6, 22769. doi:10.1038/srep22769.

Pagnozzi, A. M., Fripp, J., and Rose, S. E. (2019). Quantifying deep grey matter atrophy using automated segmentation approaches: A systematic review of structural MRI studies. *Neuroimage* 201, 116018. doi:10.1016/j.neuroimage.2019.116018.

Pahnke, J., Langer, O., and Krohn, M. (2014). Alzheimer's and ABC transporters--new opportunities for diagnostics and treatment. *Neurobiol. Dis.* 72 Pt A, 54–60. doi:10.1016/j.nbd.2014.04.001.

Palmqvist, S., Janelidze, S., Quiroz, Y. T., Zetterberg, H., Lopera, F., Stomrud, E., et al. (2020). Discriminative Accuracy of Plasma Phospho-tau217 for Alzheimer Disease vs Other Neurodegenerative Disorders. *JAMA*. doi:10.1001/jama.2020.12134.

Pantopoulos, K., Porwal, S. K., Tartakoff, A., and Devireddy, L. (2012). Mechanisms of mammalian iron homeostasis. *Biochemistry* 51, 5705–5724. doi:10.1021/bi300752r.

Papisov, M. I., Belov, V. V., and Gannon, K. S. (2013). Physiology of the intrathecal bolus: the leptomeningeal route for macromolecule and particle delivery to CNS. *Mol Pharm* 10, 1522–1532. doi:10.1021/mp300474m.

Park, M., Moon, Y., Han, S.-H., and Moon, W.-J. (2019). Motor cortex hypointensity on susceptibility-weighted imaging: a potential imaging marker of iron accumulation in patients with cognitive impairment. *Neuroradiology* 61, 675–683. doi:10.1007/s00234-019-02159-3.

Patel, M., and Ramavataram, D. V. S. S. (2012). Non Transferrin Bound Iron: Nature, Manifestations and Analytical Approaches for Estimation. *Indian J Clin Biochem* 27, 322–332. doi:10.1007/s12291-012-0250-7.

Pawlowski, M., Meuth, S. G., and Duning, T. (2017). Cerebrospinal Fluid Biomarkers in Alzheimer's Disease—From Brain Starch to Bench and Bedside. *Diagnostics (Basel)* 7. doi:10.3390/diagnostics7030042.

Pedregosa, F., Varoquaux, G., Gramfort, A., Michel, V., Thirion, B., Grisel, O., et al. Scikit-learn: Machine Learning in Python. *MACHINE LEARNING IN PYTHON*, 6.

Penkova, M., and Ivanova, N. (2019). Serum Iron Metabolism Variables in Clinically Healthy Persons. *Open Access Maced J Med Sci* 7, 318–321. doi:10.3889/oamjms.2019.083.

Permanent Magnet and Electromechanical Devices (2001). Elsevier doi:10.1016/B978-0-12-269951-1.X5000-1.

Perosa, V., Scherlek, A. A., Kozberg, M. G., Smith, L., Westerling-Bui, T., Auger, C. A., et al. (2021). Deep learning assisted quantitative assessment of histopathological markers of Alzheimer's disease and cerebral amyloid angiopathy. *Acta Neuropathologica Communications* 9, 141. doi:10.1186/s40478-021-01235-1.

Peters, D. G., Connor, J. R., and Meadowcroft, M. D. (2015). The relationship between iron dyshomeostasis and amyloidogenesis in Alzheimer's disease: Two sides of the same coin. *Neurobiol. Dis.* 81, 49–65. doi:10.1016/j.nbd.2015.08.007.

Petersen, R. C. (2004). Mild cognitive impairment as a diagnostic entity. *Journal of Internal Medicine* 256, 183–194. doi:10.1111/j.1365-2796.2004.01388.x.

Petersen, R. C., Knopman, D. S., Boeve, B. F., Geda, Y. E., Ivnik, R. J., Smith, G. E., et al. (2009). Mild Cognitive Impairment: Ten Years Later. *Arch Neurol* 66, 1447–1455. doi:10.1001/archneurol.2009.266.

Petters, C., Irrsack, E., Koch, M., and Dringen, R. (2014). Uptake and metabolism of iron oxide nanoparticles in brain cells. *Neurochem Res* 39, 1648–1660. doi:10.1007/s11064-014-1380-5.

Pfeiffer, C. M., and Looker, A. C. (2017). Laboratory methodologies for indicators of iron status: strengths, limitations, and analytical challenges. *Am J Clin Nutr* 106, 1606S-1614S. doi:10.3945/ajcn.117.155887.

Pfeiffer, C. M., Schleicher, R. L., Osterloh, J. D., Jain, R. B., Wong, L.-Y., and Sampson, E. J. (2009). National Report on Biochemical Indicators of Diet and Nutrition in the U.S. Population 1999-2002. *The FASEB Journal* 23, 551.26-551.26. doi:https://doi.org/10.1096/fasebj.23.1_supplement.551.26.

Plum, F. (1988). The physiology and pathophysiology of the cerebrospinal fluid by Hugh Davson, Keasley Welch, and Malcolm B. Segal New York. Livingstone, I987 1013 pp. illustrated, $198.00. *Annals of Neurology* 24, 106–106. doi:10.1002/ana.410240131.

Praticò, D., Uryu, K., Leight, S., Trojanoswki, J. Q., and Lee, V. M. (2001). Increased lipid peroxidation precedes amyloid plaque formation in an animal model of Alzheimer amyloidosis. *J. Neurosci.* 21, 4183–4187.

Preston, J. E. (2001). Ageing choroid plexus-cerebrospinal fluid system. *Microscopy Research and Technique* 52, 31–37. doi:10.1002/1097-0029(20010101)52:1<31::AID-JEMT5>3.0.CO;2-T.

Price, J. L., McKeel, D. W., Buckles, V. D., Roe, C. M., Xiong, C., Grundman, M., et al. (2009). Neuropathology of Nondemented Aging: Presumptive Evidence for Preclinical Alzheimer Disease. *Neurobiol Aging* 30, 1026–1036. doi:10.1016/j.neurobiolaging.2009.04.002.

Pujol, J., Junqué, C., Vendrell, P., Grau, J. M., Martí-Vilalta, J. L., Olivé, C., et al. (1992). Biological Significance of Iron-Related Magnetic Resonance Imaging Changes in the Brain. *Archives of Neurology* 49, 711–717. doi:10.1001/archneur.1992.00530310053012.

Qian, Z.-M., Chang, Y.-Z., Zhu, L., Yang, L., Du, J.-R., Ho, K.-P., et al. (2007). Development and iron-dependent expression of hephaestin in different brain regions of rats. *Journal of Cellular Biochemistry* 102, 1225–1233. doi:https://doi.org/10.1002/jcb.21352.

Quintana, C., Cowley, J. M., and Marhic, C. (2004). Electron nanodiffraction and high-resolution electron microscopy studies of the structure and composition of physiological and pathological ferritin. *Journal of Structural Biology* 147, 166–178. doi:10.1016/j.jsb.2004.03.001.

Quintana, C., and Gutiérrez, L. (2010). Could a dysfunction of ferritin be a determinant factor in the aetiology of some neurodegenerative diseases? *Biochimica et Biophysica Acta (BBA) - General Subjects* 1800, 770–782. doi:10.1016/j.bbagen.2010.04.012.

Quintana, C., Lancin, M., Marhic, C., Pérez, M., Martin-Benito, J., Avila, J., et al. (2000). Initial studies with high resolution TEM and electron energy loss spectroscopy studies of ferritin cores extracted from brains of patients with progressive supranuclear palsy and Alzheimer disease. *Cell Mol Biol (Noisy-le-grand)* 46, 807–820.

Rabinovici, G. D., Carrillo, M. C., Forman, M., DeSanti, S., Miller, D. S., Kozauer, N., et al. (2016). Multiple comorbid neuropathologies in the setting of Alzheimer's disease neuropathology and implications for drug development. *Alzheimers Dement (N Y)* 3, 83–91. doi:10.1016/j.trci.2016.09.002.

Racine, A. M., Koscik, R. L., Berman, S. E., Nicholas, C. R., Clark, L. R., Okonkwo, O. C., et al. (2016). Biomarker clusters are differentially associated with longitudinal cognitive decline in late midlife. *Brain* 139, 2261–2274. doi:10.1093/brain/aww142.

Ramaswamy, B., Kulkarni, S. D., Villar, P. S., Smith, R. S., Eberly, C., Araneda, R. C., et al. (2015). Movement of Magnetic Nanoparticles in Brain Tissue: Mechanisms and Safety. *Nanomedicine* 11, 1821–1829. doi:10.1016/j.nano.2015.06.003.

Rascovsky, K., Hodges, J. R., Knopman, D., Mendez, M. F., Kramer, J. H., Neuhaus, J., et al. (2011). Sensitivity of revised diagnostic criteria for the behavioural variant of frontotemporal dementia. *Brain* 134, 2456–2477. doi:10.1093/brain/awr179.

Reichert, C. O., de Freitas, F. A., Sampaio-Silva, J., Rokita-Rosa, L., Barros, P. de L., Levy, D., et al. (2020). Ferroptosis Mechanisms Involved in Neurodegenerative Diseases. *International Journal of Molecular Sciences* 21, 8765. doi:10.3390/ijms21228765.

Ritchie, C. W., Bush, A. I., Mackinnon, A., Macfarlane, S., Mastwyk, M., MacGregor, L., et al. (2003). Metal-protein attenuation with iodochlorhydroxyquin (clioquinol) targeting Abeta amyloid deposition and toxicity in Alzheimer disease: a pilot phase 2 clinical trial. *Arch. Neurol.* 60, 1685–1691. doi:10.1001/archneur.60.12.1685.

Rival, T., Page, R. M., Chandraratna, D. S., Sendall, T. J., Ryder, E., Liu, B., et al. (2009). Fenton chemistry and oxidative stress mediate the toxicity of the beta-amyloid peptide in a Drosophila model of Alzheimer's disease. *Eur. J. Neurosci.* 29, 1335–1347. doi:10.1111/j.1460-9568.2009.06701.x.

Roberts, B. R., Ryan, T. M., Bush, A. I., Masters, C. L., and Duce, J. A. (2012). The role of metallobiology and amyloid-β peptides in Alzheimer's disease. *Journal of Neurochemistry* 120, 149–166. doi:https://doi.org/10.1111/j.1471-4159.2011.07500.x.

Roberts, R., and Knopman, D. S. (2013). Classification and Epidemiology of MCI. *Clin Geriatr Med* 29. doi:10.1016/j.cger.2013.07.003.

Robinson, J. L., Lee, E. B., Xie, S. X., Rennert, L., Suh, E., Bredenberg, C., et al. (2018). Neurodegenerative disease concomitant proteinopathies are prevalent, age-related and APOE4-associated. *Brain* 141, 2181–2193. doi:10.1093/brain/awy146.

Roet, M., Hescham, S.-A., Jahanshahi, A., Rutten, B. P. F., Anikeeva, P. O., and Temel, Y. (2019). Progress in neuromodulation of the brain: A role for magnetic nanoparticles? *Prog. Neurobiol.* 177, 1–14. doi:10.1016/j.pneurobio.2019.03.002.

Rogers, J. T., Bush, A. I., Cho, H.-H., Smith, D. H., Thomson, A. M., Friedlich, A. L., et al. (2008). Iron and the translation of the amyloid precursor protein (APP) and ferritin mRNAs: riboregulation against neural oxidative damage in Alzheimer's disease. *Biochem. Soc. Trans.* 36, 1282–1287. doi:10.1042/BST0361282.

Rogers, J. T., and Lahiri, D. K. (2004). Metal and inflammatory targets for Alzheimer's disease. *Curr Drug Targets* 5, 535–551. doi:10.2174/1389450043345272.

Rouault, T. A., and Cooperman, S. (2006). Brain Iron Metabolism. *Seminars in Pediatric Neurology* 13, 142–148. doi:10.1016/j.spen.2006.08.002.

Rouault, T. A., Zhang, D.-L., and Jeong, S. Y. (2009). Brain iron homeostasis, the choroid plexus, and localization of iron transport proteins. *Metab Brain Dis* 24, 673. doi:10.1007/s11011-009-9169-y.

Saltelli, A., Annoni, P., Azzini, I., Campolongo, F., Ratto, M., and Tarantola, S. (2010). Variance based sensitivity analysis of model output. Design and estimator for the total sensitivity index. *Computer Physics Communications* 181, 259–270. doi:10.1016/j.cpc.2009.09.018.

Salvador, G. A. (2010). Iron in neuronal function and dysfunction. *Biofactors* 36, 103–110. doi:10.1002/biof.80.

Sandberg, D. I., Rytting, M., Zaky, W., Kerr, M., Ketonen, L., Kundu, U., et al. (2015). Methotrexate administration directly into the fourth ventricle in children with malignant fourth ventricular brain tumors: a pilot clinical trial. *J Neurooncol* 125, 133–141. doi:10.1007/s11060-015-1878-y.

Saraiva, C., Praça, C., Ferreira, R., Santos, T., Ferreira, L., and Bernardino, L. (2016). Nanoparticle-mediated brain drug delivery: Overcoming blood–brain barrier to treat neurodegenerative diseases. *Journal of Controlled Release* 235, 34–47. doi:10.1016/j.jconrel.2016.05.044.

Sasaki, K., Ikuta, K., Tanaka, H., Ohtake, T., Torimoto, Y., Fujiya, M., et al. (2011). Improved quantification for non-transferrin-bound iron measurement using high-performance liquid chromatography by reducing iron contamination. *Molecular Medicine Reports* 4, 913–918. doi:10.3892/mmr.2011.518.

Sayre, L. M., Perry, G., Harris, P. L. R., Liu, Y., Schubert, K. A., and Smith, M. A. (2000). In Situ Oxidative Catalysis by Neurofibrillary Tangles and Senile Plaques in Alzheimer's Disease. *Journal of Neurochemistry* 74, 270–279. doi:https://doi.org/10.1046/j.1471-4159.2000.0740270.x.

Schenck, J. F. (2003). Magnetic resonance imaging of brain iron. *Journal of the Neurological Sciences* 207, 99–102. doi:10.1016/S0022-510X(02)00431-8.

Schrag, M., Mueller, C., Oyoyo, U., Smith, M. A., and Kirsch, W. M. (2011). Iron, zinc and copper in the Alzheimer's disease brain: a quantitative meta-analysis. Some insight on the influence of citation bias on scientific opinion. *Prog. Neurobiol.* 94, 296–306. doi:10.1016/j.pneurobio.2011.05.001.

Schröder, N., Figueiredo, L. S., and de Lima, M. N. M. (2013). Role of Brain Iron Accumulation in Cognitive Dysfunction: Evidence from Animal Models and Human Studies. *Journal of Alzheimer's Disease* 34, 797–812. doi:10.3233/JAD-121996.

Sensenig, R., Sapir, Y., MacDonald, C., Cohen, S., and Polyak, B. (2012). Magnetic nanoparticle-based approaches to locally target therapy and enhance tissue regeneration in vivo. *Nanomedicine* 7, 1425–1442. doi:10.2217/nnm.12.109.

Serot, J. M., Christmann, D., Dubost, T., and Couturier, M. (1997). Cerebrospinal fluid transthyretin: aging and late onset Alzheimer's disease. *J. Neurol. Neurosurg. Psychiatry* 63, 506–508. doi:10.1136/jnnp.63.4.506.

Serot, J.-M., Béné, M.-C., Foliguet, B., and Faure, G. C. (2000). Morphological alterations of the choroid plexus in late-onset Alzheimer's disease. *Acta Neuropathol* 99, 105–108. doi:10.1007/PL00007412.

Serot, J.-M., Zmudka, J., and Jouanny, P. (2012). A Possible Role for CSF Turnover and Choroid Plexus in the Pathogenesis of Late Onset Alzheimer's Disease. *Journal of Alzheimer's Disease* 30, 17–26. doi:10.3233/JAD-2012-111964.

Shi, H., Bencze, K. Z., Stemmler, T. L., and Philpott, C. C. (2008). A Cytosolic Iron Chaperone That Delivers Iron to Ferritin. *Science* 320, 1207–1210. doi:10.1126/science.1157643.

Siah, C. W., Ombiga, J., Adams, L. A., Trinder, D., and Olynyk, J. K. (2006). Normal iron metabolism and the pathophysiology of iron overload disorders. *Clin Biochem Rev* 27, 5–16.

Silvestri, L., and Camaschella, C. (2008). A potential pathogenetic role of iron in Alzheimer's disease. *J. Cell. Mol. Med.* 12, 1548–1550. doi:10.1111/j.1582-4934.2008.00356.x.

Simpson, I. A., Ponnuru, P., Klinger, M. E., Myers, R. L., Devraj, K., Coe, C. L., et al. (2015). A Novel Model for Brain Iron Uptake: Introducing the Concept of Regulation. *J Cereb Blood Flow Metab* 35, 48–57. doi:10.1038/jcbfm.2014.168.

Singh, N., Haldar, S., Tripathi, A. K., Horback, K., Wong, J., Sharma, D., et al. (2014). Brain iron homeostasis: from molecular mechanisms to clinical significance and therapeutic opportunities. *Antioxid. Redox Signal.* 20, 1324–1363. doi:10.1089/ars.2012.4931.

Sintov, A. C., Velasco-Aguirre, C., Gallardo-Toledo, E., Araya, E., and Kogan, M. J. (2016). Metal Nanoparticles as Targeted Carriers Circumventing the Blood-Brain Barrier. *Int. Rev. Neurobiol.* 130, 199–227. doi:10.1016/bs.irn.2016.06.007.

Sisó, S., Jeffrey, M., and González, L. (2010). Sensory circumventricular organs in health and disease. *Acta Neuropathol* 120, 689–705. doi:10.1007/s00401-010-0743-5.

Smith, M. A., Harris, P. L., Sayre, L. M., and Perry, G. (1997). Iron accumulation in Alzheimer disease is a source of redox-generated free radicals. *Proc. Natl. Acad. Sci. U.S.A.* 94, 9866–9868. doi:10.1073/pnas.94.18.9866.

Smith, M. A., Hirai, K., Hsiao, K., Pappolla, M. A., Harris, P. L. R., Siedlak, S. L., et al. (1998). Amyloid-β Deposition in Alzheimer Transgenic Mice Is Associated with Oxidative Stress. *Journal of Neurochemistry* 70, 2212–2215. doi:https://doi.org/10.1046/j.1471-4159.1998.70052212.x.

Smith, M. A., Zhu, X., Tabaton, M., Liu, G., McKeel, D. W., Cohen, M. L., et al. (2010). Increased iron and free radical generation in preclinical Alzheimer disease and mild cognitive impairment. *J. Alzheimers Dis.* 19, 363–372. doi:10.3233/JAD-2010-1239.

Smith, S. A., Bulte, J. W. M., and Zijl, P. C. M. van (2009). Direct saturation MRI: Theory and application to imaging brain iron. *Magnetic Resonance in Medicine* 62, 384–393. doi:https://doi.org/10.1002/mrm.21980.

Sobol', I. M. (2001). Global sensitivity indices for nonlinear mathematical models and their Monte Carlo estimates. *Mathematics and Computers in Simulation* 55, 271–280. doi:10.1016/S0378-4754(00)00270-6.

Sohail, A., Ahmad, Z., Bég, O. A., Arshad, S., and Sherin, L. (2017). A review on hyperthermia via nanoparticle-mediated therapy. *Bull Cancer* 104, 452–461. doi:10.1016/j.bulcan.2017.02.003.

Spector, R., and Johanson, C. E. (2013). Sustained choroid plexus function in human elderly and Alzheimer's disease patients. *Fluids and Barriers of the CNS* 10, 28. doi:10.1186/2045-8118-10-28.

Spector, R., Robert Snodgrass, S., and Johanson, C. E. (2015). A balanced view of the cerebrospinal fluid composition and functions: Focus on adult humans. *Experimental Neurology* 273, 57–68. doi:10.1016/j.expneurol.2015.07.027.

Speeckaert, M. M., Speeckaert, R., and Delanghe, J. R. (2010). Biological and clinical aspects of soluble transferrin receptor. *Critical Reviews in Clinical Laboratory Sciences* 47, 213–228. doi:10.3109/10408363.2010.550461.

Sperling, R. A., Aisen, P. S., Beckett, L. A., Bennett, D. A., Craft, S., Fagan, A. M., et al. (2011). Toward defining the preclinical stages of Alzheimer's disease: Recommendations from the National Institute on Aging-Alzheimer's Association workgroups on diagnostic guidelines for Alzheimer's disease. *Alzheimers Dement* 7, 280–292. doi:10.1016/j.jalz.2011.03.003.

Spirou, S. V., Basini, M., Lascialfari, A., Sangregorio, C., and Innocenti, C. (2018). Magnetic Hyperthermia and Radiation Therapy: Radiobiological Principles and Current Practice †. *Nanomaterials (Basel)* 8. doi:10.3390/nano8060401.

Spotorno, N., Acosta-Cabronero, J., Stomrud, E., Lampinen, B., Strandberg, O. T., van Westen, D., et al. (2020). Relationship between cortical iron and tau aggregation in Alzheimer's disease. *Brain* 143, 1341–1349. doi:10.1093/brain/awaa089.

Squitti, R., Salustri, C., Siotto, M., Ventriglia, M., Vernieri, F., Lupoi, D., et al. (2010). Ceruloplasmin/Transferrin ratio changes in Alzheimer's disease. *Int J Alzheimers Dis* 2011, 231595. doi:10.4061/2011/231595.

Sripetchwandee, J., Wongjaikam, S., Krintratun, W., Chattipakorn, N., and Chattipakorn, S. C. (2016). A combination of an iron chelator with an antioxidant effectively diminishes the dendritic loss, tau-hyperphosphorylation, amyloids-β accumulation and brain mitochondrial dynamic disruption in rats with chronic iron-overload. *Neuroscience* 332, 191–202. doi:10.1016/j.neuroscience.2016.07.003.

Sternberg Zohara, H. Z., and Sternberg Zohara, H. Z. (2017). Serum Hepcidin Levels, Iron Dyshomeostasis and Cognitive Loss in Alzheimer's Disease. *Aging and disease* 8, 215–227. doi:10.14336/AD.2016.0811.

Stockwell, B. R., Angeli, J. P. F., Bayir, H., Bush, A. I., Conrad, M., Dixon, S. J., et al. (2017). Ferroptosis: A Regulated Cell Death Nexus Linking Metabolism, Redox Biology, and Disease. *Cell* 171, 273–285. doi:10.1016/j.cell.2017.09.021.

Sukhanova, A., Bozrova, S., Sokolov, P., Berestovoy, M., Karaulov, A., and Nabiev, I. (2018). Dependence of Nanoparticle Toxicity on Their Physical and Chemical Properties. *Nanoscale Research Letters* 13, 44. doi:10.1186/s11671-018-2457-x.

Sweeney, M. D., Kisler, K., Montagne, A., Toga, A. W., and Zlokovic, B. V. (2018a). The role of brain vasculature in neurodegenerative disorders. *Nature Neuroscience* 21, 1318–1331. doi:10.1038/s41593-018-0234-x.

Sweeney, M. D., Sagare, A. P., and Zlokovic, B. V. (2018b). Blood–brain barrier breakdown in Alzheimer disease and other neurodegenerative disorders. *Nature Reviews Neurology* 14, 133–150. doi:10.1038/nrneurol.2017.188.

Sweeney, M. D., Zhao, Z., Montagne, A., Nelson, A. R., and Zlokovic, B. V. (2019). Blood-Brain Barrier: From Physiology to Disease and Back. *Physiol. Rev.* 99, 21–78. doi:10.1152/physrev.00050.2017.

Tam, V. H., Sosa, C., Liu, R., Yao, N., and Priestley, R. D. (2016). Nanomedicine as a non-invasive strategy for drug delivery across the blood brain barrier. *Int J Pharm* 515, 331–342. doi:10.1016/j.ijpharm.2016.10.031.

Taniguchi, M., Okayama, Y., Hashimoto, Y., Kitaura, M., Jimbo, D., Wakutani, Y., et al. (2008). Sugar Chains of Cerebrospinal Fluid Transferrin as a New Biological Marker of Alzheimer's Disease. *DEM* 26, 117–122. doi:10.1159/000147479.

Tanveer, M., Richhariya, B., Khan, R. U., Rashid, A. H., Khanna, P., Prasad, M., et al. (2020). Machine Learning Techniques for the Diagnosis of Alzheimer’s Disease: A Review. *ACM Trans. Multimedia Comput. Commun. Appl.* 16, 30:1-30:35. doi:10.1145/3344998.

Tao, Y., Wang, Y., Rogers, J. T., and Wang, F. (2014). Perturbed iron distribution in Alzheimer's disease serum, cerebrospinal fluid, and selected brain regions: a systematic review and meta-analysis. *J. Alzheimers Dis.* 42, 679–690. doi:10.3233/JAD-140396.

Tarasoff-Conway, J. M., Carare, R. O., Osorio, R. S., Glodzik, L., Butler, T., Fieremans, E., et al. (2015). Clearance systems in the brain—implications for Alzheimer disease. *Nature Reviews Neurology* 11, 457–470. doi:10.1038/nrneurol.2015.119.

Telano, L. N., and Baker, S. (2020). "Physiology, Cerebral Spinal Fluid (CSF)," in *StatPearls* (Treasure Island (FL): StatPearls Publishing). Available at: http://www.ncbi.nlm.nih.gov/books/NBK519007/ [Accessed May 1, 2020].

Telling, N. D., Everett, J., Collingwood, J. F., Dobson, J., van der Laan, G., Gallagher, J. J., et al. (2017). Iron Biochemistry is Correlated with Amyloid Plaque Morphology in an Established Mouse Model of Alzheimer's Disease. *Cell Chem Biol* 24, 1205-1215.e3. doi:10.1016/j.chembiol.2017.07.014.

Templeton, D. M. (2015). Speciation in Metal Toxicity and Metal-Based Therapeutics. *Toxics* 3, 170–186. doi:10.3390/toxics3020170.

The Choroid Plexus and Cerebrospinal Fluid System: Roles in Neurodegenerative Diseases (2016). *The Choroid Plexus and Cerebrospinal Fluid*, 129–154. doi:10.1016/B978-0-12-801740-1.00008-1.

Theil, E. C. (2003). Ferritin: At the Crossroads of Iron and Oxygen Metabolism. *The Journal of Nutrition* 133, 1549S-1553S. doi:10.1093/jn/133.5.1549S.

Theil, E. C., Liu, X. S., and Tosha, T. (2008). Gated pores in the ferritin protein nanocage. *Inorganica Chimica Acta* 361, 868–874. doi:10.1016/j.ica.2007.08.025.

Theumer, A., Gräfe, C., Bähring, F., Bergemann, C., Hochhaus, A., and Clement, J. H. (2015). Superparamagnetic iron oxide nanoparticles exert different cytotoxic effects on cells grown in monolayer cell culture versus as multicellular spheroids. *Journal of Magnetism and Magnetic Materials* 380, 27–33. doi:10.1016/j.jmmm.2014.10.039.

Thomsen, L. B., Thomsen, M. S., and Moos, T. (2015). Targeted drug delivery to the brain using magnetic nanoparticles. *Ther Deliv* 6, 1145–1155. doi:10.4155/tde.15.56.

Tisato, V., Zuliani, G., Vigliano, M., Longo, G., Franchini, E., Secchiero, P., et al. (2018). Gene-gene interactions among coding genes of iron-homeostasis proteins and APOE-alleles in cognitive impairment diseases. *PLOS ONE* 13, e0193867. doi:10.1371/journal.pone.0193867.

Todorich, B., Pasquini, J. M., Garcia, C. I., Paez, P. M., and Connor, J. R. (2009). Oligodendrocytes and myelination: The role of iron. *Glia* 57, 467–478. doi:https://doi.org/10.1002/glia.20784.

Torsdottir, G., Kristinsson, J., Snaedal, J., and Jóhannesson, T. (2011). Ceruloplasmin and Iron Proteins in the Serum of Patients with Alzheimer's Disease. *Dement Geriatr Cogn Dis Extra* 1, 366–371. doi:10.1159/000330467.

Toschi, N., Lista, S., Baldacci, F., Cavedo, E., Zetterberg, H., Blennow, K., et al. (2019). Biomarker-guided clustering of Alzheimer's disease clinical syndromes. *Neurobiol. Aging* 83, 42–53. doi:10.1016/j.neurobiolaging.2019.08.032.

Tripathi, A. K., Karmakar, S., Asthana, A., Ashok, A., Desai, V., Baksi, S., et al. (2017). Transport of Non-Transferrin Bound Iron to the Brain: Implications for Alzheimer's Disease. *Journal of Alzheimer's Disease* 58, 1109–1119. doi:10.3233/JAD-170097.

Tsatsanis, A., Wong, B. X., Gunn, A. P., Ayton, S., Bush, A. I., Devos, D., et al. (2020). Amyloidogenic processing of Alzheimer's disease β-amyloid precursor protein induces cellular iron retention. *Molecular Psychiatry*, 1–9. doi:10.1038/s41380-020-0762-0.

Vargas, T., Ugalde, C., Spuch, C., Antequera, D., Morán, M. J., Martín, M. A., et al. (2010). Aβ accumulation in choroid plexus is associated with mitochondrial-induced apoptosis. *Neurobiology of Aging* 31, 1569–1581. doi:10.1016/j.neurobiolaging.2008.08.017.

Vermunt, L., Sikkes, S. A. M., van den Hout, A., Handels, R., Bos, I., van der Flier, W. M., et al. (2019). Duration of preclinical, prodromal, and dementia stages of Alzheimer's disease in relation to age, sex, and APOE genotype. *Alzheimers Dement* 15, 888–898. doi:10.1016/j.jalz.2019.04.001.

Villemagne, V. L., Pike, K. E., Darby, D., Maruff, P., Savage, G., Ng, S., et al. (2008). Abeta deposits in older non-demented individuals with cognitive decline are indicative of preclinical Alzheimer's disease. *Neuropsychologia* 46, 1688–1697. doi:10.1016/j.neuropsychologia.2008.02.008.

Wang, X., Li, G. J., and Zheng, W. (2008). Efflux of Iron from the Cerebrospinal Fluid to the Blood at the Blood-CSF Barrier: Effect of Manganese Exposure. *Exp Biol Med (Maywood)* 233, 1561–1571. doi:10.3181/0803-RM-104.

Wang, Y., and Liu, T. (2015). Quantitative susceptibility mapping (QSM): Decoding MRI data for a tissue magnetic biomarker. *Magnetic Resonance in Medicine* 73, 82–101. doi:https://doi.org/10.1002/mrm.25358.

Ward, R. J., Zucca, F. A., Duyn, J. H., Crichton, R. R., and Zecca, L. (2014). The role of iron in brain ageing and neurodegenerative disorders. *The Lancet Neurology* 13, 1045–1060. doi:10.1016/S1474-4422(14)70117-6.

Wessling-Resnick, M. (2006). Iron Imports. III. Transfer of iron from the mucosa into circulation. *American Journal of Physiology-Gastrointestinal and Liver Physiology* 290, G1–G6. doi:10.1152/ajpgi.00415.2005.

Winterbourn, C. C. (1995). Toxicity of iron and hydrogen peroxide: the Fenton reaction. *Toxicology Letters* 82–83, 969–974. doi:10.1016/0378-4274(95)03532-X.

Wong, A., Ye, M., Levy, A., Rothstein, J., Bergles, D., and Searson, P. C. (2013). The blood-brain barrier: an engineering perspective. *Front. Neuroeng.* 6. doi:10.3389/fneng.2013.00007.

Worwood, M. Indicators of the iron status of populations: ferritin. 44.

Wu, L. J., Leenders, A. G. M., Cooperman, S., Meyron-Holtz, E., Smith, S., Land, W., et al. (2004). Expression of the iron transporter ferroportin in synaptic vesicles and the blood–brain barrier. *Brain Research* 1001, 108–117. doi:10.1016/j.brainres.2003.10.066.

Wu, W. H., Wang, F. S., and Chang, M. S. (2008). Dynamic sensitivity analysis of biological systems. *BMC Bioinformatics* 9, S17. doi:10.1186/1471-2105-9-S12-S17.

Xie, W., Guo, Z., Gao, F., Gao, Q., Wang, D., Liaw, B., et al. (2018). Shape-, size- and structure-controlled synthesis and biocompatibility of iron oxide nanoparticles for magnetic theranostics. *Theranostics* 8, 3284–3307. doi:10.7150/thno.25220.

Xie, Y., Hou, W., Song, X., Yu, Y., Huang, J., Sun, X., et al. (2016). Ferroptosis: process and function. *Cell Death & Differentiation* 23, 369–379. doi:10.1038/cdd.2015.158.

Yamamoto, A., Shin, R.-W., Hasegawa, K., Naiki, H., Sato, H., Yoshimasu, F., et al. (2002). Iron (III) induces aggregation of hyperphosphorylated tau and its reduction to iron (II) reverses the aggregation: implications in the formation of neurofibrillary tangles of Alzheimer's disease. *J. Neurochem.* 82, 1137–1147. doi:10.1046/j.1471-4159.2002.t01-1-01061.x.

Yamanishi, H., Iyama, S., Yamaguchi, Y., Kanakura, Y., and Iwatani, Y. (2002). Modification of fully automated total iron-binding capacity (TIBC) assay in serum and comparison with dimension TIBC method. *Clin Chem* 48, 1565–1570.

Yamanishi, H., Iyama, S., Yamaguchi, Y., Kanakura, Y., and Iwatani, Y. (2003). Total Iron-binding Capacity Calculated from Serum Transferrin Concentration or Serum Iron Concentration and Unsaturated Iron-binding Capacity. *Clinical Chemistry* 49, 175–178. doi:10.1373/49.1.175.

Yan, N., and Zhang, J. (2020). Iron Metabolism, Ferroptosis, and the Links With Alzheimer's Disease. *Front. Neurosci.* 13. doi:10.3389/fnins.2019.01443.

Yang, D., Ng, X. Q., and Walczyk, T. (2019). Quantification of non-transferrin bound iron (NTBI) in human serum by isotope dilution mass spectrometry (IDMS). *J. Anal. At. Spectrom.* 34, 1988–1997. doi:10.1039/C9JA00142E.

Yang, W. S., Kim, K. J., Gaschler, M. M., Patel, M., Shchepinov, M. S., and Stockwell, B. R. (2016). Peroxidation of polyunsaturated fatty acids by lipoxygenases drives ferroptosis. *PNAS* 113, E4966–E4975. doi:10.1073/pnas.1603244113.

Yang, W. S., SriRamaratnam, R., Welsch, M. E., Shimada, K., Skouta, R., Viswanathan, V. S., et al. (2014). Regulation of Ferroptotic Cancer Cell Death by GPX4. *Cell* 156, 317–331. doi:10.1016/j.cell.2013.12.010.

Yang, W. S., and Stockwell, B. R. (2008). Synthetic Lethal Screening Identifies Compounds Activating Iron-Dependent, Nonapoptotic Cell Death in Oncogenic-RAS-Harboring Cancer Cells. *Chemistry & Biology* 15, 234–245. doi:10.1016/j.chembiol.2008.02.010.

Yang, W. S., and Stockwell, B. R. (2016). Ferroptosis: Death by Lipid Peroxidation. *Trends in Cell Biology* 26, 165–176. doi:10.1016/j.tcb.2015.10.014.

Yao, J., Hsu, C.-H., Li, Z., Kim, T. S., Hwang, L.-P., Lin, Y.-C., et al. (2015). Magnetic Resonance Nano-Theranostics for Glioblastoma Multiforme. *Curr. Pharm. Des.* 21, 5256–5266. doi:10.2174/1381612821666150923103307.

Yarjanli, Z., Ghaedi, K., Esmaeili, A., Rahgozar, S., and Zarrabi, A. (2017). Iron oxide nanoparticles may damage to the neural tissue through iron accumulation, oxidative stress, and protein aggregation. *BMC Neurosci* 18, 51. doi:10.1186/s12868-017-0369-9.

Young, A. L., Marinescu, R. V., Oxtoby, N. P., Bocchetta, M., Yong, K., Firth, N. C., et al. (2018). Uncovering the heterogeneity and temporal complexity of neurodegenerative diseases with Subtype and Stage Inference. *Nat Commun* 9, 4273. doi:10.1038/s41467-018-05892-0.

Zecca, L., Stroppolo, A., Gatti, A., Tampellini, D., Toscani, M., Gallorini, M., et al. (2004a). The role of iron and copper molecules in the neuronal vulnerability of locus coeruleus and substantia nigra during aging. *PNAS* 101, 9843–9848. doi:10.1073/pnas.0403495101.

Zecca, L., Youdim, M. B. H., Riederer, P., Connor, J. R., and Crichton, R. R. (2004b). Iron, brain ageing and neurodegenerative disorders. *Nat. Rev. Neurosci.* 5, 863–873. doi:10.1038/nrn1537.

Zerpa, G. A. de A., Saleh, M.-C., Fernández, P. M., Guillou, F., Monteros, A. E. de los, Vellis, J. de, et al. (2000). Alternative splicing prevents transferrin secretion during differentiation of a human oligodendrocyte cell line. *Journal of Neuroscience Research* 61, 388–395. doi:https://doi.org/10.1002/1097-4547(20000815)61:4<388::AID-JNR5>3.0.CO;2-Q.

Zhao, Z., Nelson, A. R., Betsholtz, C., and Zlokovic, B. V. (2015). Establishment and Dysfunction of the Blood-Brain Barrier. *Cell* 163, 1064–1078. doi:10.1016/j.cell.2015.10.067.

Zheng, W., Aschner, M., and Ghersi-Egea, J.-F. (2003). Brain barrier systems: a new frontier in metal neurotoxicological research. *Toxicology and Applied Pharmacology* 192, 1–11. doi:10.1016/S0041-008X(03)00251-5.

Zheng, W., and Monnot, A. D. (2012). Regulation of Brain Iron and Copper Homeostasis by Brain Barrier Systems: Implication in Neurodegenerative Diseases. *Pharmacol Ther* 133, 177–188. doi:10.1016/j.pharmthera.2011.10.006.

Zhu, W.-Z., Zhong, W., Wang, W., Zhan, C.-J., Wang, C.-Y., Qi, J.-P., et al. (2009). Quantitative MR phase-corrected imaging to investigate increased brain iron deposition of patients with Alzheimer disease. *Radiology* 253, 497–504. doi:10.1148/radiol.2532082324.

Zi, Z. (2011). Sensitivity analysis approaches applied to systems biology models. *IET Syst Biol* 5, 336–336. doi:10.1049/iet-syb.2011.0015.

Zlokovic, B. V. (2011). Neurovascular pathways to neurodegeneration in Alzheimer's disease and other disorders. *Nature Reviews Neuroscience* 12, 723–738. doi:10.1038/nrn3114.

Zorzi, G., Zibordi, F., Chiapparini, L., Bertini, E., Russo, L., Piga, A., et al. (2011). Iron-related MRI images in patients with pantothenate kinase–associated neurodegeneration (PKAN) treated with deferiprone: Results of a phase II pilot trial. *Movement Disorders* 26, 1755–1759. doi:10.1002/mds.23751.

Zullino, S., Argenziano, M., Ansari, S., Ciprian, R., Nasi, L., Albertini, F., et al. (2019). Superparamagnetic Oxygen-Loaded Nanobubbles to Enhance Tumor Oxygenation During Hyperthermia. *Front Pharmacol* 10. doi:10.3389/fphar.2019.01001.